

**Evidence for the W<sub>WW</sub> Production in pp Collisions  
with the ATLAS Detector**

by

**Ismet Siral**

**A dissertation submitted in partial fulfillment  
of the requirements for the degree of  
Doctor of Philosophy  
(Physics)  
in the University of Michigan  
2019**

**Doctoral Committee:**

**Associate Professor Junjie Zhu, Chair  
Professor Aaron T. Pierce  
Professor Bing Zhou  
Professor Ji Zhu**

Ismet Siral

[isiral@umich.edu](mailto:isiral@umich.edu)

ORCID iD: [0000-0003-4554-1831](https://orcid.org/0000-0003-4554-1831)

© Ismet Siral 2019

## ACKNOWLEDGMENTS

Pursuing a career in physics has been a long-standing dream. The last four and a half years of my life have been both challenging and enjoyable, and I would like to thank everybody who has supported me in my dream. First and foremost, I would like to thank my Ph.D. adviser Junjie Zhu who supported me unconditionally in all of the steps of my Ph.D. He has been a great mentor to me. I would also like to thank my colleagues who worked on the "Evidence for the  $WW$  Production in  $pp$  collisions" paper with me. Additional thanks goes to other Michigan professors Aaron Pierce, Bing Zhou, and Jianming Qian, and my old advisers Erkan Ozcan and Gokhan Unel who were there to support me on achieving my dreams. During my Ph.D., I worked with amazing post-docs whom are: Jacob Searcy, Alex Tuna and Siyuan Sun, and I would like to thank all of them for their patience and time. Special gratitude goes to the Department of Energy, University of Michigan, and CERN for providing the means necessary for me to complete my Ph.D. I would also like to thank Ece Akilli, Tom Cheng, Jan Jongmanns, Matthew Klein, Ann Wang, Rongkun Wang, Zirui Wang, Aaron White, Zhongyukun Xu, Zhi Zheng and many others whom I shared career paths with. Last but not least, I would like to thank my parents, my brother and all my friends near and far for making me the person who I am today.

## PREFACE

This thesis covers a portion of the research that I have conducted during my Ph.D. at the University of Michigan under the supervision of Junjie Zhu. The contents of this thesis were published in the form of two papers: [1] (8 TeV paper) [2] (13 TeV paper). Due to the collaborative nature of the physics research, not all the work listed in these papers were conducted by me. My significant contributions in these papers were the semi-leptonic ( $\ell^\pm \nu \ell^\pm \nu jj$ ) channel in the 8 TeV paper and the  $W^\pm W^\pm W^\mp$  analysis in the 13 TeV paper.

# TABLE OF CONTENTS

<b>ACKNOWLEDGMENTS</b> . . . . .	<b>ii</b>
<b>PREFACE</b> . . . . .	<b>iii</b>
<b>LIST OF FIGURES</b> . . . . .	<b>vii</b>
<b>LIST OF TABLES</b> . . . . .	<b>xiv</b>
<b>LIST OF ABBREVIATIONS</b> . . . . .	<b>xvii</b>
<b>LIST OF SYMBOLS</b> . . . . .	<b>xx</b>
<b>ABSTRACT</b> . . . . .	<b>xxii</b>
<b>CHAPTER</b>	
<b>1 Introduction</b> . . . . .	<b>1</b>
<b>2 Theory</b> . . . . .	<b>3</b>
2.1 The Standard Model Theory . . . . .	3
2.2 The Standard Model Formalism . . . . .	4
2.2.1 Quantum Electrodynamics . . . . .	5
2.2.2 The Yang-Mills Theory . . . . .	6
2.2.3 The Electroweak Theory . . . . .	7
2.2.4 The Higgs Mechanism . . . . .	8
2.2.5 Quantum Chromodynamics . . . . .	10
2.2.6 The Standard Model Lagrangian . . . . .	11
2.2.7 Triple and Quartic Gauge Couplings . . . . .	11
2.3 Effective Field Theory . . . . .	12
<b>3 The LHC and the ATLAS Experiment</b> . . . . .	<b>15</b>
3.1 The Large Hadron Collider . . . . .	15
3.2 The ATLAS Detector . . . . .	17
3.2.1 The Coordinate System . . . . .	17
3.2.2 The Inner Detector . . . . .	17
3.2.3 The Calorimeter System . . . . .	20
3.2.4 The Muon Spectrometer . . . . .	22
3.3 Trigger and Data Acquisition . . . . .	24
3.3.1 The Level-1 Trigger . . . . .	25

3.3.2	High-Level Trigger . . . . .	26
3.4	Simulation . . . . .	26
<b>4</b>	<b>Object Reconstruction at ATLAS . . . . .</b>	<b>28</b>
4.1	Track Reconstruction . . . . .	28
4.1.1	Inner Detector Track Reconstruction . . . . .	28
4.2	Vertex Reconstruction . . . . .	30
4.3	Electrons . . . . .	31
4.3.1	Electron Reconstruction . . . . .	31
4.3.2	Electron Identification . . . . .	31
4.3.3	Electron Isolation . . . . .	32
4.4	Muons . . . . .	33
4.4.1	Muon Track Reconstruction . . . . .	33
4.4.2	Muon Reconstruction . . . . .	33
4.4.3	Muon Identification . . . . .	34
4.4.4	Muon Isolation . . . . .	35
4.5	Jets . . . . .	36
4.5.1	Jet Reconstruction and Calibration . . . . .	36
4.5.2	<i>B</i> -Tagging . . . . .	37
4.6	Missing Transverse Energy . . . . .	37
<b>5</b>	<b>Physics Object Selection . . . . .</b>	<b>39</b>
5.1	Triggers . . . . .	39
5.2	Electrons . . . . .	39
5.3	Muons . . . . .	43
5.4	Jets . . . . .	45
5.5	Overlap Removal . . . . .	45
5.6	Missing Transverse Momentum . . . . .	46
<b>6</b>	<b>Signal Event Selection . . . . .</b>	<b>47</b>
6.1	Semi-Leptonic Signal Region . . . . .	47
6.2	Fully-Leptonic Signal Region . . . . .	48
<b>7</b>	<b>Data and Monte Carlo Samples . . . . .</b>	<b>49</b>
7.1	Signal Samples . . . . .	49
7.2	Background Samples . . . . .	50
<b>8</b>	<b>Background Estimations . . . . .</b>	<b>52</b>
8.1	Charge misID Background . . . . .	53
8.1.1	Charge misID Rate Estimation . . . . .	54
8.1.2	Charge misID Validation . . . . .	55
8.2	Non-Prompt Background . . . . .	58
8.2.1	Non-Prompt Factor Background Composition . . . . .	58
8.2.2	Non-Prompt Factor Determination . . . . .	64
8.3	Photon Conversion Background . . . . .	70
8.3.1	Photon Conversion Rate Determination . . . . .	70

8.4	WZ Background Validation . . . . .	73
8.5	Overall Background Validation Using the $W$ Mass Side-Band Validation Region . . . . .	80
<b>9</b>	<b>Systematic Uncertainties . . . . .</b>	<b>89</b>
9.1	Experimental Systematics . . . . .	89
9.1.1	Non-Prompt Lepton Uncertainties . . . . .	90
9.1.2	Charge misID Uncertainties . . . . .	91
9.1.3	Photon Conversion Rate Uncertainties . . . . .	92
9.1.4	Luminosity and Pile-up Uncertainty . . . . .	92
9.1.5	Muon Uncertainties . . . . .	93
9.1.6	Electron Uncertainties . . . . .	93
9.1.7	Jet Uncertainties . . . . .	94
9.1.8	Missing Transverse Energy ( $E_T^{\text{miss}}$ ) Uncertainties . . . . .	94
9.2	Theoretical Uncertainties . . . . .	94
<b>10</b>	<b>WVZ Analysis . . . . .</b>	<b>96</b>
10.1	Experimental Signatures and Backgrounds . . . . .	96
10.2	Object Selection . . . . .	97
10.3	Analysis Strategy . . . . .	97
10.3.1	Three Lepton BDT . . . . .	98
10.3.2	Four Lepton BDT . . . . .	99
10.4	Systematic Uncertainties . . . . .	101
<b>11</b>	<b>Fitting Procedure . . . . .</b>	<b>102</b>
<b>12</b>	<b>Results . . . . .</b>	<b>105</b>
12.1	WWW Results . . . . .	105
12.2	WVZ Results . . . . .	119
12.3	Fitted Results . . . . .	121
12.4	Anomalous Quartic Gauge Couplings . . . . .	125
12.5	Future Prospects . . . . .	128
<b>13</b>	<b>Summary . . . . .</b>	<b>129</b>
	<b>Appendix . . . . .</b>	<b>131</b>
	<b>Bibliography . . . . .</b>	<b>137</b>

## LIST OF FIGURES

1.1	Feynman diagrams that produce the $W^\pm W^\pm W^\mp$ final state in $pp$ collisions. . . .	1
2.1	Properties of all known fermions and bosons [4]. . . . .	4
2.2	The Higgs potential as a function of $\Phi$ [10]. . . . .	9
3.1	The LHC complex [19]. . . . .	16
3.2	Overview of the ATLAS detector and its sub-detectors [27]. . . . .	18
3.3	Overview of the ATLAS inner detector [29]. . . . .	19
3.4	Overview of the ATLAS Calorimeter System [31]. . . . .	20
3.5	Overview of the whole MS. The side view is on the left and the transverse view is on the right [33]. . . . .	22
3.6	Detailed view of the $2 \times 3/2 \times 4$ MDT chamber structure [33]. The Monitored Drift Tubes (MDT) Chamber is composed of two layers of MDTs stacks with a gap in the middle. Each of these stacks are formed of 3 or 4 layers MDT tubes.	23
3.7	Internal structure of the CSC detector. The multiwire proportional chamber structure can be seen with its anode wires and cathode strips [33]. The anode-cathode spacing ( $d$ ) and wire pitch ( $S$ ) is 2.54mm, and the cathode readout pitch ( $W$ ) is 5.08 mm. . . . .	24
3.8	Overview of the TDAQ system [34]. The diagram shows the information flow path from the detector to the trigger systems on the left side, and the trigger decision is marked in red. The readout system is shown on the right side. . . .	25
3.9	The ATLAS simulation flow diagram [35]. The diagram starts from event generators (top left) and passes through the full detector simulation (bottom to top right) where pile-up, hits, and electronics effects are simulated. The second row of the diagram shows how the truth information is handled. . . . .	27
4.1	Slice of the A Toroidal LHC Aparatus (ATLAS) detector. Hadrons, electrons, muons, neutrinos, and photons all leave different detector signatures at different sub-detectors [39]. . . . .	29
4.2	Electron identification efficiencies as a function of the electron $E_T$ for different working points [44]. . . . .	32
4.3	Comparison between data and MC for the muon identification efficiency as a function of the muon $p_T$ (left) and $\eta$ -dependent identification efficiencies for different working points [49]. . . . .	35
4.4	The $MV2c10$ BDT output distribution (left) and tag efficiency (right) [53]. . . .	37



8.1	Electron charge-flip rate measured as a function of the electron $p_T$ (left) and $\eta$ (right). It is observed that the charge-flip rate increases with both $p_T$ and $\eta$ . . . . .	55
8.2	The leading (top left) and the sub-leading (top right) electron $p_T$ distributions, and the di-lepton invariant mass (bottom) distribution with two same-sign electrons. These events are selected using the criteria defined for the Z Mass Window Validation Region to validate the charge-flip background estimation, and overall good modeling has been observed. Only statistical uncertainties are shown. . . . .	57
8.3	Data and MC prediction for $m_{3\ell}$ , $E_T^{\text{miss}}$ , and $N_j$ in the $\ell^\pm\nu\ell^\pm\nu\ell^\mp\nu$ ID+ID+anti-ID non-prompt region, for the inclusive (left), $ee\mu$ (center), and $\mu\mu e$ (right) regions. These plots indicates that the $t\bar{t}$ process is the dominant contributor of non-prompt leptons in this region. . . . .	59
8.4	Data and MC prediction for $\Delta\phi$ between $3\ell$ and $E_T^{\text{miss}}$ , leading lepton $p_T$ and $q_0 \times q_1$ in the $\ell^\pm\nu\ell^\pm\nu\ell^\mp\nu$ ID+ID+anti-ID control region, for the inclusive (left), $ee\mu$ (center), and $\mu\mu e$ (right) regions. These plots indicates that the $t\bar{t}$ process is the dominant contributor of non-prompt leptons in this region. . . . .	60
8.5	Data and MC prediction for leading lepton $p_T$ in the $\ell^\pm\nu\ell^\pm\nu jj$ ID+anti-ID non-prompt region. The four plots in each row show the $ee$ , $e\mu$ , $\mu e$ , and $\mu\mu$ channels separately. Simulation suggests that the dominant contributors of non-prompt leptons in this region come from processes with heavy flavor decay. . . . .	61
8.6	Data and MC prediction for sub-leading lepton $p_T$ in the $\ell^\pm\nu\ell^\pm\nu jj$ ID+anti-ID non-prompt region. The four plots in each row show the $ee$ , $e\mu$ , $\mu e$ , and $\mu\mu$ channels separately. Simulation suggests that the dominant contributors of non-prompt leptons in this region come from processes with heavy flavor decay. . . . .	62
8.7	Data and MC prediction for $m_{jj}$ in the $\ell^\pm\nu\ell^\pm\nu jj$ ID+anti-ID non-prompt region. The four plots in each row show the $ee$ , $e\mu$ , $\mu e$ , and $\mu\mu$ channels separately. Simulation suggests that the dominant contributors of non-prompt leptons in this region come from processes with heavy flavor decay. . . . .	63
8.8	The leading lepton $p_T$ distribution in the $ee$ (top left), $e\mu$ (top right), $\mu e$ (bottom left) and $\mu\mu$ (bottom right) channels in the $\ell^\pm\nu\ell^\pm\nu jj$ $b$ -Tagged Region for ID+ID region. The normalization of the prediction will agree by construction, but the shapes will not necessarily agree. . . . .	66
8.9	The $E_T^{\text{miss}}$ distribution in the $ee$ (top left), $e\mu$ (top right), $\mu e$ (bottom left) and $\mu\mu$ (bottom right) channels in the $\ell^\pm\nu\ell^\pm\nu jj$ $b$ -Tagged Region for ID+ID region. The normalization of the prediction will agree by construction, but the shapes will not necessarily agree. . . . .	67
8.10	Number of jets distribution in the $ee$ (top left), $e\mu$ (top right), $\mu e$ (bottom left) and $\mu\mu$ (bottom right) channels in the $\ell^\pm\nu\ell^\pm\nu jj$ $b$ -Tagged Region for ID+ID region. The normalization of the prediction will agree by construction, but the shapes will not necessarily agree. . . . .	68
8.11	Inclusive leading (top left), sub-leading (top right) and sub-sub leading (bottom left) lepton $p_T$ distributions and $m_{\ell\ell\ell}$ (bottom right) distributions in the $\ell^\pm\nu\ell^\pm\nu\ell^\mp\nu$ $b$ -Tagged Region for ID+ID region. The normalization of the prediction will agree by construction, but the shapes will not necessarily agree. . . . .	69

8.12	The $m(\mu\mu)$ distribution for the signal electron $Z\gamma$ control region (left) and photon-like electron $Z\gamma$ control region (right). The data-driven photon prediction is included in the plot on the left. Simulation predicts very few events to satisfy the photon-like electron selection, suggesting the region is pure in photons reconstructed as electrons. . . . .	71
8.13	The third lepton $p_T$ distribution for the signal electron $Z\gamma$ control region ( $\mu\mu e$ ) (left) and photon-like electron $Z\gamma$ control region (right). The data-driven photon prediction is included in the plot on the left. Simulation predicts very few events to satisfy the photon-like electron selection, suggesting the region is pure in photons reconstructed as electrons. . . . .	71
8.14	The missing transverse energy distribution for the signal electron $Z\gamma$ control region ( $\mu\mu e$ ) (left) and “photon-like electron $Z\gamma$ control region” (right). The data-driven photon prediction is included in the plot on the left. Simulation predicts very few events to satisfy the photon-like electron selection, suggesting the region is pure in photons reconstructed as electrons. . . . .	72
8.15	The $N(\text{jets})$ distribution for the signal electron $Z\gamma$ control region ( $\mu\mu e$ ) (left) and photon-like electron $Z\gamma$ control region (right). The data-driven photon prediction is included in the plot on the left. Simulation predicts very few events to satisfy the photon-like electron selection, suggesting the region is pure in photons reconstructed as electrons. . . . .	72
8.16	The leading lepton $p_T$ distribution in the $eee$ (top left), $ee\mu$ (top right), $\mu\mu e$ (bottom left), and $\mu\mu\mu$ (bottom right) channels. These events are selected using the criteria defined for the $WZ$ control region. . . . .	74
8.17	The leading lepton $\eta$ distribution in the $eee$ (top left), $ee\mu$ (top right), $\mu\mu e$ (bottom left) and $\mu\mu\mu$ (bottom right) channels. These events are selected using the criteria defined for the $WZ$ control region. . . . .	76
8.18	Jet multiplicity distribution in the $eee$ (left), $eee$ (top left), $ee\mu$ (top right), $\mu\mu e$ (bottom left), and $\mu\mu\mu$ (bottom right) channels. These events are selected using the criteria defined for the $WZ$ control region. The $N(\text{jets})$ reweighting, discussed at the beginning of the section, is applied here and throughout the analysis. . . . .	77
8.19	The $E_T^{\text{miss}}$ distribution in the $eee$ (top left), $ee\mu$ (top right), $\mu\mu e$ (bottom left), and $\mu\mu\mu$ (bottom right) channels. These events are selected using the criteria defined for the $WZ$ control region. . . . .	78
8.20	The $M(\ell\ell\ell)$ distribution in the $eee$ (top left), $ee\mu$ (top right), $\mu\mu e$ (bottom left), and $\mu\mu\mu$ (bottom right) channels. These events are selected using the criteria defined for the $WZ$ control region. . . . .	79
8.21	The $m_{jj}$ distribution with statistical uncertainties in the $ee$ (top left), $e\mu$ (top right), $\mu e$ (bottom left), and $\mu\mu$ (bottom right) channels. These events are selected using the $W$ Mass Side-Band Validation Region criteria, which are identical to the $\ell^\pm\nu\ell^\pm\nu jj$ signal region except that $m_{jj}$ must be outside the $W$ mass window. This region is used to validate various background estimations. .	81

8.22	The $\Delta\eta_{jj}$ distribution with statistical uncertainties in the $ee$ (top left), $e\mu$ (top right), $\mu e$ (bottom left), and $\mu\mu$ (bottom right) channels. These events are selected using the $W$ Mass Side-Band Validation Region criteria, which are identical to the $\ell^\pm\nu\ell^\pm\nu jj$ signal region except that $m_{jj}$ must be outside the $W$ mass window. This region is used to validate various background estimations. . . . .	82
8.23	The leading lepton $p_T$ distribution with statistical uncertainties in the $ee$ (top left), $e\mu$ (top right), $\mu e$ (bottom left), and $\mu\mu$ (bottom right) channels. These events are selected using the $W$ Mass Side-Band Validation Region criteria, which are identical to the $\ell^\pm\nu\ell^\pm\nu jj$ signal region except that $m_{jj}$ must be outside the $W$ mass window. This region is used to validate various background estimations. . . . .	83
8.24	The subleading lepton $p_T$ distribution with statistical uncertainties in the $ee$ (top left), $e\mu$ (top right), $\mu e$ (bottom left), and $\mu\mu$ (bottom right) channels. These events are selected using the $W$ Mass Side-Band Validation Region criteria, which are identical to the $\ell^\pm\nu\ell^\pm\nu jj$ signal region except that $m_{jj}$ must be outside the $W$ mass window. This region is used to validate various background estimations. . . . .	84
8.25	The leading jet $p_T$ distribution with statistical uncertainties in the $ee$ (top left), $e\mu$ (top right), $\mu e$ (bottom left), and $\mu\mu$ (bottom right) channels. These events are selected using the $W$ Mass Side-Band Validation Region criteria, which are identical to the $\ell^\pm\nu\ell^\pm\nu jj$ signal region except that $m_{jj}$ must be outside the $W$ mass window. This region is used to validate various background estimations. . . . .	85
8.26	The subleading jet $p_T$ distribution with statistical uncertainties in the $ee$ (top left), $e\mu$ (top right), $\mu e$ (bottom left), and $\mu\mu$ (bottom right) channels. These events are selected using the $W$ Mass Side-Band Validation Region criteria, which are identical to the $\ell^\pm\nu\ell^\pm\nu jj$ signal region except that $m_{jj}$ must be outside the $W$ mass window. This region is used to validate various background estimations. . . . .	86
8.27	The $E_T^{\text{miss}}$ distribution with statistical uncertainties in the $ee$ (top left), $e\mu$ (top right), $\mu e$ (bottom left), and $\mu\mu$ (bottom right) channels. These events are selected using the $W$ Mass Side-Band Validation Region criteria, which are identical to the $\ell^\pm\nu\ell^\pm\nu jj$ signal region except that $m_{jj}$ must be outside the $W$ mass window. This region is used to validate various background estimations. . . . .	87
9.1	$p_T$ dependent non-prompt rates with statistical uncertainties for electrons (left) and muons (right) respectively. These rates are compared with inclusive non-prompt rates and the differences are introduced as a systematic uncertainty. . . . .	91
10.1	Feynman diagrams that produce the $WWZ$ final state in $pp$ collisions. . . . .	96
10.2	Boosted Decision Tree (BDT) responses in $3\ell + 1\text{jet}$ (top left), $3\ell + 2\text{jet}$ (top right), and $3\ell + 3\text{jet}$ (bottom). The BDTG label in the $x$ -axis stands for gradient boosted decision trees which is the technique used [68]. Only statistical uncertainties are shown. . . . .	99

10.3	BDT responses in $4\ell$ DF (top right), on-shell SF (top left) and off-shell SF (bottom) regions. The BDTG label in the x-axis stands for gradient boosted decision trees, which is the technique that is used [68]. Only statistical uncertainties are shown. . . . .	100
12.1	The observed data are compared to the signal plus background model in the $ee$ (left), $e\mu$ (mid left), $\mu e$ (mid right), $\mu\mu$ (right) signal regions for the $\ell^\pm\nu\ell^\pm\nu jj$ channel as a function of the $m_{jj}$ . Signal and backgrounds are pre-fit. The uncertainty is statistical uncertainty only. . . . .	107
12.2	The observed data are compared to the signal plus background model in the $ee$ (left), $e\mu$ (mid left), $\mu e$ (mid right), $\mu\mu$ (right) signal regions for the $\ell^\pm\nu\ell^\pm\nu jj$ channel as a function of the $m_{jj}$ . Signal and backgrounds are normalized to the expected number of events after the fit. The uncertainty band includes both the statistical and systematic uncertainties as obtained by the fit. In the post-fit plots, the $WWW$ tags have been replaced with $VVV$ as these results are presented with the $WVZ$ analysis. . . . .	108
12.3	The observed data are compared to the signal plus background model in the inclusive signal regions for the $\ell^\pm\nu\ell^\pm\nu jj$ (left) and $\ell^\pm\nu\ell^\pm\nu\ell^\mp\nu$ channels (right) as a function of the $m_{jj}$ for the left plot. Signal and backgrounds are normalized to the expected number of events after the fit. The uncertainty band includes both the statistical and systematic uncertainties as obtained by the fit. In the post-fit plots, the $WWW$ tags have been replaced with $VVV$ as these results are presented with the $WVZ$ analysis. . . . .	109
12.4	The observed data are compared to the signal plus background model in the $ee$ (top left), $e\mu$ (top right), $\mu e$ (bottom left), $\mu\mu$ (bottom right) signal region for the $\ell^\pm\nu\ell^\pm\nu jj$ channel as a function of the scalar sum of all particles $p_T$ . The uncertainty band is statistical uncertainty only. . . . .	110
12.5	The observed data are compared to the signal plus background model in the $ee$ (top left), $e\mu$ (top right), $\mu e$ (bottom left), $\mu\mu$ (bottom right) signal region for the $\ell^\pm\nu\ell^\pm\nu jj$ channel as a function of the leading jet $\eta$ . The uncertainty band is statistical uncertainty only. . . . .	111
12.6	The observed data are compared to the signal plus background model in the $ee$ (top left), $e\mu$ (top right), $\mu e$ (bottom left), $\mu\mu$ (bottom right) signal region for the $\ell^\pm\nu\ell^\pm\nu jj$ channel as a function of the leading jet $p_T$ . The uncertainty band is statistical uncertainty only. . . . .	112
12.7	The observed data are compared to the signal plus background model in the $ee$ (top left), $e\mu$ (top right), $\mu e$ (bottom left), $\mu\mu$ (bottom right) signal region for the $\ell^\pm\nu\ell^\pm\nu jj$ channel as a function of the $E_T^{\text{miss}}$ . The uncertainty band is statistical uncertainty only. . . . .	113
12.8	The observed data are compared to the signal plus background model in the $ee$ (top left), $e\mu$ (top right), $\mu e$ (bottom left), $\mu\mu$ (bottom right) signal region for the $\ell^\pm\nu\ell^\pm\nu jj$ channel as a function of the leading lepton $p_T$ . The uncertainty band is statistical uncertainty only. . . . .	114

12.9	The observed data are compared to the signal plus background model in the $ee$ (top left), $e\mu$ (top right), $\mu e$ (bottom left), $\mu\mu$ (bottom right) signal region for the $\ell^\pm\nu\ell^\pm\nu jj$ channel as a function of the leading lepton $m_{ll}$ . The uncertainty band is statistical uncertainty only. . . . .	115
12.10	The observed data are compared to the signal plus background model in the <i>inclusive</i> (left), $ee\mu$ (middle), $\mu\mu e$ (right) signal region for the $\ell^\pm\nu\ell^\pm\nu\ell^\mp\nu$ channel as a function of the leading lepton $m_{ll}$ . The uncertainty band is statistical uncertainty only. . . . .	116
12.11	The observed data are compared to the signal plus background model in the <i>inclusive</i> (left), $ee\mu$ (middle), $\mu\mu e$ (right) signal region for the $\ell^\pm\nu\ell^\pm\nu\ell^\mp\nu$ channel as a function of the $E_T^{\text{miss}}$ . The uncertainty band is statistical uncertainty only. . . . .	116
12.12	The observed data are compared to the signal plus background model in the <i>inclusive</i> (left), $ee\mu$ (middle), $\mu\mu e$ (right) signal region for the $\ell^\pm\nu\ell^\pm\nu\ell^\mp\nu$ channel as a function of the $N_{\text{jets}}$ . The uncertainty band is statistical uncertainty only. . . . .	117
12.13	The observed data are compared to the signal plus background model in the <i>inclusive</i> (left), $ee\mu$ (middle), $\mu\mu e$ (right) signal region for the $\ell^\pm\nu\ell^\pm\nu\ell^\mp\nu$ channel as a function of the leading lepton $p_T$ . The uncertainty band is statistical uncertainty only. . . . .	117
12.14	The observed data are compared to the signal plus background model in the <i>inclusive</i> (left), $ee\mu$ (middle), $\mu\mu e$ (right) signal region for the $\ell^\pm\nu\ell^\pm\nu\ell^\mp\nu$ channel as a function of the sub-leading lepton $p_T$ . The uncertainty band is statistical uncertainty only. . . . .	117
12.15	The observed data are compared to the signal plus background model in the <i>inclusive</i> (left), $ee\mu$ (middle), $\mu\mu e$ (right) signal region for the $\ell^\pm\nu\ell^\pm\nu\ell^\mp\nu$ channel as a function of the 3 <sup>rd</sup> lepton $p_T$ . The uncertainty band is statistical uncertainty only. . . . .	118
12.16	The observed data are compared to the signal plus background model in the $3\ell + 1\text{jet}$ (left), $3\ell + 2\text{jet}$ (middle), $3\ell + 3 + \text{jet}$ (right) signal regions for the $WVZ$ analysis as a function of the BDT discriminant. Signal and backgrounds are normalized to the expected number of events after the fit. The uncertainty band includes both the statistical and systematic uncertainties as obtained by the fit. In the post-fit plots, the $WVZ$ tags have been replaced with $VVV$ as these results are presented with the $WWW$ analysis. . . . .	119
12.17	The observed data are compared to the signal plus background model in the $4\ell$ same-flavor on shell (left), $4\ell$ same-flavor off shell (middle), $4\ell$ different-flavor signal region (right) for the $WVZ$ analysis as a function of the BDT discriminant. Signal and backgrounds are normalized to the expected number of events after the fit. The uncertainty band includes both the statistical and systematic uncertainties as obtained by the fit. In the post-fit plots, the $WVZ$ tags have been replaced with $VVV$ as these results are presented with the $WWW$ analysis. . . . .	120
12.18	Ranking of the nuisance parameters according to their post-fit impact on the signal strength for the combined $VVV$ fit to data. . . . .	122

12.19	Extracted signal strengths $\mu$ for the four analysis regions and combination. . .	123
12.20	Event yields as a function of $\log_{10}(S/B)$ for data, background B and the signal S. Events in all 11 signal regions are included, and the predicted background yield is obtained from the global signal-plus-background fit. The tri-boson signal is shown for the best-fit value ( $\mu = 1.38$ ). The hatched band corresponds to the systematic uncertainties, and the statistical uncertainties are represented by the error bars on the data points. . . . .	124
12.21	The distribution of $m_T^{3\ell}$ (invariant transverse mass of three leptons) for the $\ell^\pm \nu \ell^\pm \nu \ell^\mp \nu$ channel (left) and the distribution of $\Sigma p_T$ (scalar sum of all particle $p_T$ s) for the $\ell^\pm \nu \ell^\pm \nu jj$ channel (right) as observed in the data (dots with error bars indicating the statistical uncertainties) and as expected from SM signal and background processes. The ratios between the observed numbers of events in data and the expected SM signal plus background contributions are shown in the lower panels. The dashed bands result from the systematic uncertainties on the sum of the signal plus background contributions. The “other backgrounds” contain prompt leptons and are estimated from MC. Contributions from aQGCs are also shown, assuming the non-unitarized case ( $\Lambda = \infty$ ) and two different sets of $\frac{f_{S0}}{\Lambda^4}$ and $\frac{f_{S1}}{\Lambda^4}$ configurations ( $\frac{f_{S0}}{\Lambda^4} = 2000 \text{ TeV}^{-4}$ , $\frac{f_{S1}}{\Lambda^4} = 2000 \text{ TeV}^{-4}$ and $\frac{f_{S0}}{\Lambda^4} = 2000 \text{ TeV}^{-4}$ , $\frac{f_{S1}}{\Lambda^4} = -6000 \text{ TeV}^{-4}$ ). The highest bin also includes events falling out of the range shown. . . . .	125
12.22	Expected 68% and 95% CL contours for $f_{s,1}$ vs $f_{s,0}$ compared to the observed 95% CL contour and the observed best-fit values at 8 TeV for cases when $\Lambda_{FF} = 0.5 \text{ TeV}$ (top left), $\Lambda_{FF} = 1 \text{ TeV}$ (top right), $\Lambda_{FF} = 2 \text{ TeV}$ (middle left), $\Lambda_{FF} = 3 \text{ TeV}$ (middle right), and $\Lambda_{FF} = \infty$ (bottom). . . . .	127
13.1	Summary of several Standard Model total production cross section measurements conducted at the ATLAS experiment, corrected for leptonic branching fractions, compared to the corresponding theoretical expectations[71]. . . . .	130

## LIST OF TABLES

2.1	Quartic gauge couplings allowed in the SM theory. . . . .	13
2.2	Triple gauge couplings allowed in the SM theory. . . . .	14
3.1	Status of the LHC as of 2019 and its running parameters [17][18]. . . . .	15
4.1	Track requirements for PV reconstruction [42]. In this table, hits refer to a detector element detecting the tracked particle and holes refer to the particle passing through areas that does not have detector coverage inside the detector structure. . . . .	30
5.1	Description of single-lepton triggers used. Each trigger has different isolation, quality and $p_T$ requirements to prevent these triggers from being pre-scaled. . .	39
5.2	ID electron definition. . . . .	41
5.3	Anti-ID electron definition. . . . .	41
5.4	Anti-BL electron definition. . . . .	42
5.5	Veto electron definition. . . . .	42
5.6	ID muon definition. . . . .	43
5.7	Anti-ID muon definition. . . . .	44
5.8	Veto muon definition. . . . .	44
6.1	Selection criteria used for the $\ell^\pm \nu \ell^\pm \nu jj$ signal region. . . . .	48
6.2	Selection criteria used for the $\ell^\pm \nu \ell^\pm \nu \ell^\mp \nu$ signal region. . . . .	48
7.1	Detailed Rivet cutflow for the $\ell^\pm \nu \ell^\pm \nu jj$ analysis. . . . .	50
7.2	Detailed Rivet cutflow for the $\ell^\pm \nu \ell^\pm \nu \ell^\mp \nu$ analysis. . . . .	51
8.1	Selection criteria for the region where charge misID rate is investigated. . . .	54
8.2	Selection criteria for the Z Mass Window Validation Region. . . . .	56
8.3	Yields of the Z Mass Window Validation Region. The statistical uncertainty error bars are shown. Overall good modeling has been observed. . . . .	56
8.4	Selection criteria used for the $\ell^\pm \nu \ell^\pm \nu jj$ $b$ -tagged region. . . . .	64
8.5	Selection criteria used for the $\ell^\pm \nu \ell^\pm \nu \ell^\mp \nu$ $b$ -tagged region. . . . .	64
8.6	The non-prompt rates used for scaling the non-prompt background. The rates derived from individual regions ( $\ell^\pm \nu \ell^\pm \nu jj$ and $\ell^\pm \nu \ell^\pm \nu \ell^\mp \nu$ ) are used for validation, and the combined rates are used for estimating the non-prompt background. The uncertainties are shown for statistical only. . . . .	65
8.7	Selection criteria used for the $Z\gamma$ control region. . . . .	70

8.8	Selection criteria used for the $WZ$ control region. . . . .	73
8.9	Event yields with statistical uncertainties for data and estimated SM back-grounds in the $WZ$ control region. . . . .	75
8.10	Selection criteria used for the $W$ mass side-band region. . . . .	80
8.11	Event yields with statistical uncertainties for data and estimated SM back-grounds in the $W$ Mass Side-Band Validation Region. . . . .	88
9.1	The photon mis-identification rate as measured in $W\gamma$ MC in the $\ell^\pm\nu\ell^\pm\nu jj$ signal region, and as measured in $Z\gamma$ MC in the $Z\gamma$ control region. . . . .	92
10.1	Pre-selection cuts applied to the $WVZ$ analysis. Here the $m_{\ell\ell}^Z$ variable is the mass of the reconstructed $Z$ boson. . . . .	97
10.2	List of discriminating variables that are used for the $3\ell$ BDT trainings at the $WVZ$ analysis. In this table, the total $H_T$ stands for scalar sum of all lepton and jet $p_T$ and hadronic or leptonic $H_T$ stands for scalar sum of all jet or lepton $H_T$ respectively. The $\ell_0$ , $\ell_1$ and $\ell_2$ stand for leading, sub-leading and sub-sub-leading leptons respectively. The $j_0$ and $j_1$ stand for leading and sub-leading jets respectively. Lastly, $m_T^{W\rightarrow\ell\nu}$ stands for the reconstructed transverse mass of the leptonically decaying $W$ boson. . . . .	98
10.3	List of discriminating variables that are used for the $4\ell$ BDT trainings. In this table, the total $H_T$ stands for scalar sum of all lepton and jet $p_T$ and hadronic or leptonic $H_T$ stands for scalar sum of all jet or lepton $H_T$ respectively. . . . .	100
12.1	Pre-fit background, signal and observed yields for the $WWW \rightarrow \ell\nu\ell\nu qq$ and $\ell\nu\ell\nu\ell\nu$ channels. Uncertainties shown are statistical only. . . . .	106
12.2	Post-fit background, signal and observed yields for the $WWW \rightarrow \ell\nu\ell\nu qq$ and $\ell\nu\ell\nu\ell\nu$ channels. Uncertainties on the predictions include both statistical and systematic uncertainties added in quadrature. . . . .	106
12.3	Post-fit background, signal and observed yields for the three-lepton and four-lepton channels of $WVZ$ analysis. Uncertainties on the predictions include both statistical and systematic uncertainties added in quadrature; correlations among systematic uncertainties are taken into account in the calculation of the total. . . . .	119
12.4	Summary of the effects of the most important groups of systematic uncertainties on $\mu_{VVV}$ . . . . .	122
12.5	Expected and observed significances with respect to the SM background-only hypothesis for the four $VVV$ channels entering the combined fit. The observed significance is not quoted if the best-fit value of $\mu$ is negative. . . . .	123
12.6	Expected and observed 95% CL intervals on $f_{s,0}$ ( $f_{s,1}$ ) for different $\Lambda_{FF}$ values, assuming $f_{s,1}$ ( $f_{s,0}$ ) to be zero at 8 TeV. . . . .	126
A.1	List of DSIDs and MC tags that are being used for all MC samples in the 13 TeV analysis. For all samples the DAOD_SUSY2 derivation has been used. . . . .	131
A.2	List of MC types and DSID's that are being used for all MC samples in the 8 TeV $\ell^\pm\nu\ell^\pm\nu\ell^\pm\nu$ analysis. . . . .	133



A.3 List of MC types and Full names that are being used for all MC samples in the  
8 TeV  $\ell^\pm\nu\ell^\pm\nu jj$  analysis. . . . . 136

## LIST OF ABBREVIATIONS

**SM** Standard Model

**ATLAS** A Toroidal LHC Aparatus

**CMS** Compact Muon Solenoid

**ALICE** A Large Ion Collider Experiment

**LHCb** Large Hadron Collider Beauty Experiment

**TOTEM** TOTal cross section, Elastic scattering and diffraction dissociation Measurement  
at the LHC

**LHCf** Large Hadron Collider Forward Experiment

**MoEDAL** Monopole and Exotics Detector at the LHC Experiment

**LHC** Large Hadron Collider

**CERN** Conseil Europeen Pour la Recherche Nuclaire  
European Organization for Nuclear Research

**LINAC** Linear Accelerator

**SCT** Semiconductor Tracker

**IBL** Insertable B-Layer

**ID** Inner Detector

**TRT** Transition Radiation Tracker

**EM** Electromagnetic

**LAr** Liquid Argon

**FCAL** Forward Calorimeter

**MS** Muon Spectrometer

**MDT** Monitored Drift Tubes

**CSC** Cathode Strip Chambers

**RPC** Resistive Plate Chambers  
**TGC** Thin Gap Chambers  
**TDAQ** Trigger and Data Acquisition  
**DAQ** Data Acquisition  
**L1** Level-1 Trigger  
**L1Calo** Level-1 Calorimeter Trigger  
**L1Muon** Level-1 Muon Trigger  
**L1Topo** Level-1 Topological Trigger  
**CTP** Central Trigger Processor  
**HLT** High Level Trigger  
 $E_T$  Transverse Energy  
 $E_T^{\text{miss}}$  Missing Transverse Energy  
**PV** Primary Vertex  
**MC** Monte Carlo  
**BDT** Boosted Decision Tree  
**aQGC** anomalous Quartic Gauge Couplings Leading Order  
**NLO** Next-to-Leading Order  
**PDF** Parton Distribution Function  
**PLV** Prompt-Lepton Veto  
**JVT** Jet Vertex Tagging  
**VBS** vector boson scattering  
**SFOS** Same Flavor Opposite Sign  
**SF** Same Flavor  
**OS** Opposite Sign  
**SS** Same Sign  
**QFT** Quantum Field Theory  
**QED** Quantum Electrodynamics

**QCD** Quantum Chromodynamics

**RF** Radio Frequency

**EW** Electroweak

**LH** Likelihood

**PSB** Proton Synchrotron Booster

**PS** Proton Synchrotron

**SPS** Super Proton Synchrotron

## LIST OF SYMBOLS

- (M/G/T)eV** (Mega/Giga/Terra) Electronvolt
- (p/f/a)b** (Pico/Femto/Atto) Barn (Units of Area  $10^{-28} \text{ m}^2$ )
- $\mathcal{L}$  Lagrangian
- $\psi$  Fermion Field
- $\partial_\mu$  Partial Derivative in Four Dimensions
- $\gamma^\mu$  Gamma Matrices
- $A_\mu$  Electromagnetic Boson Field
- $W_\mu^\pm$   $W^\pm$  Boson Field
- $Z_\mu$  Z Boson Field
- $G_\mu^a$  Gluon Field
- $\Phi$  Higgs Field
- $H$  Higgs Boson
- $e^\pm$  Electron
- $\mu^\pm$  Muon
- $\ell$   $e$  or  $\mu$
- $\nu$  Neutrino
- $j$  Jet
- $q$  Quark
- $p$  Proton
- $\gamma$  Photon
- $V$   $W^\pm$  or Z Boson

$\phi$  Azimuthal Angle  
 $\theta$  Polar Angle  
 $\eta$  Pseudo Rapidity  
 $d_0$  Transverse Impact Parameter  
 $z_0$  Longitudinal Impact Parameter  
 $m$  Mass  
 $p_T$  Transverse Momentum  
 $m_T$  Transverse Mass  
 $h_T$  Scalar Sum of Lepton and Jet  $p_T$ s  
 $\mu$  Parameter of Interest  
 $\vec{\theta}$  Gaussian Constraints  
**Pois()** Poisson Distribution Function  
**Gaus()** Gaussian Distribution Function

# ABSTRACT

This thesis presents the first evidence for the production of three  $W$  bosons ( $W^\pm W^\pm W^\mp$ ) using  $79.8 \text{ fb}^{-1}$  of  $pp$  collision data at a center-of-mass energy of 13 TeV recorded by the ATLAS detector at the Large Hadron Collider (LHC) between 2015 and 2017. The search is conducted using the semi-leptonic ( $W^\pm W^\pm W^\mp \rightarrow \ell^\pm \nu \ell^\pm \nu jj$ ) and fully-leptonic ( $W^\pm W^\pm W^\mp \rightarrow \ell^\pm \nu \ell^\pm \nu \ell^\mp \nu$ ) channels where  $\ell = e, \mu$ . The semi-leptonic channel is examined in a region where the two same-sign  $W$  bosons decay leptonically while the third  $W$  boson decays hadronically, and the fully-leptonic channel is examined in a region where all three  $W$  bosons decay leptonically and without same-flavor opposite-sign lepton pairs.

In the semi-leptonic channel, a total of 798 candidate events are observed in data, to be compared with the prediction of  $\sim 68$  signal events and  $\sim 700$  background events. In the fully-leptonic channel, a total of 27 candidate events are observed in data, to be compared with the prediction of  $\sim 11$  signal events and  $\sim 23$  background events. The first evidence for  $W^\pm W^\pm W^\mp$  production is observed by rejecting the background-only hypothesis with an observed (expected) significance of 3.3 standard deviations (2.4 standard deviations). The fiducial  $W^\pm W^\pm W^\mp$  cross sections are measured to be  $1.82^{+0.33}_{-0.32}(\text{stat.})^{+0.40}_{-0.36}(\text{syst.})$  fb for the  $\ell^\pm \nu \ell^\pm \nu jj$  channel and  $0.30^{+0.054}_{-0.052}(\text{stat.})^{+0.065}_{-0.058}(\text{syst.})$  fb in the  $\ell^\pm \nu \ell^\pm \nu \ell^\mp \nu$  channel. The inclusive  $W^\pm W^\pm W^\mp$  production cross section is found to be  $690^{+125}_{-120}(\text{stat.})^{+150}_{-135}(\text{syst.})$  fb.

The  $W^\pm W^\pm W^\mp$  search results are combined with the  $WWZ$  and  $WZZ$  search results [3] using a binned maximum-likelihood fit. The first evidence for the production of three massive gauge bosons is observed with an observed (expected) significance of 4.0 standard deviations (3.1 standard deviations).

# CHAPTER 1

## Introduction

Particle physics is a branch of physics that studies fundamental particles and their interactions. Our best understanding of how these particles and three out of four fundamental forces are related to each other is encapsulated in the Standard Model (SM) of particle physics. The SM has successfully passed very precise experimental tests.

The SM predicts that electroweak bosons (which are the force carriers of the electromagnetic and weak forces) would interact with each other in the form of triple and quartic gauge couplings. These self-interactions are connected to the electroweak symmetry breaking section together with the Higgs boson. The studies of these couplings are thus important tests of the SM and are sensitive to new physics that could exist at a high energy scale.

This thesis presents the first evidence for the joint production of three  $W$  bosons ( $W^\pm W^\pm W^\mp$ ) using  $pp$  collision data recorded by the ATLAS detector. At leading order (LO) in quantum chromodynamics (QCD), the  $W^\pm W^\pm W^\mp$  production can proceed via the coupling of the vector boson to fermions, from an associated boson production with an intermediate boson ( $W$ ,  $Z/\gamma^*$ , or  $H$ ) decaying into two  $W$  bosons (triple gauge coupling), or from a quartic gauge coupling vertex. Representative Feynman diagrams are shown in Figure 1.1.

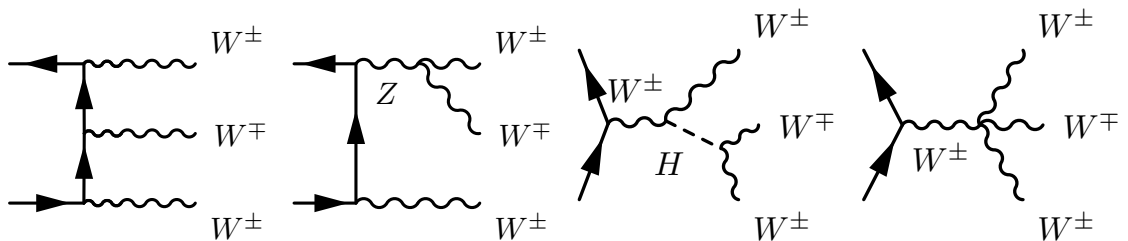


Figure 1.1: Feynman diagrams that produce the  $W^\pm W^\pm W^\mp$  final state in  $pp$  collisions.

The search for  $W^\pm W^\pm W^\mp$  production has been conducted using data taken by the ATLAS detector at two different center-of-mass energies: 8 TeV and 13 TeV. The search



results are published in two papers [1] [2]. The searches are conducted in two decay channels: semi-leptonic ( $W^\pm W^\pm W^\mp \rightarrow \ell^\pm \nu \ell^\pm \nu jj$ ) and fully-leptonic ( $W^\pm W^\pm W^\mp \rightarrow \ell^\pm \nu \ell^\pm \nu \ell^\mp \nu$ ) where  $\ell = e, \mu$ . This thesis will mainly cover the search performed at 13 TeV. In addition limits on anomalous quartic gauge couplings using 8 TeV data are shown. The  $W^\pm W^\pm W^\mp$  results at 13 TeV are combined with the  $WWZ$  and  $WZZ$  search results to obtain the first evidence of the production of three massive gauge bosons at the LHC.

This thesis is organized as follows: Chapter 2 gives an introduction to the SM and electroweak theory. Chapter 3 describes the ATLAS detector. Chapters 4-5 describe reconstruction and identification of physics objects. Chapter 6 describes how the  $W^\pm W^\pm W^\mp$  candidate events are selected. Chapter 7 discusses background and signal modeling. Chapter 8 describes background estimations. Chapter 9 describes uncertainties considered. Chapter 10 summarizes the  $WWZ$  analysis that was combined together with the  $W^\pm W^\pm W^\mp$  analysis. Chapter 11 describes the simultaneous fit used to extract the search sensitivity and the fiducial and inclusive cross sections. Chapter 12 presents a summary of the results obtained. Chapter 13 concludes the study.

## CHAPTER 2

# Theory

### 2.1 The Standard Model Theory

The SM provides an elegant theoretical framework that describes elementary particles and their interactions. Elementary particles are classified according to their spin. The half-integer spin particles are called fermions, and the integer-spin particles are called bosons.

Fermions are categorized into two groups: leptons and quarks. Leptons (electrons, muons, taus, and their corresponding neutrinos) are color-neutral particles, and quarks (up, down, charm, strange, top, and bottom) are color-charged particles. Fermions are further grouped into three generations, where each generation is composed of two quarks and two leptons. The two quarks are classified according to their electric charge of  $+2/3$  or  $-1/3$ , and the two leptons are categorized according to their electric charge of  $-1$  or  $0$ . For all fermions, the corresponding anti-particles are also found in nature. Anti-particles have identical mass and spin but have opposite charges compared with their matter counterparts. Properties of all fermions can be found in Figure 2.1.

Bosons (except the Higgs boson) are mediators of the fundamental forces. There are four known fundamental forces in the universe: electromagnetic, weak, strong, and gravitational forces:

- The electromagnetic force is mediated by the photon ( $\gamma$ ), and it is the force that binds electrons to the atomic nuclei.
- The weak force is mediated by  $W^\pm$  and  $Z$  bosons, and it is responsible for radioactive decays.
- The strong force is mediated by gluons ( $g$ ), and it is the force that binds quarks together.

- The gravitational force is proposed to be mediated by gravitons, but there are currently no experimentally supported theories regarding gravitons.

There is an additional boson called the Higgs boson ( $H$ ). It is responsible for the masses of  $W^\pm$ ,  $Z$  bosons and fermions (whether the Higgs boson is responsible for neutrino masses is still under investigation). Properties of all bosons can be found on Figure 2.1.

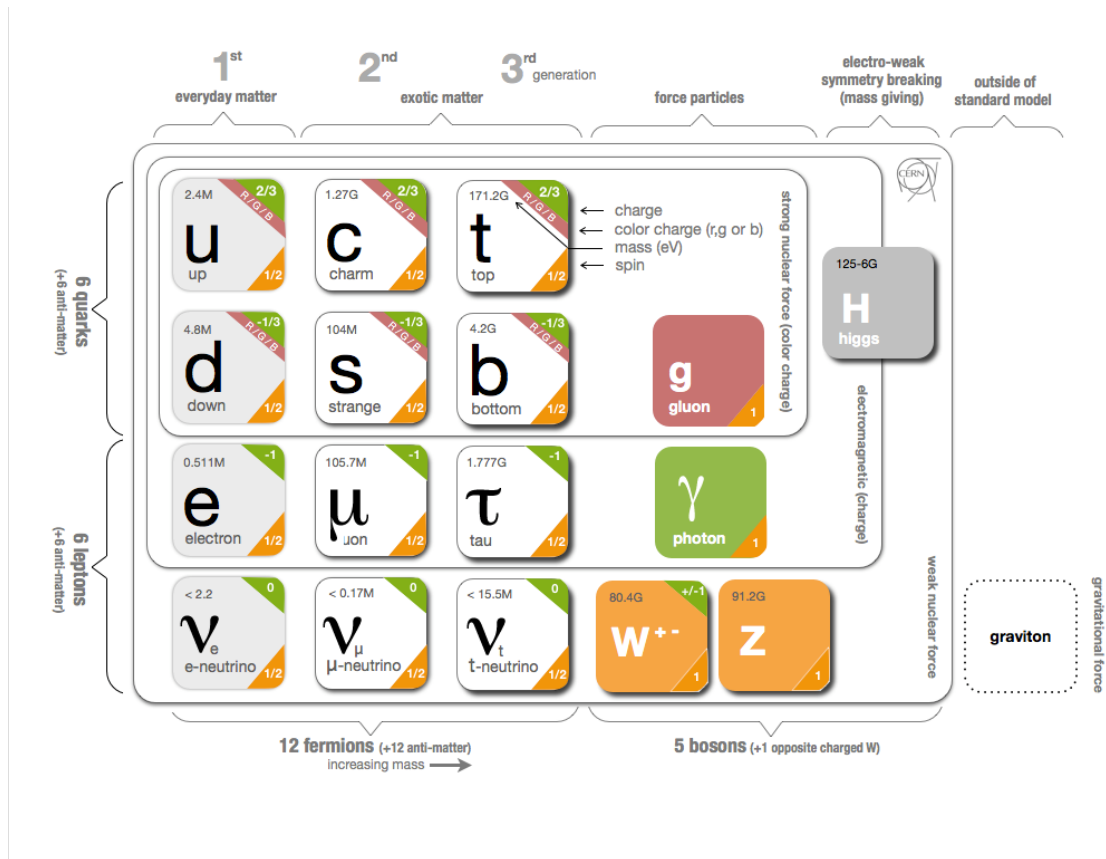


Figure 2.1: Properties of all known fermions and bosons [4].

## 2.2 The Standard Model Formalism

A Lagrangian is a mathematical construct that models the behavior of a system. Noether's theorem [5] states that when a Lagrangian is symmetric (doesn't change) under a continuous transformation, there must be a conserved quantity in this system. Group theory is a mathematical representation that defines these symmetries and transformations. Physicists use Noether's theorem and group theory to define conservation laws. As an example, in the theory of special relativity, the symmetry of the four-dimensional space-time is represented

as  $SO(3, 1)$  (the Lorentz group). This representation defines all transformation of this system (space rotation, Lorentz boost, etc.) and the conservation laws (conservation of energy, momentum, etc.).

The SM is a Quantum Field Theory (QFT) that uses a Lagrangian formalism to model the physics of fundamental particles. It is based on the gauge group  $SU(3)_C \otimes SU(2)_L \otimes U(1)_Y$  (The term gauge group refers to the group structure of the Lagrangian). This gauge group includes strong interactions ( $SU(3)_C$ ) and electroweak interactions ( $SU(2)_L \otimes U(1)_Y$ ). Here  $C$  stands for color charge,  $L$  refers to left-handed fields, and  $Y$  refers to the weak hypercharge.

## 2.2.1 Quantum Electrodynamics

Quantum Electrodynamics (QED) describes the interaction of photons with fermions. The QED Lagrangian [6] has the  $U(1)$  symmetry and can be used as a basic example.

In order to describe the QED Lagrangian, the Lagrangian with a single fermion field ( $\psi$ ) is written as:

$$\mathcal{L} = \bar{\psi}[i\gamma^\mu \partial_\mu - m]\psi. \quad (2.1)$$

Here  $\partial_\mu$  is the partial derivative in four dimensions,  $\bar{\psi}\partial_\mu\psi$  models the momentum of the field, and  $\gamma^\mu$  are gamma matrices that describe the behavior of the spin of the fermion field. This Lagrangian is expected to be gauge invariant (this means Lagrangian doesn't change under transformations), but when the electromagnetic charge is introduced as a phase ( $U(1)$ ) into the fermion field  $\psi' \xrightarrow{U(1)} e^{ie\theta}\psi$ , the derivative term brings extra terms into the Lagrangian:

$$\partial_\mu\psi \xrightarrow{U(1)} e^{ie\theta}(\partial_\mu + ie\partial_\mu\theta)\psi. \quad (2.2)$$

The extra term ( $ie\partial_\mu\theta$ ) breaks the gauge invariance. In order to fix this, an electromagnetic boson field (the photon field  $A_\mu$ ) is introduced into the Lagrangian. The new boson field transforms under the  $U(1)$  transformations as:

$$A_\mu \rightarrow A_\mu + \partial_\mu\theta. \quad (2.3)$$

This makes the Lagrangian invariant under the  $U(1)$  transformations and forms the QED Lagrangian given below:

$$\mathcal{L}_{\text{QED}} = \bar{\psi}[i\gamma^\mu \partial_\mu - m]\psi + e\bar{\psi}\gamma^\mu A_\mu\psi - \frac{1}{4}F^{\mu\nu}F_{\mu\nu}, \quad (2.4)$$

where

$$F_{\mu\nu} = \partial_\mu A_\nu - \partial_\nu A_\mu. \quad (2.5)$$

Here the term  $e\bar{\psi}\gamma^\mu A_\mu\psi$  represents the interaction of the photon field with the fermion, and the term  $\frac{1}{4}F^{\mu\nu}F_{\mu\nu}$  represents the kinetic energy of the photon field.

## 2.2.2 The Yang-Mills Theory

The QED Lagrangian defined in the previous section is invariant under U(1) transformations. The next step is to write a Lagrangian that is invariant under SU(2) transformations. For this reason, the previously defined fermion field is converted to SU(2):

$$\psi \rightarrow \psi' = \begin{pmatrix} \psi_1 \\ \psi_2 \end{pmatrix}, \quad (2.6)$$

and the basic SU(2)-invariant Lagrangian is written as:

$$\mathcal{L} = \bar{\psi}[i\gamma^\mu\partial_\mu]\psi. \quad (2.7)$$

The mass term is omitted here since the gauge invariant version of this theory cannot be written with a mass term.

This fermion field transforms under SU(2) transformations as  $\psi \rightarrow e^{\vec{\theta}\cdot\vec{\tau}}\psi$ , where  $\vec{\tau}$  represent all possible transformations in SU(2) and  $\vec{\theta}$  is the magnitude of these transformations. As it is the case in QED, these transformations break the gauge invariance of the Lagrangian. In order to make the Lagrangian gauge invariant, the new Lagrangian is rewritten in the following form called the ‘‘Yang-Mills Theory’’ [7]:

$$\mathcal{L}_{\text{YM}} = \bar{\psi}[i\gamma^\mu(\partial_\mu - ig\vec{W}_\mu \cdot \vec{\tau})]\psi - \frac{1}{4}F_i^{\mu\nu}F_{\mu\nu}^i. \quad (2.8)$$

In this equation  $\vec{W}_\mu$  represents generic boson fields that fix the gauge invariance,  $ig\vec{W}_\mu \cdot \vec{\tau}$  represents the interaction of these boson fields with fermions,  $g$  represents the coupling constants between these fields and fermions, and finally  $F_{\mu\nu}^i$  represents the kinetic term for the massless vector boson field defined below:

$$F_{\mu\nu}^i = \partial_\mu W_\nu^i - \partial_\nu W_\mu^i + g\epsilon_{ijk}W_\mu^jW_\nu^k, \quad (2.9)$$

where  $\epsilon_{ijk}$  is the Levi-Civita symbol that defines the commutation relationship between different boson fields.

This Lagrangian can also be written in terms of the covariant derivative  $D_\mu$ :

$$D_\mu = \partial_\mu - ig\vec{W}_\mu \cdot \vec{\tau}, \quad (2.10)$$

which leads to

$$\mathcal{L}_{\text{YM}} = \bar{\psi}[i\gamma^\mu D_\mu]\psi - \frac{1}{4}F_i^{\mu\nu}F_{\mu\nu}^i. \quad (2.11)$$

This Lagrangian is invariant under SU(2) transformations. The QED Lagrangian given in Equation 2.4 is invariant under U(1) transformations.

### 2.2.3 The Electroweak Theory

SM particles have an additional property called chirality. Chirality classifies leptons as either right-handed or left-handed. In nature it has been observed that weak bosons only interact with the left-handed fermions and right-handed anti-fermions. To account for this fact, the fermions are split into left-handed and right-handed counterparts using the 5<sup>th</sup> gamma matrix  $\gamma^5$  as:

$$\psi_L = \frac{1 - \gamma^5}{2}\psi \quad \text{and} \quad \psi_R = \frac{1 + \gamma^5}{2}\psi. \quad (2.12)$$

The Electroweak (EW) Lagrangian [8] has the gauge group  $\text{SU}(2)_L \otimes \text{U}(1)_Y$ , here  $L$  term shows that the SU(2) bosons only couple to left-handed fermions. When the SU(2) Yang-Mills Lagrangian is combined with the U(1) Lagrangian while ensuring the weak bosons only couple to left-handed fermions, the electroweak Lagrangian ( $\mathcal{L}_{\text{EW}}$ ) is formed:

$$\mathcal{L}_{\text{EW}} = \sum_{j=1}^3 \bar{\psi}_j[i\gamma^\mu D_\mu]\psi_j - \frac{1}{4}W_i^{\mu\nu}W_{\mu\nu}^i - \frac{1}{4}B^{\mu\nu}B_{\mu\nu}, \quad (2.13)$$

where

$$\psi_1 = \begin{pmatrix} \nu_e \\ e^- \end{pmatrix}_L, \quad \psi_2 = \nu_{eR}, \quad \psi_3 = e_R^- \quad \text{or} \quad \psi_1 = \begin{pmatrix} d \\ u \end{pmatrix}_L, \quad \psi_2 = d_R, \quad \psi_3 = u_R, \quad (2.14)$$

$$D_\mu\psi_1 = [\partial_\mu - \frac{ig}{2}\tau_i W_\mu^i - ig'Y_1 B_\mu]\psi_1, \quad (2.15)$$

$$D_\mu\psi_2 = [\partial_\mu - ig'Y_2 B_\mu]\psi_2, \quad (2.16)$$

$$D_\mu\psi_3 = [\partial_\mu - ig'Y_3 B_\mu]\psi_3, \quad (2.17)$$

$$W_{\mu\nu}^i = \partial_\mu W_\nu^i - \partial_\nu W_\mu^i + g_W \epsilon_{ijk} W_\mu^j W_\nu^k, \quad (2.18)$$

$$B_{\mu\nu} = \partial_\mu B_\nu - \partial_\nu B_\mu. \quad (2.19)$$

In this Lagrangian  $\psi_i$  are the fermion fields for the first-generation quarks or leptons,  $W^i$  and  $B_\mu$  are the SU(2) and U(1) boson fields respectively, the  $g'$  and  $g$  are coupling strength factors for the  $W^i$  and  $B_\mu$  fields,  $\tau_i$  are the SU(2) transformation operators, and  $Y_i$  are weak hypercharges of their respective fermions.

In nature the SU(2) fields ( $W_i^\mu$ ) and the U(1) fields ( $B_j^\mu$ ) are heavily mixed together to form the observed electroweak gauge bosons:

$$A_\mu = W_\mu^3 \sin \theta_W + B_\mu \cos \theta_W \quad (\text{Photon}), \quad (2.20)$$

$$Z_\mu = W_\mu^3 \cos \theta_W - B_\mu \sin \theta_W \quad (Z \text{ boson}), \quad (2.21)$$

$$W_\mu^\pm = \frac{1}{\sqrt{2}}(W_\mu^1 \pm W_\mu^2) \quad (W^\pm \text{ boson}). \quad (2.22)$$

where  $\theta_W$  is the weak mixing angle (also called the Weinberg angle) which is related to the  $g$  and  $g'$  couplings as:

$$\sin \theta_W = \frac{g}{\sqrt{g^2 + g'^2}}, \quad \cos \theta_W = \frac{g'}{\sqrt{g^2 + g'^2}} \quad (2.23)$$

The latest measurement of the weak mixing angle is  $\sin^2 \theta_W = 0.23122(4)[9]$ .

The theory described above assumes that all particles are massless, which is known to be untrue. However, introducing the mass term for any of the particles breaks the gauge invariance. This problem can be solved by introducing the Higgs mechanism.

## 2.2.4 The Higgs Mechanism

In order to explain the Higgs mechanism, a U(1) scalar field  $\Phi$  with two degrees of freedom is defined with the Lagrangian given below [6]:

$$\mathcal{L} = \partial_\mu \Phi^\dagger \partial^\mu \Phi - V(\Phi), \quad (2.24)$$

where

$$V(\Phi) = [\mu^2 \Phi^\dagger \Phi + \lambda(\Phi^\dagger \Phi)^2]. \quad (2.25)$$

Here the  $\mu^2 \Phi^\dagger \Phi + \lambda(\Phi^\dagger \Phi)^2$  term stands for the potential energy of the  $\Phi$  field. If  $\mu^2 < 0$ , this potential term has a function shaped like a Mexican hat given in Figure 2.2. This potential energy has ground energy states (lowest energy) at points where  $\Phi_0 = \pm \sqrt{\frac{-\mu^2}{2\lambda}} \equiv v$ . At these points the potential term in the Lagrangian becomes  $V(\Phi_0) = -\frac{\lambda}{4}v^4$ .

At these ground energy states,  $\Phi$  can be re-written as a function of two fields ( $\Phi_1$  and

$\Phi_2$ ) which are the excitations of the chosen ground state. This re-definition breaks the gauge symmetry of the  $\Phi$  field. This process is called spontaneous symmetry breaking. The gauge-symmetry broken  $\Phi$  field is written as:

$$\Phi = \frac{1}{\sqrt{2}}(v + \Phi_1 + i\Phi_2). \quad (2.26)$$

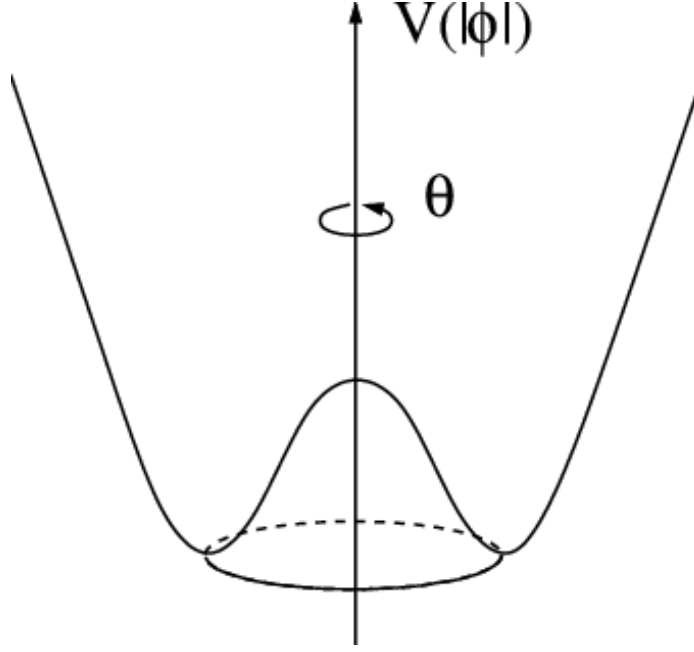


Figure 2.2: The Higgs potential as a function of  $\Phi$  [10].

The overall potential energy term now becomes:

$$V(\Phi) = V(\Phi_0) - \mu^2 \Phi_1^2 + v\lambda \Phi_1(\Phi_1^2 + \Phi_2^2) + \frac{\lambda}{4}(\Phi_1^2 + \Phi_2^2)^2. \quad (2.27)$$

In this equation the  $\mu^2 \Phi_1^2$  term becomes the mass term for the  $\Phi_1$  field while the  $\Phi_2$  field stays massless. The boson that generated this massless field is referred to as the Goldstone boson.

For the next step, the SU(2) Yang-Mills theory is combined with the Higgs field, by converting the partial derivative into the covariant derivative of the SU(2) field:

$$\mathcal{L} = D_\mu \Phi^\dagger D^\mu \Phi - [\mu^2 \Phi^\dagger \Phi + \lambda(\Phi^\dagger \Phi)^2], \quad (2.28)$$

$$D_\mu \Phi = [\partial_\mu - ig\vec{W}_\mu \cdot \vec{\tau}][\frac{1}{\sqrt{2}}(v + \Phi_1 + i\Phi_2)], \quad (2.29)$$



$$D_\mu \Phi^\dagger D^\mu \Phi = g^2 \frac{v^2}{2} \vec{\tau} \cdot \vec{W}_\mu \vec{W}^\mu \cdot \vec{\tau} + \text{Other Terms.} \quad (2.30)$$

The SU(2) boson field ( $\vec{W}_\mu$ ) gains a mass term through its interaction with the Higgs field. With this mechanism, the weak gauge bosons of the SM become massive.

The Higgs field discussed so far is a simplified version of the SM Higgs field and only has two degrees of freedom. The SM Higgs field [11][12] is a SU(2) complex scalar field with four degrees of freedom. This means it has three massless Goldstone boson fields ( $\theta_i$ ) after the spontaneous symmetry breaking and one massive Higgs boson field ( $H$ ) given by the equation below:

$$\Phi = e^{\frac{i\sigma^i \theta^i(x)}{2}} \frac{1}{\sqrt{2}} \begin{pmatrix} 0 \\ v + H \end{pmatrix}. \quad (2.31)$$

The SM Higgs field has the following Lagrangian:

$$\mathcal{L}_{\text{Higgs}} = (D_\mu \Phi)^\dagger D^\mu \Phi - [\mu^2 \Phi^\dagger \Phi + \lambda(\Phi^\dagger \Phi)^2]. \quad (2.32)$$

Here  $D_\mu$  is the EW covariant derivative and contains the  $W^i$  and  $B_\mu$  boson fields which get mixed with the Higgs field:

$$(D_\mu \Phi)^\dagger D_\mu \Phi \xrightarrow{\theta_i=0} \frac{1}{2} (\partial_\mu H)(\partial^\mu H) + (v + H)^2 \left( \frac{g^2}{4} W_\mu^+ W^{\mu-} + \frac{g^2}{8 \cos^2 \theta_W} Z_\mu Z^\mu \right), \quad (2.33)$$

where the term  $\frac{g^2}{4} W_\mu^+ W^{\mu-} + \frac{g^2}{8 \cos^2 \theta_W} Z_\mu Z^\mu$  gives the  $W^\pm$  and  $Z$  boson masses through their interactions with the Higgs field.

Fermions can also gain their mass through the interactions with the Higgs field. These interactions are given by the Yukawa couplings that are added to the SM Lagrangian as additional terms:

$$\mathcal{L}_{\text{Yukawa}} = y \bar{\psi} \Phi \psi. \quad (2.34)$$

This equation gives a single fermion Yukawa coupling, where  $y$  is the coupling constant. For each fermion that interacts with the Higgs field, an individual Yukawa term is added to the SM Lagrangian.

## 2.2.5 Quantum Chromodynamics

Similar to the electroweak interaction, the SU(3) color charges can be added to the Lagrangian by adding a gluon field ( $G_a^\mu$ ) forming the Quantum Chromodynamics (QCD) Lagrangian [13] as:

$$\mathcal{L}_{\text{QCD}} = \psi [i\gamma^\mu D_\mu - m] \psi - \frac{1}{4} G_{\mu\nu}^a G_a^{\mu\nu}, \quad (2.35)$$

$$D_\mu = \partial_\mu - ig_s \frac{\lambda^a}{2} G_a^\mu, \quad (2.36)$$

$$G_a^{\mu\nu} = \partial^\mu G_a^\nu - \partial^\nu G_a^\mu + g_s f^{abc} G_b^\mu G_c^\nu. \quad (2.37)$$

In this Lagrangian  $g_s$  is the coupling constant for the color interactions,  $\lambda^a$  are SU(3) transformations, and  $f^{abc}$  are the SU(3) structure constants.

## 2.2.6 The Standard Model Lagrangian

The SM Lagrangian [13] is the combination of the EW, QCD, and Higgs Lagrangians. The complete SM Lagrangian is written as follows.

$$\mathcal{L}_{\text{SM}} = \mathcal{L}_{\text{Higgs}} + \mathcal{L}_{\text{fermion}} + \mathcal{L}_{\text{boson}} + \mathcal{L}_{\text{Yukawa}}, \quad (2.38)$$

where

$$D_\mu = \partial_\mu - \frac{ig}{2} \vec{W}_\mu \cdot \vec{\tau} - \frac{ig'}{2} Y_i B_\mu - ig_s \frac{\lambda^a}{2} G_a^\mu, \quad (2.39)$$

$$\mathcal{L}_{\text{Higgs}} = (D_\mu \Phi)^\dagger D^\mu \Phi - \mu^2 \Phi^\dagger \Phi - \lambda (\Phi^\dagger \Phi)^2, \quad (2.40)$$

$$\mathcal{L}_{\text{fermion}} = \sum_{i,j}^{\text{fermions}} i \bar{\psi}_i \gamma^\mu D_\mu \psi_j \quad (\text{right-handed neutrino interactions excluded}), \quad (2.41)$$

$$\mathcal{L}_{\text{boson}} = -\frac{1}{4} G_{\mu\nu}^i G^{i\mu\nu} - \frac{1}{4} W_{\mu\nu}^i W^{i\mu\nu} - \frac{1}{4} B_{\mu\nu} B^{\mu\nu}, \quad (2.42)$$

and

$$\mathcal{L}_{\text{Yukawa}} = -y_u \bar{\psi}_L^q \Phi \psi_R^u - y_d \bar{\psi}_L^q \Phi \psi_R^d - y_e \bar{\psi}_L^e \Phi \psi_R^e + \text{h.c.}, \quad (2.43)$$

where h.c. are Yukawa terms for other fermions that couple to the Higgs boson.

## 2.2.7 Triple and Quartic Gauge Couplings

The  $-\frac{1}{4} W_{\mu\nu}^i W^{i\mu\nu} - \frac{1}{4} B_{\mu\nu} B^{\mu\nu}$  term in the SM Lagrangian allows self interactions of the EW bosons. The expansion of these terms give results to the the following terms with triple gauge couplings (TGCs) [6]:

$$\begin{aligned} \mathcal{L}_3 = & -ie[(\partial^\mu W^{\nu-} - \partial^{\nu-} W^\mu) W_\mu^+ (\cot\theta_W Z_\nu + A_\nu) \\ & - (\partial^\mu W^{\nu+} - \partial^{\nu+} W^\mu) W_\mu^- (\cot\theta_W Z_\nu + A_\nu) \\ & + W_\mu^- W_\nu^+ (\cot\theta_W \partial^\mu Z^\nu - \cot\theta_W \partial^\nu Z^\mu + \partial^\mu A^\nu - \partial^\nu A^\mu)], \end{aligned} \quad (2.44)$$

and terms with quartic gauge couplings (QGCs):

$$\begin{aligned}
\mathcal{L}_4 = & -\frac{e^2}{2\sin^2\theta_W}[(W_\mu^+ W^{\mu-})^2 - W_\mu^+ W^{\mu+} W_\nu^- W^{\nu-}] \\
& -e^2 \cot^2\theta_W[W_\mu^+ W^{\mu-} Z_\nu Z^\nu - W_\mu^+ Z^\mu W_\nu^- Z^\nu] \\
& -e^2 \cot\theta_W[2W_\mu^+ W^{\mu-} Z_\nu A^\nu - W_\mu^+ Z^\mu W_\nu^- A^\nu - W_\mu^+ A^\mu W_\nu^- Z^\nu] \\
& -e^2[W_\mu^+ W^{\mu-} A_\nu A^\nu - W_\mu^+ A^\mu W_\nu^- A^\nu].
\end{aligned} \tag{2.45}$$

In addition, the Higgs boson also couples to  $W^\pm$  and  $Z$  bosons resulting in the following TGC and QGC terms:

$$\mathcal{L}_{\text{TGC/QGC}}^H = [m_W^2 W_\mu^+ W^{\mu-} + \frac{1}{2}m_Z^2 Z_\mu Z^\mu][1 + \frac{2}{v}H + \frac{H^2}{v^2}]. \tag{2.46}$$

Tables 2.1, 2.2 shows a summary of all allowed triple and quartic gauge couplings in the SM.

Although the SM does not predict additional gauge interactions, some beyond-the-SM theories also predict additional gauge couplings such as  $Z\gamma\gamma$ ,  $ZZZZ$ ,  $ZZ\gamma$ .

## 2.3 Effective Field Theory

There could be undiscovered particles or completely new physics at energy scales beyond the reach of the LHC, and they may manifest themselves at low energies through anomalous gauge boson couplings. Effective field theories modify the SM by introducing additional terms to the SM Lagrangian that modify the gauge couplings. The basic effective field theory can be written in the form of:

$$\mathcal{L}_{\text{eff}} = \mathcal{L}_{\text{SM}} + \sum_{d \geq 4} \sum_i \frac{f_i^{(d)}}{\Lambda^{d-4}} O_i^{(d)}, \tag{2.47}$$

where  $f^{(d)}$  is the coupling of a higher-order interaction,  $O_i^{(d)}$  is the corresponding higher-order interaction operator, and  $\Lambda$  is the energy scale of new physics.

In this thesis, the following effective Lagrangian terms are used that introduce anomalous Quartic Gauge Couplings (aQGC). These terms are given by [14]:

$$\mathcal{L}_{S0} = \frac{f_{s0}}{\Lambda^4} [(D_\mu \Phi)^\dagger D_\nu \Phi] \times [(D^\mu \Phi)^\dagger D^\nu \Phi], \tag{2.48}$$

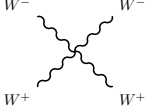
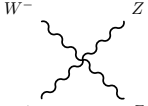

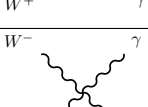
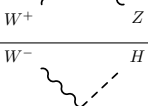
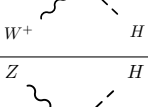
Vertex	Diagram	Lagrangian Coefficients
$W^+W^-W^+W^-$		$\frac{e^2}{2\sin^2\theta_W}$
$W^+W^-ZZ$		$-e^2\cot^2\theta_W$
$W^+W^-\gamma\gamma$		$-e^2$
$W^+W^-Z\gamma$		$-e^2\cot\theta_W$
$W^+W^-HH$		$\frac{m_W^2}{v}$
$ZZHH$		$\frac{m_Z^2}{2v^2}$

Table 2.1: Quartic gauge couplings allowed in the SM theory.

and

$$\mathcal{L}_{S1} = \frac{f_{s1}}{\Lambda^4} [(D_\mu\Phi)^\dagger D^\mu\Phi] \times [(D_\nu\Phi)^\dagger D^\nu\Phi], \quad (2.49)$$

where  $f_{s0}$ ,  $f_{s1}$  are aQGC. Unitarity is not guaranteed for effective field theories. For this reason, a form factor unitarization [15] is applied on anomalous couplings:

$$\alpha \rightarrow \frac{\alpha_0}{1 + \hat{s}/\Lambda_{FF}^2} \quad (2.50)$$

Here  $\alpha$  correspond to aQGC parameters,  $\alpha_0$  are the values of aQGCs at low energies,  $\hat{s}$  is the center-of-mass energy, and  $\Lambda_{FF}$  is the form factor cutoff scale.

The two Lagrangians terms involving  $L_{s0}$  and  $L_{s1}$  introduce additional  $WWWW$ ,  $WWZZ$  and  $ZZZZ$  couplings. The  $WWW$  analysis is sensitive to the  $WWWW$  coupling, and the analysis performed at 8TeV has set limits on the  $\frac{f_{s0}}{\Lambda^4}$  and  $\frac{f_{s1}}{\Lambda^4}$  terms.

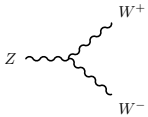
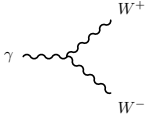
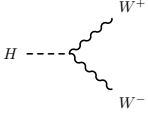
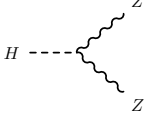
Vertex	Diagram	Lagrangian Coefficients
$W^+W^-Z$		$-ie \cot \theta_W$
$W^+W^-\gamma$		$-ie$
$W^+W^-H$		$m_W^2 \frac{2}{v}$
$ZZH$		$\frac{m_Z^2}{v}$

Table 2.2: Triple gauge couplings allowed in the SM theory.

## CHAPTER 3

# The LHC and the ATLAS Experiment

The data used in this thesis were collected by the “A Toroidal LHC Apparatus” (ATLAS) detector that resides in a cavern about 100m below ground in Geneva, Switzerland. The ATLAS detector is a general-purpose particle detector designed to study proton-proton and heavy-ion collisions provided by the LHC to test the SM theory and to search for signs of new physics.

### 3.1 The Large Hadron Collider

The LHC [16] is a 27 km-long circular particle collider for protons (it can also collide heavy ions). It is located on the border of Switzerland and France and is hosted by the European Organization for Nuclear Research (CERN). The LHC is designed to circulate/accelerate two proton beams in clockwise and counterclockwise directions and collide them with a center-of-mass energy of 14TeV with a peak instantaneous luminosity of  $10^{34} \text{ cm}^{-2} \text{ s}^{-1}$ . The LHC is yet to achieve its design goal of 14TeV but has surpassed its instantaneous luminosity goal. The LHC started its operation in 2010, and the operation parameters for different periods can be found in Table 3.1.

Parameters	2010	2011 - 2012	2015 - 2018	Design
Beam Energy [TeV]	3.5	4	6.5	7
Integrated Luminosity [ $\text{fb}^{-1}$ ]	0.048	28.3	156	
Max Peak Luminosity [ $10^{34} \text{ cm}^{-2} \text{ s}^{-1}$ ]	0.021	0.77	2.14	1
Bunch Spacing [ns]	150	50	25	25

Table 3.1: Status of the LHC as of 2019 and its running parameters [17][18].

Before protons are injected into the LHC, they are accelerated by several smaller accelerators. The first accelerator is the Linear Accelerator (LINAC) 2 which accelerates ionized hydrogen gas (protons) to 50MeV. The second accelerator is the Proton Synchrotron

Booster (PSB) which accelerates these protons to 1.4 GeV. The third accelerator is the Proton Synchrotron (PS), and it accelerates the protons to 26 GeV. The final accelerator is the Super Proton Synchrotron (SPS) which accelerates the protons to the injection energy of 450 GeV. Protons from the SPS are then injected into the LHC. The structure of the LHC can be viewed in Figure 3.1.

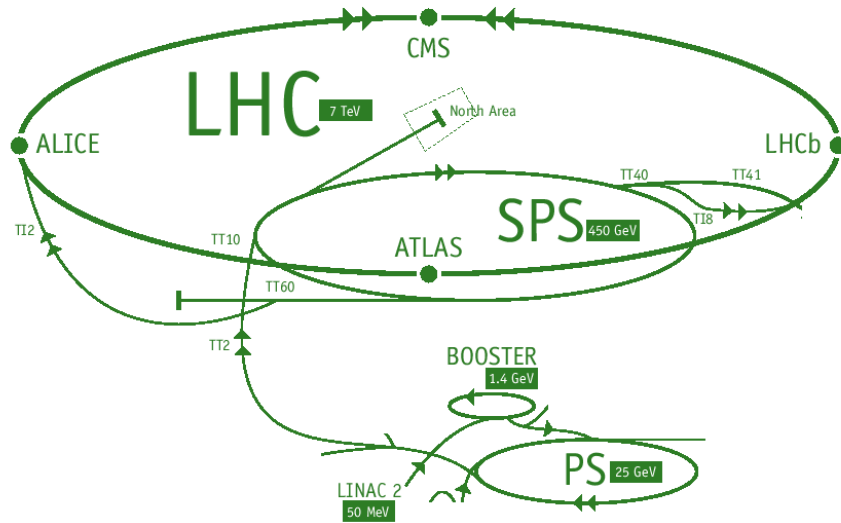


Figure 3.1: The LHC complex [19].

The LHC uses superconducting magnets to manipulate particle beams and Radio Frequency (RF) cavities to accelerate beams. The LHC dipole magnets are superconducting magnets that can produce a magnetic field up to 8.33 T. They are used to bend particle trajectories to keep them contained inside the LHC loop. In addition to dipole magnets, LHC has additional quadrupole, sextupole, and octupole superconducting magnets to focus particle beams. In a straight section of the LHC, there are 16 superconducting RF cavities that gradually boost the 450 GeV proton beams up to 7 TeV. The circular structure of the LHC allows the same RF cavities to be used repetitively.

The LHC houses four experiments: ATLAS [20], Compact Muon Solenoid (CMS) [21], A Large Ion Collider Experiment (ALICE) [22], and Large Hadron Collider Beauty Experiment (LHCb) [23]. In addition, the LHC holds a few small experiments: TOTAL cross section, Elastic scattering and diffraction dissociation Measurement at the LHC (TOTEM) [24], Large Hadron Collider Forward Experiment (LHCf) [25], and Monopole and Exotics

Detector at the LHC Experiment (MoEDAL) [26]. The ATLAS and CMS detectors are general-purpose particle detectors that test the SM and search for new physics. The ALICE experiment is designed to study lead-lead ion collisions. The LHCb’s focus lies on  $b$ -physics. The TOTEM experiment shares the CMS collision point and examines the proton structure using elastic scattering events. The MoEDAL experiment shares the cavern with the LHCb experiment and searches for magnetic monopoles or other highly ionizing stable massive particles. The LHCf experiment examines neutral pions in order to mimic the interactions of cosmic rays with the earth’s atmosphere under lab conditions.

## 3.2 The ATLAS Detector

The ATLAS detector is a general-purpose particle detector that is designed to examine the proton-proton and heavy-ion collisions. The ATLAS detector has a dimension of  $25\text{ m} \times 25\text{ m} \times 45\text{ m}$  and weighs about 7000 tons. It is layered like an onion around the collision point. The innermost layers are called the Inner Detector (ID) and is composed of a pixel detector, a Semiconductor Tracker (SCT), and a Transition Radiation Tracker (TRT). The ID is enclosed by a solenoid that provides a magnetic field of 2 Tesla. The calorimeter system resides on top of the solenoid layer. The outermost layers are formed of toroidal magnets and the Muon Spectrometer (MS). The geometry of the ATLAS detector is split into the barrel and end-cap regions. The barrel region is the cylindrical region around the beam axis. The end-caps are the wheels at the two ends of the cylinder. An overview of the ATLAS detector and its sub-detectors can be found in Figure 3.2.

### 3.2.1 The Coordinate System

The ATLAS detector’s coordinate system takes the center of the detector as the origin, where the  $x$ -axis points towards to the center of the LHC ring, the  $y$ -axis points towards the sky, and the  $z$ -axis follows the right-hand rule and is parallel to a beam line. The transverse plane is defined in the  $x - y$  plane with an azimuthal angle  $\phi$  around the beam axis defined as  $\phi = \tan^{-1}(x/y)$ , and a polar angle ( $\theta$ ) with respect to the  $z$ -axis. In addition, the pseudo-rapidity ( $\eta$ ) is defined as  $\eta = -\ln[\tan(\theta/2)]$ .

### 3.2.2 The Inner Detector

At the LHC, particle bunches cross each other at a rate of 40MHz, and within each crossing there could be multiple collisions. In order to differentiate these collisions a detector close to the beam with a good spatial resolution is needed. The ID [28] fulfills this role by



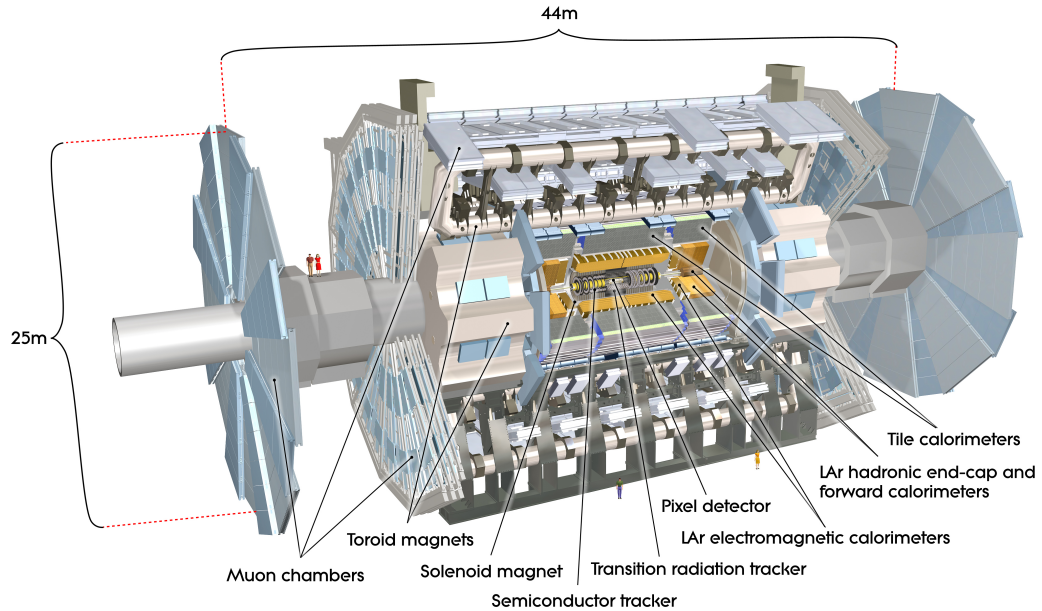


Figure 3.2: Overview of the ATLAS detector and its sub-detectors [27].

being a precision particle tracker. It covers  $|\eta| < 2.5$  in the pseudo-rapidity range and can detect charged tracks (charged particle energy deposits in the detector) with a Transverse Energy ( $E_T$ ) as low as 0.1 GeV (0.5 GeV is the nominal working point). The ID is composed of the pixel detector, the SCT, and the TRT and is situated inside a solenoid that provides a 2 T magnetic field to facilitate tracking and momentum measurements. An overview of the ID can be found in Figure 3.3.

### 3.2.2.1 The Pixel Detector

The pixel detector [28] is the innermost part of the ATLAS detector. The pixel detector is a silicon detector composed of 1744 pixel modules containing 46080 pixel sensors. The pixel modules are 250  $\mu\text{m}$  thick oxygenated  $n$ -type wafers with readout pixels of  $n^+$  doping [20]. The pixel modules are stacked into four layers in the barrel region and three layers in the end-cap regions. The innermost layer is called the Insertable B-Layer (IBL) and was installed during the 2013-2014 LHC shutdown. The pixel detector's main objective is to track particles and to identify vertices that these particles originate. The pixel detector has an average resolution of 12  $\mu\text{m}$  in the  $\phi$  axis and 66  $\mu\text{m}$  along the  $z$  axis.

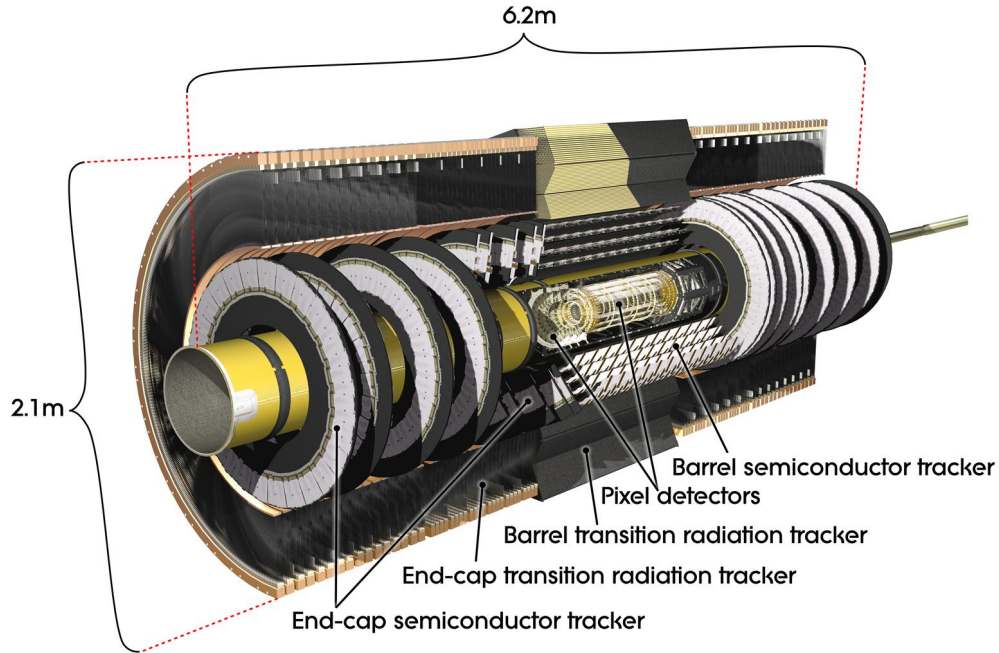


Figure 3.3: Overview of the ATLAS inner detector [29].

### 3.2.2.2 The Semiconductor Tracker

The SCT [28] is a silicon detector with 780 readout strips with a pitch of  $80\mu\text{m}$  made with single-sided p-in-n technology. The barrel region consists of four layers and the end-cap regions consist of nine layers. Together they provide tracking information for charged particles in  $\phi$  and  $\eta$  in the pseudo-rapidity range of  $|\eta| < 2.5$ . The SCT has a resolution of  $16\mu\text{m}$  in the  $\phi$  axis and  $580\mu\text{m}$  along the  $z$  axis.

### 3.2.2.3 The Transition Radiation Tracker

The TRT [28] is composed of gas-filled cylindrical tubes called straws interwoven with dielectric material that facilitate transition radiation. Each straw has a diameter of 4 mm and a maximum length of 150 cm. Each straw has a copper wire at the center that spans the length of the cylinder and is filled with a gas mixture of 70% Xe, 20%  $\text{CF}_4$ , and 10%  $\text{CO}_2$ . The wire acts as an anode, and the straw acts like a cathode creating a constant electric field inside the straw. When a charged particle passes through the straw, it ionizes the gas inside and creates a shower of particles.

The TRT detector is designed to differentiate electrons from other particles. As particles pass through matter, they radiate photons in a process called transition radiation. Compared to electrons, transition radiation from hadrons is approximately two orders of

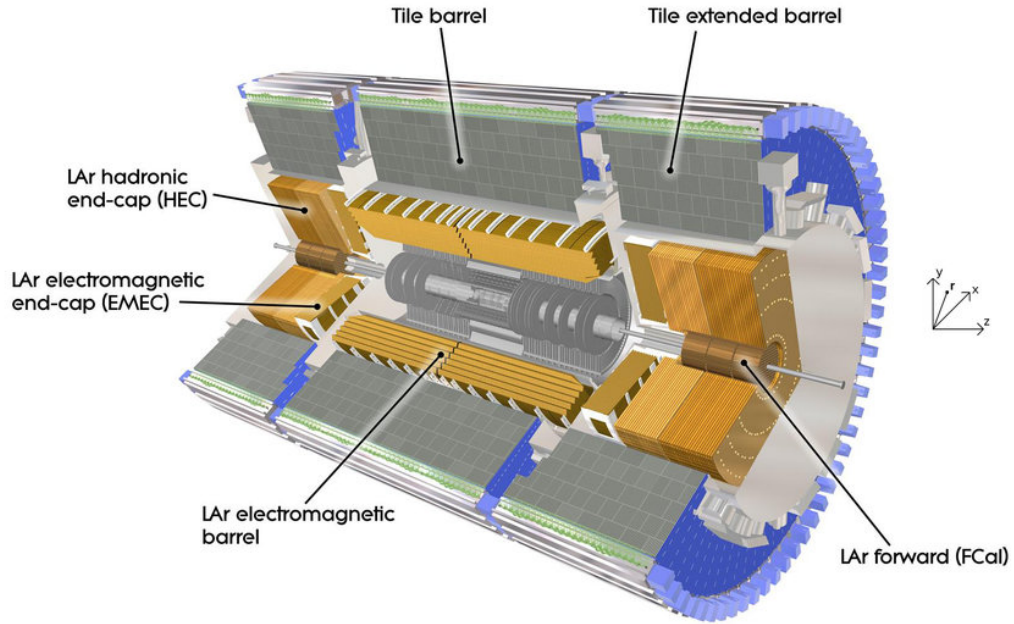


Figure 3.4: Overview of the ATLAS Calorimeter System [31].

magnitude more energetic. The TRT hardware capitalizes on this property by triggering at two different energy thresholds.

The TRT detector covers the range of  $|\eta| < 2.5$  with an average resolution of  $170\mu\text{m}$ . In the barrel region there are 73 layers of TRT straws with an average length of 74cm. These straws are placed in parallel to the beamline and distributed evenly around the  $\phi$  axis with a full  $\phi$  coverage and a pseudo-rapidity range of  $|\eta| < 0.7$ . In the end-cap regions, there are in total 18 wheels of TRT straws that are placed parallel to the transverse plane. Each wheel is composed of multiple layers of straws covering a range of  $0.7 < |\eta| < 2.5$ .

### 3.2.3 The Calorimeter System

The calorimeter system [30] does particle energy measurement by forming dense media where particles have a higher chance to interact and produce shower. The calorimeter system is split into Electromagnetic (EM) and hadronic calorimeters. The overview of the ATLAS calorimeter system can be found in Figure 3.4.

### 3.2.3.1 The Electromagnetic Calorimeter

The EM calorimeter is a sampling calorimeter made out of Liquid Argon (LAr) detectors [30] that are composed of lead absorber plates optimized to facilitate electromagnetic showers and Kapton electrodes that collect these ions. The lead absorber plates provide a radiation depth of  $> 22 X_0$  ( $X_0$  is the radiation length) for EM shower containment [32]. In the barrel region the LAr detector covers the range  $|\eta| < 1.475$ , and in the end-caps there are two LAr detectors that cover the range of  $1.375 < |\eta| < 3.2$ . The shape of the Kapton electrodes and their spacing have been optimized based on their locations to maximize the detection efficiency.

The energy resolution in the calorimeter system is parameterized as  $\sigma(E)/E \approx \frac{a}{\sqrt{E}} \oplus \frac{b}{E} \oplus c$  where  $a$  is the stochastic term,  $b$  is the noise term, and  $c$  is the constant term. The EM calorimeter has an energy resolution of  $\sigma(E)/E \approx 10\%/\sqrt{E} \oplus 0.17/E \oplus 0.7\%$  ( $E$  in terms of GeV).

### 3.2.3.2 The Hadronic Calorimeter

The hadronic calorimeter is composed of three different detectors [30]. The barrel region ( $|\eta| < 1.7$ ) is covered by the tile calorimeter, the end-cap regions at  $1.5 < |\eta| < 3.2$  are covered by LAr calorimeters, and the very forward regions ( $3.1 < |\eta| < 4.9$ ) are covered by high-density Forward Calorimeter (FCAL).

The tile calorimeter is composed of iron absorbers and scintillator tiles placed radially in an alternating pattern. Optic fibers collect signals produced by particles passing through the scintillating tiles. These signals are then amplified through photomultipliers to obtain an energy measurement. The tile calorimeter has an energy resolution of  $\sigma(E)/E \approx 0.5/\sqrt{E} \oplus 0.03$  ( $E$  in terms of GeV)

The hadronic LAr calorimeter [30] resides outside the EM LAr calorimeter. In contrast to the EM LAr, it uses copper absorber plates. The hadronic LAr calorimeter has an energy resolution of  $\sigma(E)/E \approx 70\%/\sqrt{E} \oplus 3\%$  ( $E$  in terms of GeV). In other aspects, it functions similarly to the EM calorimeter.

The FCAL [30] is also a LAr calorimeter that is placed in the forward region and is composed of three layers. The first layer is composed of LAr with copper absorbers while the other layers are made out of tungsten. The FCAL LAr has an energy resolution of  $\sigma(E)/E \approx 100\%/\sqrt{E} \oplus 10\%$  ( $E$  in terms of GeV) for hadrons, and an energy resolution of  $\sigma(E)/E \approx 25\%/\sqrt{E} \oplus 3.8\%$  ( $E$  in terms of GeV) for electrons. The FCAL is important for electron identifications since there is no EM calorimeter coverage in the forward region.

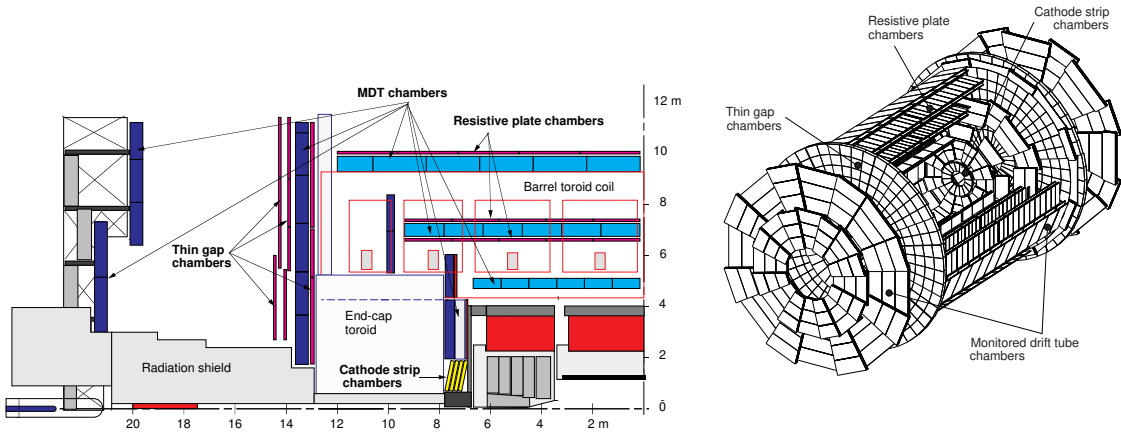


Figure 3.5: Overview of the whole MS. The side view is on the left and the transverse view is on the right [33].

### 3.2.4 The Muon Spectrometer

Muons can penetrate through the whole ATLAS detector without being absorbed. For this reason, the MS [33] is the outermost layer of the ATLAS detector. It is composed of four different detectors: MDT and Cathode Strip Chambers (CSC) for precision tracking, and Resistive Plate Chambers (RPC) and Thin Gap Chambers (TGC) for triggering. The MS is formed of three precision detector layers to track muons, and a magnetic field is applied for the pseudo-rapidity range of  $|\eta| < 2.7$  to bend the muon tracks. The whole MS structure can be viewed in Figure 3.5.

#### 3.2.4.1 Monitored Drift Chambers

The MDT [33] system is a precision muon tracker that is situated in the barrel and the end-cap regions. The MDT system is composed of tubes that are 30mm-diameter aluminum alloy cylinders with a 50 $\mu$ m-diameter anode wire passing through their centers. These tubes are filled with a gas mixture of 93% Ar and 7% CO<sub>2</sub>. As charged particles pass through an MDT tube, the gas mixture ionizes, and the ionized electron movements generate a current resulting in an electric signature. The spatial resolution of an MDT tube is 80 $\mu$ m.

The MDT tubes are layered together, forming the structure that can be viewed in Figure 3.6 called an MDT chamber. The MDT Chamber is composed of two layers of MDTs stacks with a gap in the middle. Each of these stacks is formed of 3 or 4 layers MDT tubes. In the barrel region, these chambers are distributed through concentric layers around the beam axis, and in the end-cap regions these chambers are combined into wheels. When

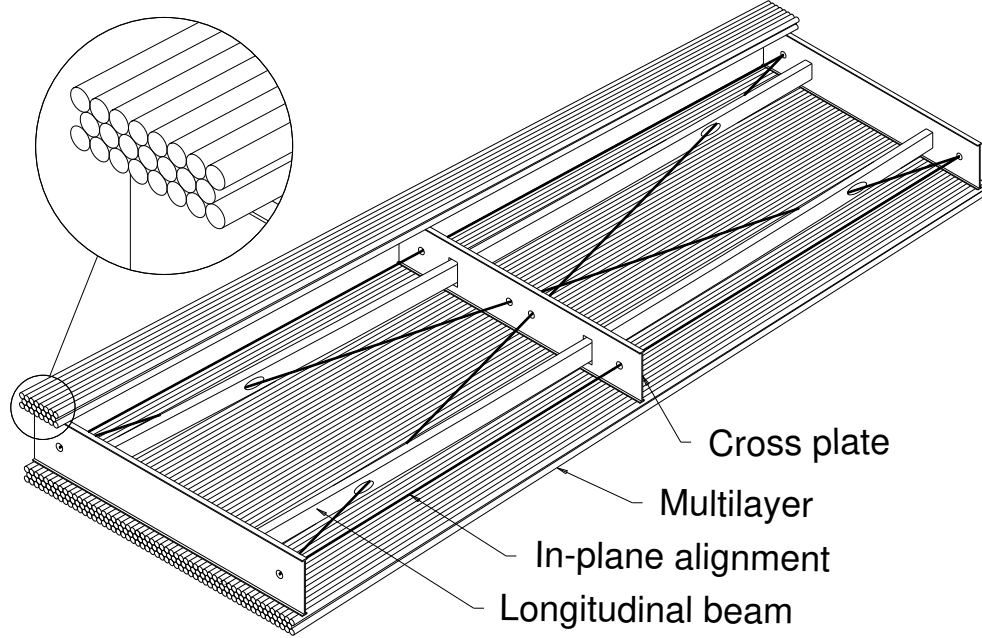


Figure 3.6: Detailed view of the  $2 \times 3/2 \times 4$  MDT chamber structure [33]. The MDT Chamber is composed of two layers of MDTs stacks with a gap in the middle. Each of these stacks are formed of 3 or 4 layers MDT tubes.

charged particles pass through the MDT chambers, they form spatial segments. These segments from each MDT layers are combined to reconstruct the paths of these particles.

### 3.2.4.2 Cathode Strip Chambers

In the very forward region ( $2.0 < |\eta| < 2.7$ ) of the end-caps where the particle flux is high, CSC detectors [33] are used for precision tracking. CSC are multiwire proportional chambers that can be viewed in Figure 3.7. They are composed of anode wires and cathode strips. The cathode strips are positioned orthogonally to the anode wires filled with 80% Ar and 20% CO<sub>2</sub>. As charged particles pass through the CSC they create particle showers between anode wires and cathode strips, creating a two-dimensional signal signature. Similar to MDTs, CSCs are layered on top of each other in four layers, placed in parallel to the transverse plane symmetrically along the  $\phi$  direction. The CSC system provides a resolution of 60  $\mu\text{m}$  in  $\eta$  and 5 mm in  $\phi$  with a time resolution of 7 ns.

### 3.2.4.3 Resistive Plate Chambers

The RPC [33] are gaseous detectors used in the barrel region for triggering. Each RPC is formed of two parallel plates with a gas gap in between filled with C<sub>2</sub>H<sub>2</sub>F<sub>4</sub>-C<sub>4</sub>H<sub>10</sub>. These parallel plates provide an average electric field of 4.5 kV mm<sup>-1</sup>. Charged particles passing

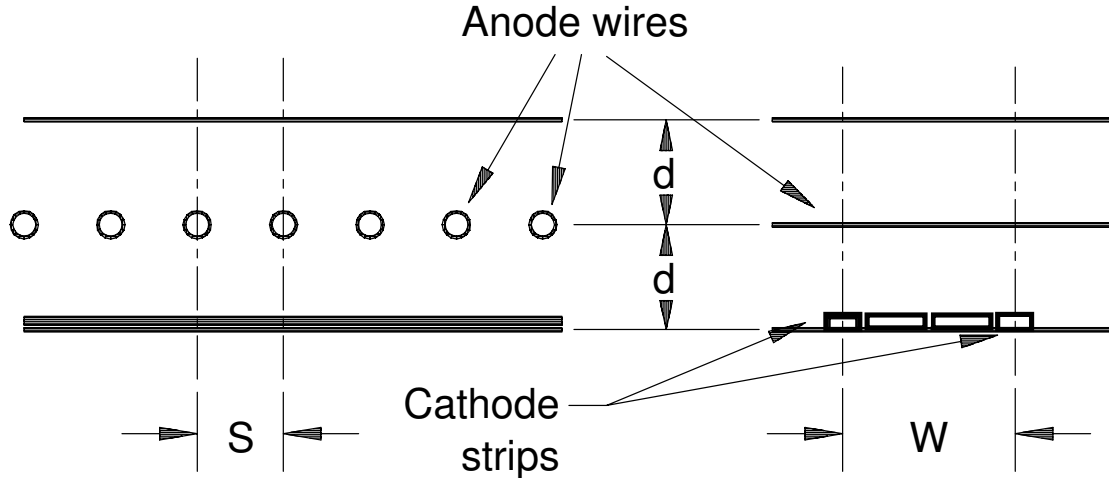


Figure 3.7: Internal structure of the CSC detector. The multiwire proportional chamber structure can be seen with its anode wires and cathode strips [33]. The anode-cathode spacing ( $d$ ) and wire pitch ( $S$ ) is 2.54 mm, and the cathode readout pitch ( $W$ ) is 5.08 mm.

through RPC ionizes the gas mixture, and the movements of these ionized electrons create an electrical signature. Two layers of RPCs placed are perpendicular to each other in order to provide coverage in both  $\eta$  and  $\phi$  directions. The RPC detectors provide a space resolution of 1 cm and a time resolution of 1.5 ns for the pseudo-rapidity range of  $|\eta| < 1.05$ .

#### 3.2.4.4 Thin Gap Chambers

TGC detectors [33] replace RPCs for muon triggering in the end-cap regions where the particle fluxes are high. They cover the pseudo-rapidity range of  $1.05 < |\eta| < 2.4$ . TGCs are similar to multiwire proportional chambers used in the CSC chambers with the difference of having a larger anode wire pitch (1.8 mm) and a larger cathode-to-anode distance (1.4 mm). A gas mixture of 55%  $\text{CO}_2$  and 45%  $n\text{-C}_5\text{H}_{12}$  is used in order to have a time response of 25 ns. TGCs are placed in parallel to the MDT wires to provide azimuthal angle information for muons.

### 3.3 Trigger and Data Acquisition

The LHC collides proton beam bunches at a rate of 40 MHz, while the ATLAS detector can only record events at a rate of  $\approx 1$  kHz. For this reason, the ATLAS detector is designed to only select and record interesting physics processes. The system that is responsible for selecting these processes is called the Trigger and Data Acquisition (TDAQ) system [34]. An overview of the TDAQ system is shown in Figure 3.8. The TDAQ system is

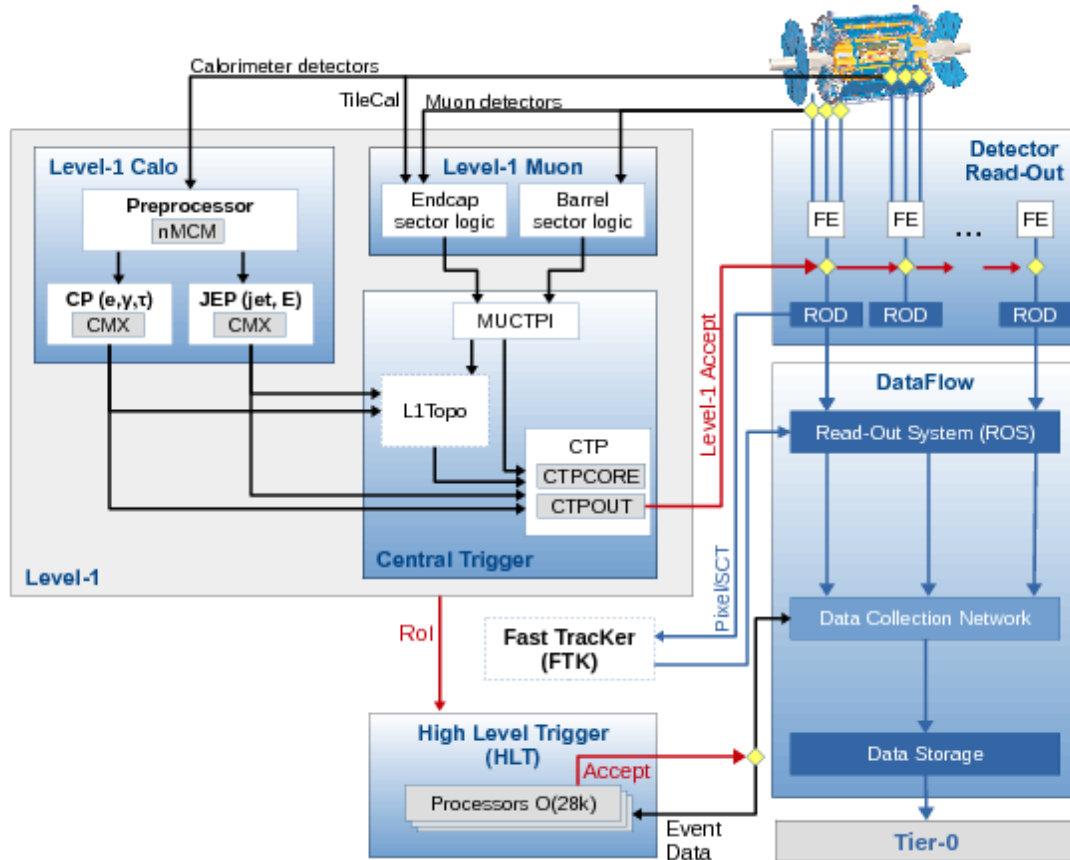


Figure 3.8: Overview of the TDAQ system [34]. The diagram shows the information flow path from the detector to the trigger systems on the left side, and the trigger decision is marked in red. The readout system is shown on the right side.

composed of the trigger system and the Data Acquisition (DAQ) system. The trigger system is responsible for selecting interesting events while the DAQ system is responsible for the storage of all selected events. The trigger system is further divided into two stages that are called Level-1 Trigger (L1) and High Level Trigger (HLT).

### 3.3.1 The Level-1 Trigger

The L1 trigger [34] receives data from muon and calorimeter systems at a rate of 40MHz. The L1 trigger makes decisions by identifying events with energetic particles or large  $E_T^{\text{miss}}$ . The trigger decisions are made in  $2.5\mu\text{s}$  and the output rate is 100kHz. The L1 system is further divided into sub-categories: Level-1 Calorimeter Trigger (L1Calo), Level-1 Muon Trigger (L1Muon), Level-1 Topological Trigger (L1Topo), and Central Trigger Processor (CTP) [34].



L1Calo reads analog signals from the calorimeters. Using the signal, L1Calo calculates the total transverse energy and identifies particle candidates. If the identified particle candidates have a  $E_T$  that is above pre-defined thresholds, the particle information is passed on to the L1Topo system. In addition the  $E_T$  information is passed on to the CTP system.

L1Muon uses muon information from RPCs and TGCs. It uses matching hits in various layers of detectors to identify and measure the  $p_T$  of muon candidates and feeds this information to the CTP system.

L1Topo uses the information given by the L1Calo and L1Muon systems to make a trigger decision based on the topology/kinematics of events, for example, the mixed flavor ( $e\mu$ ) di-lepton trigger.

The CTP system receives particle information from L1Calo, L1Muon, and L1Topo and makes the final trigger decision according to pre-sets given by the users. CTP also manages timing and pre-scaling (scaling events to match readout rates) and makes sure the readout buffers are not overflowed with data.

### 3.3.2 High-Level Trigger

Events triggered by the L1 trigger are then further processed by the HLT system [34]. The HLT system takes data in full granularity and reduces the output event rate to 1 kHz with an average event processing time of 235 ms. HLT makes trigger decisions by using information from regions of interest provided by the L1 triggers, or information from the full-detector (if required). As timing is the primary concern on triggering, the HLT operates in two stages. The first stage does a basic and partial event reconstruction in order to make a fast event selection, and the second stage uses the accepted events to make a complete but slow trigger decision. Events that pass both stages are then stored for offline analysis.

## 3.4 Simulation

Monte Carlo (MC) [35] method simulates physics processes that occur during proton-proton collisions. The simulated events are treated identically to data, but certain scale factors are applied to fix possible mis-modeling on simulation processes.

The simulation is done in several steps: generating physics events, decaying resulting particles, mimicking beam conditions, and simulating particle interactions with the sub-detectors. These steps are summarized in Figure 3.9 and described below:

- Event generation: Event generators produce individual physics events starting from proton-proton collisions. They simulate the constituents of proton-proton collisions

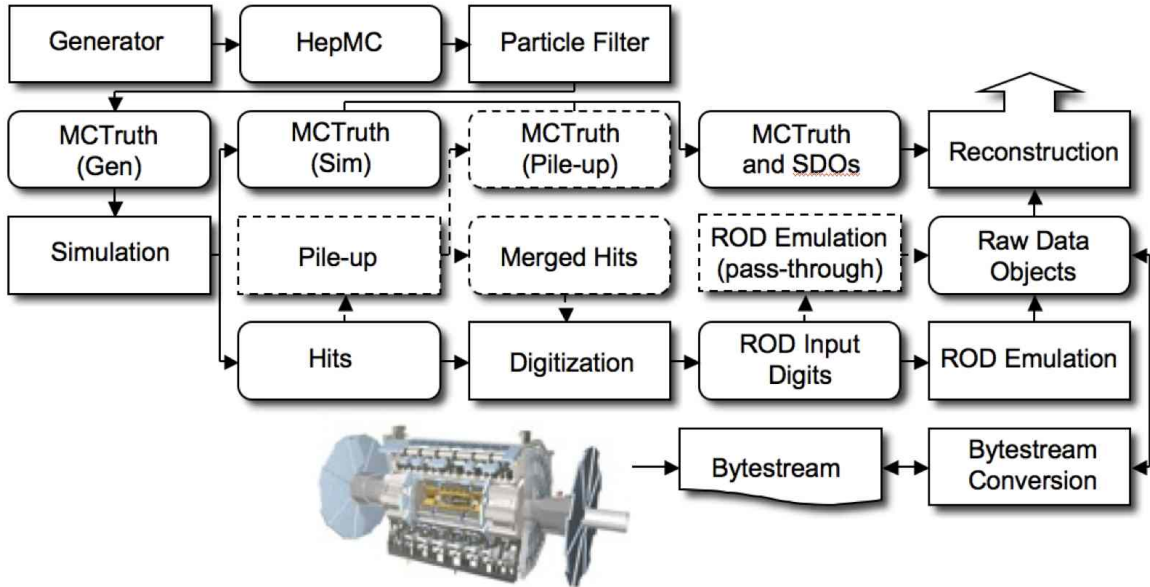


Figure 3.9: The ATLAS simulation flow diagram [35]. The diagram starts from event generators (top left) and passes through the full detector simulation (bottom to top right) where pile-up, hits, and electronics effects are simulated. The second row of the diagram shows how the truth information is handled.

using Parton Distribution Function (PDF)s [36] and calculate hard interaction matrix elements to a certain energy limit with a determined amount of final particles. These events are called processes-level events.

- Particle decays/showers: Event generators simulate the first moments of particle generation and hadronization. These particles are then showered/decayed as the second step of the MC generation. Certain groups of MC generators can shower particles by themselves, and others use external tools like PYTHIA [37] to do the showering. These showered events are referred to as parton-level or generator-level events.
- Pile-up: At the LHC multiple proton-proton collisions occur simultaneously. During event reconstruction, these additional collisions can interfere. These additional proton-proton collisions are called pile-up events and must be simulated in parallel to event generation. For this purpose, when simulating physics events, additional pile-up events are included.
- Detector simulation: Particle interactions with the ATLAS detector are simulated using GEANT 4 [38]. It simulates particle-material interactions and resulting energy deposits in detectors. These energy deposits are converted into detector signals.

## CHAPTER 4

# Object Reconstruction at ATLAS

Electrons, muon, photons, and hadrons that cross the ATLAS detector leaves different detector signatures at different sub-detectors. Figure 4.1 presents a slice of the ATLAS detector and demonstrates different detector signatures that different particles could leave. These particles are reconstructed using offline reconstruction algorithms using the detector signatures left by these particles. This chapter describes how different particles are reconstructed.

### 4.1 Track Reconstruction

A track is the reconstructed trajectory of a charged particle in the ID or the MS. Tracks can be used to identify a particles direction, production vertex, momentum, and charge.

#### 4.1.1 Inner Detector Track Reconstruction

The ID is the closest detector to the beam line. As a consequence, it observes a large population of particles from collisions. The large population of particles holds a challenge for track reconstruction. The NEWT [40] algorithm is used to reconstruct tracks with the inside-out and outside-in algorithms.

The inside-out algorithm starts by creating space points (three-dimensional representations of hits inside the ID) from hits. The space points inside the first three layers of the pixel detector are combined to form track seeds (starting tracks). A likelihood method is then used to expand the seed tracks to the SCT in order to form track candidates, which are then extended to the TRT to form full tracks.

The outside-in algorithm uses the leftover TRT track segments to seed tracks going from the TRT to the pixel detector to reconstruct additional tracks. This method is used for

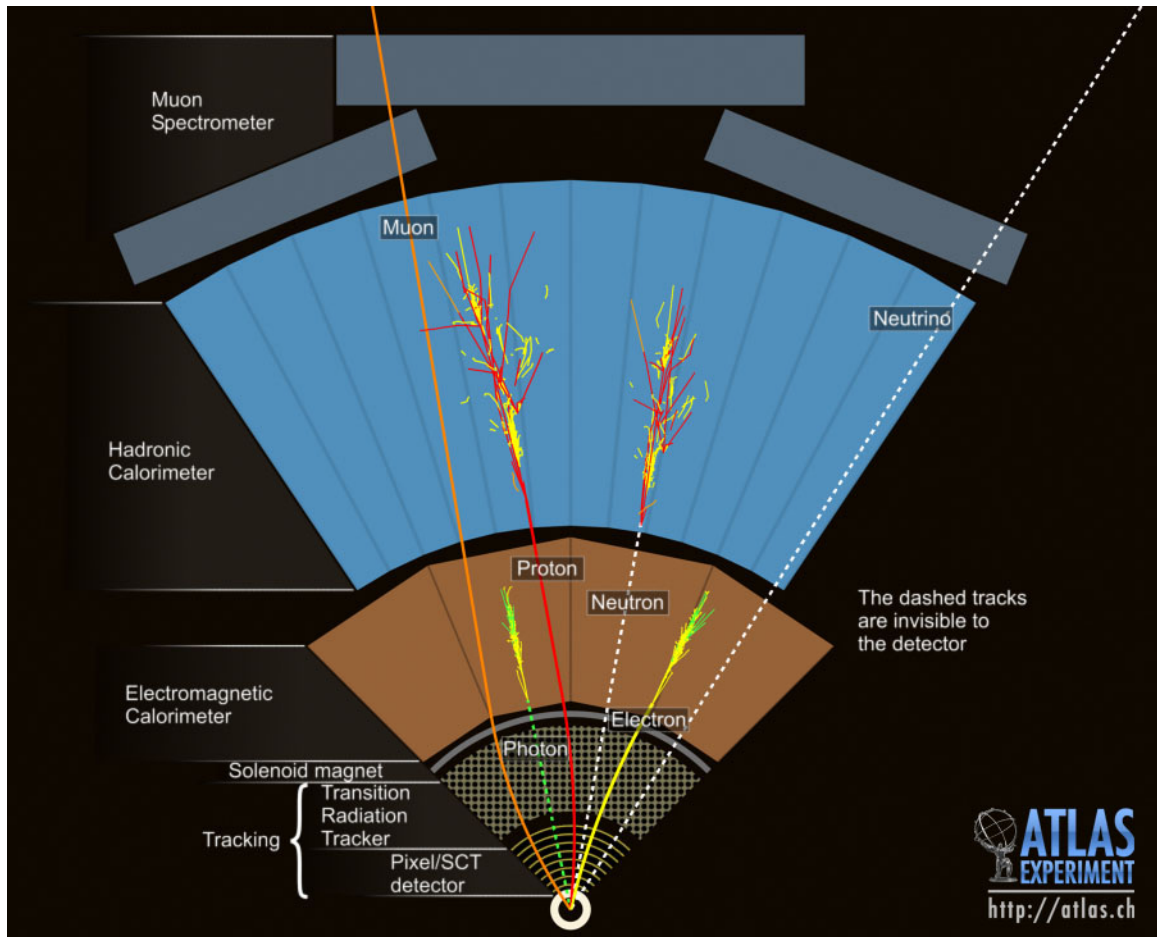


Figure 4.1: Slice of the ATLAS detector. Hadrons, electrons, muons, neutrinos, and photons all leave different detector signatures at different sub-detectors [39].

identifying secondary tracks coming from other sources (i.e. not coming from the primary vertex) like  $b$  jets or long-lived particles.

## 4.2 Vertex Reconstruction

In every bunch crossing (proton bunches passing through each other), more than one proton-proton collision may occur. Event vertices are reconstructed to differentiate these collisions. An event vertex is the point of origin of a set of particles.

The Primary Vertex (PV) [41] is the identified point of a  $pp$  collision. A PV is reconstructed using tracks reconstructed by the ID that satisfy the criteria given in Table 4.1. Selected tracks are used to identify a seed position for the beam spot. After the seed is selected, all vertex positions are calculated using an iterative  $\chi^2$  minimization method to find optimal vertex positions. At every iteration, the best vertex is reconstructed, and tracks matched to the reconstructed vertex are removed. This process is repeated until all vertices are reconstructed. Vertices that have at least two associated tracks are labeled as PVs.

Track Cut	Values
$p_T$	$p_T > 400 \text{ MeV}$
$\eta$	$ \eta  < 2.5$
Min. # hits in SCT	9
Min. # hits in SCT and Pixel	11
Max # Pixel Holes	0
Min # hits in IBL + B-layer	1
Max # Shared modules	1 pixel or 2 SCT hits
Max # SCT Holes	1

Table 4.1: Track requirements for PV reconstruction [42]. In this table, hits refer to a detector element detecting the tracked particle and holes refer to the particle passing through areas that does not have detector coverage inside the detector structure.

Impact parameters are defined in parallel to the PV as variables designed to calculate a track's distance to the PV. The  $d_0$  impact parameter is the transverse distance to the PV at the point of closest approach, and the  $z_0$  impact parameter is the  $z$  axis component of the point of closest approach.

## 4.3 Electrons

Electrons are reconstructed as energy clusters in the calorimeter that are matched to tracks formed in the ID. Electrons are reconstructed and identified in three steps. The first step is the reconstruction of electron candidates. The second step is the classification of these candidates according to their quality criteria. The last step is to apply isolation requirements to differentiate electrons from other physics objects.

### 4.3.1 Electron Reconstruction

Electron reconstruction starts by reconstructing signatures from the EM calorimeter using topo-clusters [43]. Topo-clusters are formed by identifying high significance energy clusters in the calorimeter and joining all topologically-connected energy clusters together.

The next step is to reconstruct the tracks. The majority of tracks inside the ID come from pions. For this reason, the track reconstruction gives priority to pions, and tracks are reconstructed using the pion energy loss algorithm. If a track seed has  $p_T > 1$  GeV, can be spatially matched to an energy cluster, and cannot form a full track till the energy cluster, it is re-reconstructed as an electron track using the electron energy loss algorithm where the bremsstrahlung effect is also taken into account. The reconstructed electron tracks are then matched with an EM cluster. A primary electron track is selected for every cluster according to its momentum and cluster-track distance. The selected primary electron track and the energy cluster form an electron. To differentiate an electron from a photon, further hit requirements are introduced like a hit in the first layer of the pixel detector as well as a certain number of hits in the pixel detector. Electrons can only be identified in the region of  $|\eta| < 2.47$  due to the coverage of the ID detector.

### 4.3.2 Electron Identification

Electron identification [44] uses the size of EM cluster, cluster shape, number of hits for the associated ID track, track-cluster matching information, and TRT information to differentiate other physics objects from electrons. All information is combined using a likelihood-based method. Different Likelihood (LH) criteria (working points) are defined to reject background particles from electrons. These identification points are Loose, Medium, and Tight. Tight electrons have the highest background rejection rate. Electron identification efficiencies for different electron working points can be found in Figure 4.2 as a function of the electron  $E_T$ .

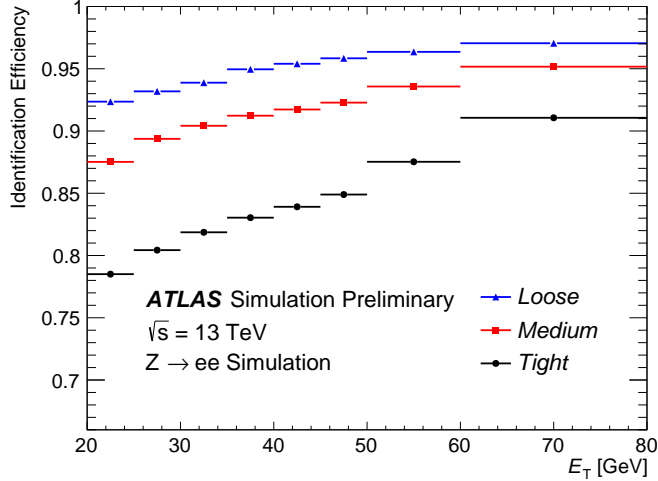


Figure 4.2: Electron identification efficiencies as a function of the electron  $E_T$  for different working points [44].

### 4.3.3 Electron Isolation

In addition to electron identification criteria, the electron isolation is defined to further differentiate real electrons from fake electrons originating from other sources like converted photons or hadron decays. Two variables are used for electron isolation:  $E_T^{\text{cone} - 0.2}$  (sum of transverse energies of all topological clusters in a given shrinking cone of  $\Delta R$ ) and  $p_T^{\text{cone} - 0.2}$  (sum of transverse momentum of all tracks in a given shrinking cone of  $\Delta R$ ). The isolation requirements for electrons are  $E_T^{\text{cone} - 0.2}/p_T < 0.3$  and  $p_T^{\text{cone} - 0.2}/p_T < 0.15$ . On top of the electron isolation, Prompt-Lepton Veto (PLV) [45], and charge flip killer [46] BDTs are also used as additional discriminants.

#### 4.3.3.1 Charge-Flip Killer

The electron charge is reconstructed using the curvature (due to the magnetic field) of the matched ID track. The bremsstrahlung process can result in a wrongly-reconstructed electron track which could lead to the charge being mismeasured. To identify these events, a BDT variable called ‘‘Charge-Flip Killer’’ is introduced. The charge-flip killer program attempts to identify these electrons using  $d_0 \times q$  (where  $q$  is the charge of the track),  $E/p$ , and other kinematic parameters by training a BDT variable. This BDT can identify electrons that have wrongly-reconstructed tracks with an efficiency of up-to 95%.

### 4.3.3.2 Prompt-Lepton Veto

PLV [45] is the name of the BDT that aims to tag electrons produced from heavy flavor decays. It uses the number of tracker-based jets close to the electron ( $\Delta R < 0.4$ ),  $E_T^{\text{cone } 0.2}/p_T$ ,  $b$ -tagging BDT values, and other kinematic variables to identify these decays. The BDT is trained on semi-leptonic  $b$ -quark decays and leptons coming from the decay of the  $W$  boson. The PLV is applied on top of the electron charge-flip killer and isolation requirements to identify electrons originating from heavy-flavor decays.

## 4.4 Muons

Muons can be differentiated from the majority of other particles produced in  $pp$  collisions. Muon signals are reconstructed and identified in three steps. Firstly, muons are reconstructed using tracks, and then are classified/identified to their quality. Lastly, additional isolation requirements are applied to differentiate them from other background particles.

### 4.4.1 Muon Track Reconstruction

Muon track reconstruction [47] starts by forming segments. Segments are vectors that connect MDT hits and trigger chamber hits in a straight line (while correcting it for bending due to the effect of the magnetic field). Muon track candidates are then formed by combining segments at different stations. Muon candidates are allowed to share segments during this process. After the candidate formation, each hit on each track candidate is fitted using a global  $\chi^2$  fit to find the best combinatorics for the global  $\chi^2$ . After a set of tracks are accepted, the  $\chi^2$  is repeated without the selected tracks and their associated hits. The process is repeated until all track candidates are sorted. An exception to this is the MS segments in the outer layer. They can be accepted as tracks without a need for segments in other layers. This exception helps the identification of muons that are at the border of the muon detector coverage.

### 4.4.2 Muon Reconstruction

Since muons can penetrate all layers of the ATLAS detector, the muon reconstruction [48] relies on tracks that are reconstructed inside both the MS and the ID. There are four commonly-used methods to reconstruct muons, and they differ by how they use tracks from the ID. The methods used for muon construction at ATLAS are:



- **Combined Muon:** This is the most common technique used at the ATLAS experiment. The muon track reconstruction is conducted independently in the MS and the ID. These tracks are then combined using a global fit, similar to the outside-in method used for electrons. The combined muon method has a higher reconstruction priority compared to other methods.
- **Segment-Tagged:** This reconstruction method is used for identifying muons that have low  $p_T$  and only a few hits in the MS. Tracks inside the ID matched with at least one CSC or MDT segment are reconstructed as segment-tagged muons.
- **Calorimeter-Tagged:** Calorimeter-tagged muons are ID tracks associated with an energy deposit in the calorimeter that belongs to a minimum-ionizing particle. This reconstruction method is used for  $|\eta| < 0.1$ .
- **Extrapolated/Standalone Muons:** This reconstruction method uses only MS tracks coming from the beam spot. It requires hits from at least two layers of the MS. This method is only used for the forward regions of the MS where there is no ID coverage ( $2.5 < |\eta| < 2.7$ ).

### 4.4.3 Muon Identification

Muon identification [48] is used for discriminating signal muons from background particles. Similar to electrons, different working points are defined for muon identification: Loose, Medium, and Tight. Tight muons have the highest background rejection rate. Detailed descriptions of the muon identification working points are given below. Comparison of muon identification efficiencies between data and MC and efficiencies as a function of the muon  $\eta$  for different working points can be found in Figure 4.3.

- **Loose:** Loose identification uses all muon types to provide a working point with high reconstruction efficiency. It uses combined muons with at least three hits in two MDT stations and standalone muons at the range of  $2.5 < |\eta| < 2.7$  with at least three MDT or CSC stations. Calorimeter-tagged and segmented-tagged muons are also used for the region of  $|\eta| < 0.1$ .
- **Medium:** Medium identification is defined to be the generic working point for most analysis. It uses combined muons with at least three hits in two MDT stations and standalone muons at the range of  $2.5 < |\eta| < 2.7$  with at least three MDT or CSC layers. As an exception the combined muons in the range of  $|\eta| < 0.1$  only need to have one hit in the MDT station but can only have at most one MDT hole (particle

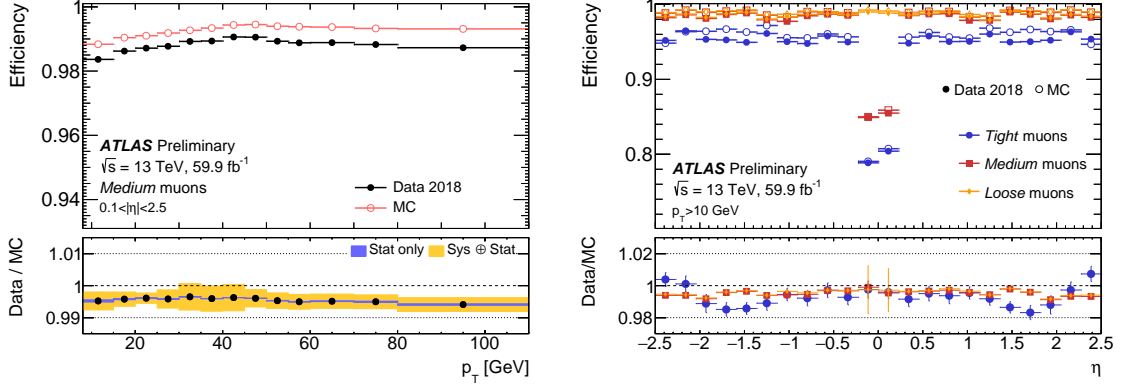


Figure 4.3: Comparison between data and MC for the muon identification efficiency as a function of the muon  $p_T$  (left) and  $\eta$ -dependent identification efficiencies for different working points [49].

passing through an uncovered region in the MDT detector). The reconstructed muons tracks are also required to satisfy additional momentum requirements.

- **Tight:** Tight identification is defined to have high purity. It only uses combined muons that satisfy all medium requirements in addition to having hits in at least two MS stations. Extra  $\chi^2$  and momentum requirements are applied on the muon track reconstruction.

#### 4.4.4 Muon Isolation

Muon isolation is an additional requirement to reduce muons originating from non-prompt particle decays. Similar to electrons, two variables are defined for muon isolation. They are  $E_T^{\text{cone} - 0.3}$  (sum of transverse energies of a topological clusters in a given shrinking  $\Delta R$  cone excluding muon energy deposits) and  $p_T^{\text{cone} - 0.3}$  (sum of transverse momentum of tracks with  $p_T > 1$  GeV in a given shrinking  $\Delta R$  cone excluding muon tracks). The muon isolation working point used in this thesis has a  $p_T$ -dependent efficiency that varies between 95% and 99%. PLV is also used for differentiating signal muons from muons originating from heavy flavor decays.

##### 4.4.4.1 Prompt Lepton Veto

PLV [45] is the name of the BDT that aims to tag muons produced by heavy flavor decays. The BDT uses the number of tracker-based jets close the muon ( $\Delta R < 0.4$ ),  $E_T^{\text{cone} - 0.2}/p_T$ ,  $b$ -tagging BDT values, and other kinematic variables to identify these decays. The BDT

is trained on semi-leptonic  $b$ -quark decays and leptons coming from the decay of the  $W$  boson. The PLV is applied on top of the charge-flip killer and isolation requirements to identify muons originating from heavy-flavor decays.

## 4.5 Jets

Jets are clusters of particles that come together within a certain angular cone to form a representation of single particle decay. In most cases, jets represent hadrons coming from quarks or gluons.

### 4.5.1 Jet Reconstruction and Calibration

Jets used in this thesis are reconstructed [50][51] from calorimeter clusters using the anti- $k_T$  algorithm [52]. The algorithm works by identifying high-energy topologically-connected energy clusters (topo-clusters) and clustering all of them in a cone of radius of 0.4 around the highest-energy cluster to form a jet.

During this reconstruction process, energy losses occur due to detector geometry and other factors like wrongly-associated clusters for overlapping jets. The jet energy losses are corrected in a five-step process that is detailed below:

- **Origin Correction:** The jet track is re-calibrated to point to the primary vertex keeping the energy constant,
- **Pile-up Correction:** A pile-up energy correction is done by removing energy and momentum from the jet according to the pile-up density of the detector.
- **MC-based Calibration:** The jet energy is re-calibrated by using calibration factors that are derived by comparing truth jet four-momentum to the reconstructed jet four-momentum.
- **Global Sequential Correction:** [51] The Global sequential correction is composed of multiple multiplicative corrections to jet energy. It uses the topology of energy deposits, tracking information and even the MS response to correct the jet energy reconstruction according to the particles constituting the jet.
- **In Situ Calibration:** As the last step, a correction is applied to data that correct the data for any MC biases created in the previous steps as all the previous steps rely on MC simulation. This correction is derived by comparing MC jet responses to data jet responses as a function of the jet  $\eta$  and  $p_T$ .

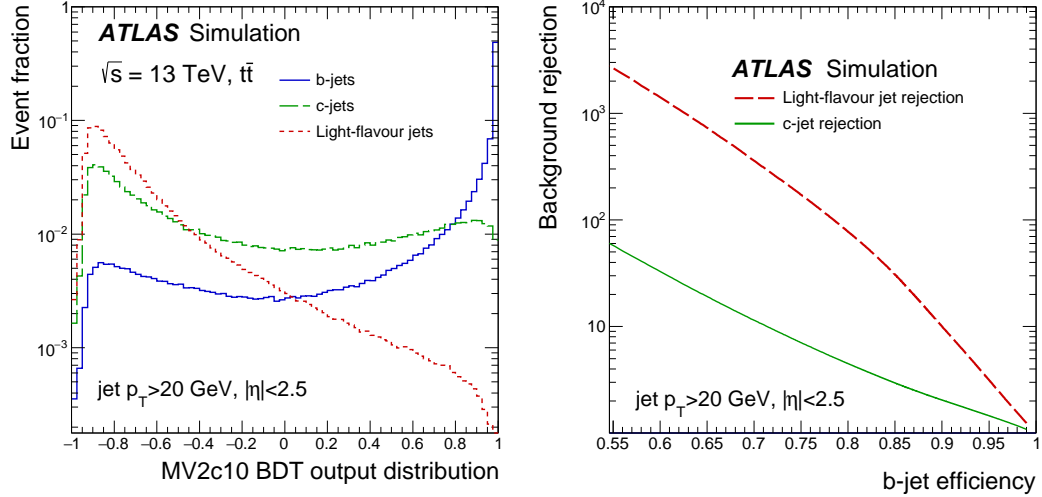


Figure 4.4: The  $MV2c10$  BDT output distribution (left) and tag efficiency (right) [53].

### 4.5.2 $B$ -Tagging

The  $b$ -hadrons have a longer lifetime compared to other hadrons. This means a  $b$ -hadron can travel small distances ( $\approx 1$  mm) before it decays; hence the decay vertex of the  $b$ -hadron can be differentiated from the PV. Capitalizing on this property becomes especially important to identify the Higgs boson or the top quark since both particles have a high tendency to decay into  $b$ -quarks.

Jets produced by  $b$ -hadrons are identified using multivariate BDT algorithms  $MV2$  [53]. These algorithms exploit the lifetime of the  $b$ -quark using secondary vertices, track  $p_T$ , and track  $\eta$  of  $b$ -jets in relation to other particles in the event. The BDTs are trained on  $t\bar{t}$  events by tagging  $b$ -jets as signals and other quarks as backgrounds. Depending on the c-jet composition in the trained backgrounds, three  $MV2$  algorithms are trained:  $MV2c00$  (no c-jets),  $MV2c10$  (7% c-jets) and  $MV2c20$  (15% c-jets). The  $MV2c10$  BDT output distribution and the  $b$ -tag efficiency can be found in Figure 4.4.

## 4.6 Missing Transverse Energy

Some stable and charge neutral particles do not interact with the ATLAS detector, and it is challenging to detect them with the ATLAS detector. This is especially true for neutrinos, as they fly through the detector without leaving any tracks or energy deposits. These particles can still be detected via the momentum imbalance. For each collision, the initial-state has a transverse momentum that is close to zero, so the final-state transverse momentum should also be zero due to the conservation of momentum. The  $E_T^{\text{miss}}$  represents this momentum

imbalance that can correspond to the transverse momentum of a neutrino generated.

The  $E_T^{\text{miss}}$  reconstruction [50] algorithm uses vectorial sum of high transverse momentum  $p_T$  particles (electrons, muons, taus, and jets) and track-based soft term to calculate the  $E_T^{\text{miss}}$ . The track-based soft term is calculated using an algorithm that computes the total energy from the tracks originating from the PV but are not associated with any hard objects. This track algorithm is robust against pile-up due to its reliance on tracks. However it cannot detect neutral particles, and is limited by the detector coverage. The  $E_T^{\text{miss}}$  calculation can be summarized using Equation 4.1:

$$\vec{E}_T^{\text{miss}} = \left( \sum_i^e \vec{E}_{T_i}^e + \sum_i^\mu \vec{E}_{T_i}^\mu + \sum_i^\tau \vec{E}_{T_i}^\tau + \sum_i^{\text{jets}} \vec{E}_{T_i}^{\text{jets}} + \vec{E}_T^{\text{Track Soft Term}} \right). \quad (4.1)$$

## CHAPTER 5

# Physics Object Selection

The object reconstruction has been described in Chapter 4. This chapter describes the specific object selection criteria that are used for the  $W^\pm W^\pm W^\mp$  analysis.

### 5.1 Triggers

The lowest  $p_T$  non-prescaled single-lepton triggers are used. The list and the description of the triggers used can be found in Table 5.1. There are two triggers for each lepton type, and each one has different  $p_T$  cuts and ID requirements. The lepton triggers with lower  $p_T$  thresholds have additional isolation cuts applied.

Each event is required to fire at least one of these triggers and needs to contain the lepton that fired that trigger. A trigger scale factor is applied on MC events to simulate the trigger inefficiency observed in data. The lepton trigger inefficiency is derived using  $Z \rightarrow \ell\ell$  samples. Usage of di-lepton triggers have also been investigated, but no significant gains were observed.

### 5.2 Electrons

This analysis uses four different electron definitions with different quality requirements that are named “ID”, “anti-ID”, “anti-BL”, and “veto” electrons. All electron definitions

Type	Trigger Name	Quality	$p_T$ threshold	Isolation
Electron	HLT_E26_LHTIGHT_NOD0_IVARLOOSE	Tight	> 26 GeV	$p_T^{\text{cone-0.3}}/p_T < 0.16$
Electron	HLT_E60_LHMEDIUM_NOD0	Medium	> 60 GeV	-
Muon	HLT_MU20_IMEDIUM (2015 data only)	-	> 20 GeV	$p_T^{\text{cone-0.3}}/p_T < 0.06$
Muon	HLT_MU26_IVARMEDIUM	-	> 26 GeV	$p_T^{\text{cone-0.3}}/p_T < 0.07$
Muon	HLT_MU50	-	> 50 GeV	-

Table 5.1: Description of single-lepton triggers used. Each trigger has different isolation, quality and  $p_T$  requirements to prevent these triggers from being pre-scaled.

but the veto lepton are orthogonal to each other.

ID (signal) electrons are nominal electrons used in this thesis. They satisfy the “Tight” identification criteria and have  $p_T > 20\text{GeV}$  and  $|\eta| < 2.47$  (also needs to be outside of the region of  $1.37 \leq |\eta| \leq 1.52$  to veto the region that transits from barrel to end-caps). Electrons are also required to be originating from the PV by imposing the impact parameter requirements of  $|\frac{d_0}{\sigma_{d_0}}| < 5$  and  $|z_0 \times \sin \theta| < 0.5\text{ mm}$ . Electron isolation is applied to reduce electrons originating from other sources. In addition to the isolation, PLV, charge-flip killer and author requirements are applied. The author requirement rejects all electrons that can be interpreted as either photons or mis-reconstructed electrons during the reconstruction process. Detailed ID electron definitions can be found in Table 5.2.

Anti-ID electrons are used for estimating the non-prompt background. They differ from ID electrons mainly by a looser identification criteria, impact parameters, and isolation requirements. In addition, the PLV and the charge flip tagger requirements are removed. The anti-ID electrons are defined to be orthogonal to ID electrons by vetoing all ID electrons. Further details on anti-ID electron definitions can be found in Table 5.3.

Anti-BL electrons are defined as electrons that have a large contribution from photons that fake electrons. These electrons are used to estimate backgrounds coming from mis-reconstructed photons. Anti-BL electrons are identical to ID electrons, but unlike ID electrons that require a hit in the first layer of the pixel detector (B-layer), they are composed of electrons without B-layer hits. The author requirement is also removed. Further details on anti-BL electron definitions can be found in Table 5.4.

In addition to these orthogonal electron definitions, veto electrons are defined to have a  $p_T > 7\text{GeV}$  requirement and have to pass the Loose identification criteria. Details on veto electron definitions can be found in Table 5.5.

MC events with reconstructed electrons are scaled using reconstruction, identification, and isolation scale factors [54]. These scale factors are applied to correct the discrepancies between MC and data regarding the modeling of energy reconstruction, identification, and isolation.

<b>ID (signal) Electron Selection</b>
Reconstructed electron candidate
Kinematic acceptance: $E_T > 20 \text{ GeV}$
Geometrical acceptance: $ \eta  < 2.47$ , outside crack region $1.37 \leq  \eta  \leq 1.52$
Object quality: $el\_author == 1$
Identification criteria: Tight
Transverse impact parameter requirement: $ \frac{d_0}{\sigma_{d_0}}  < 5$
Longitudinal impact parameter requirement: $ z_0 \times \sin \theta  < 0.5 \text{ mm}$
Isolation requirement: Applied
PLV BDT value $< -0.7$
Charge Flip Killer BDT value $> 0.7$

Table 5.2: ID electron definition.

<b>Anti-ID Electron Selection</b>
Not tagged as an ID Electron
Reconstructed electron candidate
Kinematic acceptance: $E_T > 20 \text{ GeV}$
Geometrical acceptance: $ \eta  < 2.47$ , outside crack region $1.37 \leq  \eta  \leq 1.52$
Object quality: $el\_author == 1$
Identification criteria: Medium
Does not Satisfy the Signal Electron Requirements
Transverse impact parameter requirement: $ \frac{d_0}{\sigma_{d_0}}  < 5$
Longitudinal impact parameter requirement: $ z_0 \times \sin \theta  < 0.5 \text{ mm}$
Isolation requirement: None
PLV Requirement: None
Charge Flip Killer requirement: None

Table 5.3: Anti-ID electron definition.



<b>Anti-BL Electron Selection</b>
Not tagged as an ID Electron
Reconstructed electron candidate
Kinematic acceptance: $E_T > 20 \text{ GeV}$
Geometrical acceptance: $ \eta  < 2.47$ , outside crack region $1.37 \leq  \eta  \leq 1.52$
Identification criteria: Tight but with no B-Layer Hit
Transverse impact parameter requirement: $ \frac{d_0}{\sigma_{d_0}}  < 5$
Longitudinal impact parameter requirement: $ z_0 \times \sin \theta  < 0.5 \text{ mm}$
Isolation requirement: Applied
PLV Requirement: None
Charge Flip Killer requirement: None

Table 5.4: Anti-BL electron definition.

<b>Veto Electron Selection</b>
Reconstructed electron candidate
Kinematic acceptance: $p_T > 7 \text{ GeV}$
Geometrical acceptance: $ \eta  < 2.47$ , outside crack region $1.37 \leq  \eta  \leq 1.52$
Object quality: No electron author requirement
Identification criteria: Loose
No BADCLUSTER electrons, crack veto
Isolation requirement: None
PLV requirement: None
Charge Flip Killer requirement: None

Table 5.5: Veto electron definition.

## 5.3 Muons

Muons used in the analysis are reconstructed as described in Section 4.4. Similar to electrons, three different muon definitions are used: ID, anti-ID, and veto muons.

ID (signal) muons are defined to accept muons with high purity, rejecting majority of background muons. They use combined and standalone muon reconstruction methods with the Medium working point. Muons need to satisfy  $p_T > 20\text{ GeV}$  and  $|\eta| < 2.5$ . They are also required to be originating from the PV by imposing the impact parameter requirements of  $|\frac{d_0}{\sigma_{d_0}}| < 3$  and  $|z_0 \times \sin \theta| < 0.5\text{ mm}$ . Muon isolation is applied to reduce muons originating from other sources. In addition to the isolation, PLV is used to further reduce muons arising from heavy flavor decays. Specific ID muon definitions can be found in Table 5.6.

Anti-ID muons are defined to accept muons originating from decays of secondary particles. These muons differ from ID muons by a looser muon isolation and impact parameter requirements. The PLV cut is also dropped. Anti-ID muons are defined to be orthogonal to ID muons by vetoing all ID muons from its selection. Details on the anti-ID muon definition can be found in Table 5.7.

Veto muons, similar to veto electrons, are defined to be an inclusive muon selection to identify events with additional leptons. These muons have a lower  $p_T$  and looser isolation and quality requirements. Details on the veto muon definition can be found in Table 5.8.

MC events with reconstructed muons are scaled using identification, track-vertex association, and isolation scale factors [48][47]. These scale factors are applied to correct the discrepancies observed between MC and data.

<b>ID (signal) Muon Selection</b>
Reconstructed muon
Kinematic acceptance: $p_T > 20\text{ GeV}$
Geometrical acceptance: $ \eta  < 2.5$
Object Quality: medium with TRT cut off
Longitudinal impact parameter requirement: $ z_0 \times \sin \theta  < 0.5\text{ mm}$
Transverse impact parameter requirement: $ \frac{d_0}{\sigma_{d_0}}  < 3$
Isolation Requirement: Applied
PLV BDT value $< -0.5$

Table 5.6: ID muon definition.

<b>Anti-ID Muon Selection</b>
Not tagged as an ID Muon
Reconstructed muon
Kinematic acceptance: $p_T > 20 \text{ GeV}$
Geometrical acceptance: $ \eta  < 2.5$
Object quality: medium with TRT cut off
Does not Satisfy the Signal Muon Requirements
Longitudinal impact parameter requirement: $ z_0 \times \sin \theta  < 0.5 \text{ mm}$
Transverse impact parameter requirement: $ \frac{d_0}{\sigma_{d_0}}  < 10$
Isolation requirement: None

Table 5.7: Anti-ID muon definition.

<b>Veto Muon Selection</b>
Reconstructed muon
Kinematic acceptance: $p_T > 7 \text{ GeV}$
Geometrical acceptance: $ \eta  < 2.7$
Object quality: loose with TRT cut off
Isolation requirement: None

Table 5.8: Veto muon definition.

## 5.4 Jets

Jets used in this analysis are small- $R$  jets reconstructed using the anti- $k_t$  algorithm with  $R = 0.4$  from calorimeter clusters. Details on the jet reconstruction can be found in Section 4.5.1. Jets are required to have  $p_T > 20\text{GeV}$  for  $|\eta| < 2.5$  and  $p_T > 30\text{GeV}$  for  $|\eta| > 2.5$ . For jets with  $p_T < 60\text{GeV}$  and  $|\eta| < 2.4$ , an additional  $\text{JVT} > 0.59$  cut is required. The Jet Vertex Tagging (JVT) [55] is a discriminant based on a multivariate tool that uses tracks, vertex, jet momentum and track composition of the jet to discriminate/identify pile-up jets.

In order to identify jets originating from  $b$ -quarks, all selected jets in  $|\eta| < 2.5$  are tagged using the  $MV2c10$   $b$ -tagging algorithm defined in Section 4.5.2 at a 85% working point. At this working point, a light-quark has a  $\sim 2.5\%$  chance to be tagged as a  $b$ -quark. MC events are scaled using additional scale factors to correct the data-MC discrepancies in jet vertex tagging, as well as the  $b$ -quark identification rates by the  $MV2$  tool.

## 5.5 Overlap Removal

After object reconstruction, an overlap removal procedure is applied to all reconstructed objects. The aim is to prevent a particle from being reconstructed as two different objects. In this thesis, the overlaps of  $e/\text{jet}$ ,  $\mu/e$ , and  $\mu/\text{jet}$  objects are considered. The overlap of two objects are measured by the variable called  $\Delta R$  which is defined as  $\Delta R^2 = \Delta\eta^2 + \Delta\phi^2$  where  $\Delta\eta(\Delta\phi)$  is the  $\eta(\phi)$  difference of the two objects.

Electrons and jets are both reconstructed as energy deposits in the calorimeter. Due to the nature of this reconstruction, electrons and jets can be mis-reconstructed or duplicated as a particle of the other type. In such cases, electrons have a higher priority over jets. This means if a jet and an electron lie in  $\Delta R < 0.2$ , the jet is discarded. This rule is slightly modified in the case where the overlapping jet is a  $b$ -tagged jet, then the electron is discarded. This is done to preserve the  $b$ -tagging information in the analysis to reject non-prompt leptons. If an electron and jet lie in  $0.2 < \Delta R < 0.4$ , the electron is discarded as this is generally a sign of heavy flavor decay.

When an electron and a muon are reconstructed within  $\Delta R < 0.1$ , the electron object is removed as the electron is assumed to be coming from a photon radiated from the muon. In the case where a muon is overlapping with a jet with at least three associated tracks within  $\Delta R < 0.4$ , the muon is discarded since jets penetrating the calorimeter can cause this detector signature.

## 5.6 Missing Transverse Momentum

The  $E_T^{\text{miss}}$  is defined in Section 4.6. In this analysis, the particles used in the  $E_T^{\text{miss}}$  reconstruction are electrons, muons, and jets. The leptons used are the veto leptons defined in Sections 5.2 and 5.3. The jets used are the baseline jets defined in Sections 5.4 excluding all quality cuts. All objects after the overlap removal procedure described in Section 5.5 are used in the  $E_T^{\text{miss}}$  calculation.

## CHAPTER 6

# Signal Event Selection

In  $pp$  collisions,  $pp \rightarrow W^\pm W^\pm W^\mp$  are rare processes that are hidden behind other physics backgrounds. Cut-based methods are used to select  $W^\pm W^\pm W^\mp$  candidate events in data. The  $W^\pm W^\pm W^\mp$  processes are examined in two separate decay channels ( $\ell^\pm \nu \ell^\pm \nu jj$  and  $\ell^\pm \nu \ell^\pm \nu \ell^\mp \nu$ ) with dedicated cutflows.

### 6.1 Semi-Leptonic Signal Region

The main analysis strategy for the semi-leptonic ( $\ell^\pm \nu \ell^\pm \nu jj$ ) channel is to select  $W^\pm W^\pm W^\mp$  events by avoiding  $Z$ -bosons. To achieve this, the two reconstructed leptons are always required to be same-sign. Any event with a third-lepton (veto lepton) is vetoed to reduce the  $WZ$  background. In the case where the two leptons are electrons, additional cuts are applied to reject events where one of the electrons may have a mis-reconstructed charge. These cuts are  $E_T^{\text{miss}} > 55 \text{ GeV}$  and  $Z$  boson veto ( $|m_{ee} - m_Z| > 10 \text{ GeV}$ ) where  $m_{ee}$  is the di-electron invariant mass and  $m_Z$  is the  $Z$  boson mass .

The semi-leptonic analysis requires at least two additional jets with  $p_T > (30) 20 \text{ GeV}$  (leading jet requires  $30 \text{ GeV}$ ) to reconstruct the hadronically decaying  $W$  bosons and reject events with  $b$ -tagged jets to get rid of the non-prompt background. In addition,  $m_{jj} < 300 \text{ GeV}$ ,  $m_{\ell\ell} < 400 \text{ GeV}$ , and  $|\Delta\eta_{jj}| < 1.5$  cuts are applied to make the selection orthogonal to that of same-sign  $WW$  vector boson scattering (VBS) analysis [56] [57] and improve the signal to background ratio.

The semi-leptonic region is split into  $e^\pm e^\pm$ ,  $e^\pm \mu^\pm$ ,  $\mu^\pm e^\pm$  and  $\mu^\pm \mu^\pm$  categories (the first lepton is the leading  $p_T$  lepton). The  $m_{jj}$  spectrum is used as the main discriminant and is fitted to extract the signal. A summary of the selection criteria used can be found in Table 6.1.

$\ell^\pm \nu \ell^\pm \nu jj$ <b>Signal Region</b>		
$e^\pm e^\pm$ channel	$e^\pm \mu^\pm$ channel	$\mu^\pm \mu^\pm$ channel
Two same-sign leptons with $p_T > (20) 27 \text{ GeV}$		
3 <sup>rd</sup> lepton veto		
$\geq 2$ jets with $p_T > (20) 30 \text{ GeV}$ and $ \eta  < 2.5$		
$b$ -jet veto		
$ m_{ee} - m_Z  > 10 \text{ GeV}$	None	
$40 < m_{\ell\ell} < 400 \text{ GeV}$		
$ \Delta\eta_{jj}  < 1.5$		
$m_{jj} < 300 \text{ GeV}$		
$E_T^{miss} > 55 \text{ GeV}$	None	

Table 6.1: Selection criteria used for the  $\ell^\pm \nu \ell^\pm \nu jj$  signal region.

$\ell^\pm \nu \ell^\pm \nu \ell^\mp \nu$ <b>Signal Region</b>
3 leptons, $p_T > 27, 20, 20 \text{ GeV}$
4 <sup>th</sup> lepton veto
$b$ -jet veto
$\Sigma q_\ell = \pm 1$

Table 6.2: Selection criteria used for the  $\ell^\pm \nu \ell^\pm \nu \ell^\mp \nu$  signal region.

## 6.2 Fully-Leptonic Signal Region

The fully-leptonic  $\ell^\pm \nu \ell^\pm \nu \ell^\mp \nu$  signal region adopts the same strategy as the  $\ell^\pm \nu \ell^\pm \nu jj$  signal region to avoid the  $Z$  bosons. It achieves this by requiring zero Same Flavor Opposite Sign (SFOS) leptons with a total charge of  $\pm 1$ . Due to its charge composition, the 0 SFOS ( $e^\pm e^\pm \mu^\mp$ ,  $\mu^\pm \mu^\pm e^\mp$ ) region is absent of most SM backgrounds. The 4<sup>th</sup> lepton is vetoed (veto lepton) to remove four-lepton backgrounds from the  $ZZ \rightarrow 4\ell$  process. Events with  $b$ -tagged jets are vetoed to reject  $t\bar{t}$  and  $t\bar{t}W$  events. A summary of the selection criteria used can be found in Table 6.2.

## CHAPTER 7

# Data and Monte Carlo Samples

The search for  $W^\pm W^\pm W^\mp$  production is conducted using collision data taken at a center-of-mass energy of 13 TeV during the years 2015, 2016 and 2017. Datasets used are hand selected according to beam and detector conditions. The total integrated luminosity is  $79.8 \text{ fb}^{-1}$  using un-prescaled lepton triggers.

Two separate MC sets are used. The first set uses the 2015-2016 pile-up profile and the second set uses the 2017 pile-up profile. These MC samples are scaled to different luminosities that represent 2015-2016 and 2017 datasets. Although the two MC sets differ according to their pile-up profiles, identical MC settings and generators are used.

### 7.1 Signal Samples

SHERPA 2.2.2 [58] is used to generate on-shell  $W^\pm W^\pm W^\mp$  events at the Next-to-Leading Order (NLO) accuracy in perturbative QCD. SHERPA 2.2.2 utilizes OPENLOOPS [59] to calculate the NLO matrix elements and also simulates two additional partons at LO accuracy to calculate the NLO effects and the NNPDF3.0NNLO PDF [36] set is used. Off-shell  $W^\pm H \rightarrow W^\pm W^\pm W^\mp(*)$  events are generated at the NLO level using POWHEG-BOX [60] with CT10 [61] and hadronised using PYTHIA 8 [37].

The ATLAS detector simulation is applied on all generated MC samples using GEANT 4 [38] framework. Both on-shell and off-shell events are used together to represent the cross-section and kinematics of the  $W^\pm W^\pm W^\mp$  process.

These samples are analyzed with the Rivet tool [62] to estimate the signal acceptance and fiducial cross-sections. The Rivet tool processes the generator-level MC events and produces a fiducial cross-section for the given MC sample without detector-level effects. The tool works by re-implementing all signal region cuts. The tool can simulate jet and lepton selections to a certain extent that includes isolation and overlap removal.



Tables 7.1 and 7.2 show the Rivet cutflow. The theoretical fiducial cross-section is found to be 1.32 fb with an acceptance of 1.9% for the  $\ell^\pm \nu \ell^\pm \nu jj$  analysis and 0.216 fb with an acceptance of 1.3% for the  $\ell^\pm \nu \ell^\pm \nu \ell^\mp \nu$  analysis.

Selection Cuts	WWW X-Section (fb)	WH X-Section (fb)	Total X-Section (fb)
Pre Filter	29.3	40	69.3
All	14.6	20	34.6
N(Lep)= 2	11.6	7.7	19.3
$p_T(\ell 1) > 27 \text{ GeV}$	10.9	6.73	17.6
$p_T(\ell 2) > 20 \text{ GeV}$	8.42	4.4	12.8
$\Delta R_{\ell\ell} > 0.4$	8.28	4.35	12.6
Same Sign Leptons	2.5	2.18	4.67
$m_{\ell\ell} > 40 \text{ GeV}$	2.36	2.01	4.37
$m_{\ell\ell} < 400 \text{ GeV}$	2.23	1.99	4.22
$ m_Z - m_{ee}  > 10 \text{ GeV}$	2.16	1.9	4.06
Third Lepton Veto	1.94	1.9	3.84
N(jets) $\geq 2$	1.47	0.966	2.44
$p_T(\text{jet}1) > 30 \text{ GeV}$	1.45	0.891	2.34
$\Delta\eta_{jj} < 1.5$	1.12	0.679	1.8
$m_{jj} < 300 \text{ GeV}$	0.973	0.655	1.63
$\Delta R_{jj} > 0.4$	0.973	0.655	1.63
$\Delta R_{\ell j} > 0.4$	0.927	0.559	1.49
$b$ jet Veto	0.906	0.548	1.45
$E_T^{\text{miss}} > 55 \text{ GeV}$ ( $e^\pm e^\pm$ only)	0.83	0.485	1.32

Table 7.1: Detailed Rivet cutflow for the  $\ell^\pm \nu \ell^\pm \nu jj$  analysis.

## 7.2 Background Samples

The  $W^\pm W^\pm$ ,  $VV$ ,  $VVV$ ,  $t\bar{t}V$ , and  $tZ$  backgrounds are modeled using MC. In addition,  $V$  + jets, single-top,  $t\bar{t}$ , and  $V\gamma$  MC samples are produced for checking various background assumptions done using data-driven methods.

Both electroweak and strong production of di/tri-bosons ( $W^\pm W^\pm$ ,  $VV$ , and  $VVV$ ) as well as  $V$  + jets and  $V\gamma$  samples are generated with SHERPA 2.2.2 [58] with the NNPDF3.0NNLO PDF. The  $W^\pm W^\pm$  and  $VV$  processes are calculated at the fourth electroweak order ( $O(\alpha_W) = 4$ ). These samples do not have interferences with the  $W^\pm W^\pm W^\mp$  process as  $W^\pm W^\pm W^\mp$  production requires a sixth electroweak order. The sixth-order component of the  $W^\pm W^\pm$  hasn't been included due to low contribution to the total background and the overlap with the  $W^\pm W^\pm W^\mp$  signal. The  $V\gamma$  and  $V$  + jets samples with zero or one additional jets are generated to the NLO accuracy and two or three additional jets are modeled with the LO accuracy.

Selection Cuts	<i>WWW</i> X-Section (fb)	<i>WH</i> X-Section (fb)	Total X-Section (fb)
Pre-Filter	7.20	9.64	16.8
All	3.60	4.82	8.42
N(Lep)= 3	1.43	1.72	3.15
$p_T(\ell) > 20\text{GeV}$	0.836	0.610	1.45
$\eta(\ell) < 2.5$	0.569	0.465	1.03
0 SFOS	0.143	0.116	0.259
$DR(\ell\ell) > 0.4$	0.135	0.0922	0.227
min. $\Delta R(\ell j) > 0.4$	0.129	0.0901	0.219
<i>b</i> jet veto	0.127	0.089	0.216

Table 7.2: Detailed Rivet cutflow for the  $\ell^\pm\nu\ell^\pm\nu\ell^\mp\nu$  analysis.

The  $t\bar{t}V$  and  $tZ$  samples are generated using MADGRAPH [63] at the NLO accuracy with NNPDF30NLO PDF set and hadronised using PYTHIA 8. The  $t\bar{t}$  and single-top samples are generated using POWHEG with NNPDF30NLO PDF set and hadronized with PYTHIA 8.

## CHAPTER 8

# Background Estimations

In  $pp$  collisions, it is rare to produce same-flavor same-sign leptons in the final state. For this reason, the majority of reconstructed same-flavor same-sign lepton events are due to mis-reconstructed or mis-identified leptons. The sources that can produce same-flavor and same-sign final state can be grouped into five categories:

- SM processes that produce same-flavor same-sign leptons like same-sign WW VBS production;
- Processes that produce three or more prompt leptons where one or more leptons are not detected. These can mimic the  $\ell^\pm \nu \ell^\pm \nu jj$  signature;
- Processes that produce three or more prompt leptons, including taus where tau decays hadronically resulting in  $\ell^\pm \nu \ell^\pm \nu jj$  and  $\ell^\pm \nu \ell^\pm \nu \ell^\mp \nu$  signatures;
- Processes that produce two opposite-sign leptons where a lepton's charge is mis-identified;
- Processes that have leptons originating from jets or photons.

These five categories can be used to explain the major physics background processes in the  $W^\pm W^\pm W^\mp$  signal regions. These background processes are:

- **WZ + jets and ZZ + jets Backgrounds:** The  $WZ$  + jets background is the dominant background. It contributes to the  $\ell^\pm \nu \ell^\pm \nu jj$  signal region when one of the leptons from the  $WZ$  leptonic decay is not properly reconstructed, and to 0 SFOS regions when one lepton's charge is misidentified. Similarly, the  $ZZ$  + jets background contributes to  $\ell^\pm \nu \ell^\pm \nu \ell^\mp \nu$  and  $\ell^\pm \nu \ell^\pm \nu jj$  final states by losing one or two leptons. They are modeled using MC. From this point on these backgrounds will be referred to as  $WZ$  and  $ZZ$  backgrounds.

- **Charge Mis-identified (misID) Background:** Events with a charge-flipped electron can be reconstructed as same-flavor same-sign events. In the  $\ell^\pm \nu \ell^\pm \nu jj$  channel, the  $t\bar{t}$ ,  $W^\pm W^\mp + \text{jets}$ , and  $Z/\gamma + \text{jets}$  backgrounds predominantly contribute to the charge misID background. Similarly, the  $WZ$  process with a charged-flipped electron contributes to the  $\ell^\pm \nu \ell^\pm \nu \ell^\mp \nu$  region.

The charge-flip background is estimated using a data-driven method. Details of this method can be found in Section 8.1. The charge-flip background is significantly reduced due to the cut on the charge-flip killer BDT. From this point on this background will be referred to as “Charge Flip” and “Charge misID”. The rate of charge mis-identification for muons is negligible.

- **Non-Prompt Background:** The  $t\bar{t}$ ,  $V + \text{jets}$ , single-top or QCD processes contain energetic jets. These jets can be misidentified as leptons, or they can produce non-prompt leptons. Most of these events come from  $t\bar{t}$  processes with some contribution from  $W + \text{jets}$  events. Non-prompt background events are reduced by tagging leptons using PLV. The non-prompt background is modeled using a data-driven method, and the details can be found in Section 8.2. From this point on this background will be referred to as “fakes” or “fake leptons”.
- **Photon Conversion Background:** A photon can be misidentified as an electron. Although this process is suppressed using lepton isolation and reconstruction, the  $V\gamma$  background is still a dominant background for the  $WWW$  analysis. This background is modeled using a data-driven method. Further details on the data-driven  $V\gamma$  background estimation can be found in Section 8.3.
- **Same-sign WW VBS Background:** The same-sign  $WW$  VBS process is one of the few SM process that produces the same  $\ell^\pm \nu \ell^\pm \nu jj$  detector signature. It majorly contributes to the  $\ell^\pm \nu \ell^\pm \nu jj$  analysis and specially designed cuts are applied to reduce its contribution.
- **Other Backgrounds:** In addition to backgrounds listed above, other processes like tri-boson,  $t\bar{t}V$  have minor contributions to the overall background. These backgrounds are modeled using MC and are categorized under the “others” category.

## 8.1 Charge misID Background

When an electron radiates an energetic photon that converts into an  $e^+e^-$  pair, the original electron can get mixed up with the new electrons and can be reconstructed with a wrong

<b>Z Mass Region</b>	
# Leptons	Exactly two signal electrons
Lepton $p_T$	$p_T > 20$ (27) GeV
Z Mass Window	$75 < m_{ee} < 105$ GeV
Z Mass Sideband	$60 < m_{ee} < 75$ GeV $105 < m_{ee} < 120$ GeV

Table 8.1: Selection criteria for the region where charge misID rate is investigated .

charge. This charge flip allows many SM processes to leak into the  $W^\pm W^\pm W^\mp$  signal region. A data-driven method is used to estimate these backgrounds. The data-driven method predicts the charge-flip background by defining a new region that has reversed charge requirements and scaling this region by a charge-flip rate. In the  $\ell^\pm \nu \ell^\pm \nu jj$  channel the new region is defined by reversing the Same Sign (SS) cut to the Opposite Sign (OS) cut, and in the  $\ell^\pm \nu \ell^\pm \nu \ell^\mp \nu$  channel, it is defined by changing the 0 SFOS cut into the 1 SFOS cut.

### 8.1.1 Charge misID Rate Estimation

The electron charge misID rate is calculated using the  $Z \rightarrow e^+ e^-$  decay. The di-electron invariant mass is required to be close to the Z boson pole mass. The comprehensive event selection criteria for this region can be found in Table 8.1. The selected di-electron candidates are categorized on whether their charges are SS or OS. In both categories, it is assumed that di-electrons mainly come from the  $Z \rightarrow e^+ e^-$  process with minor background contributions. These backgrounds are estimated using the two mass side bands. The sidebands as defined in Table 8.1 are fitted with a linear function and extrapolated into the Z mass window. This method gives an estimate of the non-Z background events.

After events are categorized and the non-Z contribution is subtracted, the charge misID rate is measured using a likelihood fit given by the equation:

$$L(\vec{\epsilon}) = \prod_i^{PT,\eta} \prod_j^{PT,\eta} P(N_{ss,ij}^{obs} | \epsilon_i, \epsilon_j, N_{ss+os,ij}^{exp}), \quad (8.1)$$

where  $P$  is a Poisson probability distribution defined as:

$$P(N_{ss} | \epsilon_i, \epsilon_j, N_{os+ss}^{exp}) = \frac{(N_{ss}^{exp})^{N_{ss}} e^{-N_{ss}^{exp}}}{N_{ss}!}, \quad (8.2)$$

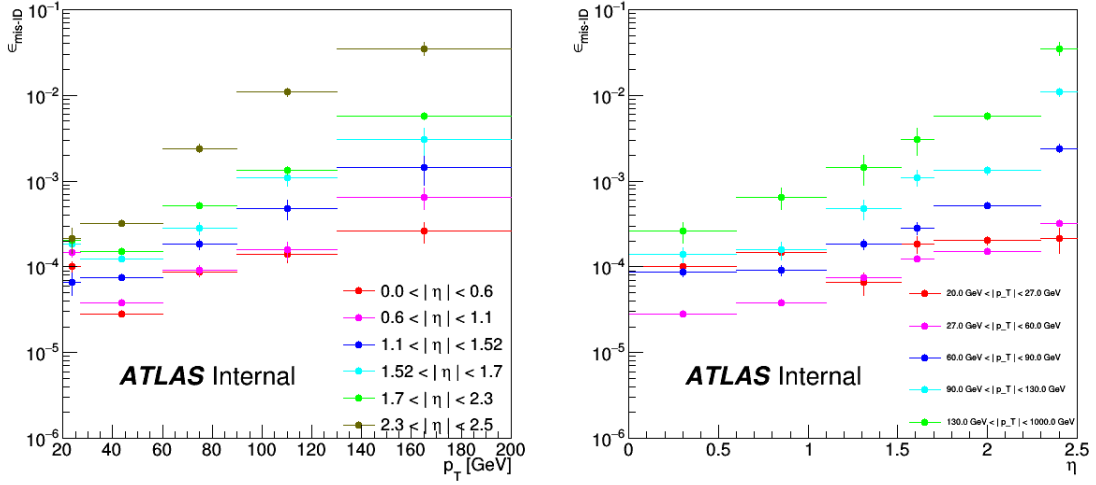


Figure 8.1: Electron charge-flip rate measured as a function of the electron  $p_T$  (left) and  $\eta$  (right). It is observed that the charge-flip rate increases with both  $p_T$  and  $\eta$ .

where  $\epsilon_i$  ( $\epsilon_j$ ) is the charge-flip rates for the electron for the  $i$ -th ( $j$ -th) bin that correspond to a  $p_T$  and  $\eta$  range,  $N_{ss/os}$  is the number of observed SS/OS events, and  $N_{SS}^{exp}$  is the expected number of SS events defined as:

$$N_{SS}^{exp} = N_{os+ss}[(1 - \epsilon_i)\epsilon_j + (1 - \epsilon_j)\epsilon_i]. \quad (8.3)$$

For the fit, the given likelihood is converted into a negative log-likelihood and is minimized to extract the charge-flip rates. The resulting  $\eta$  and  $p_T$  dependent charge-flip rates be found in Figures 8.1. It has been observed that the charge-flip rate increases with both  $p_T$  and  $\eta$  where the rates differ by a factor of  $\approx 10000$  between the lowest and the highest rate.

### 8.1.2 Charge misID Validation

The charge-flip rates are validated in the Z Mass Window Validation Region. This validation region is modeled after the semi-leptonic ( $\ell^\pm \nu \ell^\pm \nu jj$ ) signal region, where the Z mass veto cut is reversed. The comprehensive event selection for this region can be found in Table 8.2. Figure 8.2 shows the  $m_{ee}$  and lepton kinematic distributions, and Table 8.3 show the yields for the Z Mass Window Validation Region. Good modeling is observed for the charge misID rate in this region.

<b>Z Mass Window Validation Region</b>
$e^{\pm}e^{\pm}$ channel
Two same-sign leptons with $p_T > (20) 27 \text{ GeV}$
$3^{\text{rd}}$ lepton veto
$\geq 2$ jets with $p_T > (20) 30 \text{ GeV}$ and $ \eta  < 2.5$
$b$ -jet veto
$ m_{ee} - m_Z  < 10 \text{ GeV}$
$ \Delta\eta_{jj}  < 1.5$
$m_{jj} < 300 \text{ GeV}$
$E_T^{\text{miss}} > 55 \text{ GeV}$

Table 8.2: Selection criteria for the Z Mass Window Validation Region.

	$e^{\pm}e^{\pm}$
WWW	$1.2 \pm 0.1$
WZ	$6.75 \pm 0.44$
Non Prompt	$5.43 \pm 0.31$
Charge Flip	$9.07 \pm 0.21$
$V\gamma$	$5.37 \pm 1.21$
Others	$1.31 \pm 0.08$
Total Sum	$29.14 \pm 1.34$
Data	26

Table 8.3: Yields of the Z Mass Window Validation Region. The statistical uncertainty error bars are shown. Overall good modeling has been observed.

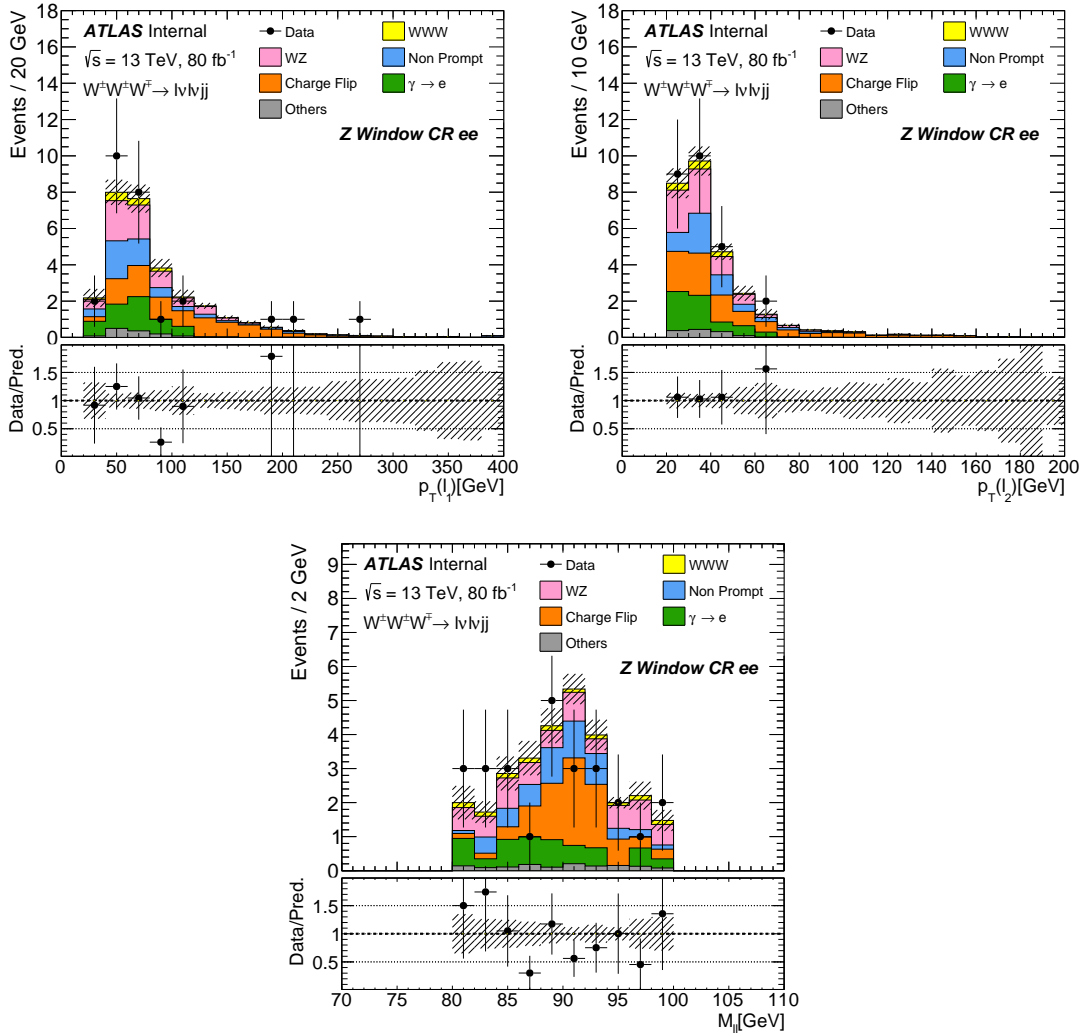


Figure 8.2: The leading (top left) and the sub-leading (top right) electron  $p_T$  distributions, and the di-lepton invariant mass (bottom) distribution with two same-sign electrons. These events are selected using the criteria defined for the Z Mass Window Validation Region to validate the charge-flip background estimation, and overall good modeling has been observed. Only statistical uncertainties are shown.



## 8.2 Non-Prompt Background

The non-prompt background originates from jets mis-identified as leptons or leptons that originate from hadron decays. MC simulation cannot accurately model the non-prompt leptons. For this reason, a data-driven method is used to model the non-prompt background. This method utilizes anti-ID leptons defined in Section 7. Anti-ID leptons have a large non-prompt lepton composition. By changing one of the ID leptons in the  $\ell^\pm\nu\ell^\pm\nu jj$  and  $\ell^\pm\nu\ell^\pm\nu\ell^\mp\nu$  signal regions to be an anti-ID lepton, a region with a sizeable non-prompt composition is obtained. It is assumed that this region would have similar non-prompt kinematic shapes as the  $\ell^\pm\nu\ell^\pm\nu jj$  and  $\ell^\pm\nu\ell^\pm\nu\ell^\mp\nu$  signal regions, and this shape can be scaled using the non-prompt rates to estimate the non-prompt background. This non-prompt scale factor represents the ratio of ID leptons to anti-ID leptons in a given region and is also determined in a data-driven way.

### 8.2.1 Non-Prompt Factor Background Composition

Before estimating the non-prompt scale factors, an understanding of the non-prompt background composition in the signal regions is needed. For this reason, a study has been conducted using the signal regions with anti-ID leptons definitions, where all backgrounds are modeled with MC. The regions used are identical to the  $\ell^\pm\nu\ell^\pm\nu jj$  and  $\ell^\pm\nu\ell^\pm\nu\ell^\mp\nu$  signal regions, but one of the leptons is required to be anti-ID. This creates signal-like regions dominated by non-prompt background. Figures 8.3 and 8.4 show the  $\ell^\pm\nu\ell^\pm\nu\ell^\mp\nu$  non-prompt region (with two ID and one anti-ID leptons) kinematic distributions and it is observed that the  $t\bar{t}$  MC can model the non-prompt background well. Figures 8.5-8.7 show the  $\ell^\pm\nu\ell^\pm\nu jj$  non-prompt region (with one ID and one anti-ID leptons) kinematic distributions and it is observed that the  $t\bar{t}$  MC together with the  $W$  + jets background can model the non-prompt background well. This study concludes that the non-prompt background in the  $\ell^\pm\nu\ell^\pm\nu\ell^\mp\nu$  SFOS signal region is primarily composed of  $t\bar{t}$  events. Similarly the  $\ell^\pm\nu\ell^\pm\nu jj$  signal non-prompt background is primarily composed of  $t\bar{t}$  events with a small contribution from  $V$  + jets events. The  $V$  + jets contributions amount to 25%, 3.1%, 17%, 5.7% in the  $ee$ ,  $e\mu$ ,  $\mu e$ ,  $\mu\mu$  channels respectively in the  $\ell^\pm\nu\ell^\pm\nu jj$  signal region.

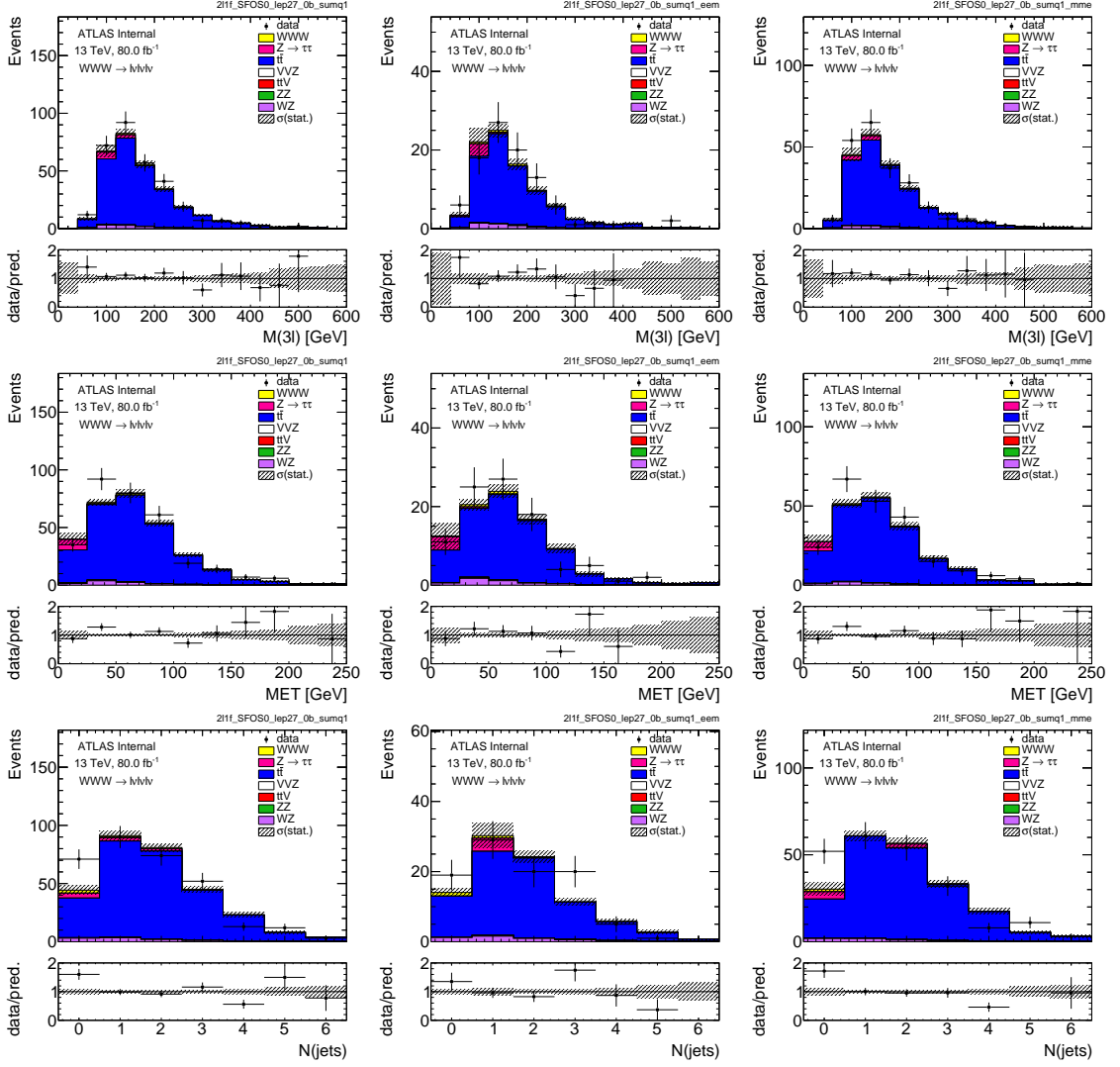


Figure 8.3: Data and MC prediction for  $m_{3\ell}$ ,  $E_T^{\text{miss}}$ , and  $N_j$  in the  $\ell^\pm \nu \ell^\pm \nu \ell^\mp \nu$  ID+ID+anti-ID non-prompt region, for the inclusive (left),  $ee\mu$  (center), and  $\mu\mu e$  (right) regions. These plots indicate that the  $t\bar{t}$  process is the dominant contributor of non-prompt leptons in this region.

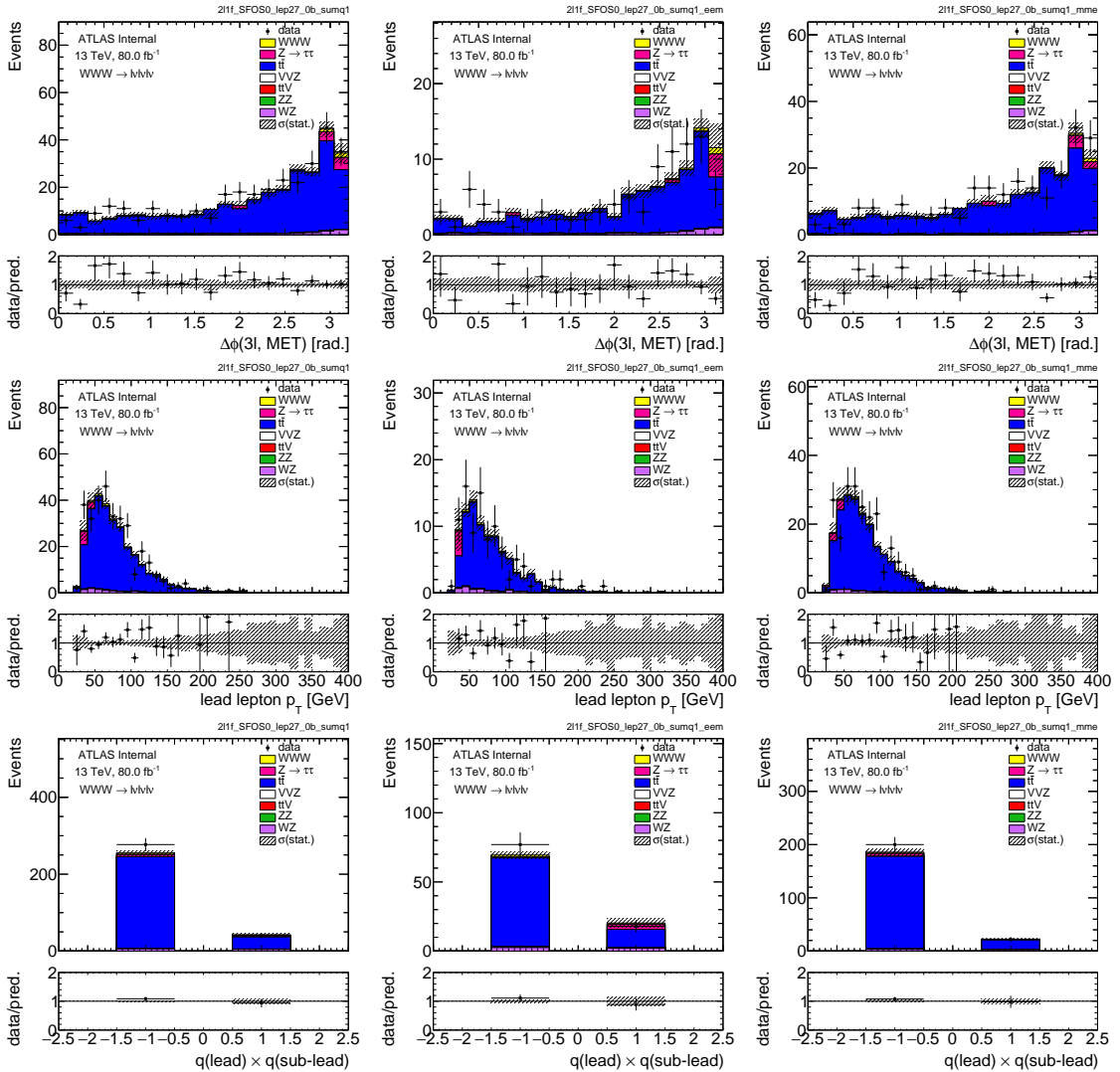


Figure 8.4: Data and MC prediction for  $\Delta\phi$  between  $3\ell$  and  $E_T^{\text{miss}}$ , leading lepton  $p_T$  and  $q_0 \times q_1$  in the  $\ell^\pm \nu \ell^\pm \nu \ell^\mp \nu$  ID+ID+anti-ID control region, for the inclusive (left),  $ee\mu$  (center), and  $\mu\mu e$  (right) regions. These plots indicate that the  $t\bar{t}$  process is the dominant contributor of non-prompt leptons in this region.

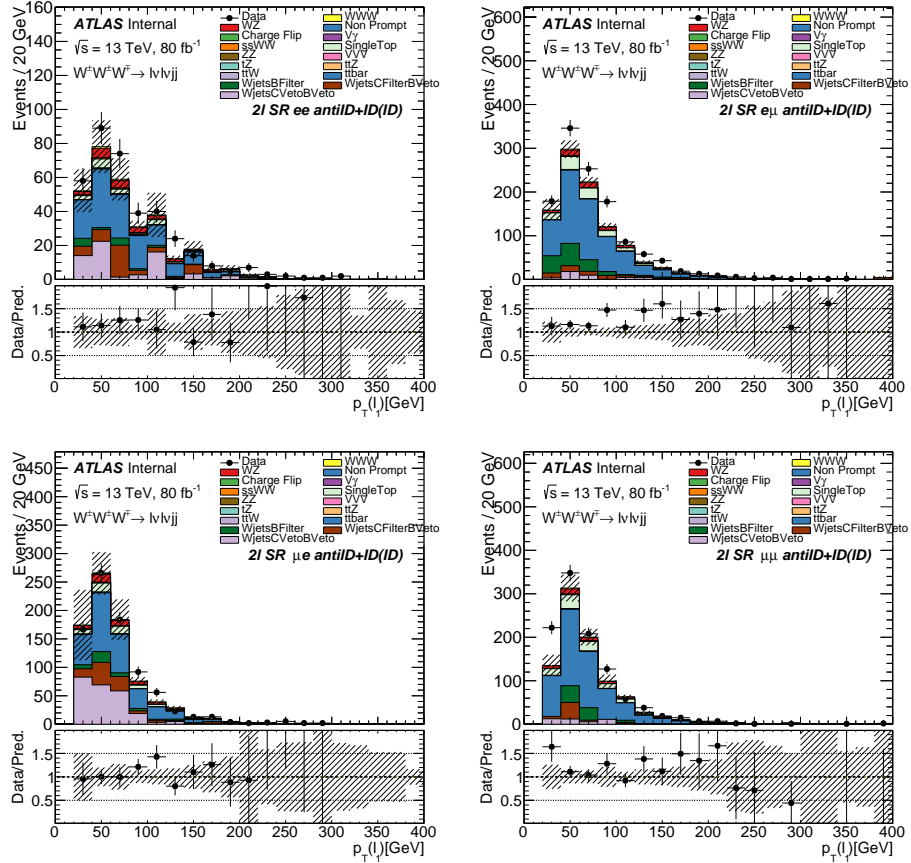


Figure 8.5: Data and MC prediction for leading lepton  $p_T$  in the  $\ell^\pm\nu\ell^\pm\nu jj$  ID+anti-ID non-prompt region. The four plots in each row show the  $ee$ ,  $e\mu$ ,  $\mu e$ , and  $\mu\mu$  channels separately. Simulation suggests that the dominant contributors of non-prompt leptons in this region come from processes with heavy flavor decay.

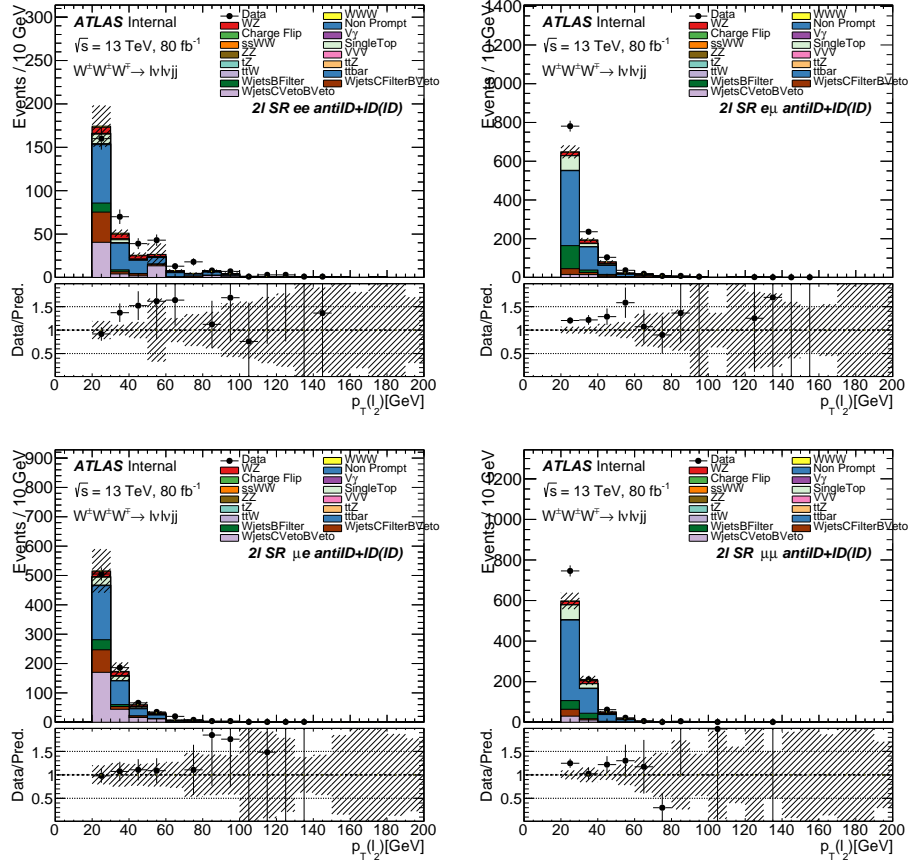


Figure 8.6: Data and MC prediction for sub-leading lepton  $p_T$  in the  $\ell^\pm v \ell^\pm v j j$  ID+anti-ID non-prompt region. The four plots in each row show the  $ee$ ,  $e\mu$ ,  $\mu e$ , and  $\mu\mu$  channels separately. Simulation suggests that the dominant contributors of non-prompt leptons in this region come from processes with heavy flavor decay.

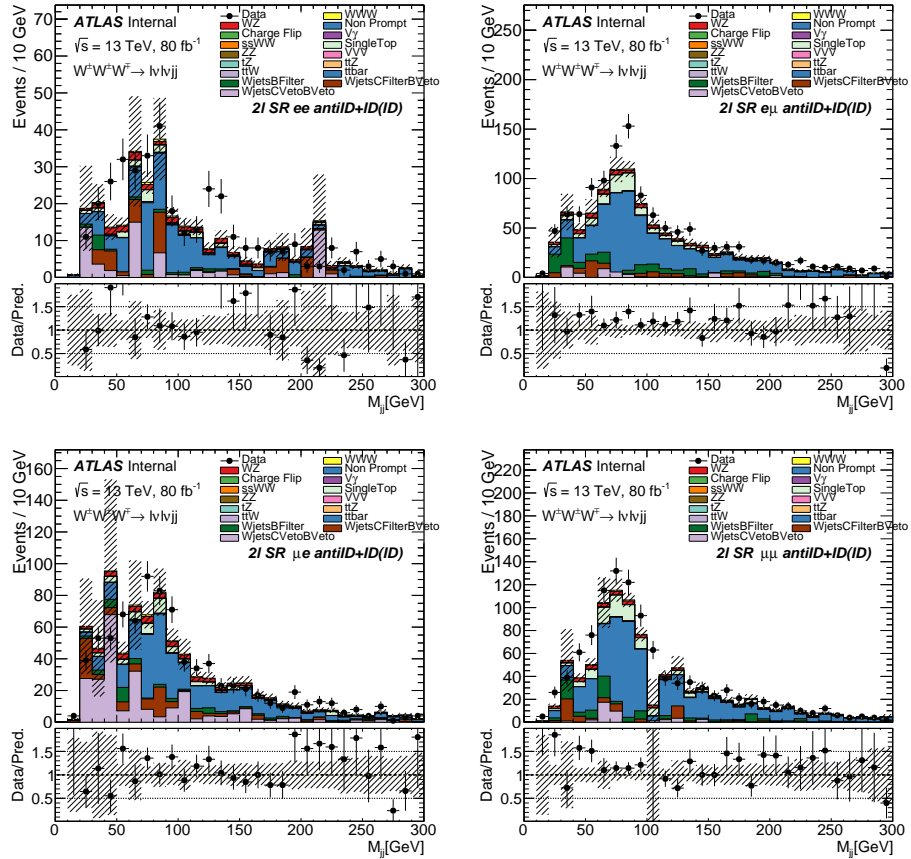


Figure 8.7: Data and MC prediction for  $m_{jj}$  in the  $\ell^\pm \nu \ell^\pm \nu jj$  ID+anti-ID non-prompt region. The four plots in each row show the  $ee$ ,  $e\mu$ ,  $\mu e$ , and  $\mu\mu$  channels separately. Simulation suggests that the dominant contributors of non-prompt leptons in this region come from processes with heavy flavor decay.

## 8.2.2 Non-Prompt Factor Determination

The non-prompt factor is estimated in two regions dominated by  $t\bar{t}$  events: the  $\ell^\pm\nu\ell^\pm\nu jj$  and the  $\ell^\pm\nu\ell^\pm\nu\ell^\mp\nu$   $b$ -tagged regions. These regions are identical to  $\ell^\pm\nu\ell^\pm\nu jj$  and  $\ell^\pm\nu\ell^\pm\nu\ell^\mp\nu$  signal regions with a reversed  $b$ -jet veto requirement where both regions require exactly one  $b$ -tagged jet. The detailed cutflow for the  $\ell^\pm\nu\ell^\pm\nu jj$  and  $\ell^\pm\nu\ell^\pm\nu\ell^\mp\nu$   $b$ -tagged regions can be found in Tables 8.4 and 8.5.

$\ell^\pm\nu\ell^\pm\nu jj$ $b$ -Tagged Region		
$e^\pm e^\pm$ channel	$e^\pm\mu^\pm$ channel	$\mu^\pm\mu^\pm$ channel
Two same-sign leptons with $p_T > (20) 27$ GeV		
3 <sup>rd</sup> lepton veto		
$\geq 2$ jets with $p_T > (20) 30$ GeV and $ \eta  < 2.5$		
Exactly 1 $b$ -jet		
$40 < m_{\ell\ell} < 80$ GeV	$40 < m_{\ell\ell} < 400$ GeV	
$100 < m_{\ell\ell} < 400$ GeV		
$ \Delta\eta_{jj}  < 1.5$		
$m_{jj} < 300$ GeV		
$E_T^{miss} > 55$ GeV	None	

Table 8.4: Selection criteria used for the  $\ell^\pm\nu\ell^\pm\nu jj$   $b$ -tagged region.

$\ell^\pm\nu\ell^\pm\nu\ell^\mp\nu$ $b$ -Tagged Region
3 leptons, $p_T > 27, 20, 20$ GeV
0 SFOS
4 <sup>th</sup> lepton veto
Exactly 1 $b$ -jet
$\Sigma q_\ell = \pm 1$

Table 8.5: Selection criteria used for the  $\ell^\pm\nu\ell^\pm\nu\ell^\mp\nu$   $b$ -tagged region.

These regions are further divided into two sub-categories whether they contain only ID leptons or have ID leptons with a single anti-ID lepton. The non-prompt scale factor is derived using these two sub-categories, and the basic scale factor can be simplified as the ratio of non-prompt events in the ID+ID region to the anti-ID+ID region. The challenge comes from the fact that in the region with all ID leptons, lepton that originates from non-prompt processes cannot be differentiated. For this region, a general likelihood function that fits all channels and signal regions is used to estimate the non-prompt factor for electrons and

muons simultaneously. This likelihood equation is given as:

$$L(\vec{\epsilon}) = \prod_i^{ee, e\mu, \mu\mu} P(N_{ID+ID,i}^{obs} | \epsilon_e, \epsilon_\mu, N_{ID+ID,i}^{exp}) \times \prod_j^{ee\mu, \mu\mu e} P(N_{ID+ID+ID,j}^{obs} | \epsilon_e, \epsilon_\mu, N_{ID+ID+ID,j}^{exp}), \quad (8.4)$$

where

$$P(N_{ID+ID} | \epsilon_e, \epsilon_\mu, N_{ID+ID}^{exp}) = \frac{(N_{ID+ID}^{exp})^{N_{ID+ID}} e^{-N_{ID+ID}^{exp}}}{N_{ID+ID}!}, \quad (8.5)$$

$$N_{ID,ID(ID)}^{exp} = N_{anti-ID,ID(ID)}^{obs} \times \epsilon_{f(anti-ID)} + N_{ID,anti-ID(ID)}^{obs} \times \epsilon_{f(anti-ID)}. \quad (8.6)$$

Here  $\epsilon_{e/\mu}$  is the non-prompt factor for the given anti-ID lepton flavor, and  $N_{category}^{obs}$  is the observed number of events for the given category/channel after background events are subtracted. The likelihood is converted into a negative log-likelihood and is minimized to extract the non-prompt rates. Independent non-prompt rates per-category are also derived using the same method. The resulting non-prompt rates can be found in Table 8.6.

There is no dedicated validation regions to validate the non-prompt factors. The non-prompt rates are validated by the fact that the non-prompt rates derived in two separate regions agree with each other and the fact that the side-band control region (defined in Section 8.5) has good background modeling. Figures 8.8-8.10 (Figure 8.10) shows the kinematic distributions of the  $\ell^\pm \nu \ell^\pm \nu jj$   $b$ -tagged region (the  $\ell^\pm \nu \ell^\pm \nu \ell^\mp \nu$   $b$ -tagged region). The fact that the shape of the kinematic distributions agree gives confidence in the non-prompt modeling.

Region	Type	Non-Prompt Factor
$\ell^\pm \nu \ell^\pm \nu jj$	$\epsilon_e$	$0.018 \pm 0.011$
$\ell^\pm \nu \ell^\pm \nu jj$	$\epsilon_\mu$	$0.035 \pm 0.006$
$\ell^\pm \nu \ell^\pm \nu \ell^\mp \nu$	$\epsilon_e$	$0.010 \pm 0.026$
$\ell^\pm \nu \ell^\pm \nu \ell^\mp \nu$	$\epsilon_\mu$	$0.031 \pm 0.012$
<b>Combined</b>	$\epsilon_e$	$0.017 \pm 0.010$
<b>Combined</b>	$\epsilon_\mu$	$0.035 \pm 0.005$

Table 8.6: The non-prompt rates used for scaling the non-prompt background. The rates derived from individual regions ( $\ell^\pm \nu \ell^\pm \nu jj$  and  $\ell^\pm \nu \ell^\pm \nu \ell^\mp \nu$ ) are used for validation, and the combined rates are used for estimating the non-prompt background. The uncertainties are shown for statistical only.



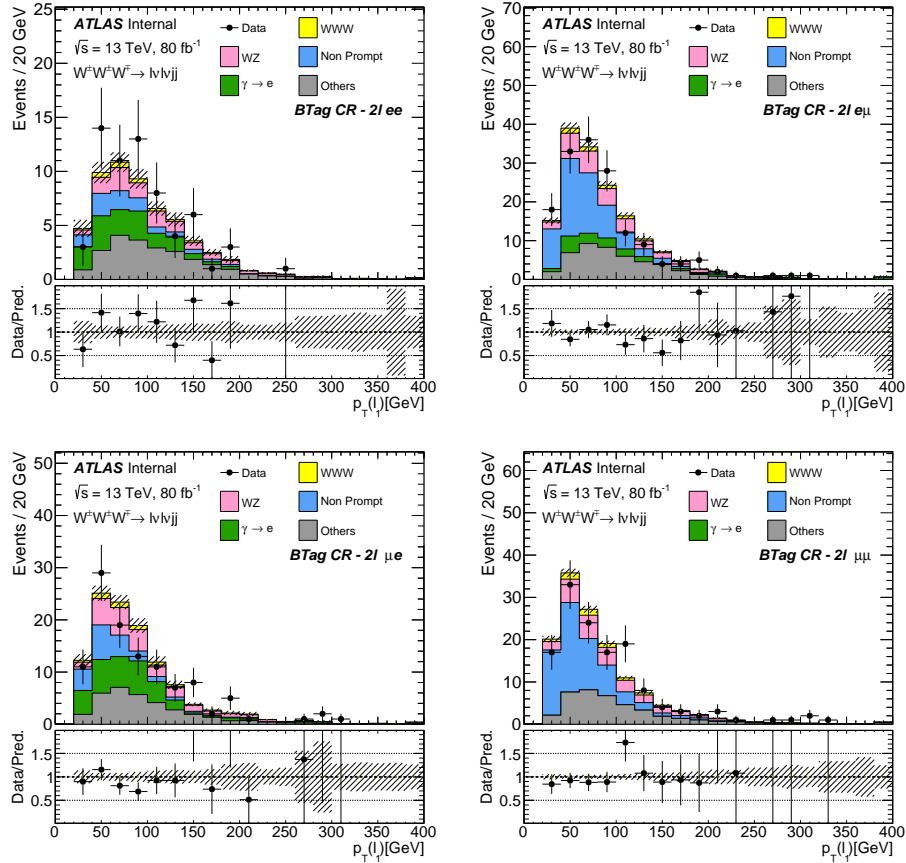


Figure 8.8: The leading lepton  $p_T$  distribution in the  $ee$  (top left),  $e\mu$  (top right),  $\mu e$  (bottom left) and  $\mu\mu$  (bottom right) channels in the  $\ell^\pm\nu\ell^\pm\nu jj$   $b$ -Tagged Region for ID+ID region. The normalization of the prediction will agree by construction, but the shapes will not necessarily agree.

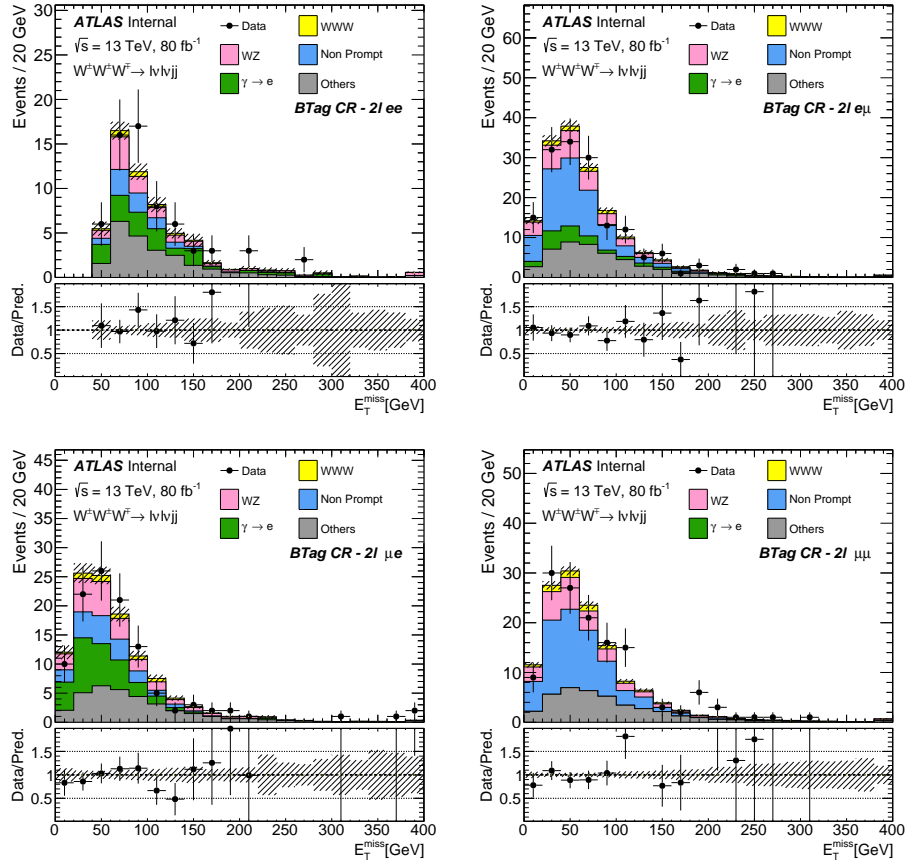


Figure 8.9: The  $E_T^{\text{miss}}$  distribution in the  $ee$  (top left),  $e\mu$  (top right),  $\mu e$  (bottom left) and  $\mu\mu$  (bottom right) channels in the  $\ell^{\pm}\nu\ell^{\pm}\nu jj$   $b$ -Tagged Region for ID+ID region. The normalization of the prediction will agree by construction, but the shapes will not necessarily agree.

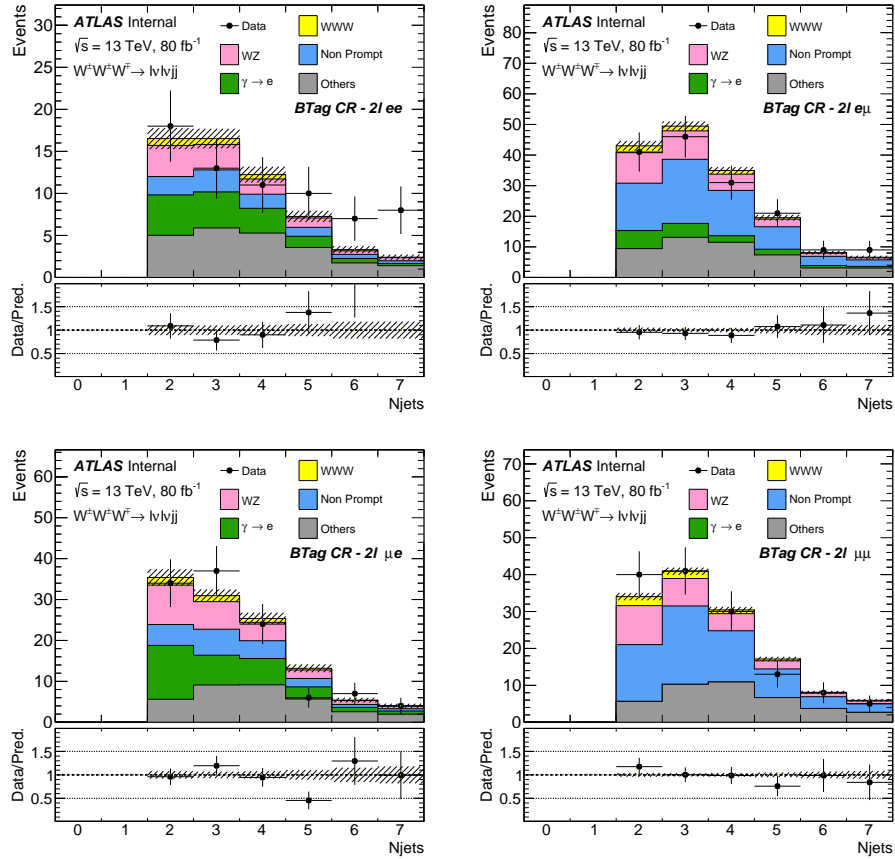


Figure 8.10: Number of jets distribution in the  $ee$  (top left),  $e\mu$  (top right),  $\mu e$  (bottom left) and  $\mu\mu$  (bottom right) channels in the  $\ell^\pm\nu\ell^\pm\nu jj$   $b$ -Tagged Region for ID+ID region. The normalization of the prediction will agree by construction, but the shapes will not necessarily agree.

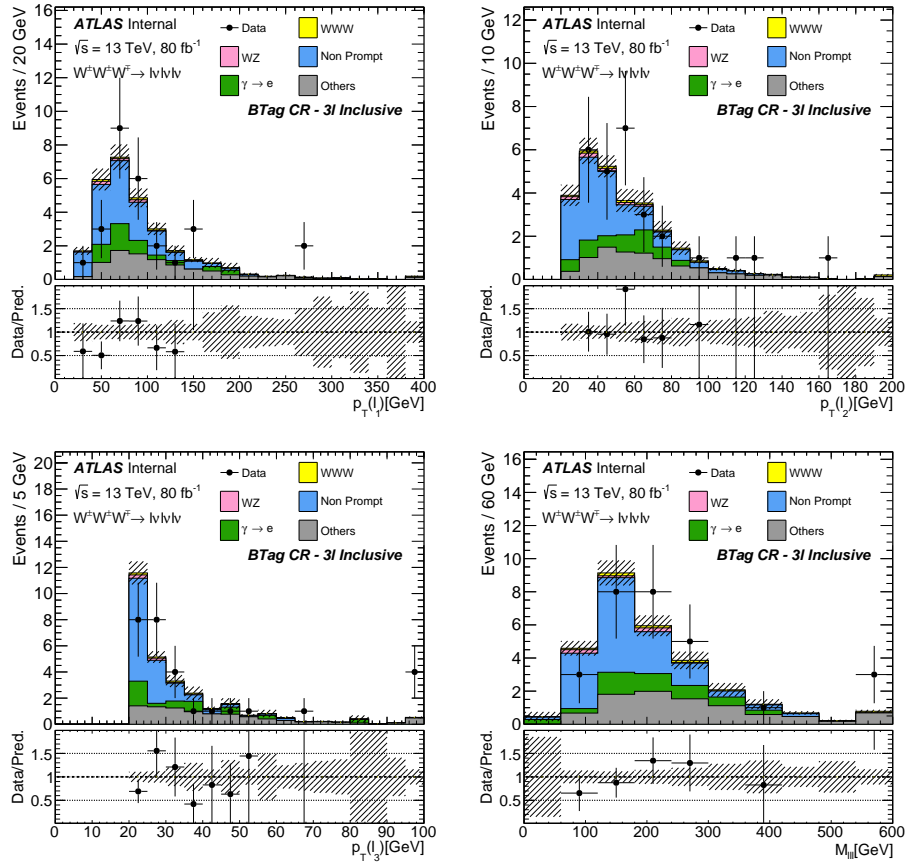


Figure 8.11: Inclusive leading (top left), sub-leading (top right) and sub-sub leading (bottom left) lepton  $p_T$  distributions and  $m_{\ell\ell}$  (bottom right) distributions in the  $\ell^\pm\nu\ell^\pm\nu\ell^\mp\nu$   $b$ -Tagged Region for ID+ID region. The normalization of the prediction will agree by construction, but the shapes will not necessarily agree.

## 8.3 Photon Conversion Background

Photons can be misidentified as electrons and photons can also create an electron-positron pair. This mis-identification can create the same final states as the  $W^\pm W^\pm W^\mp$  processes when a photon is produced together with a  $W/Z$  boson. The photon conversion background is determined using a data-driven method. ID and anti-BL electrons are used for determining the photon conversion rate. Anti-BL electrons are identical to ID electrons except not having a hit in the  $b$ -layer (the innermost pixel layer) of the ID, meaning that they have a higher chance of originating from a photon.

By changing one of the ID electrons in the  $\ell^\pm \nu \ell^\pm \nu jj$  and  $\ell^\pm \nu \ell^\pm \nu \ell^\mp \nu$  signal regions to be anti-BL, a region with a sizable photon conversion background composition is obtained. It is assumed that this region would have similar photon conversion kinematic shapes as the  $\ell^\pm \nu \ell^\pm \nu jj$  and  $\ell^\pm \nu \ell^\pm \nu \ell^\mp \nu$  signal regions. The photon conversion ( $V\gamma$ ) background in the signal regions is estimated by scaling this shape using the photon conversion rate.

### 8.3.1 Photon Conversion Rate Determination

The photon conversion rate is calculated in the  $Z\gamma$  control region. This region requires three leptons with the  $\mu^\pm \mu^\mp e^\pm$  configuration, where it is assumed that the muon pair comes from a  $Z$  boson decay, and the electron is an artifact of the photon radiation. The  $Z$  mass peak is reconstructed using a  $Z$  window cut on the trilepton invariant mass ( $m_{\ell\ell\ell}$ ). Detailed definitions of this  $Z\gamma$  control region can be found in Table 8.7. The photon conversion rate is given by the ratio of events with ID electron to events with an anti-BL electron in the  $Z\gamma$  control region after background subtracted (modeled by MC). The photon conversion rate is found to be  $0.27 \pm 0.024$ . Figures 8.12-8.15 show various distributions in the  $Z\gamma$  region where these rates are extracted.

$Z\gamma$ CR
3 leptons with $p_T > 27, 20, 20$ GeV
Lepton Configuration $\mu^\pm \mu^\mp e^\pm$
3 leptons with $80 < m_{\ell\ell\ell} < 100$ GeV

Table 8.7: Selection criteria used for the  $Z\gamma$  control region.

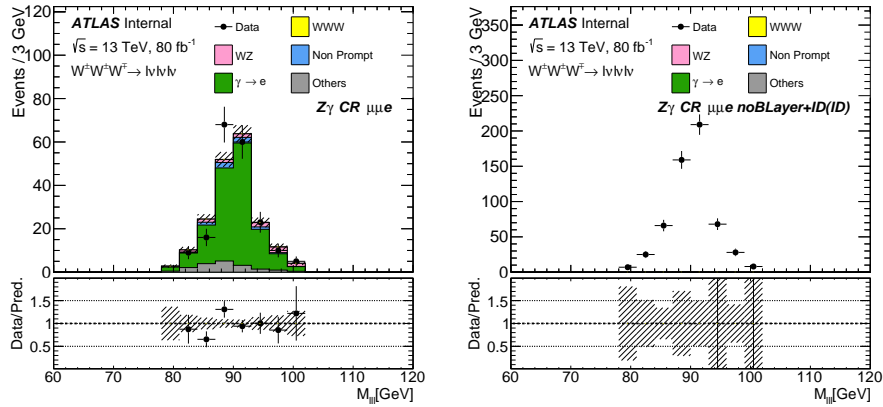


Figure 8.12: The  $m(\mu\mu)$  distribution for the signal electron  $Z\gamma$  control region (left) and photon-like electron  $Z\gamma$  control region (right). The data-driven photon prediction is included in the plot on the left. Simulation predicts very few events to satisfy the photon-like electron selection, suggesting the region is pure in photons reconstructed as electrons.

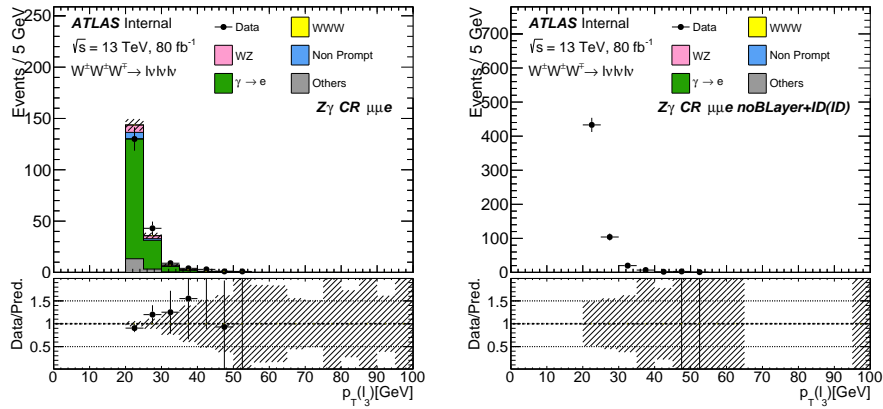


Figure 8.13: The third lepton  $p_T$  distribution for the signal electron  $Z\gamma$  control region ( $\mu\mu e$ ) (left) and photon-like electron  $Z\gamma$  control region (right). The data-driven photon prediction is included in the plot on the left. Simulation predicts very few events to satisfy the photon-like electron selection, suggesting the region is pure in photons reconstructed as electrons.

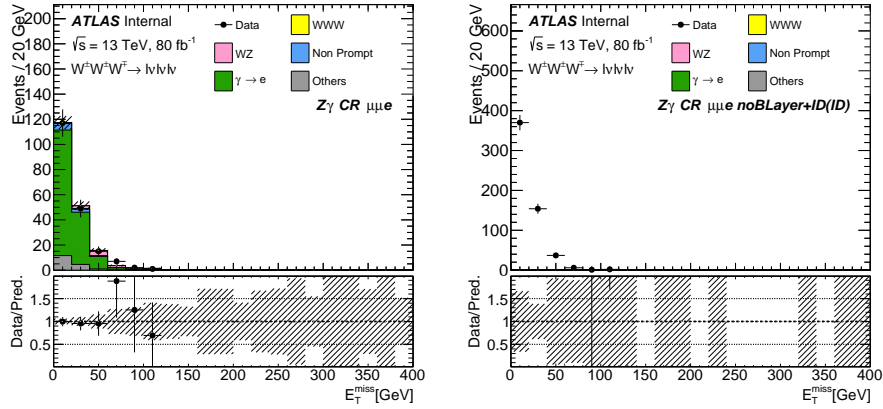


Figure 8.14: The missing transverse energy distribution for the signal electron  $Z\gamma$  control region ( $\mu\mu e$ ) (left) and “photon-like electron  $Z\gamma$  control region” (right). The data-driven photon prediction is included in the plot on the left. Simulation predicts very few events to satisfy the photon-like electron selection, suggesting the region is pure in photons reconstructed as electrons.

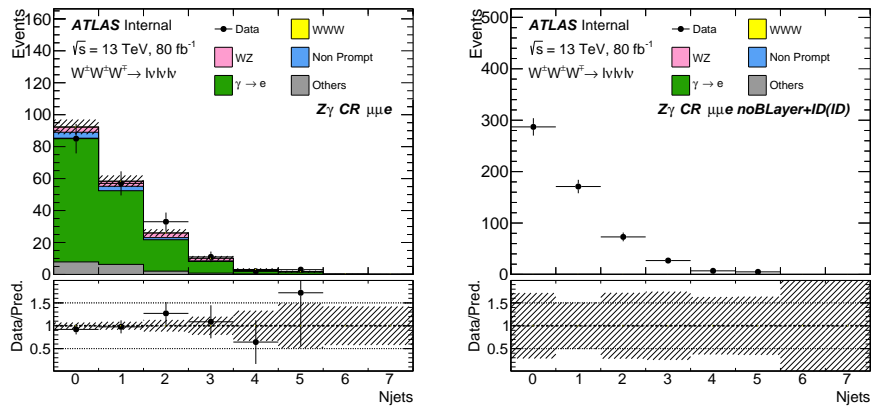


Figure 8.15: The  $N(\text{jets})$  distribution for the signal electron  $Z\gamma$  control region ( $\mu\mu e$ ) (left) and photon-like electron  $Z\gamma$  control region (right). The data-driven photon prediction is included in the plot on the left. Simulation predicts very few events to satisfy the photon-like electron selection, suggesting the region is pure in photons reconstructed as electrons.

## 8.4 WZ Background Validation

The largest background in the  $W^\pm W^\pm W^\mp$  analysis is the  $WZ/ZZ$  + jets background. When one or two leptons from the fully-leptonic decay of  $WZ/ZZ$  events are not properly reconstructed, they become indistinguishable from the  $W^\pm W^\pm W^\mp$  signatures. The  $WZ/ZZ$  backgrounds are modeled using MC with a free-floating parameter for the overall normalization, and the modeling of this background is validated using the  $WZ$  control region.

The  $WZ$  control region requires exactly three leptons with 1SFOS ( $e^\pm e^\mp \mu^\pm$ ,  $\mu^\pm \mu^\mp e^\pm$ ) and 2SFOS ( $e^\pm e^\pm e^\mp$ ,  $\mu^\pm \mu^\pm \mu^\mp$ ) configurations. The  $m_{\ell\ell\ell} > 110\text{ GeV}$  and  $E_T^{\text{miss}} > 55\text{ GeV}$  cuts are applied to make this region orthogonal to the  $Z\gamma$  control region and to reduce the  $Z\gamma$  contribution. Detailed descriptions of the  $WZ$  control region can be found in Table 8.8.

<b>WZ CR</b>
3 Leptons with $p_T > 27, 20, 20\text{ GeV}$
Lepton Configurations: $e^\pm e^\mp \mu^\pm$ , $\mu^\pm \mu^\mp e^\pm$ , $e^\pm e^\pm e^\mp$ , $\mu^\pm \mu^\pm \mu^\mp$
$m_{\ell\ell\ell} > 110\text{ GeV}$
$E_T^{\text{miss}} > 55\text{ GeV}$
No $b$ -tagged jets

Table 8.8: Selection criteria used for the  $WZ$  control region.

Table 8.9 shows the number of observed events compared to the estimated backgrounds from various sources in this control region. Figures 8.16-8.20 show various kinematic distributions such as leading lepton  $p_T$ , jet multiplicity,  $E_T^{\text{miss}}$ , and  $m_{\ell\ell\ell}$  in the  $eee$ ,  $ee\mu$ ,  $\mu\mu e$ , and  $\mu\mu\mu$  channels. Overall good modeling for the  $WZ$  background has been observed.



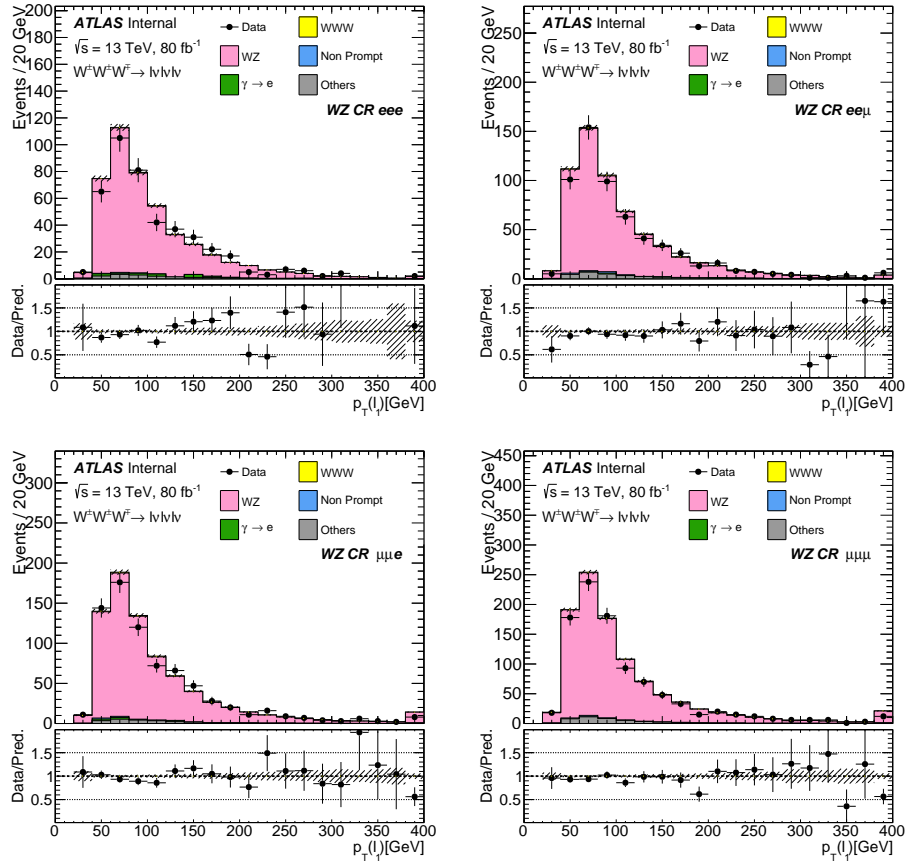


Figure 8.16: The leading lepton  $p_T$  distribution in the  $eee$  (top left),  $ee\mu$  (top right),  $\mu\mu e$  (bottom left), and  $\mu\mu\mu$  (bottom right) channels. These events are selected using the criteria defined for the  $WZ$  control region.

	$eee$	$ee\mu$	$e\mu\mu$	$\mu\mu\mu$
WWW	$2.36 \pm 0.28$	$4.65 \pm 0.4$	$6.31 \pm 0.45$	$4.29 \pm 0.39$
WZ	$420.21 \pm 4.58$	$574.22 \pm 5.29$	$726.92 \pm 6.05$	$955.53 \pm 6.92$
Non Prompt	$2.03 \pm 0.38$	$6.32 \pm 0.67$	$4.81 \pm 0.68$	$7.83 \pm 0.92$
Charge Flip	$0.0 \pm 0.0$	$0.0 \pm 0.0$	$0.0 \pm 0.0$	$0.0 \pm 0.0$
$V\gamma$	$8.88 \pm 1.9$	$2.93 \pm 1.37$	$5.83 \pm 1.49$	$0.0 \pm 0.0$
ssWW	$0.0 \pm 0.0$	$0.0 \pm 0.0$	$0.0 \pm 0.0$	$0.0 \pm 0.0$
ZZ	$7.95 \pm 0.24$	$17.88 \pm 0.37$	$13.9 \pm 0.31$	$31.91 \pm 0.52$
VVV	$1.74 \pm 0.04$	$2.38 \pm 0.05$	$3.04 \pm 0.06$	$3.53 \pm 0.06$
tZ	$2.26 \pm 0.16$	$2.53 \pm 0.17$	$3.81 \pm 0.2$	$4.37 \pm 0.23$
ttZ	$3.09 \pm 0.14$	$3.73 \pm 0.16$	$4.04 \pm 0.17$	$5.12 \pm 0.18$
ttW	$0.54 \pm 0.07$	$0.91 \pm 0.1$	$1.4 \pm 0.12$	$0.95 \pm 0.09$
Total Sum	$449.07 \pm 4.99$	$615.56 \pm 5.54$	$770.07 \pm 6.3$	$1013.53 \pm 7.01$
Data	439	597	762	972

Table 8.9: Event yields with statistical uncertainties for data and estimated SM backgrounds in the WZ control region.

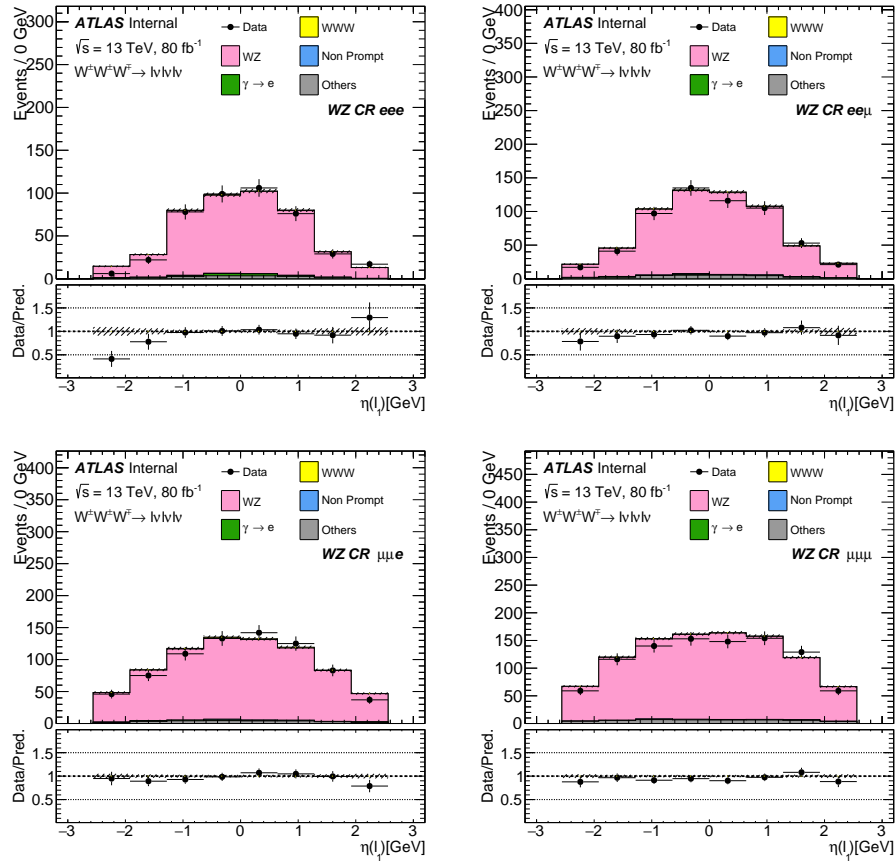


Figure 8.17: The leading lepton  $\eta$  distribution in the  $eee$  (top left),  $ee\mu$  (top right),  $\mu\mu e$  (bottom left) and  $\mu\mu\mu$  (bottom right) channels. These events are selected using the criteria defined for the  $WZ$  control region.

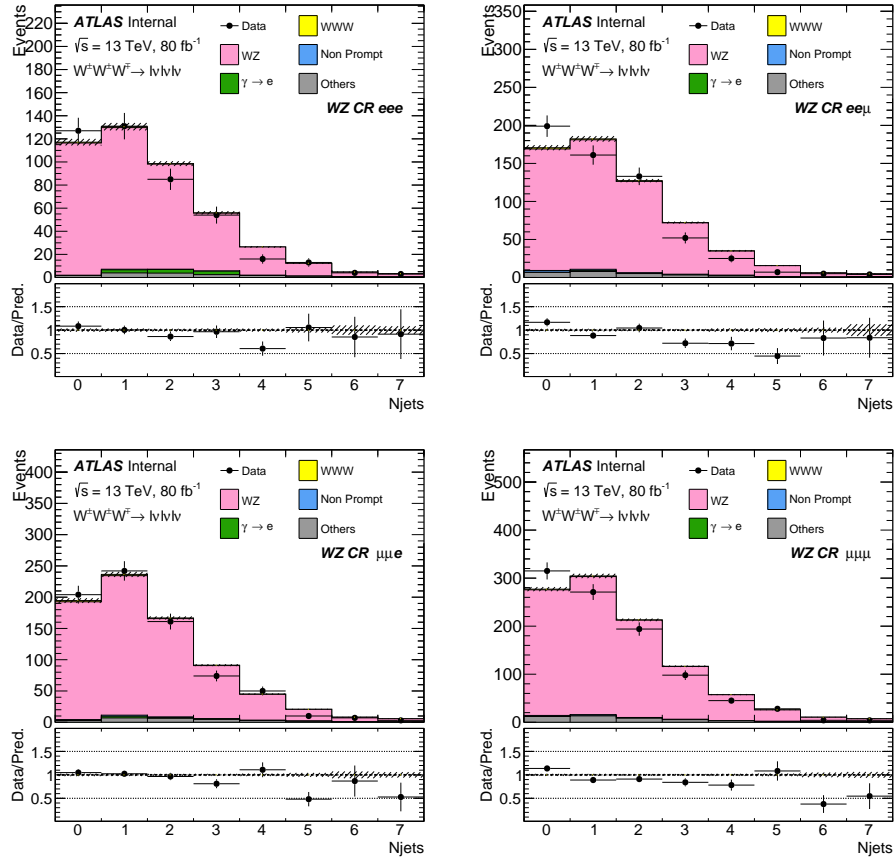


Figure 8.18: Jet multiplicity distribution in the  $eee$  (left),  $eee$  (top left),  $ee\mu$  (top right),  $\mu\mu e$  (bottom left), and  $\mu\mu\mu$  (bottom right) channels. These events are selected using the criteria defined for the  $WZ$  control region. The  $N(\text{jets})$  reweighting, discussed at the beginning of the section, is applied here and throughout the analysis.

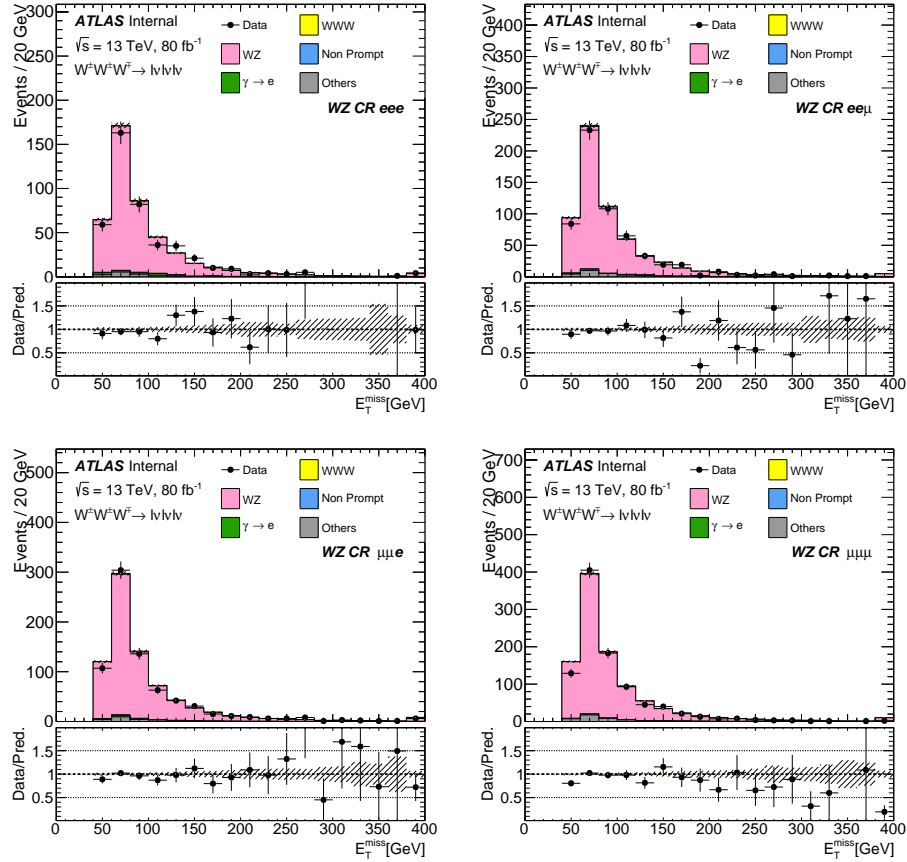


Figure 8.19: The  $E_T^{\text{miss}}$  distribution in the  $eee$  (top left),  $ee\mu$  (top right),  $\mu\mu e$  (bottom left), and  $\mu\mu\mu$  (bottom right) channels. These events are selected using the criteria defined for the  $WZ$  control region.

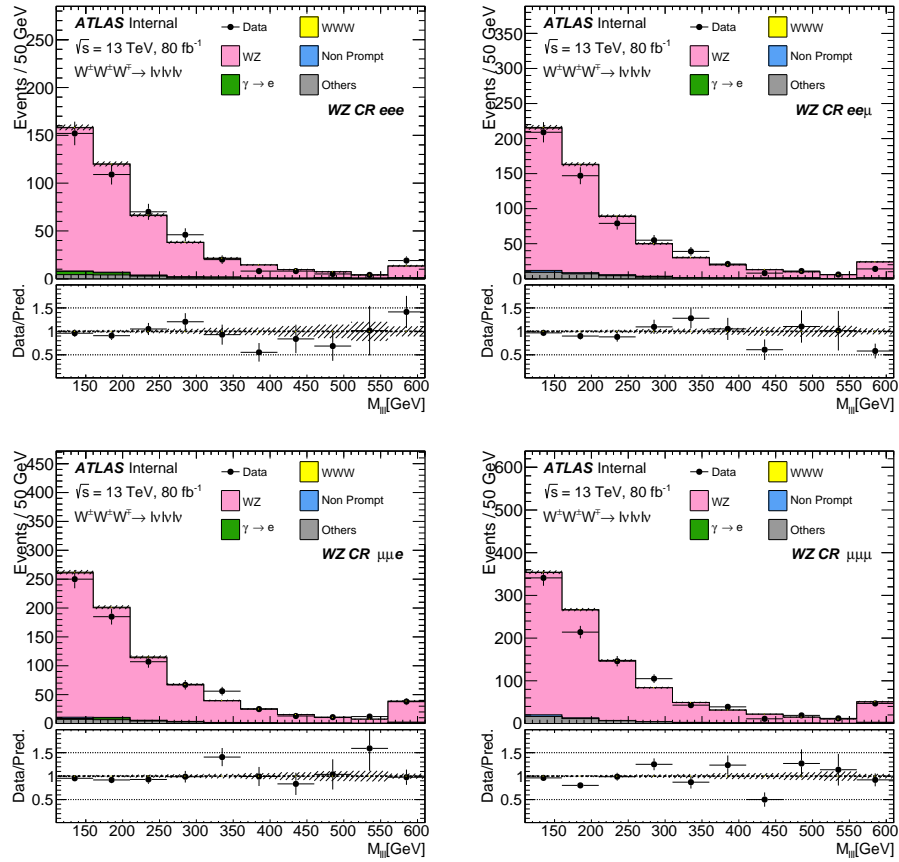


Figure 8.20: The  $M(\ell\ell\ell)$  distribution in the  $eee$  (top left),  $ee\mu$  (top right),  $\mu\mu e$  (bottom left), and  $\mu\mu\mu$  (bottom right) channels. These events are selected using the criteria defined for the  $WZ$  control region.

<b>W Mass Side-Band Region</b>		
$e^\pm e^\pm$ channel	$e^\pm \mu^\pm$ channel	$\mu^\pm \mu^\pm$ channel
Two same-sign leptons with $p_T > (20) 27 \text{ GeV}$		
3 <sup>rd</sup> lepton veto		
$\geq 2$ jets with $p_T > (20) 30 \text{ GeV}$ and $ \eta  < 2.5$		
$b$ -jet veto		
$ m_{ee} - m_Z  > 10 \text{ GeV}$	-	
$40 < m_{\ell\ell} < 400 \text{ GeV}$		
$ \Delta\eta_{jj}  < 1.5$		
$m_{jj} < 50 \text{ GeV}$		
$120 < m_{jj} < 300 \text{ GeV}$		
$E_T^{\text{miss}} > 55 \text{ GeV}$	None	

Table 8.10: Selection criteria used for the  $W$  mass side-band region.

## 8.5 Overall Background Validation Using the $W$ Mass Side-Band Validation Region

The  $m_{jj}$  distribution inside the  $\ell^\pm \nu \ell^\pm \nu jj$  signal region has a varying amount of signal sensitivity. Vetoing the  $W$  mass window of the  $m_{jj}$  distribution creates a region with relatively low signal contribution called the  $W$  Mass Side-Band Validation Region (side-band region for short). Detailed descriptions of the region can be found in Table 8.10. The side-band region is used for validating all background modelings in the  $\ell^\pm \nu \ell^\pm \nu jj$  signal region.

The event yield in the side-band region can be found in Table 8.11. Figures 8.21-8.27 show the di-jet invariant mass, di-jet pseudorapidity separation, leading lepton  $p_T$ , sub-leading lepton  $p_T$ , leading jet  $p_T$ , sub-leading jet  $p_T$ , and  $E_T^{\text{miss}}$  distributions in the  $ee$ ,  $e\mu$ ,  $\mu e$ , and  $\mu\mu$  channels for the  $W$  Mass Side-Band Validation Region. Overall good background modeling has been observed.

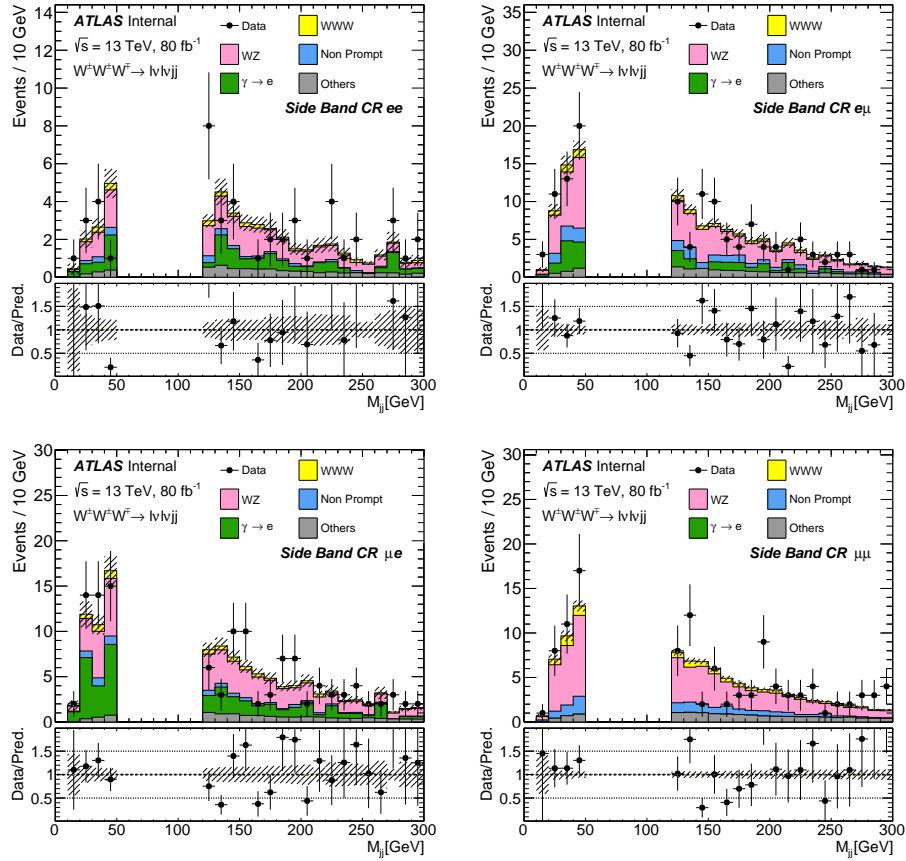


Figure 8.21: The  $m_{jj}$  distribution with statistical uncertainties in the  $ee$  (top left),  $e\mu$  (top right),  $\mu e$  (bottom left), and  $\mu\mu$  (bottom right) channels. These events are selected using the  $W$  Mass Side-Band Validation Region criteria, which are identical to the  $\ell^{\pm}\nu\ell^{\pm}jj$  signal region except that  $m_{jj}$  must be outside the  $W$  mass window. This region is used to validate various background estimations.



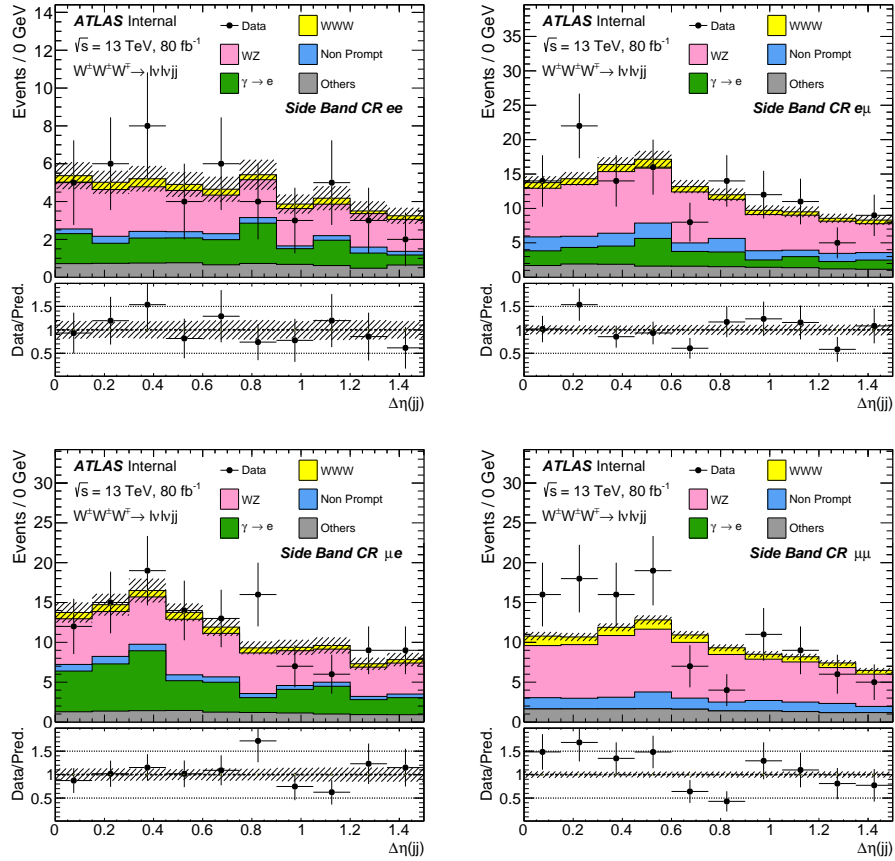


Figure 8.22: The  $\Delta\eta_{jj}$  distribution with statistical uncertainties in the  $ee$  (top left),  $e\mu$  (top right),  $\mu e$  (bottom left), and  $\mu\mu$  (bottom right) channels. These events are selected using the  $W$  Mass Side-Band Validation Region criteria, which are identical to the  $\ell^\pm\nu\ell^\pm\nu jj$  signal region except that  $m_{jj}$  must be outside the  $W$  mass window. This region is used to validate various background estimations.

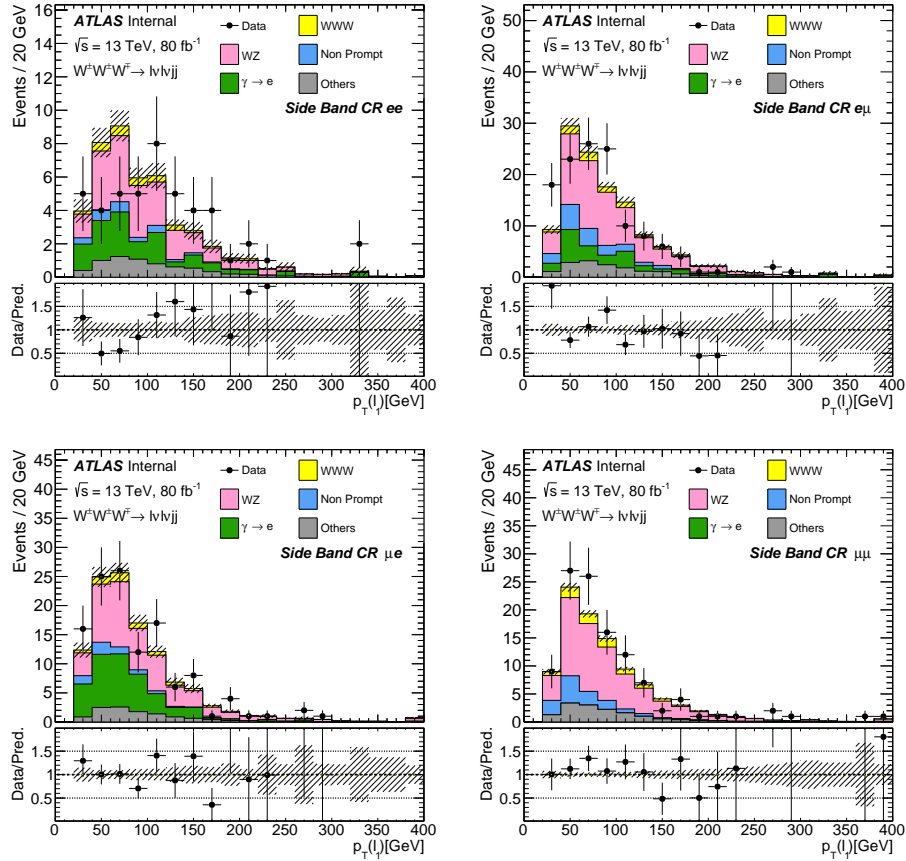


Figure 8.23: The leading lepton  $p_T$  distribution with statistical uncertainties in the  $ee$  (top left),  $e\mu$  (top right),  $\mu e$  (bottom left), and  $\mu\mu$  (bottom right) channels. These events are selected using the  $W$  Mass Side-Band Validation Region criteria, which are identical to the  $\ell^\pm \nu \ell^\pm \nu jj$  signal region except that  $m_{jj}$  must be outside the  $W$  mass window. This region is used to validate various background estimations.

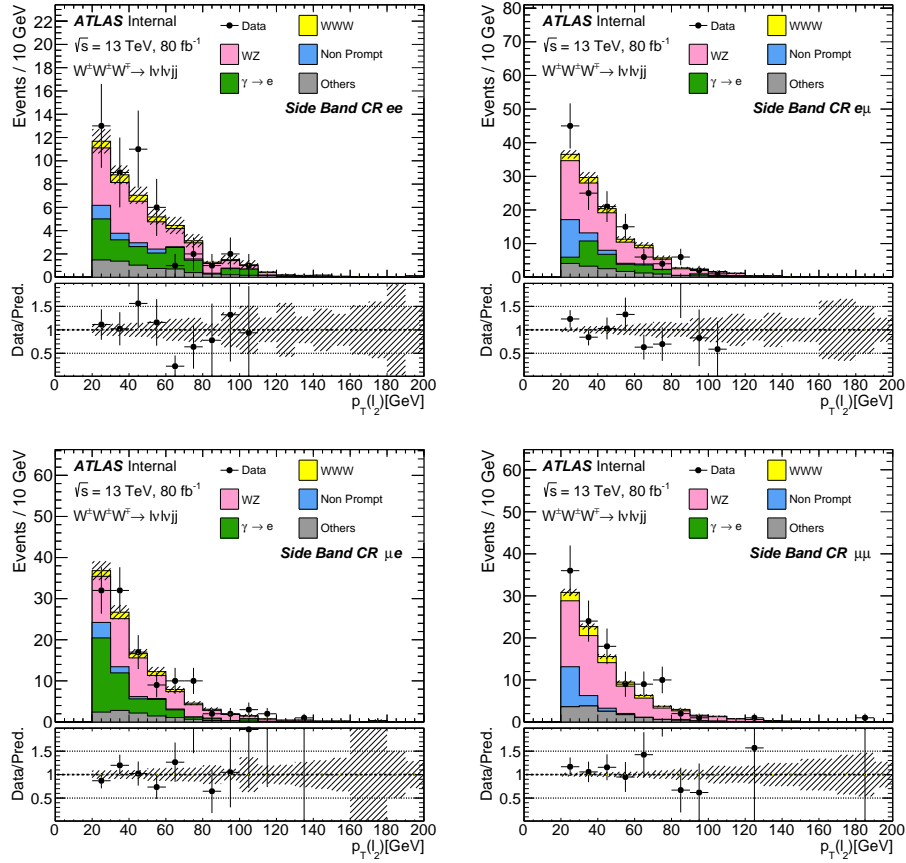


Figure 8.24: The subleading lepton  $p_T$  distribution with statistical uncertainties in the  $ee$  (top left),  $e\mu$  (top right),  $\mu e$  (bottom left), and  $\mu\mu$  (bottom right) channels. These events are selected using the  $W$  Mass Side-Band Validation Region criteria, which are identical to the  $\ell^\pm\nu\ell^\pm\nu jj$  signal region except that  $m_{jj}$  must be outside the  $W$  mass window. This region is used to validate various background estimations.

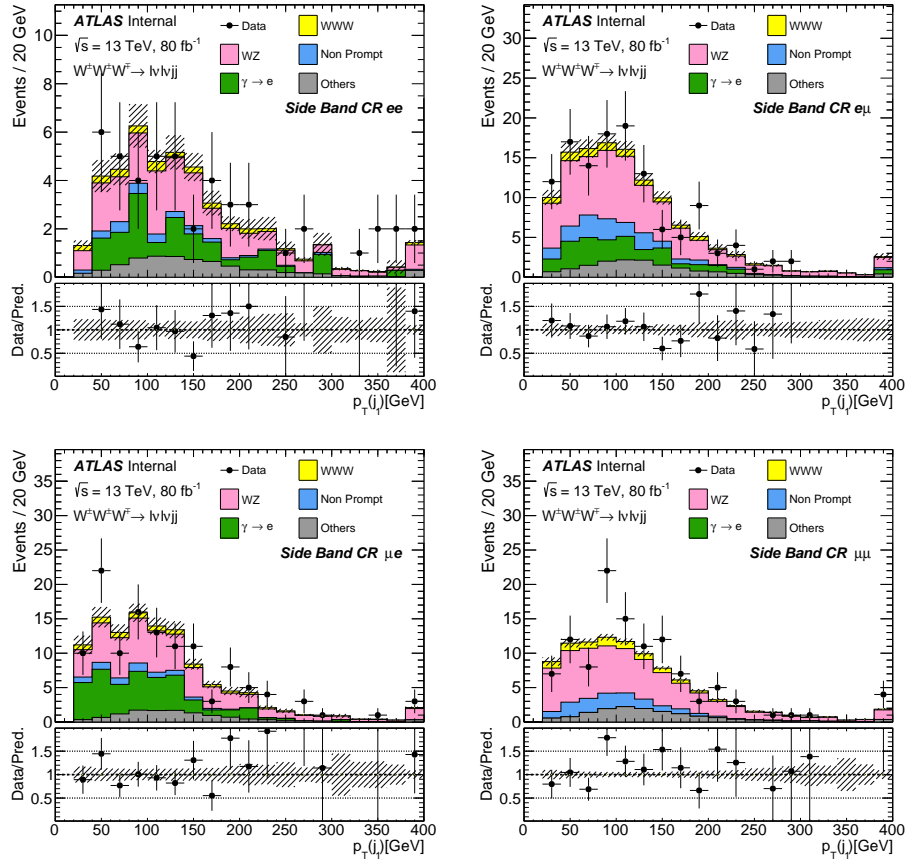


Figure 8.25: The leading jet  $p_T$  distribution with statistical uncertainties in the  $ee$  (top left),  $e\mu$  (top right),  $\mu e$  (bottom left), and  $\mu\mu$  (bottom right) channels. These events are selected using the  $W$  Mass Side-Band Validation Region criteria, which are identical to the  $\ell^\pm\nu\ell^\pm\nu jj$  signal region except that  $m_{jj}$  must be outside the  $W$  mass window. This region is used to validate various background estimations.

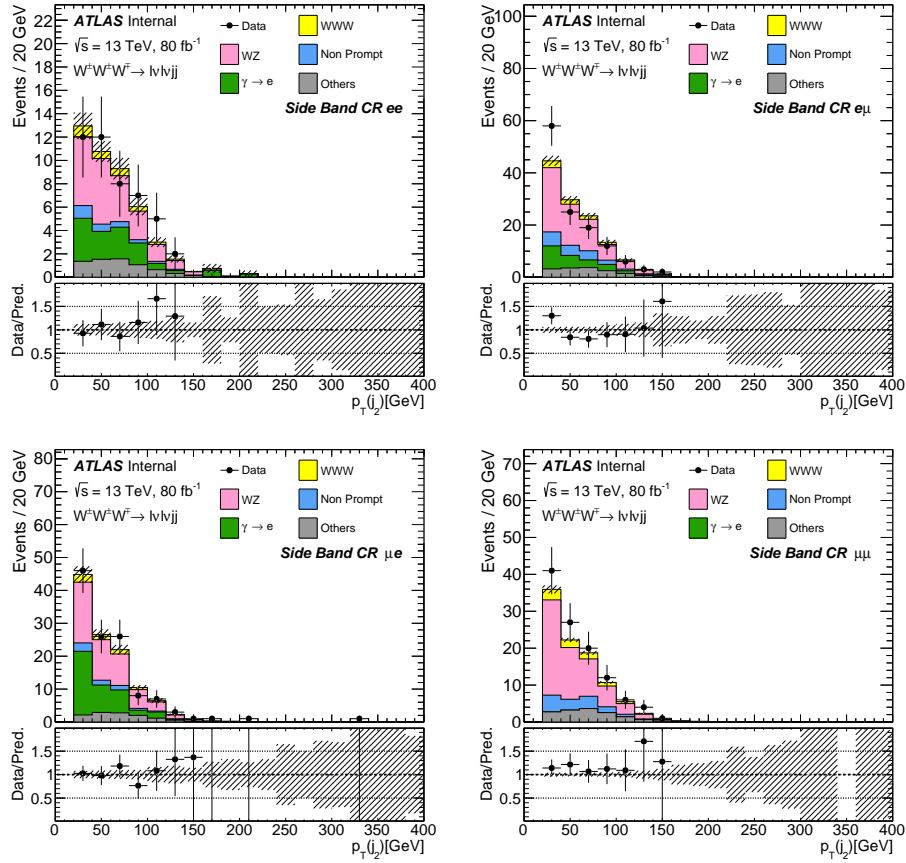


Figure 8.26: The subleading jet  $p_T$  distribution with statistical uncertainties in the  $ee$  (top left),  $e\mu$  (top right),  $\mu e$  (bottom left), and  $\mu\mu$  (bottom right) channels. These events are selected using the  $W$  Mass Side-Band Validation Region criteria, which are identical to the  $\ell^\pm\nu\ell^\pm\nu jj$  signal region except that  $m_{jj}$  must be outside the  $W$  mass window. This region is used to validate various background estimations.

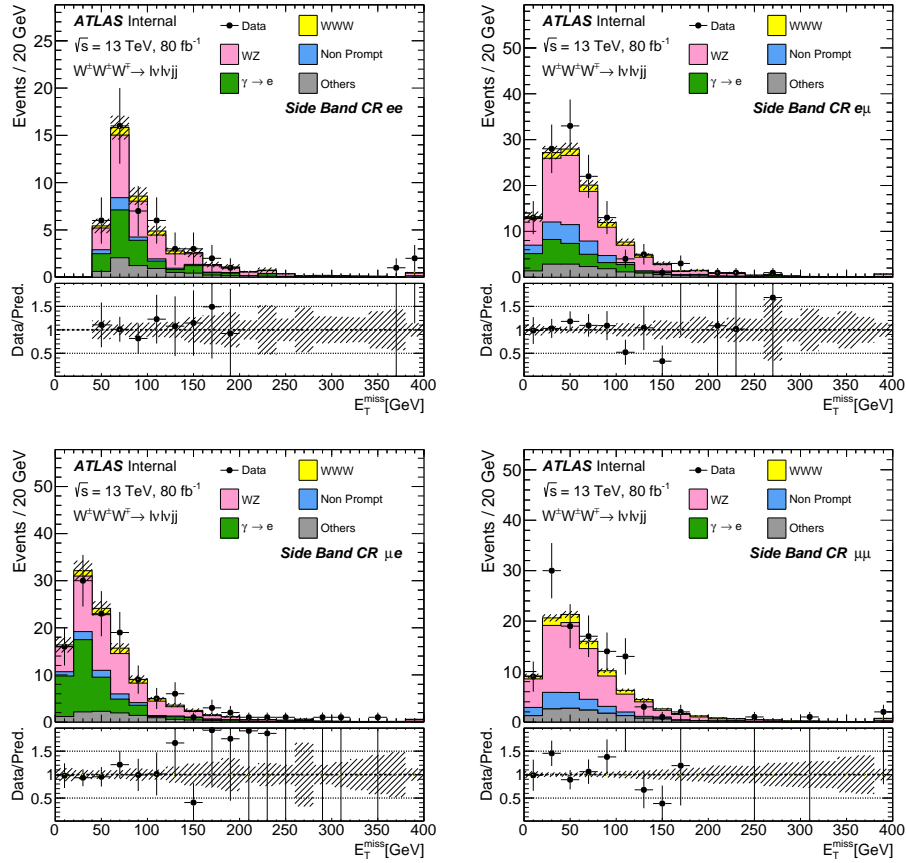


Figure 8.27: The  $E_T^{\text{miss}}$  distribution with statistical uncertainties in the  $ee$  (top left),  $e\mu$  (top right),  $\mu e$  (bottom left), and  $\mu\mu$  (bottom right) channels. These events are selected using the  $W$  Mass Side-Band Validation Region criteria, which are identical to the  $\ell^\pm \nu \ell^\pm \nu jj$  signal region except that  $m_{jj}$  must be outside the  $W$  mass window. This region is used to validate various background estimations.

	$e^\pm e^\pm$	$e^\pm \mu^\pm$	$\mu^\pm e^\pm$	$\mu^\pm \mu^\pm$
WWW	$2.93 \pm 0.14$	$7.45 \pm 0.28$	$6.47 \pm 0.23$	$8.44 \pm 0.27$
WZ	$20.71 \pm 0.69$	$64.13 \pm 1.38$	$51.08 \pm 1.19$	$60.8 \pm 1.18$
Non Prompt	$2.87 \pm 0.23$	$15.64 \pm 0.74$	$6.48 \pm 0.38$	$13.61 \pm 0.71$
Charge Flip	$1.68 \pm 0.09$	$1.8 \pm 0.11$	$0.47 \pm 0.02$	$0.0 \pm 0.0$
$V\gamma$	$12.24 \pm 1.83$	$21.13 \pm 2.4$	$39.46 \pm 3.27$	$0.0 \pm 0.0$
ssWW	$3.28 \pm 0.06$	$8.0 \pm 0.09$	$7.25 \pm 0.09$	$9.64 \pm 0.11$
ZZ	$0.3 \pm 0.03$	$2.35 \pm 0.09$	$1.6 \pm 0.08$	$1.91 \pm 0.08$
VVV	$0.07 \pm 0.01$	$0.13 \pm 0.01$	$0.11 \pm 0.01$	$0.11 \pm 0.01$
tZ	$0.14 \pm 0.05$	$0.19 \pm 0.04$	$0.11 \pm 0.03$	$0.15 \pm 0.05$
ttZ	$0.3 \pm 0.05$	$0.55 \pm 0.07$	$0.48 \pm 0.07$	$0.54 \pm 0.07$
ttW	$1.01 \pm 0.11$	$2.48 \pm 0.16$	$1.93 \pm 0.16$	$2.3 \pm 0.16$
Total Sum	$45.53 \pm 1.99$	$123.85 \pm 2.89$	$115.44 \pm 3.52$	$97.49 \pm 1.42$
Data	46	127	124	112

Table 8.11: Event yields with statistical uncertainties for data and estimated SM backgrounds in the  $W$  Mass Side-Band Validation Region.

## CHAPTER 9

# Systematic Uncertainties

This chapter covers experimental and systematic uncertainties in the  $W^\pm W^\pm W^\mp$  analysis.

### 9.1 Experimental Systematics

Potential mis-modelings of data and backgrounds are estimated using experimental systematic uncertainties. Experimental systematic uncertainties considered are:

- **Data-Driven Background Uncertainties**
  - Non-prompt lepton rate uncertainties
  - Charge misID rate uncertainties
  - Photon conversion rate uncertainties
- **MC-Driven Background Uncertainties**
  - Luminosity uncertainty
  - Pileup uncertainty
  - Muon isolation efficiency uncertainty
  - Muon scale uncertainty
  - Muon spectrometer momentum smearing uncertainty
  - Muon inner detector momentum smearing uncertainty
  - Muon reconstruction efficiency uncertainty
  - Muon trigger efficiency uncertainty
  - Muon TTVA efficiency uncertainty
  - Muon sagitta bias correction uncertainty



- Electron identification efficiency uncertainty
- Electron reconstruction efficiency uncertainty
- Electron resolution uncertainty
- Electron energy scale uncertainty
- Electron isolation efficiency uncertainty
- Electron trigger efficiency uncertainty
- Jet energy scale uncertainty
- Jet energy resolution uncertainty
- Jet vertex tagger uncertainty
- $b$ -tagging efficiency uncertainty
- $b$ -tagging efficiency uncertainty Extrapolation
- Uncertainty on the track soft term of MET

All uncertainties for the MC-driven backgrounds are provided by various ATLAS performance groups. These uncertainties affect event weights or kinematics of reconstructed objects.

### 9.1.1 Non-Prompt Lepton Uncertainties

Two systematic uncertainties are used for estimating uncertainties on the non-prompt lepton background estimation.

The first is the statistical uncertainty used in the non-prompt method. It is the largest uncertainty. Tables 8.6 shows the non-prompt rates with their statistical uncertainties. The statistical uncertainties are largely due to low statistics in the  $\ell^\pm\nu\ell^\pm\nu jj$  and  $\ell^\pm\nu\ell^\pm\nu\ell^\mp\nu$   $b$ -tagged regions where all leptons are ID leptons. This uncertainty is also the largest uncertainty for the  $W^\pm W^\pm W^\mp$  analysis.

The second uncertainty is the  $p_T$  dependence of the non-prompt rate. The non-prompt rates are calculated with an inclusive method. To check the  $p_T$  dependence of the non-prompt rates, they are re-derived in the  $\ell^\pm\nu\ell^\pm\nu jj$   $b$ -tagged region as a function of  $p_T$ . The difference between non-prompt rates with and without  $p_T$  dependence is then introduced as a systematic uncertainty. The  $p_T$  dependent rates for electrons and muons are shown in Figure 9.1. For electrons, no  $p_T$  dependence has been observed. To avoid double counting the statistical uncertainty, the  $p_T$  modeling uncertainty is omitted for electrons. The statistical uncertainty of this method is not taken into account for this uncertainty.

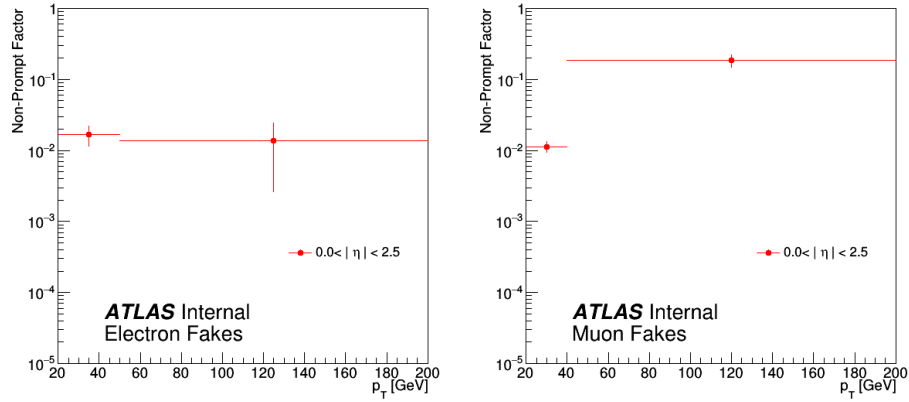


Figure 9.1:  $p_T$  dependent non-prompt rates with statistical uncertainties for electrons (left) and muons (right) respectively. These rates are compared with inclusive non-prompt rates and the differences are introduced as a systematic uncertainty.

### 9.1.2 Charge misID Uncertainties

Two systematic uncertainties are considered for the charge misID background: statistical uncertainty and background modeling uncertainties.

- The statistical uncertainty of the measured charge misID rate is the leading uncertainty. This uncertainty is large as a result of low statistics of the  $Z \rightarrow e^\pm e^\pm$  events where one of the leptons is required to be charge-flipped. Figure 8.1 shows the bin-wise statistical uncertainties and due to low statistics, the statistical uncertainty is large at high  $p_T$  and  $\eta$  regions.
- The charge misID rate calculation method uses a  $Z$  mass window to estimate the signal and a  $Z$  mass side-band for the background estimation. The choice of the size of the  $Z$  mass window is arbitrary. To prevent any bias caused by the  $Z$  mass window choice, the charge misID rate is calculated with a different  $Z$  mass window. The difference between the nominal and the expanded  $Z$  window is used as a systematic uncertainty. Overall this effects has been observed to be small but can go up to 20% in  $p_T$  and  $\eta$  bins with low statistics.

Both uncertainties are applied by scaling the mis-identification rate up and down by the given uncertainty and re-applying them to data in the signal regions.

### 9.1.3 Photon Conversion Rate Uncertainties

Two systematic uncertainties are defined for the photon conversion rate.

- The first uncertainty considered is the statistical uncertainty of the measured photon conversion rate. This uncertainty is dominated by the statistics of  $Z\gamma$  data events at the  $Z\gamma$  control region and is calculated to be around 9%.
- The second uncertainty considered aims to test if the photon conversion rates determined from  $W\gamma$  and  $Z\gamma$  processes are compatible. The dominant photon conversion process in the  $\ell^\pm\nu\ell^\pm\nu jj$  signal region is the  $W\gamma$  process, while the photon conversion rates are determined from  $Z\gamma$  events. In order to avoid a potential bias, photon-conversion rates are derived from MC for  $W\gamma$  and  $Z\gamma$  processes. The photon conversion rate for the  $W\gamma$  process is computed in the  $\ell^\pm\nu\ell^\pm\nu jj$  signal region and the photon conversion rate for the  $Z\gamma$  process is computed in the  $Z\gamma$  control region. The different photon conversion rates are given in Table 9.1. A 4% difference in the photon conversion rates between  $W\gamma$  and  $Z\gamma$  MC is observed. This difference is considered as a systematic uncertainty.

Both uncertainties are applied by scaling the photon conversion rate up and down by the given uncertainty and re-applying them to data in the signal regions.

Process	N(Signal)	N(Anti-BL)	Factor
$W\gamma$ MC	31.0	257.5	0.120
$Z\gamma$ MC	48.22	415.22	0.116
Percent diff.			4%

Table 9.1: The photon mis-identification rate as measured in  $W\gamma$  MC in the  $\ell^\pm\nu\ell^\pm\nu jj$  signal region, and as measured in  $Z\gamma$  MC in the  $Z\gamma$  control region.

### 9.1.4 Luminosity and Pile-up Uncertainty

The uncertainty on the integrated luminosity is determined to be 2.0% [18] by the ATLAS Collaboration. This uncertainty is applied to all MC-driven backgrounds.

The pile-up uncertainties used in this analysis are also provided by the ATLAS Collaboration and is applied to MC-driven backgrounds. The pile-up uncertainties are found to be  $\approx 2 - 3\%$ .

### 9.1.5 Muon Uncertainties

Muon uncertainties [47] are provided by the Muon Combined Performance group of the ATLAS Collaboration and can be summarized as follows. These uncertainties are defined for each set of muon selections:

- Track Uncertainties: Variation in the smearing of ID and MS tracks.
- Isolation Efficiency Uncertainty: Uncertainty on the isolation scale factor based on the tag and probe method on the  $Z$  mass peak.
- Sagitta Uncertainty: Uncertainties for the scale of the momentum caused by the combination of corrections on the  $Z$  scale or residual charge-dependent bias.
- Momentum Scale Uncertainty
- Reconstruction Efficiency Uncertainty
- Track to Vertex Association Efficiency Uncertainties
- Trigger Efficiency Uncertainty

These uncertainties have a minor impact on the final results. These uncertainties are derived using  $Z \rightarrow \mu\mu$  and  $J\psi \rightarrow \mu\mu$  events.

### 9.1.6 Electron Uncertainties

The Electron Gamma Combined Performance group provides electron uncertainties [54] for the ATLAS Collaboration. These uncertainties are defined for each set of electron selections used in the analysis. Similar to muons these uncertainties do not have a significant impact on the final results. The details of the considered uncertainties are as follows:

- Reconstruction and Identification Efficiency Uncertainty: Uncertainties on the reconstruction and ID efficiencies measured with events around the  $Z$  mass peak using tag and probe method.
- Isolation Efficiency Uncertainty: Uncertainty on the isolation scale factor based on the tag and probe method.
- Trigger Efficiency Uncertainty
- Momentum Scale and Resolution Uncertainties: Uncertainty on the electron energy scale and resolution.

### 9.1.7 Jet Uncertainties

Jet uncertainties [64][65] are defined by a dedicated  $\text{Jet}/E_T^{\text{miss}}$  and  $b$ -tagging Performance Group under the ATLAS Collaboration. The uncertainties considered in this analysis are as follows:

- Jet Energy Scale and Resolution Uncertainty: A 31 nuisance parameter scan is used to calculate the uncertainty due to jet energy modeling in the MC simulation.
- Heavy Flavor Tagging Efficiency Uncertainty: Since a  $b$ -tag veto is used to reduce the non-prompt background, the mis-modeling of  $b$ -jet tagging is introduced as an uncertainty in the MC simulation. For this reason, the loose reduction scheme is used to vary scale factors to obtain systematic uncertainties.
- JVT Efficiency Uncertainty: This uncertainty aims to capture the modeling performance of the JVT requirement on hard-scatter jets in  $Z \rightarrow \mu\mu$  data versus simulation

Among all the uncertainties that are applied to MC driven backgrounds, the jet uncertainties have the most significant impact. This is due to the  $m_{jj}$  distribution is used in the final fit for the  $\ell^\pm\nu\ell^\pm\nu jj$  channel. Di-jet mass distribution is sensitive to the jet energy scale which shifts the  $m_{jj}$  spectrum for both signal and background, and jet energy resolution which broadens the  $m_{jj}$  distribution.

### 9.1.8 $E_T^{\text{miss}}$ Uncertainties

Since  $E_T^{\text{miss}}$  is composed of different physical objects as described in Section 4.6, it is sensitive to all uncertainties that change its constituents energy/momentum. In addition, there are dedicated  $E_T^{\text{miss}}$  uncertainties [66] provided by the  $\text{JET}/E_T^{\text{miss}}$  Performance Group that are approximately the uncertainty on the track soft term of MET. The track soft term defined in Section 4.6 contains momenta of associated tracks. This uncertainty represents the energy/momentum uncertainties of these tracks.

Overall the  $E_T^{\text{miss}}$  uncertainties have minor effects on the final results. This is due to the fact that the  $E_T^{\text{miss}}$  information is only used in  $ee$  and  $e\mu$  channels for the  $\ell^\pm\nu\ell^\pm\nu jj$  analysis.

## 9.2 Theoretical Uncertainties

Theory uncertainties are calculated only for the  $WH$ ,  $WWW$ , and  $WZ$  processes. Scale, parton shower, and PDF uncertainties are taken into account in the uncertainty estimations.

For each event generator, different methods have been used to estimate these uncertainties. For the  $WZ$  samples, all uncertainties that affect the cross-sections are omitted or normalized to the cross-section due to the fact that the normalization of the  $WZ$  being a free floating parameter.

The  $WWW$  and  $WZ$  samples are generated using SHERPA 2.2.2 [58] and are treated identically when measuring scale uncertainties. The scale choices for  $WZ$  and  $WWW$  MC samples have a direct effect on theoretical cross-section and kinematic distributions. To account for the scale dependence of these processes, the factorization and re-normalization scales are varied by a factor of 2 and 0.5. The variations are estimated by applying pre-event weights generated by SHERPA 2.2.2. The difference between the nominal samples and the weighted samples are then used as scale uncertainties.

For the  $WH$  sample, the scale uncertainties are obtained by producing generator-level MC samples with different factorization and re-normalization scales that varied by a factor of 2 and 0.5. These events are then processed using Rivet [62] and the deviations from the nominal sample are used as an overall normalization uncertainty. The scale uncertainties for the  $WH$  sample is found to be  $\sim 0.5\%$  and  $\sim 3\%$  for  $\ell^\pm\nu\ell^\pm\nu jj$  and  $\ell^\pm\nu\ell^\pm\nu\ell^\mp\nu$  signal regions respectively.

Parton shower uncertainties for  $WWW$  and  $WH$  MC samples are calculated by producing generator-level MC samples with different resummation scales that varied by a factor of 2 and 0.5. These events are then processed using Rivet [62] and the deviation from the nominal sample is used as an overall normalization uncertainty. The parton shower uncertainties are found to be  $\sim 7\%$  for  $WWW$  samples and  $\sim 2\%$  for  $WH$  samples.

In addition to scale uncertainties, an overall normalization uncertainty for PDFs is calculated for  $WWW$  and  $WH$  samples following the recommendation provided by PDF4LHC paper[67]. The PDF uncertainty is estimated by generating  $WWW$  events using different PDFs ( “NNPDF3.0”[36], “NMHT2014” and “CTEQ14”). For the  $WH$  samples, different sets of PDFs are used (“CTEQ10”, “MSTW08” and “NNPDF2.3”). These events are then processed using Rivet [62]. For the  $WWW$  samples an envelope of the largest difference between different PDF sets is then applied as an overall normalization uncertainty. The PDF uncertainty on the  $WWW$  cross section is found to be 4% and 2.55% for  $\ell^\pm\nu\ell^\pm\nu jj$  and  $\ell^\pm\nu\ell^\pm\nu\ell^\mp\nu$  channels respectively. For the  $WH$  sample, the difference between the nominal and variation samples are added in quadrature to estimate the PDF uncertainty. The PDF uncertainty on the  $WH$  cross-section is found to be 1.28% and 2.99% for  $\ell^\pm\nu\ell^\pm\nu jj$  and  $\ell^\pm\nu\ell^\pm\nu\ell^\mp\nu$  channels respectively.

## CHAPTER 10

### WVZ Analysis

The  $W^\pm W^\pm W^\mp$  results will be combined with results obtained from the  $WVZ$  analysis [3]. The  $WVZ$  analysis is not within the scope of this thesis, but an understanding of the  $WVZ$  analysis is needed for the interpretation of the final results. This chapter is dedicated to the summary of the  $WVZ$  analysis.

#### 10.1 Experimental Signatures and Backgrounds

The  $WVZ$  analysis searches for the  $WWZ$  and  $WZZ$  final states through the  $WVZ \rightarrow lvqqll$ ,  $WWZ \rightarrow lvlvll$ , and  $WZZ \rightarrow qqllll$  processes. The  $WVZ$  production mechanisms are similar to the  $W^\pm W^\pm W^\mp$  analysis and can be viewed in Figure 10.1. Due to the presence of three or four leptons with at least one  $Z$  boson in each event, backgrounds are dominated by processes that produce three or four prompt leptons in the final state. As a result, all SM backgrounds are estimated using simulation. The charge-flip background is omitted due to a  $Z$  boson is reconstructed instead of being vetoed.

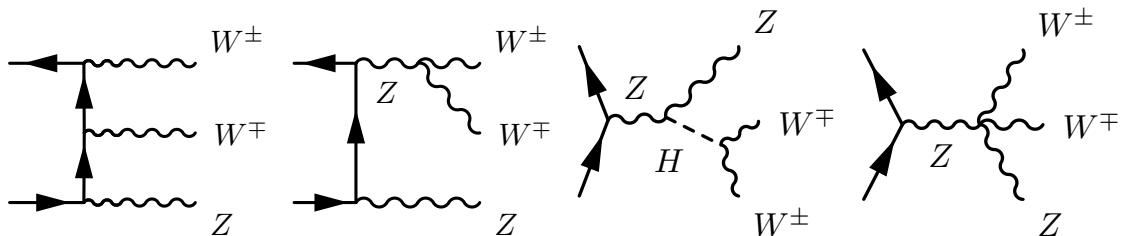


Figure 10.1: Feynman diagrams that produce the  $WWZ$  final state in  $pp$  collisions.

Final State	Three Lepton	Four Lepton
Trigger	One tight lepton triggering single lepton trigger	
# leptons	2 opposite sign loose leptons reconstructing the Z-boson mass $M_{\ell\ell}^Z$	
	1 tight lepton	2 tight leptons
Total Charge	$ \sum q_i  = 1$	$ \sum q_i  = 0$
Reco. Z Boson Mass	$M_{\ell\ell}^Z > 12 \text{ GeV}$ $ M_{\ell\ell}^Z - m_Z  < 10 \text{ GeV}$	
# Jets	$N(\text{jets}) > 1$ and $N(b\text{-jets}) = 0$	

Table 10.1: Pre-selection cuts applied to the  $WVZ$  analysis. Here the  $m_{\ell\ell}^Z$  variable is the mass of the reconstructed Z boson.

## 10.2 Object Selection

The nominal object definitions in the  $WVZ$  analysis are designed to be similar to those used in the  $W^\pm W^\pm W^\mp$  analysis [2]. The major differences are different  $p_T$  requirements ( $p_T(\ell) > 15 \text{ GeV}$ ), a looser isolation and identification used for muons. The  $WVZ$  analysis has an additional lepton definition called loose leptons. Loose leptons are identical to nominal leptons except that the lepton quality criteria is changed to loose, and the PLV and charge flip tagger requirements are dropped. These leptons are used in all signal regions in addition to nominal leptons to increase the signal acceptance.

## 10.3 Analysis Strategy

The  $WVZ$  analysis trains six different BDTs to select and identify  $WVZ$  events. The BDTs are categorized according to the decay processes. Three BDTs are trained in the three-lepton final states, and three BDTs are trained in the four-lepton final states. All six BDT distributions are used in the final fit to extract the  $WVZ$  signal.

In all decay processes, a Z boson candidate is reconstructed using a SFOS lepton pair. If there are more than two leptons which can form a Z boson candidate, the combination closest to the Z boson pole mass is used. In all decay processes a mass window cut of  $|m_{\ell\ell} - m_Z| < 10 \text{ GeV}$  is applied to ensure that the event contains a Z boson. The lepton charge configuration is required to be  $|\sum q_i| = 1$  for decays into three leptons, and is required to be  $|\sum q_i| = 0$  for decays into four leptons. In addition a  $b$ -jet veto is applied to reduce the  $t\bar{t}$  contribution. The details of event selections can be found in Table 10.1.



### 10.3.1 Three Lepton BDT

For  $WVZ \rightarrow \ell\nu qq\ell\ell$  three BDTs are trained. The third lepton (that doesn't form a  $Z$  boson) is required to be a nominal lepton. The BDTs are categorized according to the jet multiplicity: one jet ( $3\ell + 1\text{jet}$ ), two jets ( $3\ell + 2\text{jets}$ ), and three or more jets ( $3\ell + 3\text{jets}$ ). This categorization allows the  $Z$ +jets backgrounds to be differentiated from the signal without losing the overall sensitivity. Since there are no cuts applied on the BDT discriminant, there are a large fraction of  $WZ$  and  $Z + jets$  events reconstructed in the  $3\ell + 1\text{jet}$  region. These events are used for constraining the  $WZ$  background in the final fit. Table 10.2 shows all variables used in the BDT training according to their importance, and Figure 10.2 shows the BDT responses.

Input Variable	$3\ell + 1\text{jet}$	$3\ell + 2\text{jets}$	$3\ell + 3\text{jets}$
$m_{3\ell}$	×	×	×
$m_{\ell_0\ell_1}$	×	×	
$m_{\ell_0\ell_2}$	×	×	
$m_{\ell_1\ell_2}$	×	×	
leading jet $p_T$	×	×	
$p_T^{\ell_0}$	×	×	
$p_T^{\ell_1}$	×	×	×
$p_T^{\ell_2}$	×	×	×
$E_T^{\text{miss}}$		×	×
leptonic $H_T$	×	×	×
hadronic $H_T$			×
total $H_T$	×	×	
total lepton charge	×	×	×
invariant mass of all leptons, jets and $E_T^{\text{miss}}$	×		×
invariant mass of best $Z \rightarrow \ell\ell$ and leading jet	×		
subleading jet $p_T$		×	×
$m_{jj}^{01}$		×	
$m_T^{W \rightarrow \ell\nu}$		×	
n. of reconstructed jets			×
$m_{jj}^{\text{best } W}$			×
smallest $m_{jj}$			×

Table 10.2: List of discriminating variables that are used for the  $3\ell$  BDT trainings at the  $WVZ$  analysis. In this table, the total  $H_T$  stands for scalar sum of all lepton and jet  $p_T$  and hadronic or leptonic  $H_T$  stands for scalar sum of all jet or lepton  $H_T$  respectively. The  $\ell_0$ ,  $\ell_1$  and  $\ell_2$  stand for leading, sub-leading and sub-sub-leading leptons respectively. The  $j_0$  and  $j_1$  stand for leading and sub-leading jets respectively. Lastly,  $m_T^{W \rightarrow \ell\nu}$  stands for the reconstructed transverse mass of the leptonically decaying  $W$  boson.

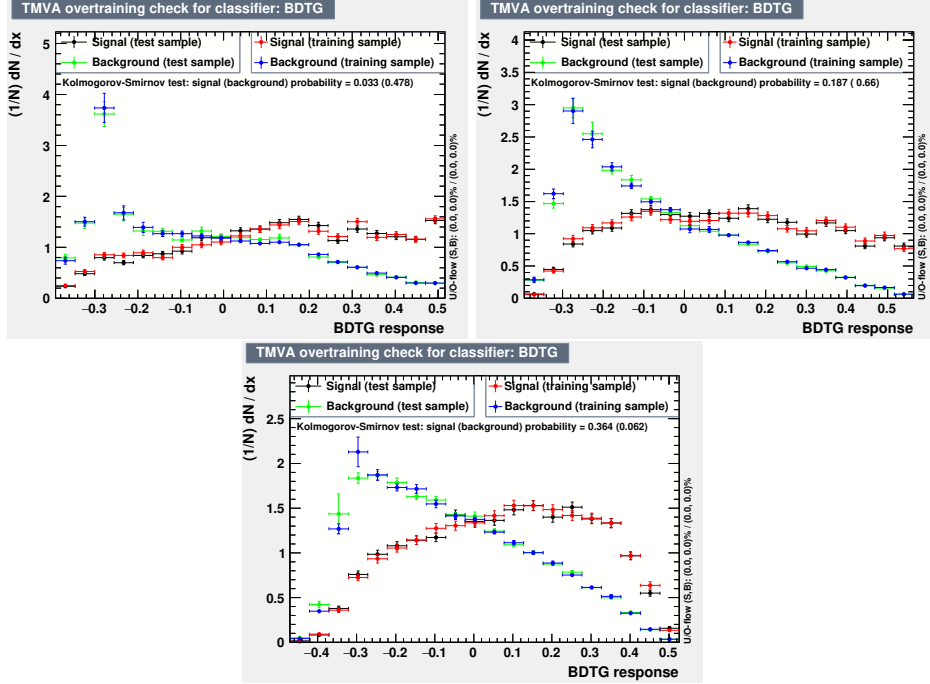


Figure 10.2: BDT responses in  $3l + 1jet$  (top left),  $3l + 2jet$  (top right), and  $3l + 3jet$  (bottom). The BDTG label in the  $x$ -axis stands for gradient boosted decision trees which is the technique used [68]. Only statistical uncertainties are shown.

### 10.3.2 Four Lepton BDT

For  $WWZ \rightarrow \ell\nu\ell\nu\ell\ell$  and  $WZZ \rightarrow q\ell\ell\ell\ell$  three BDTs are trained. Each event is required to have the total charge to be zero, and the BDTs are categorized according to the properties of the two leptons that does not form the  $Z$  boson. If these two leftover leptons are not Same Flavor (SF), it is assumed that they come from the  $WWZ \rightarrow \ell\nu\ell\nu\ell\ell$  process and one of the three BDTs is trained to identify such events. If the two leftover leptons are SF, another  $Z$  boson candidate is reconstructed. If this  $Z$  boson candidate satisfies the  $|m_{\ell\ell}^2 - m_Z^2| < 10\text{GeV}$  requirement (where  $m_{\ell\ell}^2$  is the  $Z$  boson candidates mass), it is categorized as  $WZZ \rightarrow q\ell\ell\ell\ell$ ; and if it fails the  $m_{\ell\ell}$  cut, it is categorized as  $WWZ \rightarrow \ell\nu\ell\nu\ell\ell$ . A BDT is trained for both cases, adding up to three different BDTs for the four-lepton final states. The variables used for the BDT training can be found in Table 10.3 and the BDT responses can be found in Figure 10.3.

Input Variable	DF	on-shell SF	off-shell SF
n. of reconstructed jets	×	×	×
$m_{4\ell}$	×	×	×
best Z lepton pair inv. mass		×	×
other lepton pair inv. mass	×	×	×
$E_{\text{T}}^{\text{miss}}$	×	×	×
leptonic $H_{\text{T}}$	×		
hadronic $H_{\text{T}}$	×		
total $H_{\text{T}}$		×	×

Table 10.3: List of discriminating variables that are used for the  $4\ell$  BDT trainings. In this table, the total  $H_{\text{T}}$  stands for scalar sum of all lepton and jet  $p_{\text{T}}$  and hadronic or leptonic  $H_{\text{T}}$  stands for scalar sum of all jet or lepton  $H_{\text{T}}$  respectively.

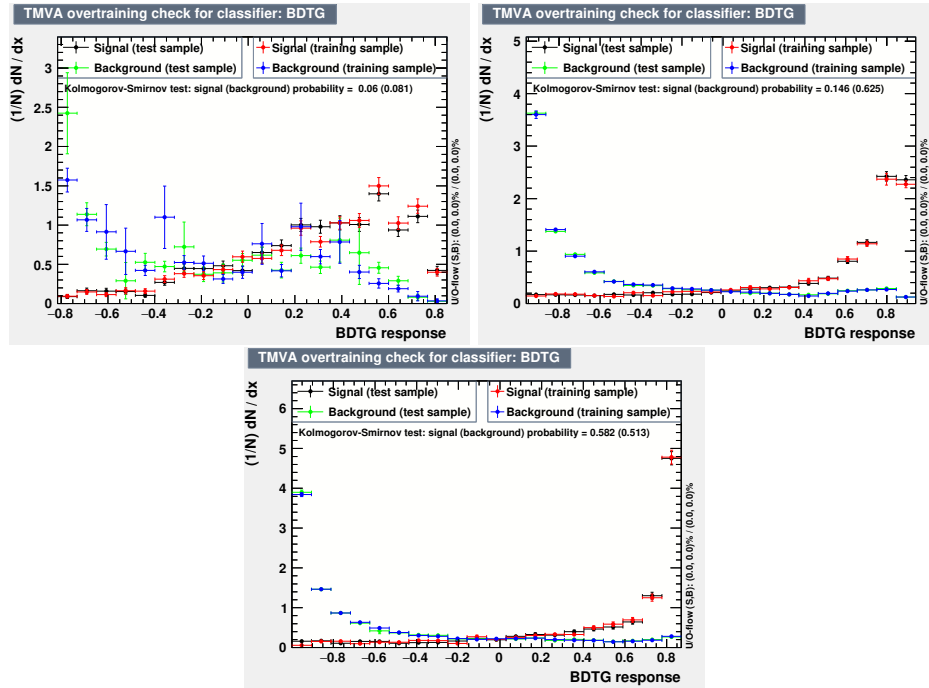


Figure 10.3: BDT responses in  $4\ell$  DF (top right), on-shell SF (top left) and off-shell SF (bottom) regions. The BDTG label in the x-axis stands for gradient boosted decision trees, which is the technique that is used [68]. Only statistical uncertainties are shown.

## 10.4 Systematic Uncertainties

The  $WVZ$  analysis has nearly identical systematic uncertainties with the  $W^\pm W^\pm W^\mp$  analysis. There are two major differences. First, due to the lack of data-driven backgrounds, none of the data-driven background uncertainties are applied to the  $WVZ$  analysis. Instead, the  $WVZ$  analysis uses large priors for background normalizations. The applied prior uncertainties for different backgrounds are: 20% for the  $WZ$  and  $ZZ$ , 40% for the  $Z + jets$ , 10% for the  $WtZ$ , 30% for  $tZ$  and  $VH$  (non- $VVV$  decays), and 11% for  $t\bar{t}Z$ . These priors for the  $WZ$  and  $Z + jets$  backgrounds are constrained to  $\sim 5\%$  levels after the fit.

## CHAPTER 11

# Fitting Procedure

The  $W^\pm W^\pm W^\mp$  and  $WVZ$  cross-sections are extracted using a log-likelihood fit, where  $\mu$  is defined as the parameter of interest in the likelihood, and the observed cross-section is quoted in terms of the  $\mu$ :

$$\sigma^{\text{obs}} = \mu \times \sigma^{\text{SM}}, \quad (11.1)$$

where the  $\sigma^{\text{SM}}$  is the SM cross-section of the signal processes and the  $\sigma^{\text{obs}}$  is the observed cross-section.

The likelihood function is defined as multiplications of Poisson distributions for each signal and control region in all channels and all bins and then multiplied by Gaussian functions due to constraints. These Poisson distributions represent the probability of observing the given amount of data events for a given expected number of events. The Gaussian constraints represent the systematic uncertainties into the fit. The likelihood used can be summarized by the following equations:

$$L^{\text{Bin}}(\mu) = \text{Pois}(N_{\text{bin}}^{\text{obs}} | N_{\text{bin}}^{\text{exp}}(\mu)), \quad (11.2)$$

$$L^{\text{Chan}}(\mu) = \prod_i^{\text{\# Bins}} L_i^{\text{Bin}}(\mu), \quad (11.3)$$

$$L^{\text{Region}}(\mu) = \prod_i^{\text{\# Channels}} L_i^{\text{Chan}}(\mu), \quad (11.4)$$

$$L^{\text{Comb.}}(\mu, \mu_{WZ}, \vec{\theta}) = \prod_i^{\text{\# Signal Regions}} L_i^{\text{Region}}(\mu) \prod_j^{\text{\# Control Regions}} L_j^{\text{Region}}(\mu_{WZ}) \prod_k^{\text{\# Syst.}} \text{Gaus}(\theta_k). \quad (11.5)$$

In these equations  $\mu$  represents the parameter of interest, and  $\mu_{WZ}$  represents the  $WZ$  background normalization parameter (that are used in some fits),  $\vec{\theta}$  represents nuisance param-

eters that are the parameterization of systematic uncertainties using Gaussian constraints.  $N^{\text{obs}}$  represent the number of observed events in the data and  $N^{\text{exp}}$  represents the number of events expected events given by the formula:

$$N^{\text{exp}}(\mu) = \mathcal{L} \times \sigma^{\text{SM}} \times \mu + \sum_i^{\text{Background}} N_i^{\text{Background}}, \quad (11.6)$$

where  $\mathcal{L}$  represent the integrated luminosity. This equation is slightly modified in the fits without the  $WVZ$  analysis to accommodate the free floating  $WZ$  normalization by introducing  $\mu_{WZ}$ . Equation 11.6 now becomes:

$$N^{\text{exp}} = \mathcal{L} \times \sigma^{\text{SM}} \times \mu + N_{WZ}^{\text{exp}} \times \mu_{WZ} + \sum_i^{\text{Background}} N_i^{\text{Background}}. \quad (11.7)$$

The  $W^\pm W^\pm W^\mp$  cross-section is extracted using the  $\ell^\pm \nu \ell^\pm \nu jj$  and  $\ell^\pm \nu \ell^\pm \nu \ell^\mp \nu$  signal regions defined in Section 6. For the combined fit with the  $WVZ$  analysis, both signal and background cross-sections are allowed to float. In the standalone (without  $WVZ$ ) fits, the  $WZ$  background normalization is defined as a free parameter and is constrained by the  $WZ$  control region defined in Section 8.4. For the combined (with  $WVZ$ ) fit, a 20% prior uncertainty is applied on the  $WZ$  and  $ZZ$  normalization which is constrained by the  $WVZ$  analysis. Systematic uncertainties and background normalization are introduced in the likelihood function via nuisance parameters given by  $\theta$ .

In this likelihood, the  $\ell^\pm \nu \ell^\pm \nu jj$  signal region is split into  $ee$ ,  $e\mu$ ,  $\mu e$ ,  $\mu\mu$  channels, and each channel is split into 30 equal-sized bins that span the range of  $0 < m_{jj} < 300 \text{ GeV}$ . The  $\ell^\pm \nu \ell^\pm \nu \ell^\mp \nu$  signal region is defined as a single inclusive bin. If used, the  $WZ$  control region is split into  $eee$ ,  $ee\mu$ ,  $\mu\mu e$ ,  $\mu\mu\mu$  channels, and each channel has 5 equal-sized bins spanning the range of  $0 < m_{\ell\ell\ell} < 600 \text{ GeV}$ . In the combined fit, the  $WVZ$  analysis is also included in the likelihood by introducing six BDT regions:  $3\ell + 1\text{jet}$ ,  $3\ell + 2\text{jets}$ ,  $3\ell + 3 + \text{jet}$ ,  $4\ell$  with opposite-flavor leftover leptons,  $4\ell$  with same-flavor leftover leptons that are on-shell and  $4\ell$  with same-flavor leftover leptons that are off-shell. The BDT discriminants of each BDT are binned in varying bin sizes that can be viewed in the post-fit distributions in Figures 12.16 and 12.17 in the next chapter.

The log-likelihood fit is conducted using the RooStats[69] tool. For the null-hypothesis, the test statistics is determined by the profile-likelihood [70] approach given by:

$$-2 \ln \lambda(\mu) = -2 \ln \frac{L(\mu, \hat{\theta})}{L(\hat{\mu}, \hat{\theta})}. \quad (11.8)$$

In this equation,  $L(\hat{\mu}, \hat{\theta})$  represents the maximum value for the likelihood for free-floating  $\mu$  and  $\theta$  values, and  $L(\mu, \hat{\theta})$  represents the likelihood value for a given value of  $\mu$  where  $\hat{\theta}$  is the best fit nuisance parameters for the given  $\mu$  value. By definition,  $-2 \ln \lambda(\mu)$  is zero at the observed/expected  $\mu$  ( $\hat{\mu}$ ), and the asymptotic approximation at  $-2 \ln \lambda(0) \simeq Z^2$  can be used to extract the significance where  $Z$  represents the significance.

# CHAPTER 12

## Results

The yields and kinematic distributions of  $WWW$  and  $WVZ$  candidate events are presented in this chapter. A discriminant that maximizes the sensitivity to the triboson signal is defined in each channel. The discriminants are combined using a binned maximum-likelihood fit as explained in Chapter 11. The fitted results together with limits on aQGC obtained from the 8 TeV analysis are presented. The chapter is concluded by the future prospects of the  $W^\pm W^\pm W^\mp$  analysis.

### 12.1 $WWW$ Results

The event yields in the  $W^\pm W^\pm W^\mp$  signal regions are obtained using the signal region cuts defined in Section 6. Backgrounds in these signal regions are estimated as described in Section 8 and the uncertainties of these backgrounds are explained in Section 9.

Table 12.1 shows the pre-fit event yields with statistical uncertainties and Table 12.2 shows the post-fit event yields with systematical and statistical uncertainties for four signal regions. Good data agreement is observed across all regions, with a slight deficit in the observed data in the  $e\mu$  channel of the  $\ell^\pm \nu \ell^\pm \nu jj$  analysis and in the  $\ell^\pm \nu \ell^\pm \nu \ell^\mp \nu$  signal region. In contrast, a slight excess in the  $\mu\mu$  channel for the  $\ell^\pm \nu \ell^\pm \nu jj$  analysis is observed.

Figure 12.1 and 12.2 show the pre-fit and post-fit  $m_{jj}$  distributions of the  $\ell^\pm \nu \ell^\pm \nu jj$  signal regions. The  $m_{jj}$  distribution is sensitive to the hadronic  $W$  decay of the  $W^\pm W^\pm W^\mp$  signal, and the overall excess of data is observed around the  $W$  pole mass. Figure 12.3 shows the post-fit inclusive  $\ell^\pm \nu \ell^\pm \nu jj$   $m_{jj}$  distribution and the post-fit  $\ell^\pm \nu \ell^\pm \nu \ell^\mp \nu$  yield. Post-fit  $\ell^\pm \nu \ell^\pm \nu jj$  distribution shows good data agreement and post-fit  $\ell^\pm \nu \ell^\pm \nu \ell^\mp \nu$  signal region observes a large data deficit. Other  $\ell^\pm \nu \ell^\pm \nu jj$  and  $\ell^\pm \nu \ell^\pm \nu \ell^\mp \nu$  kinematic distributions can be found in Figures 12.4-12.15. Overall good shape agreement is observed in all distributions.



	$e^\pm e^\pm jj$	$e^\pm \mu^\pm jj$	$\mu^\pm e^\pm jj$	$\mu^\pm \mu^\pm jj$	$3\ell$ 0-SFOS
WWW	7.6±0.3	19.9±0.4	17.9±0.4	23.0±0.4	11.3±0.2
WZ	38.1±1.0	124.7±2.1	97.9±1.7	121.6±1.8	8.6±0.7
ZZ	0.44±0.06	5.0±0.1	3.4±0.2	4.1±0.1	0.69±0.07
Non-prompt	5.6±0.3	36.0±1.1	14.1±0.6	35.0±1.1	9.1±0.6
$\gamma$ conv.	22.8±2.5	38.2±3.2	83.5±4.7	-	1.2±0.6
Others	11.2±0.2	21.8±0.3	16.7±0.3	20.7±0.3	3.5±0.9
Total	85.8±2.7	245.8±4.0	233.5±5.1	204.4±2.2	34.4±1.1
Data	87	239	235	237	27

Table 12.1: Pre-fit background, signal and observed yields for the  $WWW \rightarrow \ell\nu\ell\nu qq$  and  $\ell\nu\ell\nu\ell\nu$  channels. Uncertainties shown are statistical only.

	$e^\pm e^\pm jj$	$e^\pm \mu^\pm jj$	$\mu^\pm e^\pm jj$	$\mu^\pm \mu^\pm jj$	$3\ell$ 0-SFOS
WWW	10.6 ± 3.3	28 ± 9	25 ± 8	30 ± 10	16 ± 5
WZ	37.6 ± 2.3	122 ± 6	97 ± 5	120 ± 6	8.6 ± 0.5
ZZ	0.46 ± 0.05	5.12 ± 0.25	3.45 ± 0.18	4.13 ± 0.24	0.690 ± 0.033
Non-prompt	6.1 ± 3.0	35 ± 5	17 ± 9	37 ± 7	9.5 ± 1.5
$\gamma$ conv.	21.0 ± 2.0	35.1 ± 3.1	76 ± 7	-	1.06 ± 0.11
Others	11 ± 1.0	22.3 ± 1.6	17.3 ± 1.2	21.4 ± 1.5	3.5 ± 0.4
Total	87 ± 4	248 ± 9	240 ± 10	215 ± 9	39 ± 4
Data	87	239	235	237	27

Table 12.2: Post-fit background, signal and observed yields for the  $WWW \rightarrow \ell\nu\ell\nu qq$  and  $\ell\nu\ell\nu\ell\nu$  channels. Uncertainties on the predictions include both statistical and systematic uncertainties added in quadrature.

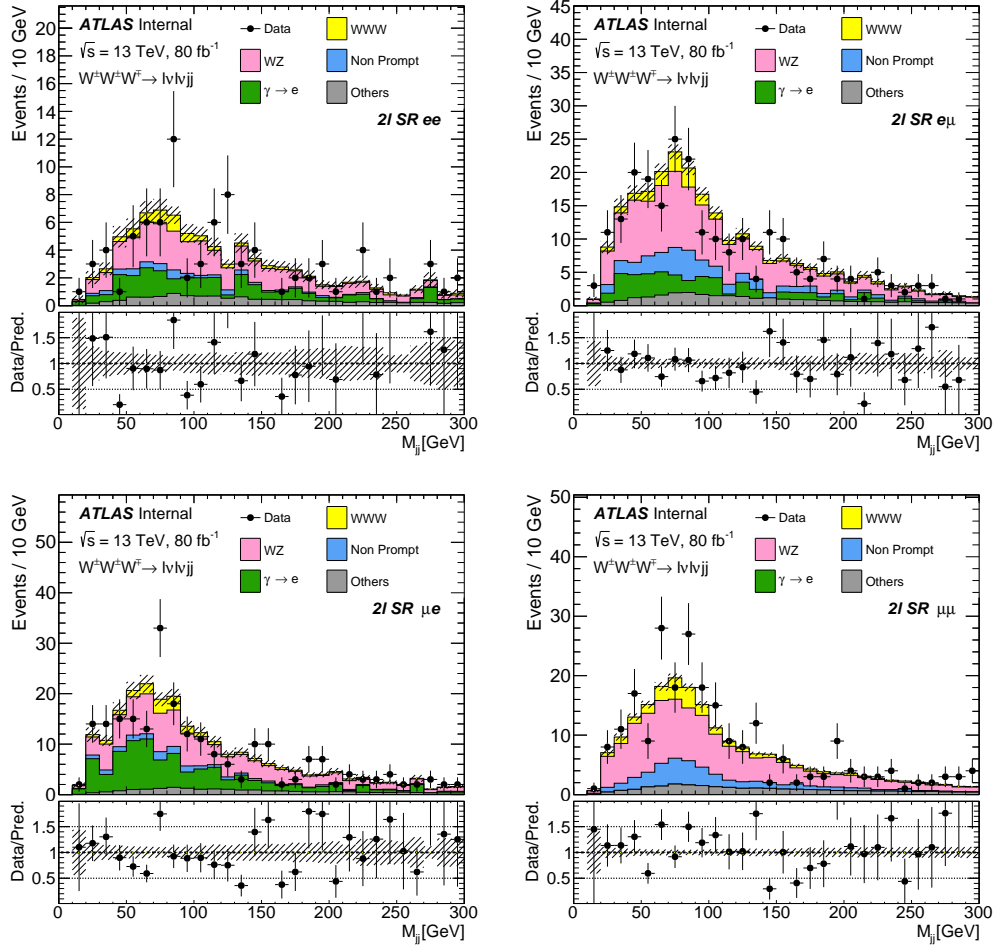


Figure 12.1: The observed data are compared to the signal plus background model in the  $ee$  (left),  $e\mu$  (mid left),  $\mu e$  (mid right),  $\mu\mu$  (right) signal regions for the  $\ell^\pm\nu\ell^\pm\nu jj$  channel as a function of the  $m_{jj}$ . Signal and backgrounds are pre-fit. The uncertainty is statistical uncertainty only.

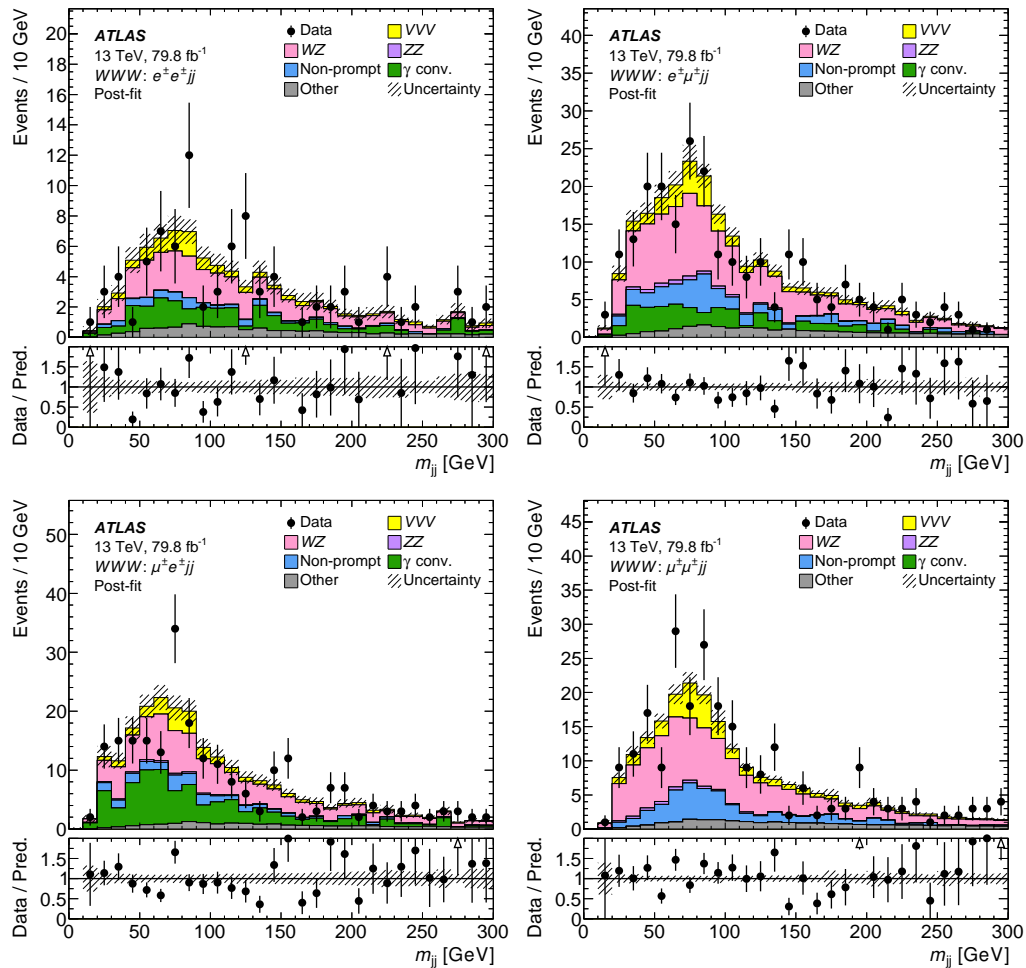


Figure 12.2: The observed data are compared to the signal plus background model in the  $ee$  (left),  $e\mu$  (mid left),  $\mu e$  (mid right),  $\mu\mu$  (right) signal regions for the  $\ell^\pm\nu\ell^\pm\nu jj$  channel as a function of the  $m_{jj}$ . Signal and backgrounds are normalized to the expected number of events after the fit. The uncertainty band includes both the statistical and systematic uncertainties as obtained by the fit. In the post-fit plots, the  $WWW$  tags have been replaced with  $VVV$  as these results are presented with the  $WVZ$  analysis.

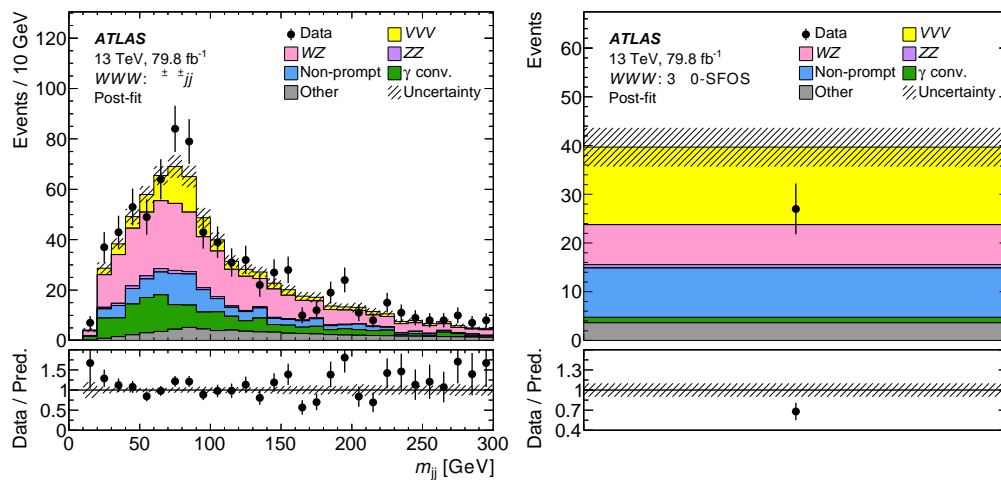


Figure 12.3: The observed data are compared to the signal plus background model in the inclusive signal regions for the  $\ell^\pm\nu\ell^\pm\nu jj$  (left) and  $\ell^\pm\nu\ell^\pm\nu\ell^\pm\nu$  channels (right) as a function of the  $m_{jj}$  for the left plot. Signal and backgrounds are normalized to the expected number of events after the fit. The uncertainty band includes both the statistical and systematic uncertainties as obtained by the fit. In the post-fit plots, the  $WWW$  tags have been replaced with  $VVV$  as these results are presented with the  $WVZ$  analysis.

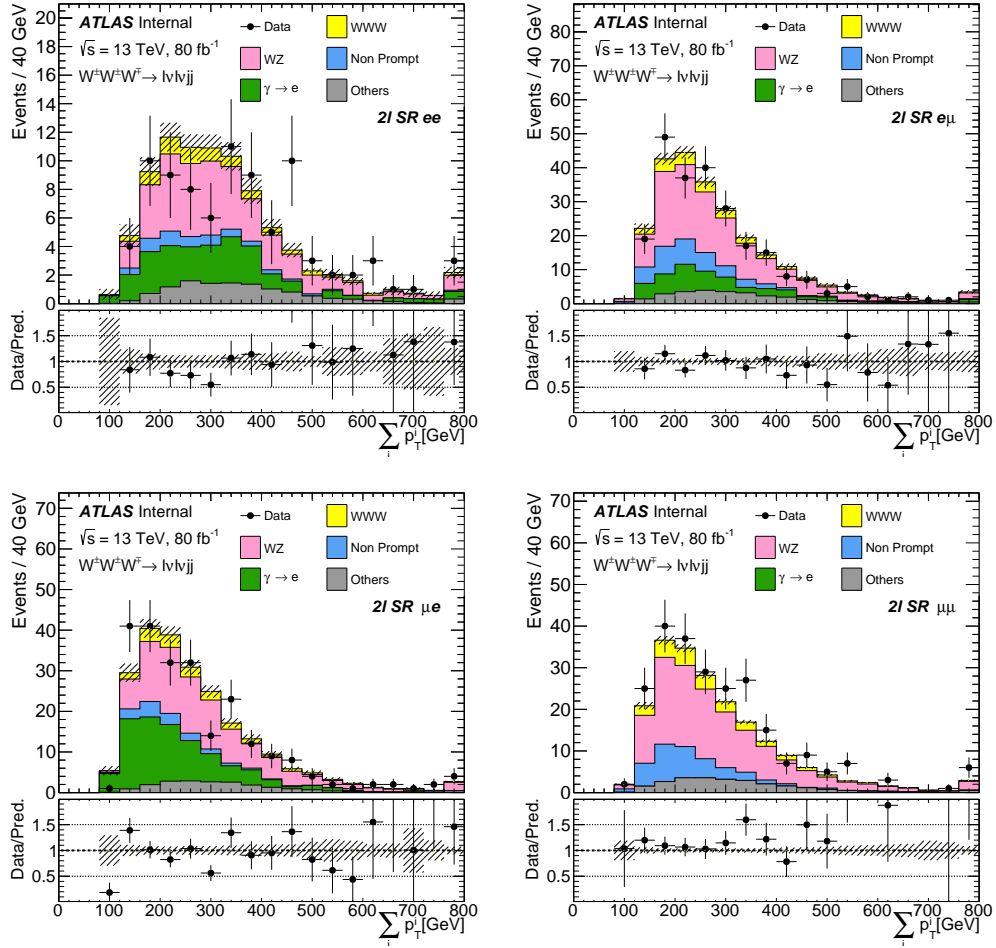


Figure 12.4: The observed data are compared to the signal plus background model in the  $ee$  (top left),  $e\mu$  (top right),  $\mu e$  (bottom left),  $\mu\mu$  (bottom right) signal region for the  $\ell^\pm\nu\ell^\pm jj$  channel as a function of the scalar sum of all particles  $p_T$ . The uncertainty band is statistical uncertainty only.

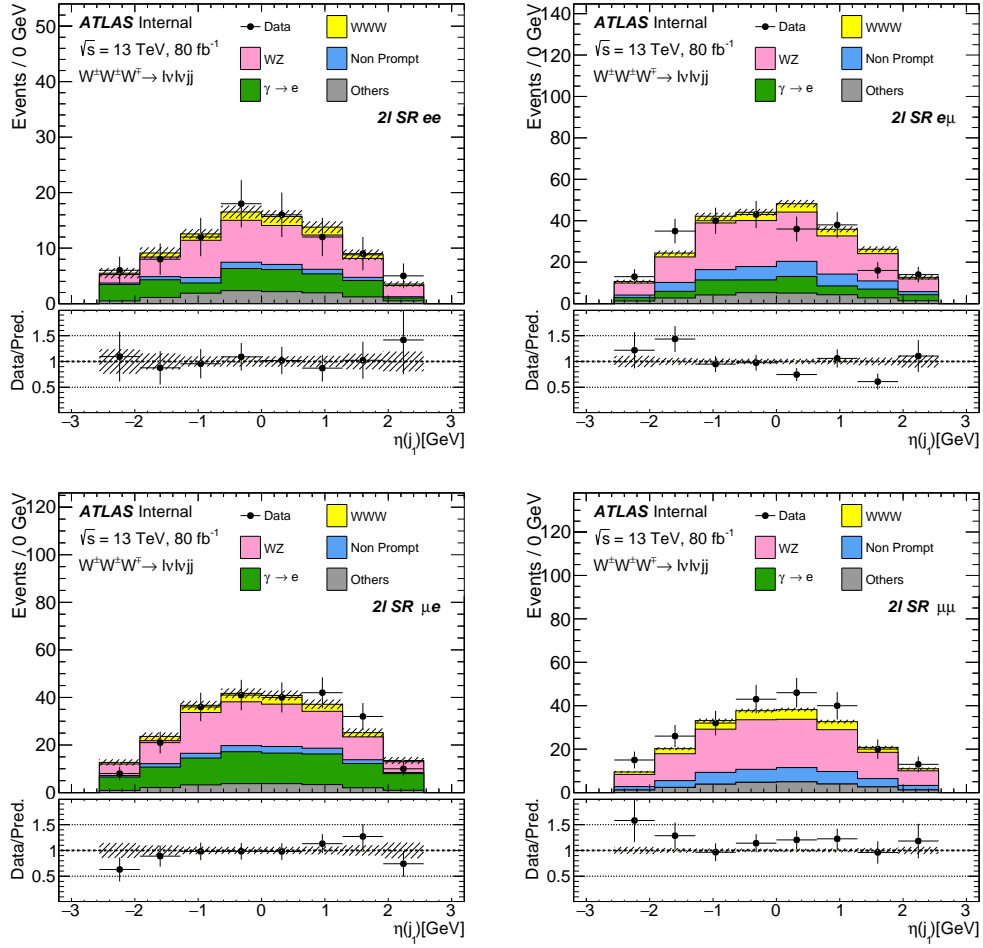


Figure 12.5: The observed data are compared to the signal plus background model in the  $ee$  (top left),  $e\mu$  (top right),  $\mu e$  (bottom left),  $\mu\mu$  (bottom right) signal region for the  $\ell^\pm\nu\ell^\pm\nu jj$  channel as a function of the leading jet  $\eta$ . The uncertainty band is statistical uncertainty only.

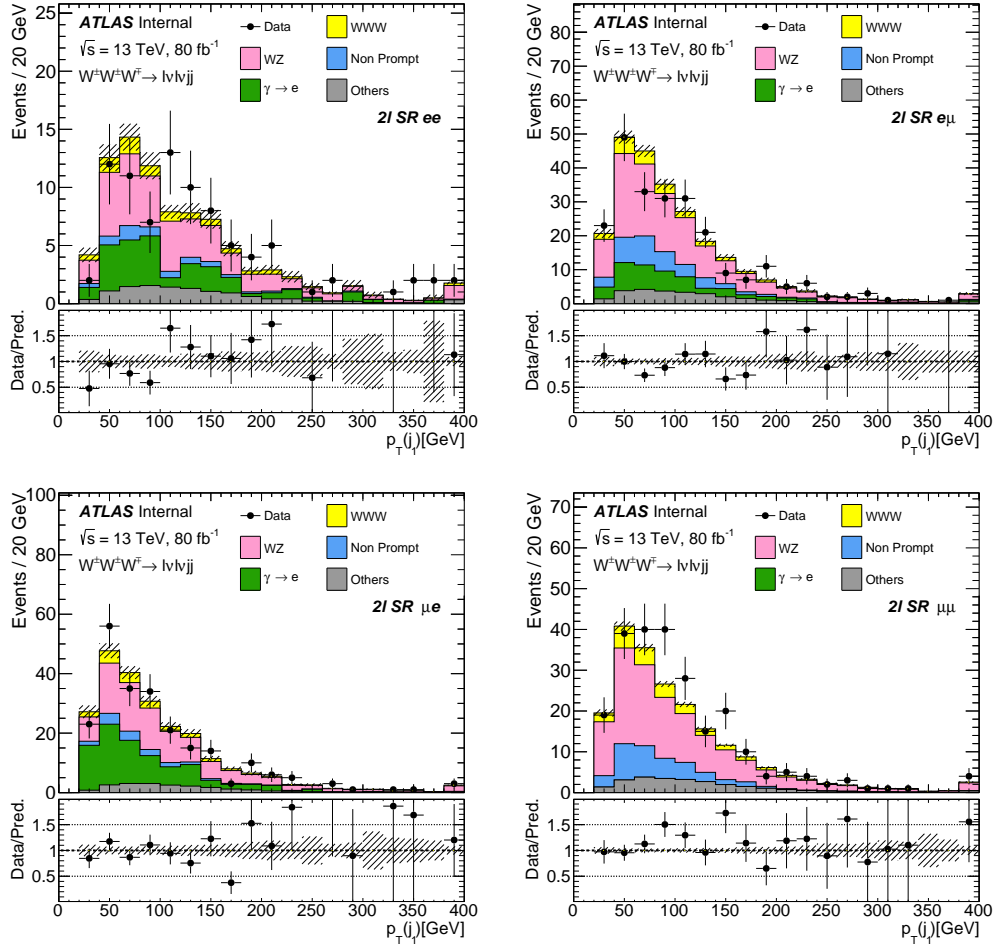


Figure 12.6: The observed data are compared to the signal plus background model in the  $ee$  (top left),  $e\mu$  (top right),  $\mu e$  (bottom left),  $\mu\mu$  (bottom right) signal region for the  $\ell^\pm\nu\ell^\pm\nu jj$  channel as a function of the leading jet  $p_T$ . The uncertainty band is statistical uncertainty only.

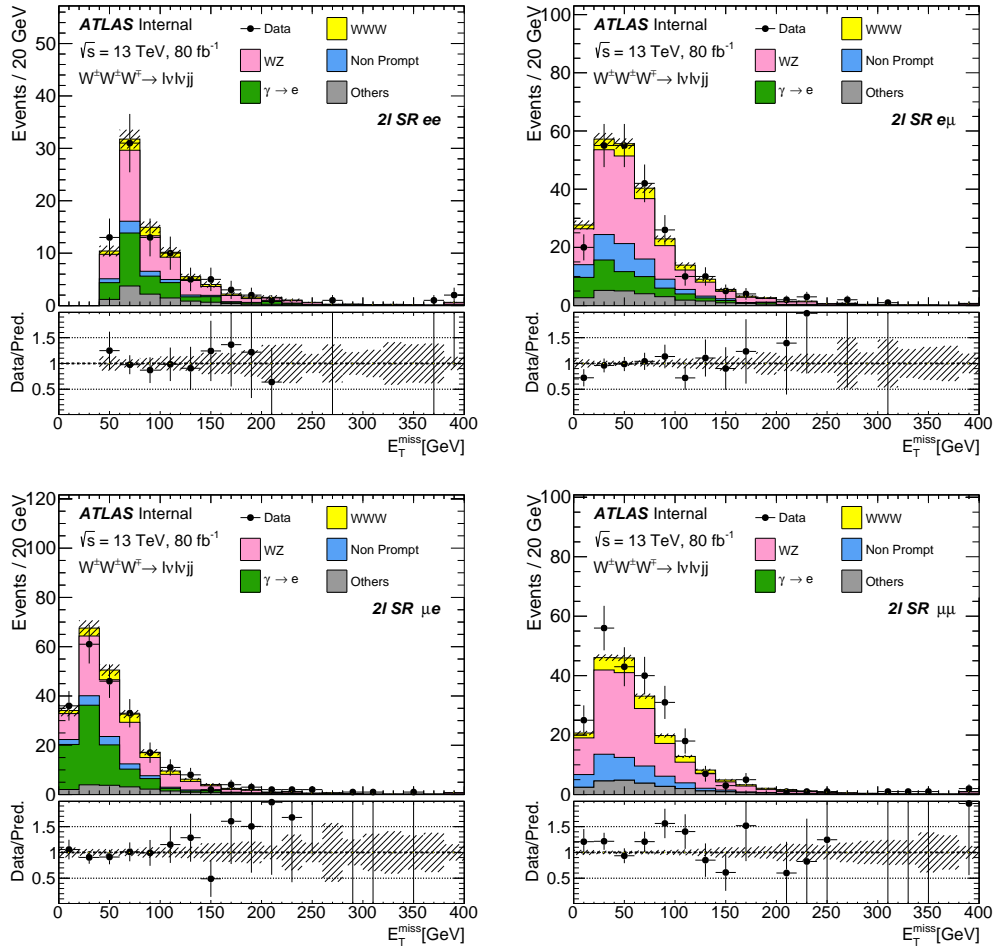


Figure 12.7: The observed data are compared to the signal plus background model in the  $ee$  (top left),  $e\mu$  (top right),  $\mu e$  (bottom left),  $\mu\mu$  (bottom right) signal region for the  $\ell^\pm \nu \ell^\pm \nu jj$  channel as a function of the  $E_T^{\text{miss}}$ . The uncertainty band is statistical uncertainty only.



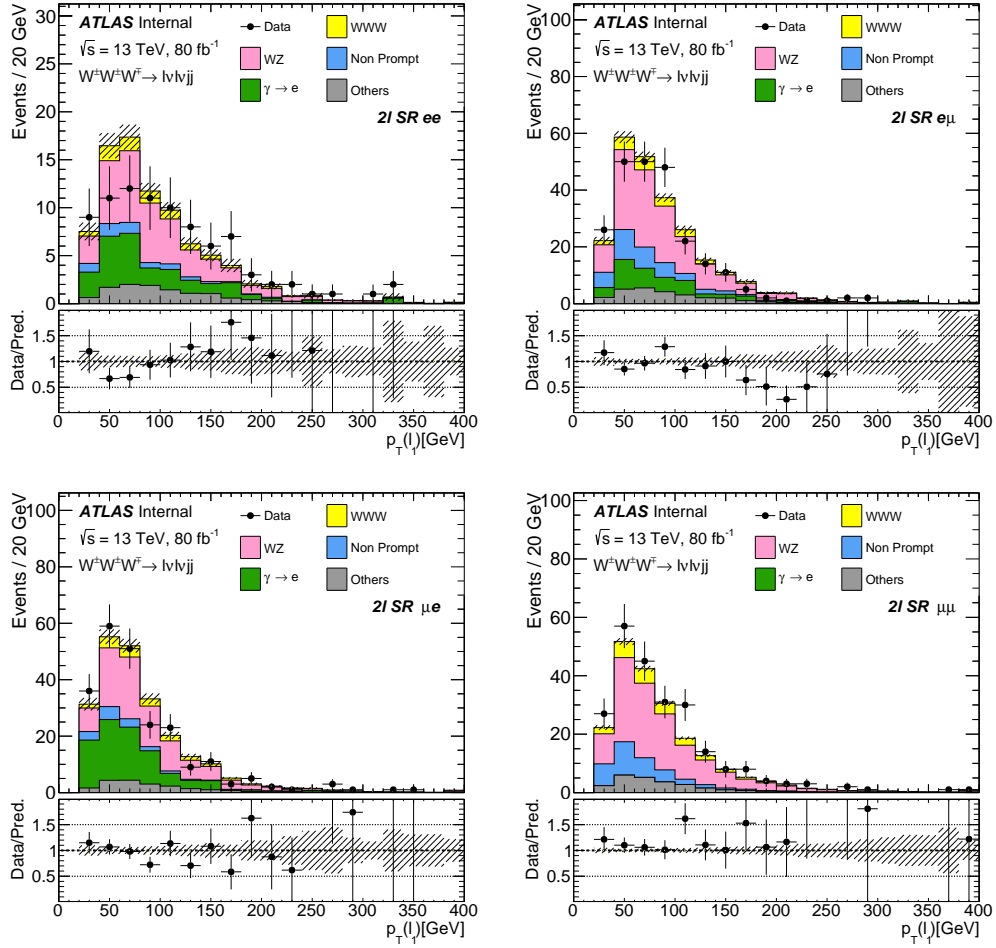


Figure 12.8: The observed data are compared to the signal plus background model in the  $ee$  (top left),  $e\mu$  (top right),  $\mu e$  (bottom left),  $\mu\mu$  (bottom right) signal region for the  $\ell^\pm\nu\ell^\pm\nu jj$  channel as a function of the leading lepton  $p_T$ . The uncertainty band is statistical uncertainty only.

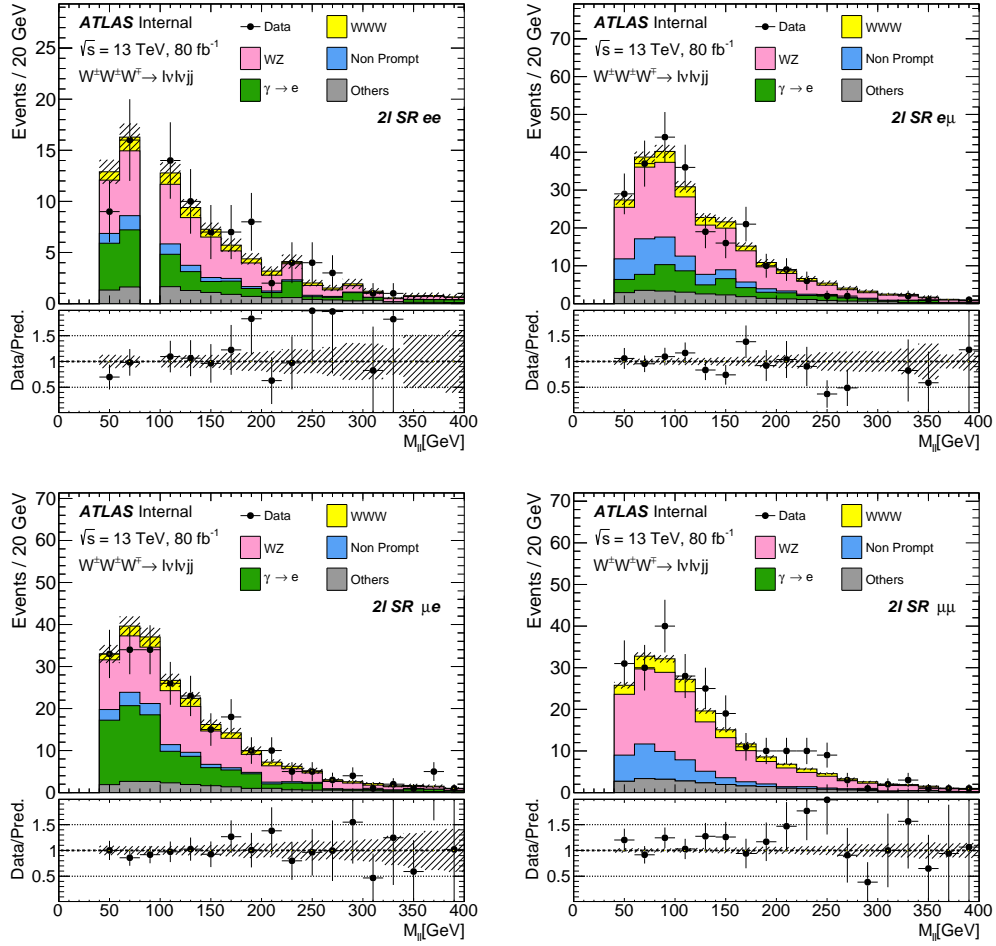


Figure 12.9: The observed data are compared to the signal plus background model in the  $ee$  (top left),  $e\mu$  (top right),  $\mu e$  (bottom left),  $\mu\mu$  (bottom right) signal region for the  $\ell^\pm\nu\ell^\pm\nu jj$  channel as a function of the leading lepton  $m_{l\ell}$ . The uncertainty band is statistical uncertainty only.

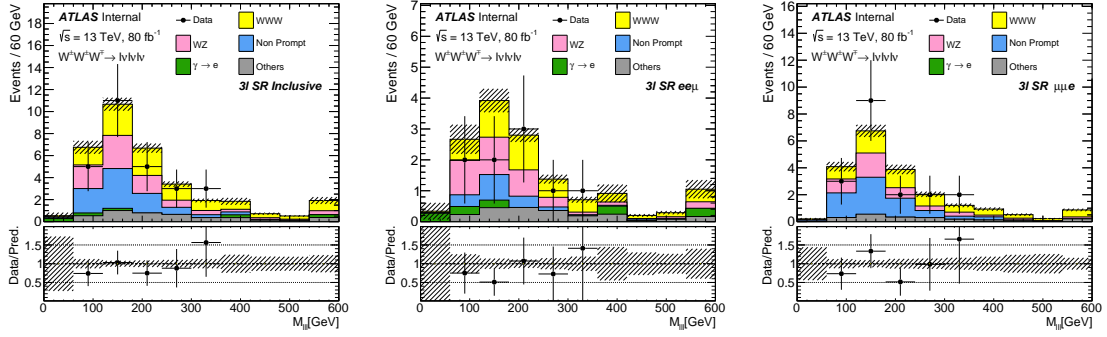


Figure 12.10: The observed data are compared to the signal plus background model in the *inclusive* (left),  $ee\mu$  (middle),  $\mu\mu e$  (right) signal region for the  $\ell^\pm\nu\ell^\pm\nu\ell^\mp\nu$  channel as a function of the leading lepton  $m_{ll}$ . The uncertainty band is statistical uncertainty only.

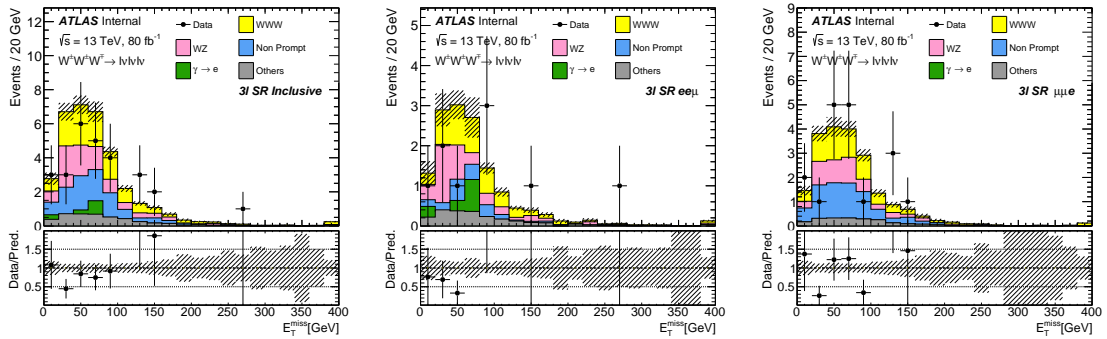


Figure 12.11: The observed data are compared to the signal plus background model in the *inclusive* (left),  $ee\mu$  (middle),  $\mu\mu e$  (right) signal region for the  $\ell^\pm\nu\ell^\pm\nu\ell^\mp\nu$  channel as a function of the  $E_T^{\text{miss}}$ . The uncertainty band is statistical uncertainty only.

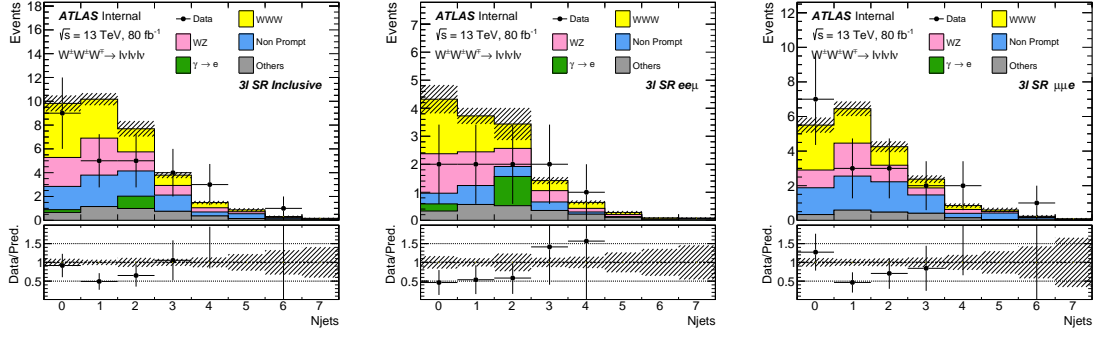


Figure 12.12: The observed data are compared to the signal plus background model in the *inclusive* (left),  $ee\mu$  (middle),  $\mu\mu e$  (right) signal region for the  $\ell^\pm\nu\ell^\pm\nu\ell^\mp\nu$  channel as a function of the  $N_{\text{jets}}$ . The uncertainty band is statistical uncertainty only.

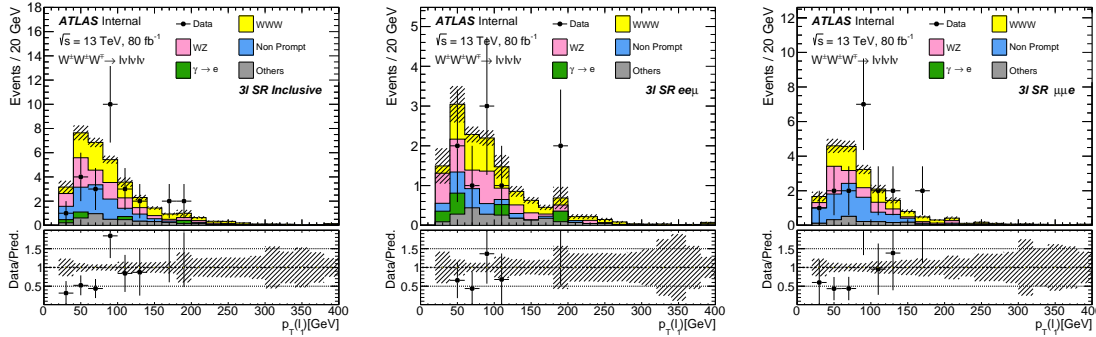


Figure 12.13: The observed data are compared to the signal plus background model in the *inclusive* (left),  $ee\mu$  (middle),  $\mu\mu e$  (right) signal region for the  $\ell^\pm\nu\ell^\pm\nu\ell^\mp\nu$  channel as a function of the leading lepton  $p_T$ . The uncertainty band is statistical uncertainty only.

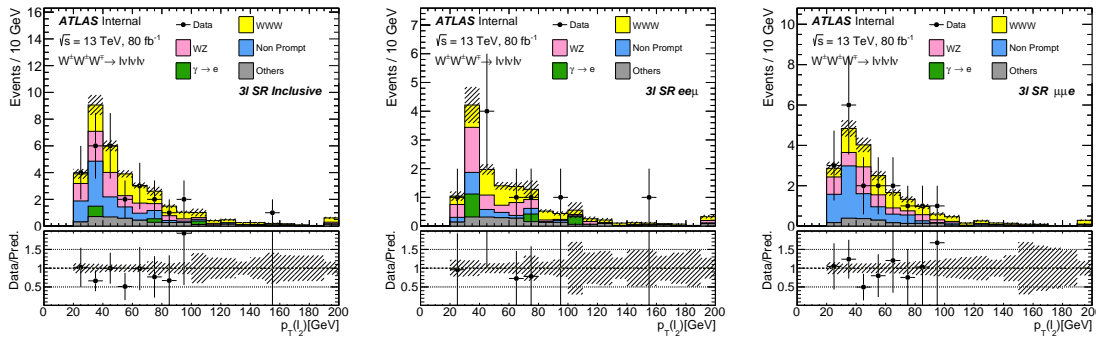


Figure 12.14: The observed data are compared to the signal plus background model in the *inclusive* (left),  $ee\mu$  (middle),  $\mu\mu e$  (right) signal region for the  $\ell^\pm\nu\ell^\pm\nu\ell^\mp\nu$  channel as a function of the sub-leading lepton  $p_T$ . The uncertainty band is statistical uncertainty only.

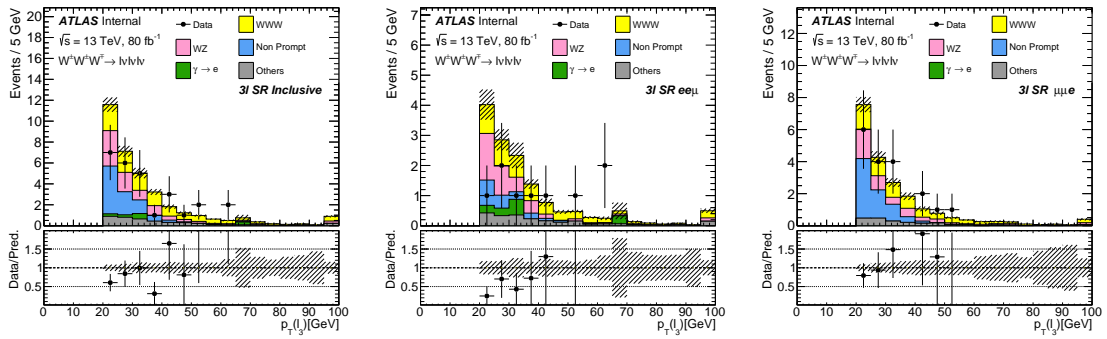


Figure 12.15: The observed data are compared to the signal plus background model in the *inclusive* (left), *eeμ* (middle), *μμe* (right) signal region for the  $\ell^\pm \nu \ell^\pm \nu \ell^\pm \nu$  channel as a function of the 3<sup>rd</sup> lepton  $p_T$ . The uncertainty band is statistical uncertainty only.

## 12.2 $WVZ$ Results

The  $WVZ$  analysis has been conducted as explained in Chapter 10. After the pre-selection cuts are applied, the resulting post-fit yields are shown in Table 12.3. In the post-fit yields, there is good agreement between data and predictions. Figures 12.16 and 12.17 show the  $WVZ$  BDT distributions for  $3\ell$  and  $4\ell$  respectively.  $3\ell + 3\text{jet}$  and  $4\ell$  different flavor BDT discriminants have the highest sensitivity.

	$4\ell\text{-DF}$	$4\ell\text{-SF-Z}$	$4\ell\text{-SF-noZ}$	$3\ell\text{-1j}$	$3\ell\text{-2j}$	$3\ell\text{-3j}$
$WVZ$	$8.4 \pm 3.4$	$4.4 \pm 1.7$	$9 \pm 4$	$55 \pm 22$	$75 \pm 30$	$73 \pm 29$
$WZ$	$1.19 \pm 0.14$	–	$1.10 \pm 0.15$	$2580 \pm 80$	$1840 \pm 60$	$1120 \pm 50$
$ZZ$	$6.7 \pm 0.5$	$935 \pm 28$	$310 \pm 10$	$344 \pm 12$	$183 \pm 13$	$100 \pm$
$t\bar{t}Z$	$5.1 \pm 0.5$	$0.55 \pm 0.08$	$4.5 \pm 0.5$	$7.7 \pm 1.1$	$22.6 \pm 2.5$	$82 \pm 8$
$tWZ$	$1.9 \pm 0.4$	$0.23 \pm 0.10$	$1.6 \pm 0.4$	$4.2 \pm 0.9$	$11.2 \pm 2.2$	$20 \pm 4$
Nonprompt	–	–	$0.18 \pm 0.12$	$140 \pm 60$	$80 \pm 30$	$60 \pm 24$
$\gamma$ conv.	–	–	–	$42 \pm 8$	$32 \pm 7$	$9.6 \pm 3.4$
Other	$0.4 \pm 0.4$	$1.8 \pm 1.1$	$1.0 \pm 0.7$	$200 \pm 16$	$182 \pm 16$	$120 \pm 10$
Total	$23.7 \pm 3.4$	$942 \pm 27$	$329 \pm 10$	$3370 \pm 60$	$2420 \pm 1590$	$40 \pm 160$
Data	28	912	360	3351	2438	1572

Table 12.3: Post-fit background, signal and observed yields for the three-lepton and four-lepton channels of  $WVZ$  analysis. Uncertainties on the predictions include both statistical and systematic uncertainties added in quadrature; correlations among systematic uncertainties are taken into account in the calculation of the total.

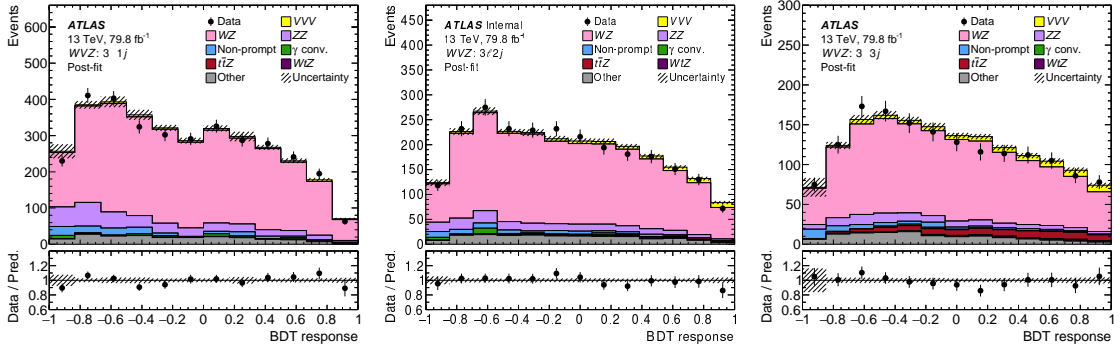


Figure 12.16: The observed data are compared to the signal plus background model in the  $3\ell + 1\text{jet}$  (left),  $3\ell + 2\text{jet}$  (middle),  $3\ell + 3 + \text{jet}$  (right) signal regions for the  $WVZ$  analysis as a function of the BDT discriminant. Signal and backgrounds are normalized to the expected number of events after the fit. The uncertainty band includes both the statistical and systematic uncertainties as obtained by the fit. In the post-fit plots, the  $WVZ$  tags have been replaced with  $VVV$  as these results are presented with the  $WWW$  analysis.

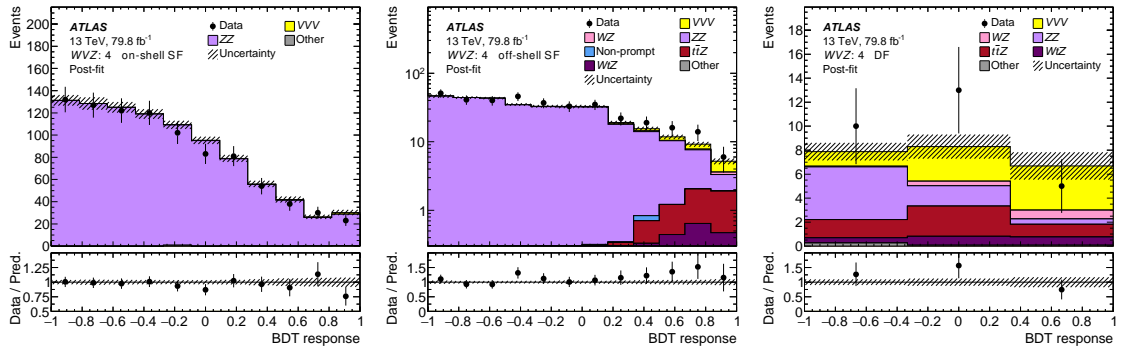


Figure 12.17: The observed data are compared to the signal plus background model in the  $4\ell$  same-flavor on shell (left),  $4\ell$  same-flavor off shell (middle),  $4\ell$  different-flavor signal region (right) for the  $WZ$  analysis as a function of the BDT discriminant. Signal and backgrounds are normalized to the expected number of events after the fit. The uncertainty band includes both the statistical and systematic uncertainties as obtained by the fit. In the post-fit plots, the  $WZ$  tags have been replaced with  $VW$  as these results are presented with the  $WW$  analysis.

## 12.3 Fitted Results

The first evidence for the production of three  $W$  bosons ( $W^\pm W^\pm W^\mp$ ) using  $79.8 \text{ fb}^{-1}$  of  $pp$  collision data at a center-of-mass energy of 13 TeV is obtained using a log-likelihood fit as explained in Chapter 11.

In the  $\ell^\pm \nu \ell^\pm \nu jj$  signal region, due to the slight excess of data around the  $W$  pole mass, the  $\mu$  value is measured to be  $2.24_{-0.57}^{+0.62}$  and the background-only hypothesis is rejected by  $4.3\sigma$ . In the  $\ell^\pm \nu \ell^\pm \nu \ell^\mp \nu$  signal region, due to the deficit observed in data, the  $\mu$  value is measured to be  $0.47_{-0.47}^{+0.54}$  and the background-only hypothesis is rejected with  $1\sigma$ . When both regions are combined together in the fit, the  $\mu$  value is measured to be  $1.37_{-0.42}^{+0.46}$  and the background hypothesis is rejected with  $3.33\sigma$ .

The fiducial cross sections are measured to be:

$$\sigma_{\text{Observed}}(\ell^\pm \nu \ell^\pm \nu jj \text{ Fiducial}) = 1.82_{-0.32}^{+0.33}(\text{stat.})_{-0.36}^{+0.40}(\text{syst.}) \text{ fb}, \quad (12.1)$$

$$\sigma_{\text{Observed}}(\ell^\pm \nu \ell^\pm \nu \ell^\mp \nu \text{ Fiducial}) = 0.30_{-0.052}^{+0.054}(\text{stat.})_{-0.058}^{+0.065}(\text{syst.}) \text{ fb}, \quad (12.2)$$

and the total inclusive  $W^\pm W^\pm W^\mp$  cross-section is measured to be:

$$\sigma_{\text{Observed}}(\text{Total}) = 690_{-120}^{+125}(\text{stat.})_{-135}^{+150}(\text{syst.}) \text{ fb}. \quad (12.3)$$

The  $WWW$  signal regions are combined with the  $WVZ$  signal regions to obtain a final combined fit. For this combined fit, the  $\mu$  is assumed to be the same for the  $W^\pm W^\pm W^\mp$  and  $WVZ$  processes. The  $\mu$  value is measured to be  $1.38_{-0.37}^{+0.39}$ , and the background-only hypothesis for the production of three massive gauge bosons  $VVV$  is rejected at  $4.0\sigma$ .

Results of the individual fits of the regions and the combined fit can be found in Table 12.5 and Figure 12.19. Figure 12.20 shows the combination of  $W^\pm W^\pm W^\mp$  and  $WVZ$  signal regions binned in  $\log(S/B)$ , which shows good data and MC agreement in all bins when  $\mu$  is set to the observed combined  $\mu$ .

Systematic uncertainties for the final combined fit can be found in Table 12.4. The systematic ranking for this fit is also provided in Figure 12.18. It is observed that the fake factor (non-prompt rate) uncertainties and  $WZ$  normalization uncertainty have the largest impact. Overall the data-driven, experimental, and theory uncertainties have a similar impact on the combined fit.



Uncertainty source	$\Delta\mu$
Data-driven	+0.14 -0.15
Experimental	+0.11 -0.09
Statistical	+0.05 -0.05
Theory	+0.16 -0.13
Total systematic uncertainty	+0.30 -0.27

Table 12.4: Summary of the effects of the most important groups of systematic uncertainties on  $\mu_{VVV}$ .

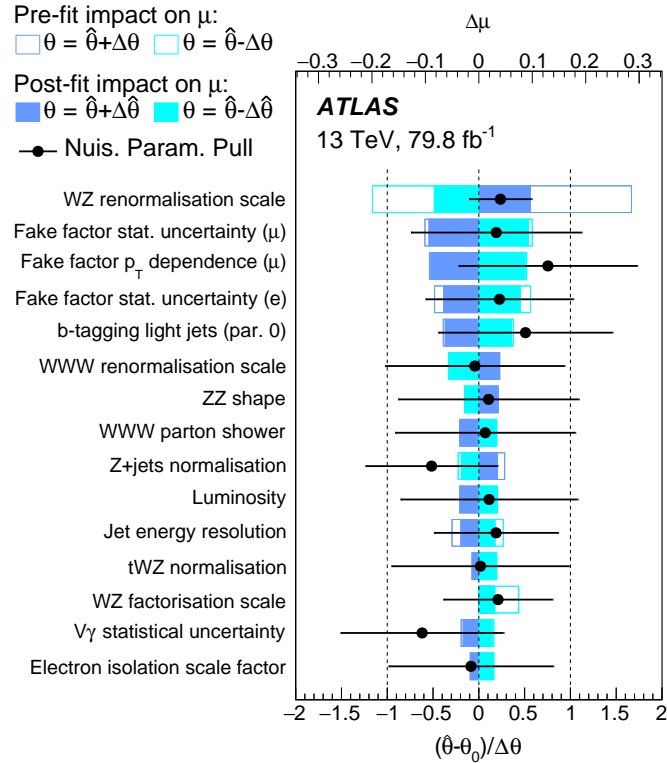


Figure 12.18: Ranking of the nuisance parameters according to their post-fit impact on the signal strength for the combined  $VVV$  fit to data.

Decay channel	Significance	
	Observed	Expected
<i>WWW</i> combined	$3.3\sigma$	$2.4\sigma$
<i>WWW</i> $\rightarrow \ell\nu\ell\nu qq$	$4.3\sigma$	$1.7\sigma$
<i>WWW</i> $\rightarrow \ell\nu\ell\nu\ell\nu$	$1.0\sigma$	$2.0\sigma$
<i>WVZ</i> combined	$2.9\sigma$	$2.0\sigma$
<i>WVZ</i> $\rightarrow \ell\nu qq\ell\ell$	–	$1.0\sigma$
<i>WVZ</i> $\rightarrow \ell\nu\ell\nu\ell\ell/qq\ell\ell\ell$	$3.5\sigma$	$1.8\sigma$
<i>VVV</i> combined	$4.0\sigma$	$3.1\sigma$

Table 12.5: Expected and observed significances with respect to the SM background-only hypothesis for the four *VVV* channels entering the combined fit. The observed significance is not quoted if the best-fit value of  $\mu$  is negative.

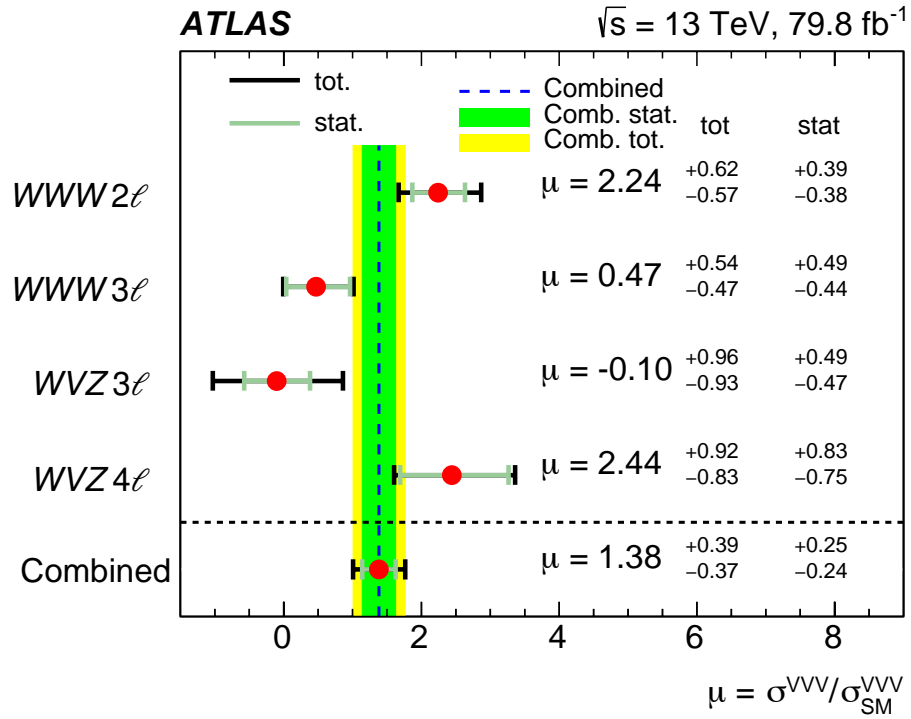


Figure 12.19: Extracted signal strengths  $\mu$  for the four analysis regions and combination.

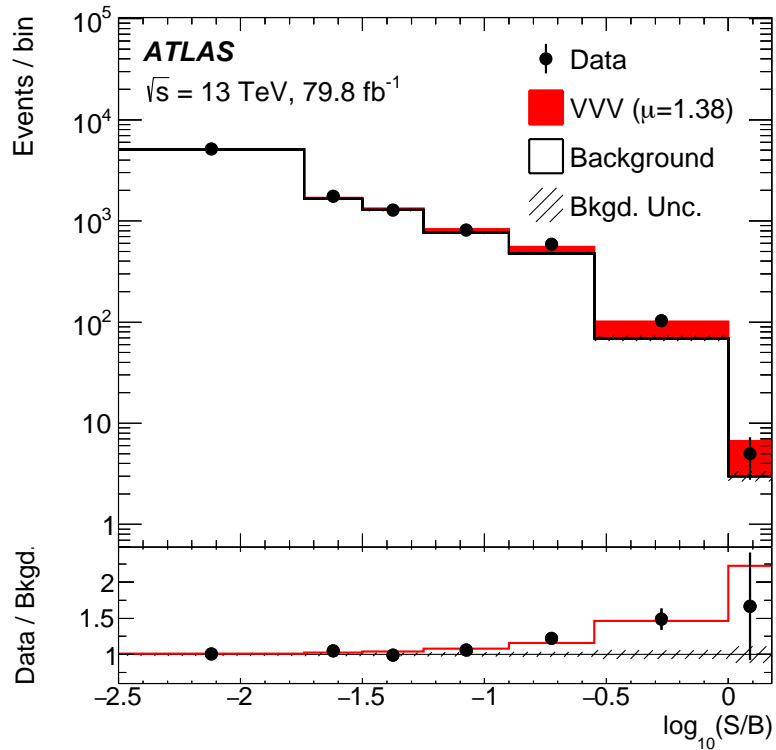


Figure 12.20: Event yields as a function of  $\log_{10}(S/B)$  for data, background B and the signal S. Events in all 11 signal regions are included, and the predicted background yield is obtained from the global signal-plus-background fit. The tri-boson signal is shown for the best-fit value ( $\mu = 1.38$ ). The hatched band corresponds to the systematic uncertainties, and the statistical uncertainties are represented by the error bars on the data points.

## 12.4 Anomalous Quartic Gauge Couplings

The results obtained in the search for the  $W^\pm W^\pm W^\mp$  production can also be used to test physics beyond the SM using effective field theories as explained in Section 2.3. aQGCs were measured in the 8 TeV analysis [1].

The aQGCs tend to modify lepton and jet kinematics. As a result, the kinematic distributions of the  $W^\pm W^\pm W^\mp$  signals would be effected by the aQGCs. Figure 12.21 shows the  $m_T^{3\ell}$  (invariant transverse mass of three leptons) of the  $\ell^\pm \nu \ell^\pm \nu \ell^\mp \nu$  signal region and the  $\Sigma p_T$  (scalar sum of all particle  $p_T$ s) in the  $\ell^\pm \nu \ell^\pm \nu jj$  signal region. Both distributions are sensitive to aQGC, but signal acceptances are found to be consistent with the one obtained for the SM sample within 20%. As shown in these diagrams, the 8 TeV analysis is statistically limited, and these kinematic distributions are not used in the final fit. Instead, the final limits are set using a cut-and-count method.

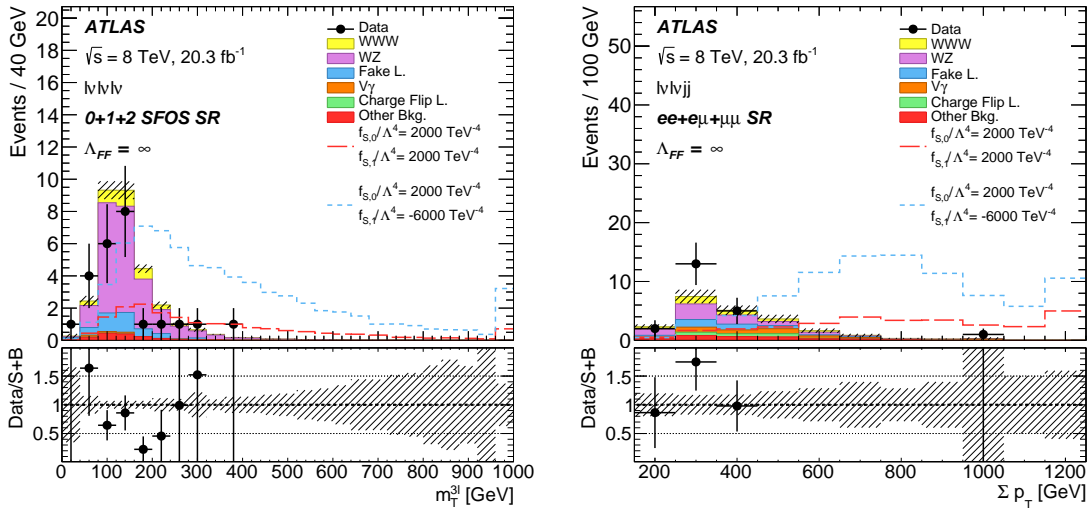


Figure 12.21: The distribution of  $m_T^{3\ell}$  (invariant transverse mass of three leptons) for the  $\ell^\pm \nu \ell^\pm \nu \ell^\mp \nu$  channel (left) and the distribution of  $\Sigma p_T$  (scalar sum of all particle  $p_T$ s) for the  $\ell^\pm \nu \ell^\pm \nu jj$  channel (right) as observed in the data (dots with error bars indicating the statistical uncertainties) and as expected from SM signal and background processes. The ratios between the observed numbers of events in data and the expected SM signal plus background contributions are shown in the lower panels. The dashed bands result from the systematic uncertainties on the sum of the signal plus background contributions. The “other backgrounds” contain prompt leptons and are estimated from MC. Contributions from aQGCs are also shown, assuming the non-unitarized case ( $\Lambda = \infty$ ) and two different sets of  $\frac{f_{S0}}{\Lambda^4}$  and  $\frac{f_{S1}}{\Lambda^4}$  configurations ( $\frac{f_{S0}}{\Lambda^4} = 2000 \text{ TeV}^{-4}$ ,  $\frac{f_{S1}}{\Lambda^4} = 2000 \text{ TeV}^{-4}$  and  $\frac{f_{S0}}{\Lambda^4} = 2000 \text{ TeV}^{-4}$ ,  $\frac{f_{S1}}{\Lambda^4} = -6000 \text{ TeV}^{-4}$ ). The highest bin also includes events falling out of the range shown.

Limits on the aQGCs are set by modifying the likelihood fit given in Equation 11.2. The number of expected events in the likelihood function is modified by the following equation:

$$N_{sig} = w_0 + w_1 \left(\frac{f_{S0}}{\Lambda^4}\right)^2 + w_2 \left(\frac{f_{S1}}{\Lambda^4}\right)^2 + 2w_3 \left(\frac{f_{S0}}{\Lambda^4}\right) + 2w_4 \left(\frac{f_{S1}}{\Lambda^4}\right) + 2w_5 \left(\frac{f_{S0}}{\Lambda^4}\right) \left(\frac{f_{S1}}{\Lambda^4}\right) + \sum_i^{BG} N_i^{BG}, \quad (12.4)$$

where  $w_i$  ( $i = 0-5$ ) are functional parameters that predicts the expect number of  $W^\pm W^\pm W^\mp$  events as a function of aQGC parameters ( $\frac{f_{S0}}{\Lambda^4}$  and  $\frac{f_{S1}}{\Lambda^4}$ ). These aQGC parameters replace the  $\mu$  value of the nominal fit.

The aQGC studies were conducted using the  $\frac{f_{s,0}}{\Lambda^4}$  and  $\frac{f_{s,1}}{\Lambda^4}$  parameters with different form-factor cutoff scales of  $\Lambda = \infty, 0.5, 1, 2, 3$  TeV. Figure 12.22 shows the two-dimensional 95%  $CL_S$  confidence intervals given by the aQGC parameters that are extracted using the fit-method explained in Section 11. The calculated 95%  $CL_S$  upper limits are summarized in Table 12.6.

$\Lambda_{FF}$ [TeV]	Expected CI [ $\times 10^4 \text{ TeV}^{-4}$ ]		Observed CI [ $\times 10^4 \text{ TeV}^{-4}$ ]	
	$f_{s,0}$	$f_{s,1}$	$f_{s,0}$	$f_{s,1}$
0.5	[-0.79, 0.89]	[-1.06, 1.27]	[-0.74, 0.86]	[-0.99, 1.20]
1	[-0.36, 0.41]	[-0.52, 0.60]	[-0.34, 0.40]	[-0.48, 0.58]
2	[-0.22, 0.25]	[-0.33, 0.39]	[-0.20, 0.24]	[-0.29, 0.36]
3	[-0.19, 0.22]	[-0.29, 0.36]	[-0.16, 0.21]	[-0.25, 0.33]
$\infty$	[-0.16, 0.19]	[-0.25, 0.30]	[-0.13, 0.18]	[-0.21, 0.27]

Table 12.6: Expected and observed 95% CL intervals on  $f_{s,0}$  ( $f_{s,1}$ ) for different  $\Lambda_{FF}$  values, assuming  $f_{s,1}$  ( $f_{s,0}$ ) to be zero at 8 TeV.

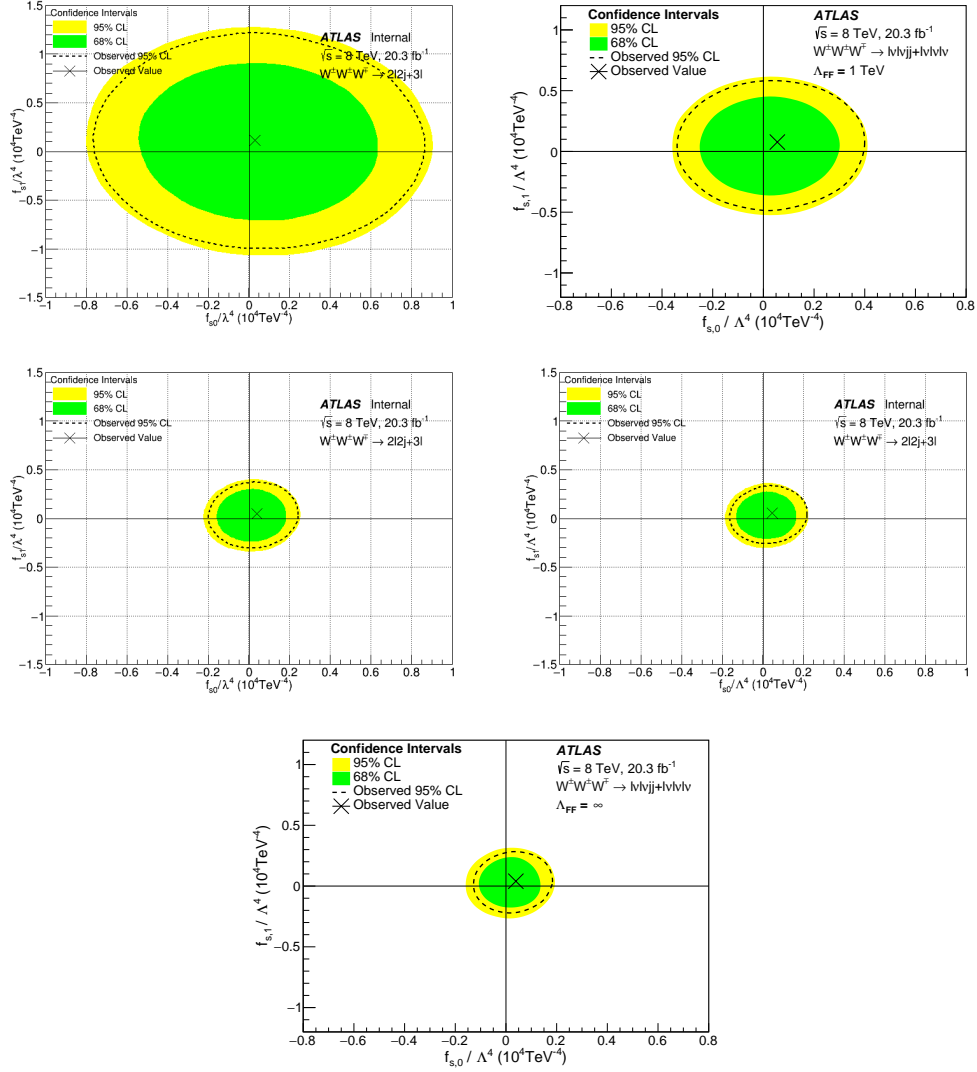


Figure 12.22: Expected 68% and 95% CL contours for  $f_{s,1}$  vs  $f_{s,0}$  compared to the observed 95% CL contour and the observed best-fit values at 8 TeV for cases when  $\Lambda_{FF} = 0.5$  TeV (top left),  $\Lambda_{FF} = 1$  TeV (top right),  $\Lambda_{FF} = 2$  TeV (middle left),  $\Lambda_{FF} = 3$  TeV (middle right), and  $\Lambda_{FF} = \infty$  (bottom).

## 12.5 Future Prospects

A new effort is ongoing to expand the  $WWW$  analysis to include the 2018 ATLAS dataset (adding up to a total integrated luminosity of  $\sim 140 \text{ fb}^{-1}$ ). The boost in the total integrated luminosity is expected to boost the expected significance by a factor of  $\sim 1.3$  ( $2.4 \sigma \rightarrow \sim 3 \sigma$ ). In order to boost the significance even more, a few changes are proposed to reduce the  $WZ$  background and its uncertainty.

A truth study has been conducted on the  $WZ$  background to understand why a lepton in the  $WZ$  background is not properly reconstructed and has identified three major causes:

- The unreconstructed lepton has a small  $p_T$  or its trajectory lies outside the detector coverage ( $\approx 50\%$ ).
- The  $Z$  boson decays into two  $\tau$  leptons and one of the  $\tau$  lepton's decay hadronically resulting in an undetected lepton ( $\approx 15\%$ ).
- The unreconstructed lepton overlaps with another particle and is discarded due to overlap removal ( $\approx 20\%$ ).

A BDT is proposed to recover the unreconstructed leptons that have a small  $p_T$  or that lie outside the detector coverage. This BDT will use tracks that are not associated with other particles, all lepton information and calorimeter clusters from forward calorimeters. Initial BDT tests done without tracks and calorimeter clusters showed a minor reduction ( $\approx 20\%$ ) of the  $WZ$  background without any impact on the  $WWW$  signal. Up to 50% reduction of the  $WZ$  background could be expected when the BDT is trained with full track and calorimeter information.

In both 13 TeV and 8 TeV analysis,  $\tau$  leptons were ignored. In this new iteration, it is planned to tag  $\tau$  leptons. It is expected that this approach will increase the  $WWW$  signal rate and reduce the contributions from the  $WZ \rightarrow \ell \nu \tau \nu \tau \nu$  decays.

In the new iteration, the overlap procedure on the leptons will also be revised to recover the leptons lost due to the overlap removal procedure, providing a small reduction on the  $WZ$  background.

There are additional changes proposed. One major proposal is to change the  $WZ$  background to a data-driven one and reduce the  $WZ$  normalization uncertainty. Another proposed change is to include aQGC studies and set limits on the aQGCs. A considerable improvement of the aQGC limits is expected due to the increase in total integrated luminosity and center-of-mass energy. With all the proposed changes, it could be expected to reject the background only hypothesis by  $\sim 4\sigma$ .

## CHAPTER 13

### Summary

The first evidence for the production of three  $W$  bosons ( $W^\pm W^\pm W^\mp$ ) has been presented in this thesis using  $79.8\text{fb}^{-1}$  of  $pp$  collision data at a center-of-mass energy of 13 TeV recorded by the ATLAS detector at the LHC between 2015 and 2017. The search is conducted using the semi-leptonic ( $W^\pm W^\pm W^\mp \rightarrow \ell^\pm \nu \ell^\pm \nu jj$ ) and fully-leptonic ( $W^\pm W^\pm W^\mp \rightarrow \ell^\pm \nu \ell^\pm \nu \ell^\mp \nu$ ) channels where  $\ell = e, \mu$ . The semi-leptonic channel is examined in a region where the two same-sign  $W$  bosons decay leptonically while the third  $W$  boson decays hadronically, and the fully-leptonic channel is examined in a region where all three  $W$  bosons decay leptonically and without same-flavor opposite-sign lepton pairs.

In the semi-leptonic channel, a total of 798 candidate events are observed in data, to be compared with the prediction of  $\sim 68$  signal events and  $\sim 700$  background events. In the fully-leptonic channel, a total of 27 candidate events are observed in data, to be compared with the prediction of  $\sim 11$  signal events and  $\sim 23$  background events. The first evidence for  $W^\pm W^\pm W^\mp$  production is observed by rejecting the background-only hypothesis with an observed (expected) significance of 3.3 standard deviations (2.4 standard deviations). The fiducial  $W^\pm W^\pm W^\mp$  cross section is measured to be  $1.82^{+0.33}_{-0.32}(\text{stat.})^{+0.40}_{-0.36}(\text{syst.})$  fb for the  $\ell^\pm \nu \ell^\pm \nu jj$  channel and  $0.30^{+0.054}_{-0.052}(\text{stat.})^{+0.065}_{-0.058}(\text{syst.})$  fb in the  $\ell^\pm \nu \ell^\pm \nu \ell^\mp \nu$  channel. The inclusive  $W^\pm W^\pm W^\mp$  production cross section is found to be  $690^{+125}_{-120}(\text{stat.})^{+150}_{-135}(\text{syst.})$  fb.

The  $W^\pm W^\pm W^\mp$  search results are combined with the  $WWZ$  and  $WZZ$  search results using a binned maximum-likelihood fit. The first evidence for the production of three massive gauge bosons is observed with an observed (expected) significance of 4.0 standard deviations (3.1 standard deviations). The results have been published in Ref. [2]. The measured inclusive cross sections have been added to the list of SM cross-sections measured by the ATLAS Collaboration, as shown in Figure 13.1.



### Standard Model Total Production Cross Section Measurements Status: March 2019

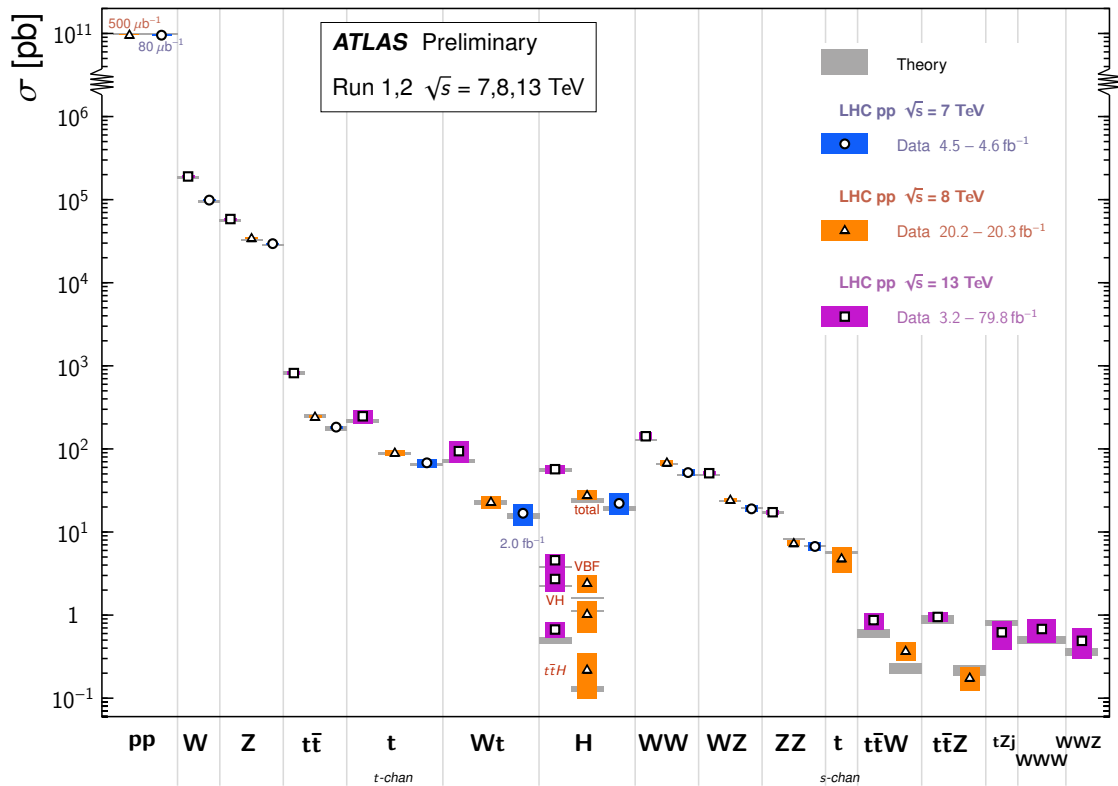


Figure 13.1: Summary of several Standard Model total production cross section measurements conducted at the ATLAS experiment, corrected for leptonic branching fractions, compared to the corresponding theoretical expectations[71].

# APPENDIX

## Detailed List of MC Samples Used

MC Type	MC IDs	Extra Info	Found in WVZ	MC16 a Tag	MC16 d Tag
WZ	364253	lllv	yes	e5916_s3126_r9364_r9315_p3387	e5916_e5984_s3126_r10201_r10210_p3387
	364284	lllvjj	yes	e6055_e5984_s3126_r9364_r9315_p3387	e6055_e5984_s3126_r10201_r10210_p3495
	364255	lvvv	no	e5916_s3126_r9364_r9315_p3387	e5916_e5984_s3126_r10201_r10210_p3387
ZZ	364283	lllljj EW6	no	e6055_e5984_s3126_r9364_r9315_p3387	e6055_e5984_s3126_r10201_r10210_p3401
	364250	llll	yes	e5894_s3126_r9364_r9315_p3387	e5894_e5984_s3126_r10201_r10210_p3387
ttZ	410218-410220	ttll	yes	e5070_s3126_r9364_r9315_p3387	e5070_e5984_s3126_r10201_r10210_p3387
ttW	410155	ttlv	yes	e5070_s3126_r9364_r9315_p3387	e5070_e5984_s3126_r10201_r10210_p3387
tZ	410560		yes	e5803_s3126_r9364_r9315_p3401	e5803_e5984_s3126_r10201_r10210_p3401
VVV	364243:364249		yes	e5887_s3126_r9364_r9315_p3387	e5887_e5984_s3126_r10201_r10210_p3387
same-sign WW	364286		N/A	e6055_e5984_s3126_r9364_p3387	e6055_e5984_s3126_r10201_p3387
SingleTop	410642-410647		Different MC	e6536_e5984_a875_r9364_r9315_p3443	e6536_e5984_a875_r10201_r10210_p3443
WWW	364336-364340	WWW-2l	no	e6377_e5984_s3126_r9364_r9315_p3404	e6377_e5984_s3126_r10201_r10210_p3404
	341421-341436	WH-WWW	no	e4210_e5984_s3126_r9364_r9315_p3387/p3404	e4210_e5984_s3126_r10201_r10210_p3387
	364242	WWW-3l	yes	e5887_s3126_r9364_r9315_p3387	e5887_e5984_s3126_r10201_r10210_p3404
tt	410470	nonallhad		e6337_e5984_s3126_r9364_r9315_p3387	e6337_e5984_s3126_r10201_r10210_p3401
Z+jets	364100-364141			e5271_s3126_r9364_r9315_p3387	e5307_e5984_s3126_r10201_r10210_p3387
W+jets	364156-364197			e5340_s3126_r9364_r9315_p3387	e5307_e5984_s3126_r10201_r10210_p3387
W $\gamma$	364521-364535			e5928_e5984_s3126_r9364_r9315_p3387	e5928_e5984_s3126_r10201_r10210_p3387
Z $\gamma$	364500-364514			e5928_e5984_s3126_r9364_r9315_p3387	e5984_s3126_r10201_r10210_p3387

Table A.1: List of DSIDs and MC tags that are being used for all MC samples in the 13 TeV analysis. For all samples the DAOD.SUSY2 derivation has been used.

Sample	Generator	Sample type	Cross-Section [pb]	k-factor	Event filter efficiency	used in signal region
167007	MadGraphPythia	ZWWStar ll $\nu$ ll $\nu$	0.0015546	1	1	Yes
167008	MadGraphPythia	ZZZStar nunullll	0.00033239	1	1	Yes
145161	Sherpa	eegammaPt10	32.26	1	1	Yes
145162	Sherpa	mumugammaPt10	32.317	1	1	Yes
146436	AlpGenJimmy	Wgamma Np0	229.88	1.15	0.31372	No
146437	AlpGenJimmy	Wgamma Np1	59.518	1.15	0.44871	No
146438	AlpGenJimmy	Wgamma Np2	21.39	1.15	0.54461	No
146439	AlpGenJimmy	Wgamma Np3	7.1203	1.15	0.62974	No
126928	PowhegPythia8	WpWm ee	0.62	1.0	1	No
126929	PowhegPythia8	WpWm me	0.62	1.0	1	No
126930	PowhegPythia8	WpWm te	0.62	1.0	1	No
126931	PowhegPythia8	WpWm em	0.62	1.0	1	No
126932	PowhegPythia8	WpWm mm	0.62	1.0	1	No
126933	PowhegPythia8	WpWm tm	0.62	1.0	1	No
126934	PowhegPythia8	WpWm et	0.62	1.0	1	No
126935	PowhegPythia8	WpWm mt	0.62	1.0	1	No
126936	PowhegPythia8	WpWm tt	0.62	1.0	1	No
185813	PowhegPythia8	ZZ 4e ml4 TriLeptonFilter	0.07677	1	0.57204	Yes
185814	PowhegPythia8	ZZ 2e2mu ml4 TriLeptonFilter	0.1757	1	0.49893	Yes
185815	PowhegPythia8	ZZ 2e2tau ml4 TriLeptonFilter	0.1757	1	0.086032	Yes
185816	PowhegPythia8	ZZ 4mu ml4 TriLeptonFilter	0.07677	1	0.58293	Yes
185817	PowhegPythia8	ZZ 2mu2tau ml4 TriLeptonFilter	0.1757	1	0.087166	Yes
185818	PowhegPythia8	ZZ 4tau ml4 TriLeptonFilter	0.07677	1	0.0076557	Yes

181471	Sherpa	$ZZ^* \rightarrow eeee$ $m_{Z,1} > 4$ GeV, $m_{Z,2} < 4$ GeV	2.8286	0.880	1.0	No
181472	Sherpa	$ZZ^* \rightarrow ee\mu\mu$ $m_{Z,1} > 4$ GeV, $m_{Z,2} < 4$ GeV	2.34503	0.880	1.0	No
181473	Sherpa	$ZZ^* \rightarrow eett$ $m_{Z,1} > 4$ GeV, $m_{Z,2} < 4$ GeV	1.59326	0.880	1.0	No
181474	Sherpa	$ZZ^* \rightarrow \mu\mu ee$ $m_{Z,1} > 4$ GeV, $m_{Z,2} < 4$ GeV	0.48613	0.880	1.0	No
181475	Sherpa	$ZZ^* \rightarrow \mu\mu\mu\mu$ $m_{Z,1} > 4$ GeV, $m_{Z,2} < 4$ GeV	0.50835	0.880	1.0	No
181476	Sherpa	$ZZ^* \rightarrow \mu\mu\tau\tau$ $m_{Z,1} > 4$ GeV, $m_{Z,2} < 4$ GeV	0.42288	0.880	1.0	No
181477	Sherpa	$ZZ^* \rightarrow \tau\tau ee$ $m_{Z,1} > 4$ GeV, $m_{Z,2} < 4$ GeV	0.00403	0.880	1.0	No
181478	Sherpa	$ZZ^* \rightarrow \tau\tau\mu\mu$ $m_{Z,1} > 4$ GeV, $m_{Z,2} < 4$ GeV	0.00401	0.880	1.0	No
181479	Sherpa	$ZZ^* \rightarrow \tau\tau\tau\tau$ $m_{Z,1} > 4$ GeV, $m_{Z,2} < 4$ GeV	0.00411	0.880	1.0	No
126949	PowhegPythia8	ZZlnunu ee ml4	0.168	1	1	No
126950	PowhegPythia8	ZZlnunu mm ml4	0.168	1	1	No
126951	PowhegPythia8	ZZlnunu tt ml4	0.168	1	1	No
185795	PowhegPythia8	WmZ 3e ml0p25 TriLeptonFilter	0.9655	1	0.051928	Yes
185796	PowhegPythia8	WmZ e2mu ml0p4614 TriLeptonFilter	0.6326	1	0.073874	Yes
185797	PowhegPythia8	WmZ e2tau ml3p804 TriLeptonFilter	0.1125	1	0.012544	Yes
185798	PowhegPythia8	WmZ mu2e ml0p25 TriLeptonFilter	0.9687	1	0.054302	Yes
185799	PowhegPythia8	WmZ 3mu ml0p4614 TriLeptonFilter	0.6479	1	0.071268	Yes
185800	PowhegPythia8	WmZ mu2tau ml3p804 TriLeptonFilter	0.1125	1	0.01258	Yes
185801	PowhegPythia8	WmZ tau2e ml0p25 TriLeptonFilter	0.9687	1	0.012075	Yes
185802	PowhegPythia8	WmZ tau2mu ml0p4614 TriLeptonFilter	0.6326	1	0.01664	Yes
185803	PowhegPythia8	WmZ 3tau ml3p804 TriLeptonFilter	0.1108	1	0.0034037	Yes
185804	PowhegPythia8	WpZ 3e ml0p25 TriLeptonFilter	1.416	1	0.053051	Yes
185805	PowhegPythia8	WpZ e2mu ml0p4614 TriLeptonFilter	0.9421	1	0.075904	Yes
185806	PowhegPythia8	WpZ e2tau ml3p804 TriLeptonFilter	0.1755	1	0.013867	Yes
185807	PowhegPythia8	WpZ mu2e ml0p25 TriLeptonFilter	1.412	1	0.055296	Yes
185808	PowhegPythia8	WpZ 3mu ml0p4614 TriLeptonFilter	0.9572	1	0.073362	Yes
185809	PowhegPythia8	WpZ mu2tau ml3p804 TriLeptonFilter	0.1755	1	0.013891	Yes
185810	PowhegPythia8	WpZ tau2e ml0p25 TriLeptonFilter	1.412	1	0.012105	Yes
185811	PowhegPythia8	WpZ tau2mu ml0p4614 TriLeptonFilter	0.9421	1	0.016718	Yes
185812	PowhegPythia8	WpZ 3tau ml3p804 TriLeptonFilter	0.172	1	0.0036427	Yes
116600	gg2ZZJimmy	ZZ4lep	0.00459	1	1	Yes
116601	gg2ZZJimmy	ZZ4e	0.000675	1	1	Yes
116602	gg2ZZJimmy	ZZ4mu	0.000675	1	1	Yes
116603	gg2ZZJimmy	ZZ2e2mu	0.00134539	1	1	Yes
169471	gg2wwJimmy	WpWmenuenu	0.017	1	1	No
169472	gg2wwJimmy	WpWmenumunu	0.017	1	1	No
169473	gg2wwJimmy	WpWmenutaunu	0.017	1	1	No
169474	gg2wwJimmy	WpWmmunumunu	0.017	1	1	No
169475	gg2wwJimmy	WpWmmunuenue	0.017	1	1	No
169476	gg2wwJimmy	WpWmmunutaunu	0.017	1	1	No
169477	gg2wwJimmy	WpWmtaunutaunu	0.017	1	1	No
169478	gg2wwJimmy	WpWmtaunuenue	0.017	1	1	No
169479	gg2wwJimmy	WpWmtaunumunu	0.017	1	1	No
147280	Pythia8	DPI W W 2l	0.0258	1	0.48	Yes
147281	Pythia8	DPI W W 2l2j	0.0258	1	0.0752	Yes
147282	Pythia8	DPI W Z 2l	0.139	1	0.0539	Yes
147283	Pythia8	DPI W Z 2l2j	0.139	1	0.00873	Yes
147284	Pythia8	DPI W gamma 1l1gm	9.86	1	0.159	Yes
147285	Pythia8	DPI Z Z 2l	0.213	1	0.0547	Yes
147286	Pythia8	DPI Z Z 2l2j	0.213	1	0.00457	Yes
147287	Pythia8	DPI Z gamma 1l1gm	26.5	1	0.012	Yes
147288	Pythia8	DPI WZ dijet 2l2j	1.43	1	0.102	Yes
147289	Pythia8	DPI ZZ dijet 2l2j	1.86	1	0.0422	Yes
147290	Pythia8	DPI W diphoton 1l2gm	0.012	1	0.0632	Yes
147291	Pythia8	DPI Zl diphoton 1l2gm	0.00581	1	0.0259	Yes
147292	Pythia8	DPI Zvv diphoton 2gm	0.00221	1	0.0898	Yes
147293	Pythia8	DPI gamma gamma 2gm	943	1	0.00422	Yes
147770	Sherpa	Zee	1241.2	1	1	No
147771	Sherpa	Zmumu	1241.2	1	1	No
147772	Sherpa	Ztautau	1241.2	1	1	No
173041	Sherpa	DYeeM08to15	92.148	1	1	No
173042	Sherpa	DYeeM015to40	279.06	1	1	No
173043	Sherpa	DYmumuM015to40	92.097	1	1	No
173044	Sherpa	DYmumuM015to40	279.31	1	1	No
173045	Sherpa	DYtautauM015to40	92.121	1	1	No
173046	Sherpa	DYtautauM015to40	279.26	1	1	No
107680	AlpGenJimmy	WenuNp0	8037.1	1.19	1	No
107681	AlpGenJimmy	WenuNp1	1579.2	1.19	1	No
107682	AlpGenJimmy	WenuNp2	477.2	1.19	1	No
107683	AlpGenJimmy	WenuNp3	133.93	1.19	1	No
107684	AlpGenJimmy	WenuNp4	35.622	1.19	1	No
107685	AlpGenJimmy	WenuNp5	10.553	1.19	1	No
107690	AlpGenJimmy	WmumuNp0	8040	1.19	1	No

107691	AlpgeJimmy	WmunuNp1	1580.3	1.19	1	No
107692	AlpgeJimmy	WmunuNp2	477.5	1.19	1	No
107693	AlpgeJimmy	WmunuNp3	133.94	1.19	1	No
107694	AlpgeJimmy	WmunuNp4	35.636	1.19	1	No
107695	AlpgeJimmy	WmunuNp5	10.571	1.19	1	No
107700	AlpgeJimmy	WtaunuNp0	8035.8	1.19	1	No
107701	AlpgeJimmy	WtaunuNp1	1579.8	1.19	1	No
107702	AlpgeJimmy	WtaunuNp2	477.55	1.19	1	No
107703	AlpgeJimmy	WtaunuNp3	133.79	1.19	1	No
107704	AlpgeJimmy	WtaunuNp4	35.583	1.19	1	No
107705	AlpgeJimmy	WtaunuNp5	10.54	1.19	1	No
110001	McAtNloJimmy	ttbar dilepton	21.81	1.146	1	No
108343	McAtNloJimmy	SingleTopSChanWenu	0.564	1	1	No
108344	McAtNloJimmy	SingleTopSChanWmunu	0.564	1	1	No
108345	McAtNloJimmy	SingleTopSChanWtaunu	0.564	1	1	No
108346	McAtNloJimmy	SingleTopWtChanIncl	22.37	1	1	No
117360	AcerMCPythia	singletop tchan e	9.48	1	1	No
117361	AcerMCPythia	singletop tchan mu	9.48	1	1	No
117362	AcerMCPythia	singletop tchan tau	9.48	1	1	No
185878	MadGraphPythia	ttbarW Np0 3lep	0.0036	1	0.51933	Yes
185879	MadGraphPythia	ttbarW Np1 3lep	0.0032	1	0.53383	Yes
117489	MadGraphPythia	ttbarZ Np0 1lep	0.069058	1	0.6978	Yes
117490	MadGraphPythia	ttbarZ Np1 1lep	0.013819	1	0.908	Yes

Table A.2: List of MC types and DSID's that are being used for all MC samples in the 8 TeV  $\ell^{\pm} \nu \ell^{\pm} \nu$  analysis.

Sample Name	Reconstruction Tag	Cross Section (pb)	k-Factor	Filter Efficiency
Diboson Samples				
mc12.8TeV.185393.Sherpa_CT10.lnln.ls_EWK_MassiveCB.merge	e2504_s1773_s1776_r4485_r4540_p1328/	0.02762	0.8356	1.0
mc12.8TeV.147193.Sherpa_CT10.lnlnjj.WWjj_EW6.merge	e1613_s1499_s1504_r3658_r3549_p1328/	0.09588	1.0	1.0
mc12.8TeV.185396.Sherpa_CT10.llnu.WZ_EWK_MassiveCB.merge	e2486_s1773_s1776_r4485_r4540_p1328/	0.082102	0.8944	1.0
mc12.8TeV.161982.Sherpa_CT10.llnu.ZZ_EW6.merge	e1434_s1499_s1504_r3658_r3549_p1328/	0.0041	1.0	1.0
mc12.8TeV.147196.Sherpa_CT10.lllnjj.ZZjj_EW6	e1613_s1499_s1504_r3658_r3549_p1328/	0.00691	1.0	1.0
mc12.8TeV.185394.Sherpa_CT10.lnln.ls_QCD_MassiveCB.merge	e2494_s1773_s1776_r4485_r4540_p1328/	0.01608	1.0354	1.0
mc12.8TeV.126892.Sherpa_CT10.llnu.WW	e1434_s1499_s1504_r3658_r3549_p1328/	5.4982	1.06	1.0
mc12.8TeV.179974.Sherpa_CT10.llnu.WZ_MassiveCB.merge	e2203_s1581_s1586_r4485_r4540_p1328/	9.7446	1.2704	1.0
mc12.8TeV.185397.Sherpa_CT10.llnu.WZ_l10_MassiveCB.merge	e2486_s1773_s1776_r4485_r4540_p1328/	9.7446	1.2704	0.24041
mc12.8TeV.126895.Sherpa_CT10.llnu.ZZ	e1434_s1499_s1504_r3658_r3549_p1328/	0.4962	1.05	1.0
mc12.8TeV.126894.Sherpa_CT10.llln.ZZ	e1434_s1499_s1504_r3658_r3549_p1328/	8.7345	1.0	1.0
Top Quark Samples				
mc12.8TeV.110001.McAtNloJimmy_CT10.tbar_dilepton	e1576_s1499_s1504_r3658_r3549_p1328/	238.06	1.0	1.0
mc12.8TeV.105200.McAtNloJimmy_CT10.tbar_LeptonFilter	e1576_s1499_s1504_r3658_r3549_p1328/	238.06	1.0	1.0
mc12.8TeV.105204.McAtNloJimmy_AUET2CT10.tbar_allhad	e1513_s1499_s1504_r3945_r3549_p1328/	238.06	1.0	1.0
mc12.8TeV.119353.MadGraphPythia_AUET2BCTEQ6L1.tbarW	e1576_s1499_s1504_r3658_r3549_p1328/	0.1041	1.18	1.0
mc12.8TeV.174830.MadGraphPythia_AUET2BCTEQ6L1.tbarWjExcl	e1672_s1499_s1504_r3658_r3549_p1328/	0.053372	1.18	1.0
mc12.8TeV.174831.MadGraphPythia_AUET2BCTEQ6L1.tbarWjjIncl	e1672_s1499_s1504_r3658_r3549_p1328/	0.041482	1.18	1.0
mc12.8TeV.119355.MadGraphPythia_AUET2BCTEQ6L1.tbarZ	e1352_s1499_s1504_r3658_r3549_p1328/	0.0678	1.34	1.0
mc12.8TeV.174832.MadGraphPythia_AUET2BCTEQ6L1.tbarZjExcl	e1672_s1499_s1504_r3658_r3549_p1328/	0.045357	1.34	1.0
mc12.8TeV.174833.MadGraphPythia_AUET2BCTEQ6L1.tbarZjjIncl	e1672_s1499_s1504_r3658_r3549_p1328/	0.039772	1.34	1.0
mc12.8TeV.108343.McAtNloJimmy_CT10NLOME_AUET2CTEQ6L1MPI.SingleTopSChanWenu	e1525_s1499_s1504_r3658_r3549_p1328/	0.606	1.0	
mc12.8TeV.108344.McAtNloJimmy_CT10NLOME_AUET2CTEQ6L1MPI.SingleTopSChanWmunu	e1525_s1499_s1504_r3658_r3549_p1328/	0.606	1.0	1.0
mc12.8TeV.108345.McAtNloJimmy_CT10NLOME_AUET2CTEQ6L1MPI.SingleTopSChanWtaunu	e1525_s1499_s1504_r3658_r3549_p1328/	0.606	1.0	1.0
mc12.8TeV.108346.McAtNloJimmy_CT10NLOME_AUET2CTEQ6L1MPI.SingleTopWtChanIncl	e1525_s1499_s1504_r3658_r3549_p1328/	22.37	1.0	1.0
mc12.8TeV.117360.AcerMCPythia_AUET2BCTEQ6L1_singletop_tchan_e	e1346_s1499_s1504_r3658_r3549_p1328/	9.48	1.0	1.0
mc12.8TeV.117361.AcerMCPythia_AUET2BCTEQ6L1_singletop_tchan_mu	e1346_s1499_s1504_r3658_r3549_p1328/	9.48	1.0	1.0
mc12.8TeV.117362.AcerMCPythia_AUET2BCTEQ6L1_singletop_tchan_tau	e1346_s1499_s1504_r3658_r3549_p1328/	9.48	1.0	1.0
Z $\gamma^*$ +Jets Samples				
mc12.8TeV.107650.AlpGenJimmy_AUET2CTEQ6L1_ZeeNp0	e1218_s1469_s1470_r3542_r3549_p1328/	712.	1.23	1.0
mc12.8TeV.107651.AlpGenJimmy_AUET2CTEQ6L1_ZeeNp1	e1218_s1469_s1470_r3542_r3549_p1328/	155.	1.23	1.0
mc12.8TeV.107652.AlpGenJimmy_AUET2CTEQ6L1_ZeeNp2	e1218_s1469_s1470_r3542_r3549_p1328/	48.8	1.23	1.0
mc12.8TeV.107653.AlpGenJimmy_AUET2CTEQ6L1_ZeeNp3	e1218_s1469_s1470_r3542_r3549_p1328/	14.2	1.23	1.0
mc12.8TeV.107654.AlpGenJimmy_AUET2CTEQ6L1_ZeeNp4	e1218_s1469_s1470_r3542_r3549_p1328/	3.77	1.23	1.0
mc12.8TeV.107655.AlpGenJimmy_AUET2CTEQ6L1_ZeeNp5	e1218_s1469_s1470_r3542_r3549_p1328/	1.12	1.23	1.0
mc12.8TeV.107660.AlpGenJimmy_AUET2CTEQ6L1_ZmumuNp0	e1218_s1469_s1470_r3542_r3549_p1328/	712.	1.23	1.0
mc12.8TeV.107661.AlpGenJimmy_AUET2CTEQ6L1_ZmumuNp1	e1218_s1469_s1470_r3542_r3549_p1328/	155.	1.23	1.0
mc12.8TeV.107662.AlpGenJimmy_AUET2CTEQ6L1_ZmumuNp2	e1218_s1469_s1470_r3542_r3549_p1328/	48.8	1.23	1.0
mc12.8TeV.107663.AlpGenJimmy_AUET2CTEQ6L1_ZmumuNp3	e1218_s1469_s1470_r3542_r3549_p1328/	14.2	1.23	1.0
mc12.8TeV.107664.AlpGenJimmy_AUET2CTEQ6L1_ZmumuNp4	e1218_s1469_s1470_r3542_r3549_p1328/	3.77	1.23	1.0
mc12.8TeV.107665.AlpGenJimmy_AUET2CTEQ6L1_ZmumuNp5	e1218_s1469_s1470_r3542_r3549_p1328/	1.12	1.23	1.0
mc12.8TeV.107670.AlpGenJimmy_AUET2CTEQ6L1_ZtautauNp0	e1218_s1469_s1470_r3542_r3549_p1328/	712.	1.23	1.0
mc12.8TeV.107671.AlpGenJimmy_AUET2CTEQ6L1_ZtautauNp1	e1218_s1469_s1470_r3542_r3549_p1328/	155.	1.23	1.0
mc12.8TeV.107672.AlpGenJimmy_AUET2CTEQ6L1_ZtautauNp2	e1218_s1469_s1470_r3542_r3549_p1328/	48.8	1.23	1.0
mc12.8TeV.107673.AlpGenJimmy_AUET2CTEQ6L1_ZtautauNp3	e1218_s1469_s1470_r3542_r3549_p1328/	14.2	1.23	1.0
mc12.8TeV.107674.AlpGenJimmy_AUET2CTEQ6L1_ZtautauNp4	e1218_s1469_s1470_r3542_r3549_p1328/	3.77	1.23	1.0

mc12.8TeV.107675.AlpgenJimmy_AUET2CTEQ6L1.ZtautauNp5	e1218_s1469_s1470_r3542_r3549_p1328/	1.12	1.23	1.0
mc12.8TeV.109300.AlpgenJimmy_AUET2CTEQ6L1.ZeebbNp0	e1303_s1469_s1470_r3542_r3549_p1328/	8.378	1.23	1.0
mc12.8TeV.109301.AlpgenJimmy_AUET2CTEQ6L1.ZeebbNp1	e1303_s1469_s1470_r3542_r3549_p1328/	3.253	1.23	1.0
mc12.8TeV.109302.AlpgenJimmy_AUET2CTEQ6L1.ZeebbNp2	e1303_s1469_s1470_r3542_r3549_p1328/	1.190	1.23	1.0
mc12.8TeV.109303.AlpgenJimmy_AUET2CTEQ6L1.ZeebbNp3	e1303_s1469_s1470_r3542_r3549_p1328/	0.503	1.23	1.0
mc12.8TeV.109305.AlpgenJimmy_AUET2CTEQ6L1.ZmumubbNp0	e1303_s1469_s1470_r3542_r3549_p1328/	8.374	1.23	1.0
mc12.8TeV.109306.AlpgenJimmy_AUET2CTEQ6L1.ZmumubbNp1	e1303_s1469_s1470_r3542_r3549_p1328/	3.254	1.23	1.0
mc12.8TeV.109307.AlpgenJimmy_AUET2CTEQ6L1.ZmumubbNp2	e1303_s1469_s1470_r3542_r3549_p1328/	1.181	1.23	1.0
mc12.8TeV.109308.AlpgenJimmy_AUET2CTEQ6L1.ZmumubbNp3	e1303_s1469_s1470_r3752_r3549_p1328/	0.507	1.23	1.0
mc12.8TeV.109310.AlpgenJimmy_AUET2CTEQ6L1.ZtautauNp0	e1303_s1469_s1470_r3542_r3549_p1328/	8.376	1.23	1.0
mc12.8TeV.109311.AlpgenJimmy_AUET2CTEQ6L1.ZtautauNp1	e1303_s1469_s1470_r3752_r3549_p1328/	3.243	1.23	1.0
mc12.8TeV.109312.AlpgenJimmy_AUET2CTEQ6L1.ZtautauNp2	e1303_s1469_s1470_r3542_r3549_p1328/	1.194	1.23	1.0
mc12.8TeV.109313.AlpgenJimmy_AUET2CTEQ6L1.ZtautauNp3	e1303_s1469_s1470_r3542_r3549_p1328/	0.498	1.23	1.0
mc12.8TeV.126414.AlpgenJimmy_AUET2CTEQ6L1.ZeeccNp0	e1303_s1469_s1470_r3752_r3549_p1328/	15.654	1.23	1.0
mc12.8TeV.126415.AlpgenJimmy_AUET2CTEQ6L1.ZeeccNp1	e1303_s1469_s1470_r3542_r3549_p1328/	6.8946	1.23	1.0
mc12.8TeV.126416.AlpgenJimmy_AUET2CTEQ6L1.ZeeccNp2	e1303_s1469_s1470_r3542_r3549_p1328/	2.9204	1.23	1.0
mc12.8TeV.126417.AlpgenJimmy_AUET2CTEQ6L1.ZeeccNp3	e1303_s1469_s1470_r3542_r3549_p1328/	1.1411	1.23	1.0
mc12.8TeV.126418.AlpgenJimmy_AUET2CTEQ6L1.ZmumuccNp0	e1303_s1469_s1470_r3752_r3549_p1328/	15.649	1.23	1.0
mc12.8TeV.126419.AlpgenJimmy_AUET2CTEQ6L1.ZmumuccNp1	e1303_s1469_s1470_r3542_r3549_p1328/	6.8930	1.23	1.0
mc12.8TeV.126420.AlpgenJimmy_AUET2CTEQ6L1.ZmumuccNp2	e1303_s1469_s1470_r3542_r3549_p1328/	2.9176	1.23	1.0
mc12.8TeV.126421.AlpgenJimmy_AUET2CTEQ6L1.ZmumuccNp3	e1303_s1469_s1470_r3542_r3549_p1328/	1.1377	1.23	1.0
mc12.8TeV.117706.AlpgenJimmy_AUET2CTEQ6L1.ZtautauNp0	e1303_s1469_s1470_r3542_r3549_p1328/	15.652	1.23	1.0
mc12.8TeV.117707.AlpgenJimmy_AUET2CTEQ6L1.ZtautauNp1	e1303_s1469_s1470_r3542_r3549_p1328/	6.8979	1.23	1.0
mc12.8TeV.117708.AlpgenJimmy_AUET2CTEQ6L1.ZtautauNp2	e1303_s1469_s1470_r3542_r3549_p1328/	2.9100	1.23	1.0
mc12.8TeV.117709.AlpgenJimmy_AUET2CTEQ6L1.ZtautauNp3	e1303_s1469_s1470_r3542_r3549_p1328/	1.1340	1.23	1.0
mc12.8TeV.146830.AlpgenJimmy_Auto_AUET2CTEQ6L1.ZeeNp0Excl.MII10to60	e1254_s1469_s1470_r3542_r3549_p1328/	3480.	1.19	1.0
mc12.8TeV.146831.AlpgenJimmy_Auto_AUET2CTEQ6L1.ZeeNp1Excl.MII10to60	e1254_s1469_s1470_r3542_r3549_p1328/	110.	1.19	1.0
mc12.8TeV.146832.AlpgenJimmy_Auto_AUET2CTEQ6L1.ZeeNp2Excl.MII10to60	e1254_s1469_s1470_r3542_r3549_p1328/	52.3	1.19	1.0
mc12.8TeV.146833.AlpgenJimmy_Auto_AUET2CTEQ6L1.ZeeNp3Excl.MII10to60	e1254_s1469_s1470_r3542_r3549_p1328/	11.3	1.19	1.0
mc12.8TeV.146834.AlpgenJimmy_Auto_AUET2CTEQ6L1.ZeeNp4Excl.MII10to60	e1274_s1469_s1470_r3542_r3549_p1328/	2.59	1.19	1.0
mc12.8TeV.146835.AlpgenJimmy_Auto_AUET2CTEQ6L1.ZeeNp5Incl.MII10to60	e1274_s1469_s1470_r3542_r3549_p1328/	0.693	1.19	1.0
mc12.8TeV.146840.AlpgenJimmy_Auto_AUET2CTEQ6L1.ZmumuNp0Excl.MII10to60	e1254_s1469_s1470_r3542_r3549_p1328/	3480.	1.19	1.0
mc12.8TeV.146841.AlpgenJimmy_Auto_AUET2CTEQ6L1.ZmumuNp1Excl.MII10to60	e1254_s1469_s1470_r3542_r3549_p1328/	110.	1.19	1.0
mc12.8TeV.146842.AlpgenJimmy_Auto_AUET2CTEQ6L1.ZmumuNp2Excl.MII10to60	e1254_s1469_s1470_r3542_r3549_p1328/	52.3	1.19	1.0
mc12.8TeV.146843.AlpgenJimmy_Auto_AUET2CTEQ6L1.ZmumuNp3Excl.MII10to60	e1254_s1469_s1470_r3542_r3549_p1328/	11.3	1.19	1.0
mc12.8TeV.146844.AlpgenJimmy_Auto_AUET2CTEQ6L1.ZmumuNp4Excl.MII10to60	e1274_s1469_s1470_r3542_r3549_p1328/	2.59	1.19	1.0
mc12.8TeV.146845.AlpgenJimmy_Auto_AUET2CTEQ6L1.ZmumuNp5Incl.MII10to60	e1274_s1469_s1470_r3542_r3549_p1328/	0.693	1.19	1.0
mc12.8TeV.146850.AlpgenJimmy_Auto_AUET2CTEQ6L1.ZtautauNp0Excl.MII10to60	e1254_s1469_s1470_r3542_r3549_p1328/	3480.	1.19	1.0
mc12.8TeV.146851.AlpgenJimmy_Auto_AUET2CTEQ6L1.ZtautauNp1Excl.MII10to60	e1254_s1469_s1470_r3542_r3549_p1328/	110.	1.19	1.0
mc12.8TeV.146852.AlpgenJimmy_Auto_AUET2CTEQ6L1.ZtautauNp2Excl.MII10to60	e1254_s1469_s1470_r3542_r3549_p1328/	52.3	1.19	1.0
mc12.8TeV.146853.AlpgenJimmy_Auto_AUET2CTEQ6L1.ZtautauNp3Excl.MII10to60	e1254_s1469_s1470_r3542_r3549_p1328/	11.3	1.19	1.0
mc12.8TeV.146854.AlpgenJimmy_Auto_AUET3CTEQ6L1.ZtautauNp4Excl.MII10to60	e1274_s1469_s1470_r3542_r3549_p1328/	2.59	1.19	1.0
mc12.8TeV.146855.AlpgenJimmy_Auto_AUET2CTEQ6L1.ZtautauNp5Incl.MII10to60	e1274_s1469_s1470_r3752_r3549_p1328/	0.693	1.19	1.0
W+Jets Samples				
mc12.8TeV.107680.AlpgenJimmy_AUET2CTEQ6L1.WenuNp0	e1218_s1469_s1470_r3542_r3549_p1328/	8037.1	1.18	1.0
mc12.8TeV.107681.AlpgenJimmy_AUET2CTEQ6L1.WenuNp1	e1218_s1469_s1470_r3542_r3549_p1328/	1579.2	1.18	1.0
mc12.8TeV.107682.AlpgenJimmy_AUET2CTEQ6L1.WenuNp2	e1218_s1469_s1470_r3542_r3549_p1328/	477.2	1.18	1.0
mc12.8TeV.107683.AlpgenJimmy_AUET2CTEQ6L1.WenuNp3	e1218_s1469_s1470_r3542_r3549_p1328/	133.9	1.18	1.0
mc12.8TeV.107684.AlpgenJimmy_AUET2CTEQ6L1.WenuNp4	e1218_s1469_s1470_r3542_r3549_p1328/	35.62	1.18	1.0

mc12.8TeV.107685.AlpgeJimmy_AUET2CTEQ6L1.WenuNp5	e1218_s1469_s1470_r3542_r3549_p1328/	10.55	1.18	1.0
mc12.8TeV.107690.AlpgeJimmy_AUET2CTEQ6L1.WmunuNp0	e1218_s1469_s1470_r3542_r3549_p1328/	8040.0	1.18	1.0
mc12.8TeV.107691.AlpgeJimmy_AUET2CTEQ6L1.WmunuNp1	e1218_s1469_s1470_r3542_r3549_p1328/	1580.3	1.18	1.0
mc12.8TeV.107692.AlpgeJimmy_AUET2CTEQ6L1.WmunuNp2	e1218_s1469_s1470_r3542_r3549_p1328/	477.5	1.18	1.0
mc12.8TeV.107693.AlpgeJimmy_AUET2CTEQ6L1.WmunuNp3	e1218_s1469_s1470_r3542_r3549_p1328/	133.9	1.18	1.0
mc12.8TeV.107694.AlpgeJimmy_AUET2CTEQ6L1.WmunuNp4	e1218_s1469_s1470_r3542_r3549_p1328/	35.64	1.18	1.0
mc12.8TeV.107695.AlpgeJimmy_AUET2CTEQ6L1.WmunuNp5	e1218_s1469_s1470_r3542_r3549_p1328/	10.57	1.18	1.0
mc12.8TeV.107700.AlpgeJimmy_AUET2CTEQ6L1.WtaunuNp0	e1218_s1469_s1470_r3542_r3549_p1328/	8035.8	1.18	1.0
mc12.8TeV.107701.AlpgeJimmy_AUET2CTEQ6L1.WtaunuNp1	e1218_s1469_s1470_r3542_r3549_p1328/	1579.8	1.18	1.0
mc12.8TeV.107702.AlpgeJimmy_AUET2CTEQ6L1.WtaunuNp2	e1218_s1469_s1470_r3542_r3549_p1328/	477.6	1.18	1.0
mc12.8TeV.107703.AlpgeJimmy_AUET2CTEQ6L1.WtaunuNp3	e1218_s1469_s1470_r3542_r3549_p1328/	133.8	1.18	1.0
mc12.8TeV.107704.AlpgeJimmy_AUET2CTEQ6L1.WtaunuNp4	e1218_s1469_s1470_r3542_r3549_p1328/	35.6	1.18	1.0
mc12.8TeV.107705.AlpgeJimmy_AUET2CTEQ6L1.WtaunuNp5	e1218_s1469_s1470_r3542_r3549_p1328/	10.5	1.18	1.0
mc12.8TeV.117284.AlpgeJimmy_AUET2CTEQ6L1.WccNp0	e1297_s1469_s1470_r3542_r3549_p1328/	150.2	1.18	1.0
mc12.8TeV.117285.AlpgeJimmy_AUET2CTEQ6L1.WccNp1	e1297_s1469_s1470_r3542_r3549_p1328/	132.7	1.18	1.0
mc12.8TeV.117286.AlpgeJimmy_AUET2CTEQ6L1.WccNp2	e1297_s1469_s1470_r3542_r3549_p1328/	71.8	1.18	1.0
mc12.8TeV.117287.AlpgeJimmy_AUET2CTEQ6L1.WccNp3	e1297_s1469_s1470_r3542_r3549_p1328/	30.3	1.18	1.0
mc12.8TeV.117293.AlpgeJimmy_AUET2CTEQ6L1.WcNp0	e1297_s1469_s1470_r3542_r3549_p1328/	807.9	1.18	1.0
mc12.8TeV.117294.AlpgeJimmy_AUET2CTEQ6L1.WcNp1	e1297_s1469_s1470_r3542_r3549_p1328/	267.6	1.18	1.0
mc12.8TeV.117295.AlpgeJimmy_AUET2CTEQ6L1.WcNp2	e1297_s1469_s1470_r3542_r3549_p1328/	69.8	1.18	1.0
mc12.8TeV.117296.AlpgeJimmy_AUET2CTEQ6L1.WcNp3	e1297_s1469_s1470_r3542_r3549_p1328/	20.6	1.18	1.0
mc12.8TeV.117297.AlpgeJimmy_AUET2CTEQ6L1.WcNp4	e1297_s1469_s1470_r3542_r3549_p1328/	4.3	1.18	1.0
mc12.8TeV.107280.AlpgeJimmy_AUET2CTEQ6L1.WbbNp0	e1297_s1469_s1470_r3752_r3549_p1328/	55.7	1.18	1.0
mc12.8TeV.107281.AlpgeJimmy_AUET2CTEQ6L1.WbbNp1	e1297_s1469_s1470_r3752_r3549_p1328/	45.2	1.18	1.0
mc12.8TeV.107282.AlpgeJimmy_AUET2CTEQ6L1.WbbNp2	e1297_s1469_s1470_r3542_r3549_p1328/	23.3	1.18	1.0
mc12.8TeV.107283.AlpgeJimmy_AUET2CTEQ6L1.WbbNp3	e1297_s1469_s1470_r3542_r3549_p1328/	11.1	1.18	1.0
W + $\gamma$ Samples				
mc12.8TeV.146436.AlpgeJimmy_AUET2CTEQ6L1.WgammaNp0_LeptonPhotonFilter	e1260_s1469_s1470_r3542_r3549_p1328/	230.	1.15	0.314
mc12.8TeV.146437.AlpgeJimmy_AUET2CTEQ6L1.WgammaNp1_LeptonPhotonFilter	e1260_s1469_s1470_r3542_r3549_p1328/	59.5	1.15	0.449
mc12.8TeV.146438.AlpgeJimmy_AUET2CTEQ6L1.WgammaNp2_LeptonPhotonFilter	e1260_s1469_s1470_r3542_r3549_p1328/	21.4	1.15	0.545
mc12.8TeV.146439.AlpgeJimmy_AUET2CTEQ6L1.WgammaNp3_LeptonPhotonFilter	e1293_s1469_s1470_r3542_r3549_p1328/	7.12	1.15	0.630
mc12.8TeV.146434.AlpgeJimmy_AUET2CTEQ6L1.WgammaNp4	e1293_s1469_s1470_r3542_r3549_p1328/	2.12	1.15	1.0
mc12.8TeV.146435.AlpgeJimmy_AUET2CTEQ6L1.WgammaNp5	e1293_s1469_s1470_r3542_r3549_p1328/	0.467	1.15	1.0
mc12.8TeV.185304.Sherpa_CT10.Wenugamma2jetVBS.merge	e2366_s1581_s1586_r4485_r4540_p1328/	0.4496	1.0	1.0
mc12.8TeV.185305.Sherpa_CT10.Wmunugamma2jetVBS.merge	e2366_s1581_s1586_r4485_r4540_p1328/	0.4496	1.0	1.0
mc12.8TeV.185306.Sherpa_CT10.Wtaunugamma2jetVBS.merge	e2366_s1581_s1586_r4485_r4540_p1328/	0.4496	1.0	1.0
DPI Samples				
mc12.8TeV.147281.Pythia8_AU2CTEQ6L1.DPI.W_Z_2l2j	e1720_s1581_s1586_r3658_r3549_p1328/	0.0258	1.0	0.0752
mc12.8TeV.147283.Pythia8_AU2CTEQ6L1.DPI.W_Z_2l2j	e1720_s1581_s1586_r3658_r3549_p1328/	0.139	1.0	0.00873
mc12.8TeV.147286.Pythia8_AU2CTEQ6L1.DPI.Z_Z_2l2j	e1720_s1581_s1586_r3658_r3549_p1328/	0.213	1.0	0.00457
mc12.8TeV.147288.Pythia8_AU2CTEQ6L1.DPI.W_Z_dijet_2l2j	e1720_s1581_s1586_r3658_r3549_p1328/	1.43	1.0	0.102
mc12.8TeV.147289.Pythia8_AU2CTEQ6L1.DPI.ZZ_dijet_2l2j	e1720_s1581_s1586_r3658_r3549_p1328/	1.86	1.0	0.0422
W <sup>±</sup> W <sup>±</sup> W <sup>±</sup> Samples				
mc12.8TeV.185863.VBFNLOPythia8_AU2CTEQ6L1.WpWpWm_lvlvqq_0jExclusive.merge.NTUP.SMWZ	e3173_s1773_s1776_r4485_r4540_p1328_tid01573101_00	.001137	1.539	1
mc12.8TeV.185864.VBFNLOPythia8_AU2CTEQ6L1.WpWpWm_lvlvqq_1jInclusive.merge.NTUP.SMWZ	e3173_s1773_s1776_r4485_r4540_p1328_tid01573099_00	.003485	1.539	1
mc12.8TeV.185865.VBFNLOPythia8_AU2CTEQ6L1.WmWmWp_lvlvqq_0jExclusive.merge.NTUP.SMWZ	e3173_s1773_s1776_r4485_r4540_p1328_tid01573098_00	.000607	1.45	1
mc12.8TeV.185866.VBFNLOPythia8_AU2CTEQ6L1.WmWmWp_lvlvqq_1jInclusive.merge.NTUP.SMWZ	e3173_s1773_s1776_r4485_r4540_p1328_tid01573100_00	.001795	1.45	1

Table A.3: List of MC types and Full names that are being used for all MC samples in the 8TeV  $\ell^{\pm}v\ell^{\pm}vjj$  analysis.

# Bibliography

- [1] The ATLAS Collaboration. “Search for triboson  $W^\pm W^\pm W^\mp$  production in  $pp$  collisions at  $\sqrt{s} = 8$  TeV with the ATLAS detector”. In: *The European Physical Journal C* 77.3 (Mar. 2017), p. 141. ISSN: 1434-6052. DOI: [10.1140/epjc/s10052-017-4692-1](https://doi.org/10.1140/epjc/s10052-017-4692-1).
- [2] The ATLAS Collaboration. “Evidence for the production of three massive vector bosons with the ATLAS detector”. In: (2019). arXiv: [1903.10415](https://arxiv.org/abs/1903.10415) [hep-ex].
- [3] Andrea Sciandra. “Probing the Standard Model of particle physics with ttH, WWZ and WZZ multilepton final states”. PhD thesis. Universitat Bonn, 2019.
- [4] Andrew Purcell. “Go on a particle quest at the first CERN webfest. Le premier webfest du CERN se lance a la conquete des particules”. In: BUL-NA-2012-269. 35/2012 (Aug. 2012), p. 10. URL: <https://cds.cern.ch/record/1473657>.
- [5] Emmy Noether. “Invariant variation problems”. In: *Transport Theory and Statistical Physics* 1.3 (1971), pp. 186–207. DOI: [10.1080/00411457108231446](https://doi.org/10.1080/00411457108231446).
- [6] Antonio Pich. “The Standard model of electroweak interactions”. In: [1(2007)]. 2008. arXiv: [0705.4264](https://arxiv.org/abs/0705.4264) [hep-ph].
- [7] C. N. Yang and R. L. Mills. “Conservation of Isotopic Spin and Isotopic Gauge Invariance”. In: *Phys. Rev.* 96 (1 Oct. 1954), pp. 191–195. DOI: [10.1103/PhysRev.96.191](https://doi.org/10.1103/PhysRev.96.191). URL: <https://link.aps.org/doi/10.1103/PhysRev.96.191>.
- [8] Steven Weinberg. “A Model of Leptons”. In: *Phys. Rev. Lett.* 19 (21 Nov. 1967), pp. 1264–1266. DOI: [10.1103/PhysRevLett.19.1264](https://doi.org/10.1103/PhysRevLett.19.1264).
- [9] M. Tanabashi et al. “Review of Particle Physics”. In: *Phys. Rev. D* 98 (3 Aug. 2018), p. 030001. DOI: [10.1103/PhysRevD.98.030001](https://doi.org/10.1103/PhysRevD.98.030001).
- [10] Ulf-G. Meissner. “Chiral QCD: baryon dynamics”. In: (2000), pp. 417–505. DOI: [10.1142/9789812810458\\_0015](https://doi.org/10.1142/9789812810458_0015). arXiv: [hep-ph/0007092](https://arxiv.org/abs/hep-ph/0007092) [hep-ph].



- [11] F. Englert and R. Brout. “Broken Symmetry and the Mass of Gauge Vector Mesons”. In: *Phys. Rev. Lett.* 13 (9 Aug. 1964), pp. 321–323. DOI: [10.1103/PhysRevLett.13.321](https://doi.org/10.1103/PhysRevLett.13.321).
- [12] Peter W. Higgs. “Broken Symmetries and the Masses of Gauge Bosons”. In: *Phys. Rev. Lett.* 13 (16 Oct. 1964), pp. 508–509. DOI: [10.1103/PhysRevLett.13.508](https://doi.org/10.1103/PhysRevLett.13.508).
- [13] Paul Langacker. *The Standard Model and Beyond*. 2017. DOI: [10.1201/b22175](https://doi.org/10.1201/b22175).
- [14] O. J. P. Eboli, M. C. Gonzalez-Garcia, and J. K. Mizukoshi. “ $pp \rightarrow jje^\pm\mu^\pm\nu\nu$  and  $jje^\pm\mu^\mp\nu\nu$  at  $\mathcal{O}(\alpha_{\text{em}}^6)$  and  $\mathcal{O}(\alpha_{\text{em}}^4\alpha_s^2)$  for the study of the quartic electroweak gauge boson vertex at CERN LHC”. In: *Phys. Rev. D* 74 (2006), p. 073005. DOI: [10.1103/PhysRevD.74.073005](https://doi.org/10.1103/PhysRevD.74.073005). arXiv: [hep-ph/0606118](https://arxiv.org/abs/hep-ph/0606118) [hep-ph].
- [15] O. J. P. Eboli, M. C. Gonzalez-Garcia, and S. M. Lietti. “Bosonic quartic couplings at CERN LHC”. In: *Phys. Rev. D* 69 (2004), p. 095005. DOI: [10.1103/PhysRevD.69.095005](https://doi.org/10.1103/PhysRevD.69.095005). arXiv: [hep-ph/0310141](https://arxiv.org/abs/hep-ph/0310141) [hep-ph].
- [16] Lyndon Evans and Philip Bryant. “LHC Machine”. In: *Journal of Instrumentation* 3.08 (Aug. 2008), S08001–S08001. DOI: [10.1088/1748-0221/3/08/s08001](https://doi.org/10.1088/1748-0221/3/08/s08001).
- [17] Roderik Bruce et al. “LHC Run 2: Results and challenges”. In: CERN-ACC-2016-0103 (July 2016), MOAM5P50. 7 p. URL: <http://cds.cern.ch/record/2201447>.
- [18] The ATLAS Collaboration. *ATLAS Experiment Public Results*. Accessed: 2019-01-10. URL: <https://twiki.cern.ch/twiki/bin/view/AtlasPublic/LuminosityPublicResultsRun2>.
- [19] Michael Richmond. *The LHC is not going to destroy the Earth*. Accessed: 2019-01-10. URL: <http://spiff.rit.edu/richmond/asras/lhc/lhc.html>.
- [20] The ATLAS Collaboration. “The ATLAS Experiment at the CERN Large Hadron Collider”. In: *Journal of Instrumentation* 3.08 (2008), S08003. URL: <http://stacks.iop.org/1748-0221/3/i=08/a=S08003>.
- [21] The CMS Collaboration. “The CMS experiment at the CERN LHC”. In: *Journal of Instrumentation* 3.08 (Aug. 2008), S08004–S08004. DOI: [10.1088/1748-0221/3/08/s08004](https://doi.org/10.1088/1748-0221/3/08/s08004).
- [22] The ALICE Collaboration. “The ALICE experiment at the CERN LHC”. In: *Journal of Instrumentation* 3.08 (Aug. 2008), S08002–S08002. DOI: [10.1088/1748-0221/3/08/s08002](https://doi.org/10.1088/1748-0221/3/08/s08002).

- [23] The LHCb Collaboration. “The LHCb Detector at the LHC”. In: *Journal of Instrumentation* 3.08 (Aug. 2008), S08005–S08005. DOI: [10.1088/1748-0221/3/08/s08005](https://doi.org/10.1088/1748-0221/3/08/s08005).
- [24] The TOTEM Collaboration. “The TOTEM Experiment at the CERN Large Hadron Collider”. In: *Journal of Instrumentation* 3.08 (Aug. 2008), S08007–S08007. DOI: [10.1088/1748-0221/3/08/s08007](https://doi.org/10.1088/1748-0221/3/08/s08007).
- [25] The LHCf Collaboration. “The LHCf detector at the CERN Large Hadron Collider”. In: *Journal of Instrumentation* 3.08 (Aug. 2008), S08006–S08006. DOI: [10.1088/1748-0221/3/08/s08006](https://doi.org/10.1088/1748-0221/3/08/s08006).
- [26] J. L. Pinfold. “The MoEDAL Experiment at the LHC - a New Light on the Terascale Frontier”. In: *J. Phys. Conf. Ser.* 631.1 (2015), p. 012014.
- [27] Joao Pequena. *Computer generated image of the whole ATLAS detector*. Image. 2008. URL: <https://cds.cern.ch/record/1095924/>.
- [28] The ATLAS Collaboration. *ATLAS inner detector: Technical Design Report, 1*. Technical Design Report ATLAS. Geneva: CERN, 1997. URL: <http://cds.cern.ch/record/331063>.
- [29] Joao Pequena. *Computer generated image of the ATLAS inner detector*. Image. 2008. URL: <https://cds.cern.ch/record/1095926>.
- [30] The ATLAS Collaboration. “The ATLAS Experiment at the CERN Large Hadron Collider”. In: *Journal of Instrumentation* 3.08 (2008). URL: <http://stacks.iop.org/1748-0221/3/i=08/a=S08003>.
- [31] The ATLAS Collaboration. “Mechanical construction and installation of the ATLAS tile calorimeter”. In: *Journal of Instrumentation* 8.11 (2013). URL: <http://stacks.iop.org/1748-0221/8/i=11/a=T11001>.
- [32] J del Peso. *Design and Performance of the ATLAS LAr Calorimeter*. Tech. rep. ATL-LARG-PROC-2011-003. Geneva: CERN, Sept. 2011. URL: <https://cds.cern.ch/record/1385899>.
- [33] The ATLAS Collaboration. *ATLAS muon spectrometer: Technical Design Report*. Technical Design Report ATLAS. Geneva: CERN, 1997. URL: <https://cds.cern.ch/record/331068>.
- [34] The ATLAS Collaboration. “Performance of the ATLAS trigger system in 2015”. In: *The European Physical Journal C* 77.5 (2017). DOI: [10.1140/epjc/s10052-017-4852-3](https://doi.org/10.1140/epjc/s10052-017-4852-3).

- [35] The ATLAS Collaboration. “The ATLAS Simulation Infrastructure”. In: *The European Physical Journal C* 70.3 (Dec. 2010), pp. 823–874. ISSN: 1434-6052. DOI: [10.1140/epjc/s10052-010-1429-9](https://doi.org/10.1140/epjc/s10052-010-1429-9).
- [36] The NNPDF collaboration. “Parton distributions for the LHC run II”. In: *Journal of High Energy Physics* 2015.4 (Apr. 2015), p. 40. ISSN: 1029-8479. DOI: [10.1007/JHEP04\(2015\)040](https://doi.org/10.1007/JHEP04(2015)040).
- [37] Torbjorn Sjostrand, Stephen Mrenna, and Peter Z. Skands. “A Brief Introduction to PYTHIA 8.1”. In: *Comput. Phys. Commun.* 178 (2008), p. 89. DOI: [10.1016/j.cpc.2008.01.036](https://doi.org/10.1016/j.cpc.2008.01.036).
- [38] S. Agostinelli et al. “GEANT4: A Simulation toolkit”. In: *Nucl. Instrum. Meth. A* 506 (2003), pp. 250–303. DOI: [10.1016/S0168-9002\(03\)01368-8](https://doi.org/10.1016/S0168-9002(03)01368-8).
- [39] The ATLAS Collaboration. *Slice of the ATLAS detector*. Image. Accessed: 2019-01-10. URL: [http://atlasexperiment.org/atlas\\_photos/selected-photos/events/eve\\_gen\\_0806\\_001.jpg](http://atlasexperiment.org/atlas_photos/selected-photos/events/eve_gen_0806_001.jpg).
- [40] T Cornelissen et al. “Concepts, Design and Implementation of the ATLAS New Tracking (NEWT)”. In: ATL-SOFT-PUB-2007-007. ATL-COM-SOFT-2007-002 (Mar. 2007). URL: <http://cds.cern.ch/record/1020106>.
- [41] The ATLAS Collaboration. “Reconstruction of primary vertices at the ATLAS experiment in Run 1 proton proton collisions at the LHC”. In: *The European Physical Journal C* 77.5 (May 2017), p. 332. ISSN: 1434-6052. DOI: [10.1140/epjc/s10052-017-4887-5](https://doi.org/10.1140/epjc/s10052-017-4887-5).
- [42] The ATLAS Collaboration. *Vertex Reconstruction Performance of the ATLAS Detector at 13TeV*. Tech. rep. ATL-PHYS-PUB-2015-026. Geneva, July 2015. URL: <http://cds.cern.ch/record/2037717>.
- [43] The ATLAS Collaboration. *Electron and photon reconstruction and performance in ATLAS using a dynamical, topological cell clustering-based approach*. Tech. rep. ATL-PHYS-PUB-2017-022. Geneva: CERN, Dec. 2017. URL: <http://cds.cern.ch/record/2298955>.
- [44] The ATLAS Collaboration. *Electron efficiency measurements with the ATLAS detector using the 2015 LHC proton proton collision data*. Tech. rep. ATLAS-CONF-2016-024. Geneva, June 2016. URL: <http://cds.cern.ch/record/2157687>.

- [45] Rustem Ospanov, Rhys Thomas Roberts, and Terry Richard Wyatt. *Tagging non-prompt electrons and muons*. Tech. rep. ATL-COM-PHYS-2016-1444. Geneva: CERN, Oct. 2016. URL: <https://cds.cern.ch/record/2220954>.
- [46] Christos Anastopoulos et al. *Electron identification and efficiency measurements in 2017 data*. Tech. rep. ATL-COM-PHYS-2018-1727. Geneva: CERN, Jan. 2019. URL: <https://cds.cern.ch/record/2652163>.
- [47] The ATLAS Collaboration. “Muon reconstruction performance of the ATLAS detector in proton proton collision data at 13TeV”. In: *The European Physical Journal C* 76.5 (May 2016). ISSN: 1434-6052. DOI: [10.1140/epjc/s10052-016-4120-y](https://doi.org/10.1140/epjc/s10052-016-4120-y).
- [48] The ATLAS Collaboration. “Muon reconstruction performance of the ATLAS detector in proton proton collision data at 13 TeV”. In: *The European Physical Journal C* 76.5 (May 2016), p. 292. ISSN: 1434-6052. DOI: [10.1140/epjc/s10052-016-4120-y](https://doi.org/10.1140/epjc/s10052-016-4120-y).
- [49] Johannes Josef Junggeburth and Nicolas Maximilian Koehler. *Muon reconstruction efficiency on full 2018 pp data set evaluated using  $Z \rightarrow \mu\mu$  events*. Tech. rep. ATL-COM-PHYS-2018-1624. Geneva: CERN, Nov. 2018. URL: <https://cds.cern.ch/record/2648573>.
- [50] Aliaksei Hrynevich. *ATLAS jet and missing energy reconstruction, calibration and performance in LHC Run-2*. Tech. rep. ATL-PHYS-PROC-2017-045. 06. Geneva: CERN, May 2017. URL: <https://cds.cern.ch/record/2263777>.
- [51] The ATLAS Collaboration. *Jet global sequential corrections with the ATLAS detector in proton proton collisions at  $\sqrt{s} = 8$  TeV*. Tech. rep. ATLAS-CONF-2015-002. Geneva: CERN, Mar. 2015. URL: <https://cds.cern.ch/record/2001682>.
- [52] Matteo Cacciari, Gavin P. Salam, and Gregory Soyez. “The anti- $k_t$  jet clustering algorithm”. In: *Journal of High Energy Physics* 2008.04 (2008), p. 063. URL: <http://stacks.iop.org/1126-6708/2008/i=04/a=063>.
- [53] The ATLAS Collaboration. “Measurements of b-jet tagging efficiency with the ATLAS detector using  $t\bar{t}$  at  $s=13$  TeV”. In: *Journal of High Energy Physics* 2018.8 (Aug. 2018), p. 89. ISSN: 1029-8479. DOI: [10.1007/JHEP08\(2018\)089](https://doi.org/10.1007/JHEP08(2018)089).

- [54] The ATLAS Collaboration. “Electron and photon energy calibration with the ATLAS detector using 2015-2016 LHC proton-proton collision data”. In: *JINST* 14.03 (2019), P03017. DOI: [10.1088/1748-0221/14/03/P03017](https://doi.org/10.1088/1748-0221/14/03/P03017). arXiv: 1812.03848 [hep-ex].
- [55] The ATLAS Collaboration. “Tagging and suppression of pileup jets”. In: (2014).
- [56] The ATLAS Collaboration. “Evidence for Electroweak Production of  $W^\pm W^\pm jj$  in  $pp$  Collisions at  $\sqrt{s} = 8$  TeV with the ATLAS Detector”. In: *Phys. Rev. Lett.* 113 (14 Oct. 2014), p. 141803. DOI: [10.1103/PhysRevLett.113.141803](https://doi.org/10.1103/PhysRevLett.113.141803).
- [57] The ATLAS Collaboration. “Measurement of  $W^\pm W^\pm$  vector-boson scattering and limits on anomalous quartic gauge couplings with the ATLAS detector”. In: *Phys. Rev. D* 96 (1 July 2017), p. 012007. DOI: [10.1103/PhysRevD.96.012007](https://doi.org/10.1103/PhysRevD.96.012007).
- [58] T. Gleisberg et al. “Event generation with SHERPA 1.1”. In: *JHEP* 0902 (2009), p. 007. DOI: [10.1088/1126-6708/2009/02/007](https://doi.org/10.1088/1126-6708/2009/02/007). arXiv: 0811.4622 [hep-ph].
- [59] Fabio Cascioli, Philipp Maierhofer, and Stefano Pozzorini. “Scattering Amplitudes with Open Loops”. In: *Phys. Rev. Lett.* 108 (2012), p. 111601. DOI: [10.1103/PhysRevLett.108.111601](https://doi.org/10.1103/PhysRevLett.108.111601). arXiv: 1111.5206 [hep-ph].
- [60] Gionata Luisoni et al. “ $HW^\pm/HZ + 0$  and 1 jet at NLO with the POWHEG BOX interfaced to GoSam and their merging within MiNLO”. In: *JHEP* 10 (2013), p. 083. DOI: [10.1007/JHEP10\(2013\)083](https://doi.org/10.1007/JHEP10(2013)083). arXiv: 1306.2542 [hep-ph].
- [61] Jun Gao et al. “CT10 next-to-next-to-leading order global analysis of QCD”. In: *Phys. Rev. D* 89.3 (2014), p. 033009. DOI: [10.1103/PhysRevD.89.033009](https://doi.org/10.1103/PhysRevD.89.033009). arXiv: 1302.6246 [hep-ph].
- [62] Andy Buckley et al. “Rivet user manual”. In: *Comput.Phys.Commun.* 184 (2013), pp. 2803–2819. DOI: [10.1016/j.cpc.2013.05.021](https://doi.org/10.1016/j.cpc.2013.05.021). arXiv: 1003.0694 [hep-ph].
- [63] Johan Alwall et al. “MadGraph 5 : Going Beyond”. In: *JHEP* 1106 (2011), p. 128. DOI: [10.1007/JHEP06\(2011\)128](https://doi.org/10.1007/JHEP06(2011)128). arXiv: 1106.0522 [hep-ph].
- [64] The ATLAS Collaboration. “Jet energy scale measurements and their systematic uncertainties in proton proton collisions at 13TeV with the ATLAS detector”. In: *Phys. Rev. D* 96 (7 Oct. 2017), p. 072002. URL: <https://link.aps.org/doi/10.1103/PhysRevD.96.072002>.

- [65] The ATLAS Collaboration. “Measurements of b-jet tagging efficiency with the ATLAS detector using  $t\bar{t}$  events at  $\sqrt{s} = 13$  TeV”. In: *JHEP* 08 (2018), p. 089. DOI: [10.1007/JHEP08\(2018\)089](https://doi.org/10.1007/JHEP08(2018)089). arXiv: [1805.01845](https://arxiv.org/abs/1805.01845) [hep-ex].
- [66] The ATLAS Collaboration. “Performance of missing transverse momentum reconstruction with the ATLAS detector using proton-proton collisions at  $\sqrt{s} = 13$  TeV”. In: *Eur. Phys. J. C* 78.11 (2018), p. 903. DOI: [10.1140/epjc/s10052-018-6288-9](https://doi.org/10.1140/epjc/s10052-018-6288-9). arXiv: [1802.08168](https://arxiv.org/abs/1802.08168) [hep-ex].
- [67] Jon Butterworth et al. “PDF4LHC recommendations for LHC Run II”. In: *J. Phys. G* 43 (2016), p. 023001. DOI: [10.1088/0954-3899/43/2/023001](https://doi.org/10.1088/0954-3899/43/2/023001). arXiv: [1510.03865](https://arxiv.org/abs/1510.03865) [hep-ph].
- [68] Jerome H. Friedman. “Greedy Function Approximation: A Gradient Boosting Machine”. In: *The Annals of Statistics* 29.5 (2001), pp. 1189–1232. ISSN: 00905364. URL: <http://www.jstor.org/stable/2699986>.
- [69] L. Moneta et al. “The RooStats project”. In: *Proceedings of the 13th International Workshop on Advanced Computing and Analysis Techniques in Physics Research. February 22-27. Jan. 2010*, p. 57. arXiv: [1009.1003](https://arxiv.org/abs/1009.1003) [physics.data-an].
- [70] Glen Cowan et al. “Asymptotic formulae for likelihood-based tests of new physics”. In: *Eur. Phys. J. C* 71 (2011). [Erratum: *Eur. Phys. J. C* 73,2501(2013)], p. 1554. DOI: [10.1140/epjc/s10052-011-1554-0](https://doi.org/10.1140/epjc/s10052-011-1554-0), [10.1140/epjc/s10052-013-2501-z](https://doi.org/10.1140/epjc/s10052-013-2501-z). arXiv: [1007.1727](https://arxiv.org/abs/1007.1727) [physics.data-an].
- [71] The ATLAS Collaboration. *Standard Model Summary Plots Spring 2019*. Tech. rep. ATL-PHYS-PUB-2019-010. Geneva: CERN, Mar. 2019. URL: <http://cds.cern.ch/record/2668559>.